

# Novel synthesis methods for the production of human circulating metabolites of natural products

being a Thesis submitted for the Degree of

Doctor of Philosophy

in the University of Hull

by

Bradley Doyle, MSc

July 2023

# Abstract

Upon entering the body, any given xenobiotic can undergo metabolism which facilitates its excretion from the body. When metabolised, a compound typically has the same effects of the initial drug/nutraceutical, however this is not always the case and can significantly differ. The determination of these beneficial and toxicological effects is vital to allow for effective drug development and to increase current knowledge of nutraceuticals. This is because contradictory knowledge of their pharmacological effects is often found. Currently there is no method available that allows for the synthesis of these compounds in useable quantities (mg). This study aimed to provide a method that can be used to simply synthesise these metabolic products in sufficient amounts for further testing.

Three different enzymes families (UGT1a1, SULT1a1 and CYP1a1) were immobilised *via* a silanization followed by a glutaraldehyde functionalization and tested. These were compared to a variety of different controls being excluding co-factor or enzyme from the system or immobilising an alternative unreactive enzyme towards the substrate. In each of the chapters it was determined that metabolite formation was only observed when both the correct enzyme and co-factor was available within the system. The true run for each enzyme was optimised at two different parameters: flow rate and temperature. For all three of the enzymes used the optimal temperature depicted in their recommended instructions was 37 °C.

The UDP-glucuronosyl transferase immobilised device showed no significant difference at any of the three tested flow rates. However, temperature showed a

significant difference oppositely to expected in which 37 °C yielded almost no product at all ( $97.9 \pm 38.5 \mu\text{M}$  substrate remaining), and both room temperature and 30 °C yielded significant conversion ( $11.0 \pm 8.0 \mu\text{M}$  and  $0.0 \pm 0.0 \mu\text{M}$  remaining respectively).

The Sulfotransferase immobilised device also showed no significant difference between any of the three tested flow rates. Temperature also yielded the contrary results to that which was expected and almost no product at all was formed ( $81.3 \pm 21.8 \mu\text{M}$  substrate remaining) and both room temperature and 30 °C yielded significant conversion ( $92.9 \pm 7.2$  and  $92.2 \pm 10.2 \mu\text{M}$  remaining respectively).

The cytochrome P450 based device showed no significant difference between any of the three tested flow rates, the further parameters were not tested due to fluorescence interference issues and further testing is needed.

The UGT and SULT devices were then compared to directly incubating both the substrate and co-factor with the enzyme. A 2-hour period for both methods yielded comparable results (0.22 ng in static conditions and 0.24 ng in flow conditions) but the formation of a complex biological matrix is not formed. Alongside this allowing the reaction to occur over a longer period of time (4 hours) the immobilised enzyme reactor continued to yield product in which the incubation method plateaued; leading to significantly higher metabolite formation (0.2 ng in static conditions and 0.47 ng in batch conditions). This data was not observed in the case of the CYP device due to a fluorescence interference observed in the effluent of the device preventing comparable measurements.

With further optimisation or scaling up of these devices they will likely be viable for the synthesis of sufficient quantities of metabolite to allow for pharmacological testing, with an improvement on the currently available methods by bypassing the necessary complex separation, high costs and commonly observed low yields.

# Acknowledgements

The last five years have been a journey, to say the least; a long-distance relationship, shared accommodation, COVID and becoming a father, all on top of the stresses of being a PhD student. Looking back at the start of my PhD to now, it's unbelievable how different my life is, which makes the journey I've been on seem even longer.

Thank you to the University of Hull and its scholarship programme for their financial support allowing me to complete this research, without your funding this would have not been possible; I am truly honoured to have been a part of the programme.

Nicole and Huw, thank you for believing in me to do this PhD, your feedback and continuous support have been second to none. You allowed me the flexibility to complete the research and your dedication to my studies allowed me to push myself outside my comfort zone, enabling me to achieve more than the PhD itself. Leigh, I am beyond grateful for you taking me on as a student and for all your support throughout the years. Your feedback always made me strive for more and enabled me to push myself further.

Alex, without your technical advice things wouldn't have gone as smoothly as they did! Thank you for fabricating the chips used throughout my research, I literally couldn't have done it without them. Dean, thank you for imparting your wisdom on the instruments used throughout this research. It was greatly appreciated!

Stephan, my best friend, thank you for your consistent support throughout our PhD journeys. Thank you for giving feedback and always being honest. Our friendship is something I will always cherish.

Nathan, my research brother. Thank you for your ideas and company throughout the years. It has been a pleasure working with you and I am grateful for the distractions when I've needed them the most! Working with the Feren's Laboratory Group has been a delight and I would like to thank my fellow members for keeping me sane during laboratory hours!

My family have been so supportive throughout my entire life but especially throughout my PhD, I am so grateful for their encouragement during my studies – it never went unnoticed.

Thank you to my fiancée, T; your support has been unmatched even though we spent more than half our time together 255 miles away, you never gave up on me or let me give up.

Last but not least, I would like to give special mention to my beautiful daughter, Aoife. Not only for giving me something to work for but for being the brightest light at the end of every tunnel.

# List of Abbreviations

Food and drug administration	FDA
High resolution mass spectrometry	HRMS
Cytochrome P450	CYP
Sulfotransferase	SULT
Catechol-o-methyl transferase	COMT
<i>N</i> -Arachidonoylphenolamine	AM404
<i>N</i> -Acetyl- <i>p</i> -benzoquinone imine	NAPQI
Molecular oxygen	O <sub>2</sub>
Morphine-3-glucuronide	M3G
Morphine-6-glucuronide	M6G
Sulfate	SO <sup>3-</sup>
3'-Phosphoadenosine-5'-phosphosulfate	PAPS
3', 5'-Diphosphoadenosine	PAP
Adenosine triphosphate	ATP
Adenosine 5'-phosphate	APS
Mass to charge ratio	m/z
Nuclear magnetic resonance	NMR
Ethoxyresorufin-O-deethylase	EROD
UDP-glucuronic acid	UDP-GA
<i>Escherichia coli</i>	<i>E. coli.</i>
Deoxyribonucleic acid	DNA
Isopropyl β- d-1-thiogalactopyranoside	IPTG
Dimethyl siloxane	DMSO
Fetal calf serum	FCS
High performance liquid chromatography	HPLC
Deionised	DI
Hydrofluoric acid	HF
Ultraviolet	UV
Polydimethyl siloxane	PDMS
Carbon dioxide	CO <sub>2</sub>
2-Dimensional	2D
3-Dimensional	3D
Amide	NH <sub>2</sub>
Carboxylic acid	COOH
3-Aminopropyl trimethoxysilane	APTMS
Liquid chromatography-mass spectrometer	LC-MS

Liquid chromatography-triple quadrupole mass Spectrometer	LC-TQ-MS
Polytetrafluoroethylene	PTFE
Outer diameter	OD
Inner diameter	ID
Computer aided design	CAD
Computer numerical control	CNC
Trifluoroacetic acid	TFA
Multiple reaction measurement	MRM
Analysis of Variance	ANOVA
Ultrapressure liquid chromatography	UPLC
Single ion monitoring	SIM
Product ion scan	ProIS
Precursor ion scan	PreIS
Tandem mass spectrometry	MS-MS
Triosephosphate isomerase	TPI
Standard deviation	SD
Liquid-liquid extraction	LLE
Immobilised microfluidic enzyme reactor	IMER
Nicotinamide adenine dinucleotide phosphate	NADPH
Dimethyl formamide	DMF
Dinitrophenol	DNP
Fourier transform infrared	FT-IR
Scanning electron microscopy	SEM

# Table of contents

## Contents

Abstract .....	i
Acknowledgements .....	iv
List of Abbreviations .....	vi
1. Motivation and State of the art .....	1
1.1.1. Drug metabolism.....	2
Metabolisms effect on drug pharmacological activity .....	4
Cytochrome P450s .....	5
UDP-Glucuronosyl transferases.....	6
Sulfotransferases .....	7
1.2. Substrate considerations for enzymatic conversion .....	9
1.3. Current methods for metabolite synthesis.....	11
In silico	11
Traditional organic synthesis.....	12
S9 fractions.....	13
Bacterial expression of enzymes .....	14
Liver cell incubations.....	15
Liver microsomes.....	17
1.4. Microfluidics.....	18
1.5. Fabrication of microfluidic devices.....	21
1.6. Application of microfluidics to metabolomics .....	27
1.7. Enzyme immobilisation techniques.....	29
1.8. Applied immobilisation of microsomal enzymes .....	34
1.9. Aims of thesis.....	40
1.10. Gap in the field.....	42
2. Experimental .....	44
2.1. Chemicals and materials.....	44
2.2. Device designing, preparing, interfacing and cleaning.....	47
2.3. Microfluidic substrate metabolism.....	50

2.4.	Conventional static metabolism .....	51
2.5.	Fluorescence analysis of resorufin .....	51
2.6.	LC-TQ-MS analysis of substrates and expected products.....	51
2.7.	Statistical analysis .....	54
3.	Optimisation of mass spectrometry for the determination of phase II metabolites and their precursors <i>via</i> LC-TQ-MS .....	56
3.1.	Introduction.....	56
3.2.	Methods.....	58
	Optimisation of fragments and collision energy .....	58
	Isocratic flow .....	60
	Gradient flow .....	61
3.3.	Results and Discussion .....	62
	Resorufin .....	62
	Resorufin glucuronide.....	69
	Mixture of resorufin and resorufin glucuronide.....	75
	Nitrophenol .....	81
	Nitrophenyl sulfate .....	88
	7-Ethoxyresorufin .....	95
3.4.	Comparison between isocratic and gradient.....	102
3.5.	Discussion .....	103
3.6.	Conclusion.....	109
4.	Optimisation of the synthesis of naturally occurring metabolites using UGT1a1 110	
4.1.	Introduction.....	110
4.2.	Experimental procedure .....	112
	Determination of resorufin concentration.....	112
	Determination of resorufins fluorometric properties.....	113
	Fabrication of microfluidic devices .....	113
	Immobilisation of UGT supersomes.....	114
	Metabolism of test substrates.....	114
	Mass spectrometry .....	116
	Methanol crash.....	117
	Liquid-liquid extraction (LLE).....	118
	C18 ZipTip extraction.....	118
4.3.	Results.....	119
	Plate reader analysis .....	119

Proof of product formation for UGT1a1 reactor.....	123
Flow rate .....	125
Effect of temperature on resorufin metabolism .....	126
Static vs. Flow .....	127
Product confirmation.....	128
4.4. Discussion.....	140
Optimisation of enzymatic reactor.....	140
4.5. Conclusion.....	144
5. Optimisation of a method for the synthesis of naturally occurring metabolites using SULT1a1 .....	146
5.1. Introduction.....	146
5.2. Experimental procedure .....	148
Microplate reader method.....	148
Fabrication of microfluidic devices .....	148
Immobilisation of SULT1a1 supersomes.....	148
Metabolism of test substrates.....	148
Mass spectrometry .....	149
5.3. Results.....	149
Comparison between controls and experimental enzymatic run .....	149
Comparison between devices and flow rates.....	150
Comparison between temperatures.....	152
Product confirmation .....	153
Static vs. Flow .....	158
5.4. Discussion .....	159
5.5. Conclusion.....	163
6. Optimisation of the synthesis of naturally occurring metabolites using CYP1a1	165
6.1. Introduction.....	165
6.2. Experimental procedure .....	167
Determination of resorufin concentration.....	167
Fabrication of microfluidic devices .....	167
Immobilisation of CYP1a1 supersomes.....	167
Metabolism of test substrates.....	167
Mass spectrometry .....	168
6.3. Results.....	168
CYP supersomes .....	168

Cypexpress.....	175
Product confirmation.....	180
Mass spectra semi-quantification.....	186
6.4. Discussion.....	188
6.5. Conclusion.....	191
7. General discussion.....	192
7.1. Limitations of this work.....	195
7.2. Future Work.....	198
8. Conclusion.....	202
References.....	204
Appendix.....	215

# 1. Motivation and State of the art

When a xenobiotic enters the human body it typically undergoes metabolism *via* enzymatic catalysis. There are two types of metabolism: phase I which involves the formation of reactive groups; and phase II which conjugates a hydrophilic compound to either the newly formed reactive site provided by phase I or *via* one of the already available sites. This metabolism typically does not have a large effect on a compound's pharmacological effect. However, this is not always the case and some can significantly differ from the original parent compound. In 2008 the US Food and Drug Administration (FDA) implemented the study of metabolites alongside the parent compound when developing a drug compound known as metabolites in safety testing (MIST). This has led to a shift in the focus of metabolic studies from the previously used radio chromatography for metabolite determination to high resolution mass spectrometry (HRMS).

Currently the study of a metabolite is only undertaken if it is found at a 10% higher concentration than those found in animal studies.<sup>1</sup> However, due to the infrequent large differences between a parent compound and its metabolite, it is likely that these rules will become even stricter and metabolic studies will potentially be required to take any compound to human testing and/or pharmacological use. Currently there is no single method that allows for the synthesis of a naturally forming metabolite in bulk and available synthesis methods come with their own deficits and downfalls. These typically suffer from extremely low yields and the necessity of an extremely complex separation of a single compound from similar isomer, or the original parent compound from within a biological matrix in which there is also not a universal method. The

studies on these metabolites have focussed on their rate of formation and concentrations within the body and no methods appear to be focusing on the synthesis of these compounds in large quantities. This is likely due to the FDA guidelines. Once these become stricter, another shift will (likely) occur, leading to the development of methods to form the needed quantities. Due to this there is currently a gap in the field in which no methods are synthesising large quantities of these products, preventing the metabolites from being widely available for pharmacological studies. The aim of this thesis is to develop a method that allows for the synthesis of these needed quantities to allow for a wide variety of studies to undergo both on the original parent compound and their metabolites, both independently and within a mixture.

### **1.1.1. Drug metabolism**

Based on cellular studies, many drug candidates do not yield the expected therapeutic effects in humans *in vivo* due to either inactivation or further activation *via* biotransformation.<sup>2</sup> This biotransformation naturally occurs in living organisms to facilitate the excretion of both exogenous and endogenous substances.<sup>3</sup> For a drug to yield any beneficial or toxicological effect it must be absorbed and distributed across various biological barriers at clinically relevant levels, before binding or interacting with a biological target.<sup>4</sup> This can lead to either target activation, inducing a response, or inactivation, preventing a response.<sup>5</sup> If a compound is hydrophilic, it is readily excreted *via* sweat, bile, faeces, and urine before reaching its biological target.<sup>6</sup> Whereas, if a compound is lipophilic, it typically penetrates the lipid bilayer of cellular membranes and can also be stored in fat tissues until metabolised. Due to this, typically lipophilic compounds are necessary for effective drug development, by allowing the compound

to be absorbed and distributed to the target organ/receptor prior to excretion,<sup>7</sup> resulting in the desired biological effects. Upon entering the liver, drugs are metabolised *via* biological catalysts (enzymes) naturally formed within living organisms.<sup>8</sup> Drug-metabolising enzymes are split into two groups, one of which involves revealing functional groups *via* reactions such as oxidation, reduction and hydrolysis and the latter facilitating conjugation of hydrophilic moieties such as glucuronic acid, sulfate and glutathione, leading to a more water-soluble compound.<sup>3, 9-11</sup> Upon the addition of these moieties the hydrophilicity of the resulting product largely increases allowing for excretion *via* urine or bile.<sup>12</sup>

There are a wide variety of drug-metabolism enzymes utilised within the body, the major being: Cytochrome P450 (CYP), UDP-glucuronosyl transferase (UGT), Sulfotransferase (SULT) and catechol-o-methyl transferase (COMT). The CYP family is predominantly utilised for oxidative and reductive reactions, whilst the UGT, SULT and COMT are conjugative enzymes (addition of a glucuronide, sulfate and methyl group respectively).<sup>13, 14</sup> Most given enzymes typically facilitate one specific reaction (an example exception to this rule being CYP, which facilitates multiple under the category of oxidation and reduction) and each of which is split into families which can each react differently to specific substrates, or can only conjugate to specific functional groups.<sup>15, 16</sup> Although this specificity exists there is still a wide amount of overlap between enzyme isomers (isozymes) and substrates especially with respect to xenobiotics.<sup>17</sup> For example CYP3A4 can metabolise more than 30% of drugs in addition to a wide variety of endogenous steroids.<sup>18</sup> Thus, whilst an enzyme has their specific substrates there is also cross-selectivity between them meaning the study of a specific isomer of an enzyme is suitable for the formation of metabolic products that

are seen *in vivo*, but is not representative for the determination of rates and metabolic yields frequently observed in human metabolic pathways.<sup>19, 20</sup>

## **Metabolisms effect on drug pharmacological activity**

CYP and UGT catalysed reactions have been much more extensively researched in comparison to SULT and COMT.<sup>21</sup> Figure.1.1 describes the metabolism of a commonly used drug utilised for pain relief, paracetamol. UGT1a1, UGT1a6, UGT1a9 and UGT2B15 all have the ability to facilitate paracetamol metabolism.<sup>22</sup> Paracetamol undergoes both oxidative and conjugative metabolisms separately.<sup>23</sup> The most common metabolite formed is paracetamol glucuronide, accounting for over 50%. Sulfation accounts for approximately 30% and oxidation 10% (Figure.1.1).<sup>24</sup> Although only AM404 of these metabolites provide the relevant analgesic effects paracetamol is commonly utilised for, metabolism *via* UGT and SULT have been shown to facilitate safe excretion.<sup>23</sup> Upon metabolism *via* CYP the product formed *N*-acetyl-*p*-benzoquinone imine (NAPQI) is theorised to cause hypothermic, antipyretic, hepato- and nephro-toxic effects which are usually detoxified by the addition of glutathione.<sup>23, 25</sup> Excessive taking of paracetamol can deplete the body of available glutathione groups causing an increase in this toxic metabolite (NAPQI).<sup>26</sup>

Typically, upon undergoing metabolism a xenobiotic reduction or complete loss of pharmacological effects is observed, but this is not always the case and a compound with higher therapeutic or toxicological effects can be formed. Drugs that require metabolism to yield their pharmacological effects are known as pro-drugs.<sup>27, 28</sup> The analysis of these products and their effects are of considerable interest to allow for the effective development and determination of the effects of a potential new drug.<sup>29</sup> A

method that allows for the synthesis of standard quantities of a single isomer metabolite is required to allow further studies.<sup>30, 31</sup>

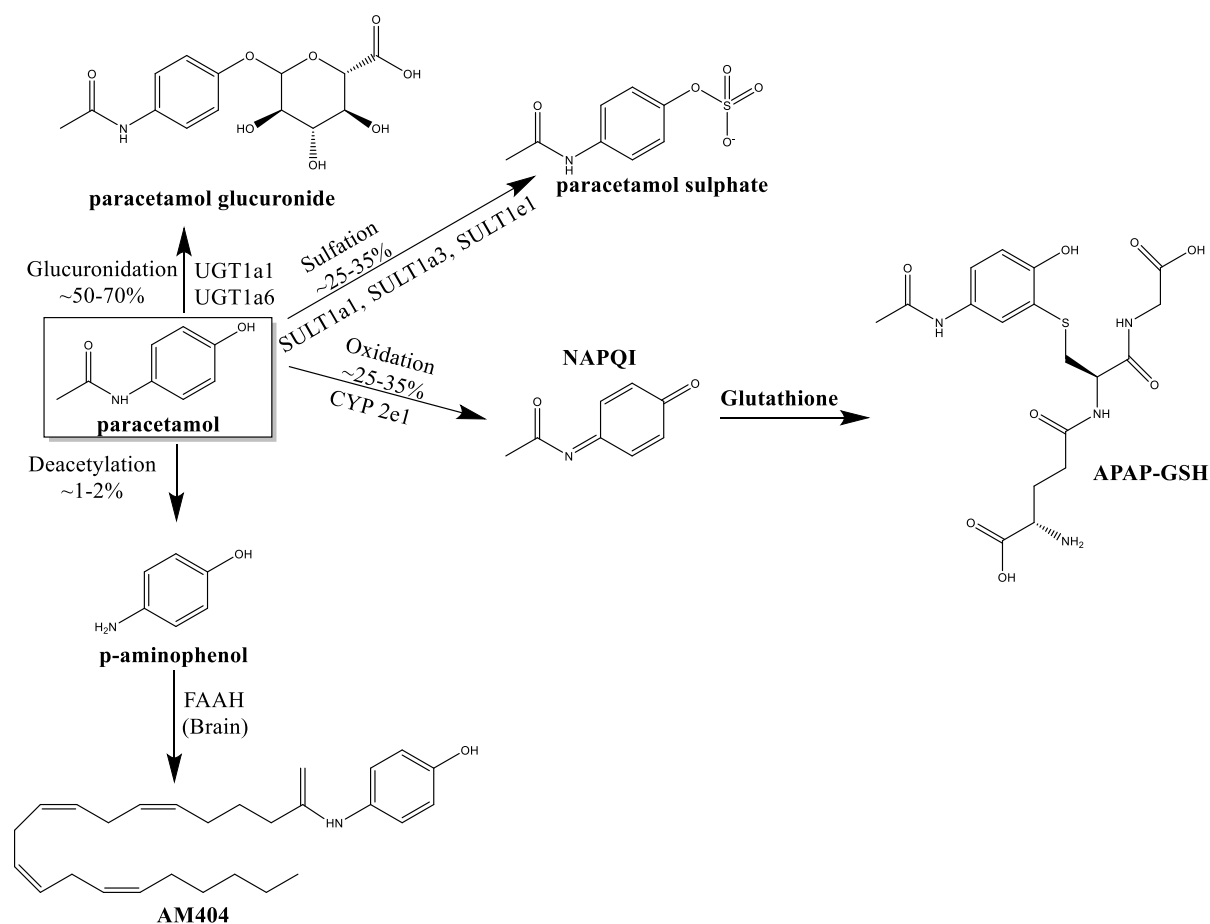


Figure. 1.1: Reaction scheme of paracetamol through the many different metabolic reactions undergone within the human body.

The three major enzymes that are known to metabolise paracetamol (CYP, UGT and metabolites extracted in both urine and blood.<sup>32-34</sup>

## Cytochrome P450s

CYP450 are membrane bound enzymes found within the endoplasmic reticulum, which metabolise approximately 75% of all commercially available drugs.<sup>35, 36</sup> These heme-containing enzymes primarily function as monooxygenases for fatty acids, steroids and xenobiotics.<sup>37</sup> This family of enzymes utilise molecular oxygen ( $O_2$ ) with the unused oxygen forming water using available hydrogen atoms.<sup>38</sup> CYP mediated

metabolism requires electrons to facilitate this reduction reaction which is provided by nicotinamide adenine dinucleotide phosphate (NADPH, the co-factor in this reaction) and NADP<sup>+</sup> is formed.<sup>39</sup> NADP<sup>+</sup> in animals is typically regenerated back into NADPH *via* the pentose phosphate pathway utilising glucose-6-phosphate dehydrogenase and 6-phosphoglucuronate dehydrogenase and a different process occurs in plants.<sup>40</sup>

## **UDP-Glucuronosyl transferases**

UGT are microsomal enzymes found within the smooth endoplasmic reticulum, metabolising approximately 15% of FDA approved drugs. UGT mediates the conjugation of a glucuronic acid (modified sugar group formed in the human body) group onto available oxygen, nitrogen, sulfur and carbons. CYP450 based reactions lead to the formation of these groups on a xenobiotic allowing further conjugation. The glucuronic acid group is provided by a UDP-GA which is formed within cytosol *via* the glucose-1-phosphate pathway.<sup>40</sup> As mentioned previously typically reactions facilitated by UGT cause deactivation of a xenobiotic compound however this is not always the case.<sup>41</sup> For example, with morphine two isomers are formed: morphine-3-glucuronide (M3G) and morphine-6-glucuronide (M6G).<sup>42</sup> It has been observed that M6G provides an even higher analgesic affect than its precursor morphine and M3G has recently been linked to unwanted side effects or even pain enhancement.<sup>43</sup>

## Sulfotransferases

SULT is a cytosolic enzyme which facilitates the addition of sulfate ( $\text{SO}_3^-$ ) to the same groups as UGT (oxygen, nitrogen, sulfur and carbon).<sup>44</sup> This enzyme relies on the co-factor 3'-phosphoadenosine-5'-phosphosulfate (PAPS) to provide the sulfate group and forms 3', 5'-diphosphoadenosine (PAP) once used within a reaction.<sup>45</sup> PAPS is formed using sulfate obtained from the diet or biodegradation of proteins within the body and the enzymes adenosine triphosphatase (ATP) sulfurylase and APS kinase (Figure 1.2).<sup>46</sup>

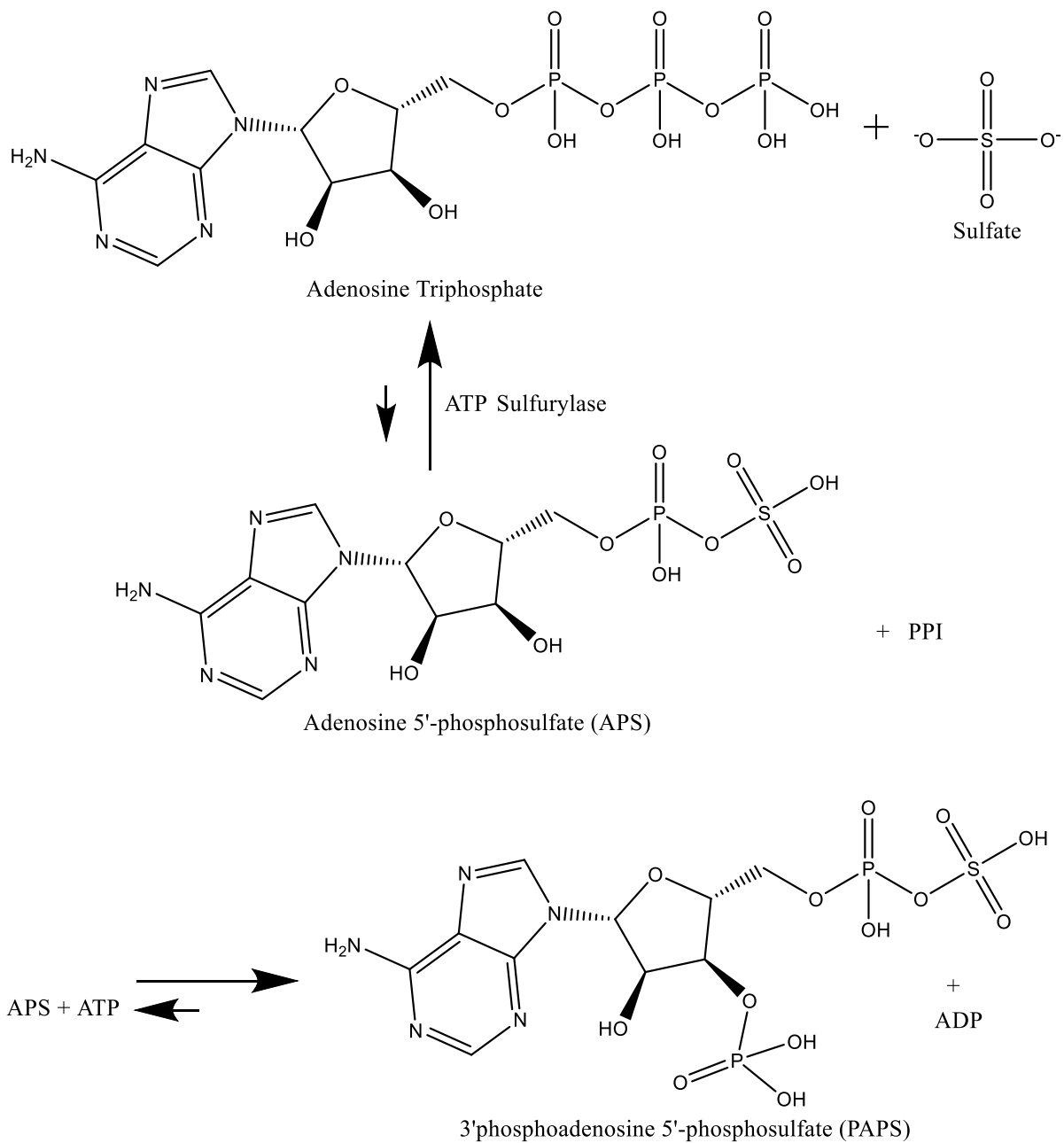


Figure 1.2: Reaction scheme for the formation of PAPS within the human body.

When developing a method focussing on the synthesis it is very important to determine which initial substrate is being used careful to ensure compatibility between the enzyme, cofactor and substrate.

## 1.2. Substrate considerations for enzymatic conversion

For the synthesis of naturally circulating metabolites a test molecule is required thus, an understanding of compatibility between substrates and an enzymes specific isoform is vital.<sup>47</sup> However, there is a large amount of overlap in isoform cross compatibility. The majority of which being *N*- and *O*- conjugating, and in some cases *C*- and *S*- are also observed.<sup>48, 49</sup>

The two compounds utilised throughout this thesis (*para*-nitrophenol and resorufin) have been frequently investigated within published literature. This is due to their wide applicability for the majority of conjugative enzymes due to their readily accessible hydroxyl group that requires no modifications prior to metabolic studies.<sup>50</sup>

*para*-Nitrophenol has been of wide interest for initial metabolic studies due to its applicability for not only conjugative enzymes but also hydroxylation.<sup>51, 52</sup> This allows for studies that involve multiple enzymes within the respective study to determine an overall study of rates and yield of multiple isoforms comparable to that which is found naturally *in vivo*.<sup>53</sup> Alongside this wide applicability an ease of analysis is also observed, with a  $\lambda_{\max}$  of 400 nm at any pH >8 and 315 nm at pH<8, utilising absorbance-based methods. However, due to developments in mass spectrometry, by utilising their parent ions it has become viable to quantitatively measure conjugative products too.<sup>54</sup> When analysed *via* mass spectrometry, sulfate and glucuronic conjugated products provide a characteristic loss of 80 and 176 *m/z* units respectively. In terms of nitrophenyl sulphate (studied in this thesis), a loss of 218>138 *m/z* is observed.<sup>55</sup> These characteristic losses allow for a proof of conjugation or deconjugation and if a calibration curve is created also allow for a quantitative proof of product formation.

Single enzyme studies commonly utilise resorufin. Resorufin is highly fluorescent at 570 nm  $\lambda_{ex}$  and 585 nm  $\lambda_{em}$ , which, similarly to nitrophenol, allows for the ease of quantitative analysis for a given deconjugation.<sup>56</sup> However, when analysing conjugative products it is important to note that a fluctuation of fluorescence/absorbance is not always directly proportional to product formation, thus it is important to confirm the metabolite formed *via* a second analytical method such as mass spectrometry.<sup>57</sup> Prior to this secondary analysis there is no clarification of which metabolic product is formed, which is especially important when conducting research utilising multi-enzyme systems. If a large amount of product is formed (0.1 mg to g quantities) then other techniques can also be applied for the analysis of products such as nuclear magnetic resonance (NMR) and X-Ray diffraction.<sup>58, 59</sup>

One other important substrate related to resorufin is 7-ethoxyresorufin, in which resorufin is formed upon undergoing CYP1- mediated oxidative deacetylation.<sup>60</sup> The ethoxyresorufin-O-deethylase (EROD) assay has been of frequent use for the studies of metabolic products.<sup>61</sup> Due to the formation of resorufin, fluorescence analysis is especially useful in which a highly accurate amount of product formed can be measured.<sup>62</sup> Further to this, if the reaction is undertaken in static/batch conditions within a plate reader then constant measurements over time can be used to create a rate of product formation.<sup>63</sup> For the analysis of cascade reactions (multiple enzymes undergone sequentially) the use of 7-ethoxyresorufin as a substrate is especially convenient as a measurement of fluorescence increasing (resorufin formation). This can be measured over time and a sequential loss of fluorescence (potential metabolite formation) can be measured. Alternatively, following incubation with biological samples, the resulting reaction products can be assessed for resorufin concentrations after incubation with deconjugation enzymes (and compared to buffer only

incubations) to give an assessment of follow-on conjugative reactions. There are a wide variety of methods that have already been successfully utilised for the synthesis of metabolic products and thus understanding which test substrates are compatible is relatively simple.

### **1.3. Current methods for metabolite synthesis**

Due to the current need for the determination of which metabolites are formed *in vivo* to further understand their pharmacological properties, a wide variety of methods have been applied for the formation of metabolites including *in silico*, traditional organic synthesis, s9 fractions (extraction from liver homogenate), bacterial expression of enzymes, liver cell Incubations and liver microsomes.

#### **In silico**

Computer simulations (*in silico*) have largely been used for the determination of metabolites formed *in vivo* allowing the researcher to conduct tests on a wide variety of parameters simultaneously.<sup>64</sup> These methods come with very different drawbacks in comparison to all synthetic methods, due to the time and understanding required to truly simulate the environment that these metabolic pathways are undergoing.<sup>65</sup> The time for a simulation to take place is mostly affected by the processing power needed to study the formation of a wide variety of different isomers and different conjugative pathways, whilst also altering other naturally fluctuating properties such as health conditions and age/gender effects. Multiple studies have demonstrated the effectiveness of this technique when comparing the results observed *via* simulation to those naturally found *in vivo*. For example, Huang *et al.* observed an upper accuracy

of 0.898 and a lower of 0.835.<sup>66</sup> Alongside this Moreira *et al* conducted a simulative study on tumour growth in mice yielding inhibition of tumour growth using a combination of, metformin, METABLOC and diclofenac which was compared to experimental results providing comparative demonstrating the power of this technique.<sup>67</sup> Whilst this method is powerful for the use of predictive modelling of metabolites formed, unfortunately no physical product is formed and thus does not allow for any further testing demonstrating that a synthesis method is required to be used in conjunction of *in silico* tests.

### **Traditional organic synthesis**

Traditional organic chemistry approaches have been applied for the synthesis of a variety of different metabolites.<sup>68</sup> These methods have been utilised frequently for the synthesis of already known metabolites. However previous knowledge of its specific isomer is needed prior to undergoing the synthesis of its specific compound; allowing these techniques to be utilised better in conjunction with the previous methods which allow for the determination of these naturally occurring metabolites. A significant amount of product can be formed *via* these methods, although protection groups are necessary due to a drug compounds typically containing reactive groups, such as amides, alcohols and amines for example.<sup>69</sup> Due to this a much more complex understanding of protecting groups is required. This results in a longer synthesis pathway and a reduction in yield. It is worth noting that the substrates formed from this method are typically of lower complexity; it is much more difficult where a substrate contains multiple reactive functional groups such as polyphenols. This leads to a challenge where the stereoisomers formed *via* this method do not match those formed *in vivo* from enzymatic reactions.

## S9 fractions

S9 fractions are the supernatant of a centrifuged liver homogenate containing both cytosolic and microsomal fractions. This allows a much more representative formation of metabolites than other methods which provide one or the other.<sup>19</sup> S9 fractions are typically used for the determination of metabolites alongside their respective formation properties i.e., rates and inhibitions whilst considerably reducing costs in comparison to the other described methods.<sup>70, 71</sup> Due to the extensive amount of research undertaken utilising these fractions their inherent benefits and deficits are well documented.<sup>72</sup> When used, the person from which the s9 fraction was obtained from makes a significant difference on the metabolites formed.<sup>73</sup> For example, if the liver fraction is obtained from a neonate, very little glucuronide substituted products are formed. This is demonstrated with the products formed upon incubation with a respective substrate *i.e.* resorufin may be formed from 7-ethoxyresorufin however resorufin glucuronide may not be formed provided even with the sufficient amount of time and respective co-factor, UDP-GA.<sup>74</sup> This has been readily solved by forming mixtures of s9 fractions providing an overall average of enzymes within the body<sup>73</sup>. This method has been thoroughly utilised for the determination of metabolites formed due to its low cost in comparison to other alternative methods. The major deficit of this method specifically as a synthetic method is due to its ability to form all of the expected metabolites within the body. Due to this, usually a mixture of metabolites are formed and due to their structural similarity can be extremely difficult to separate and form sufficient amounts for further pharmacological testing.<sup>75, 76</sup> Chen *et al.* utilised s9 fractions within a direct incubation method in which very little metabolite was observed. However, enough product was formed to allow confirmation of the major metabolite formed but is not sufficient as a synthetic technique.<sup>77</sup>

As this method involves incubating the respective substrate directly with the s9 fractions, problems are observed including difficult separations and products inhibiting enzymatic activity.

## **Bacterial expression of enzymes**

In this method gene expression is induced in bacteria, typically *Escherichia coli* (*E. coli*). *E. coli* initially is not viable for a transformation process therefore, a parameter known as competency must be increased.<sup>78</sup> If the bacteria is being heat-shock transformed the cells are treated with cations or reagents, most commonly calcium chloride is used; increasing the cell membrane permeability.<sup>79</sup> Or if the cells are undergoing electroporation, the cells are thoroughly rinsed with deionised water *via* pelleting and suspension to remove unwanted salts that interfere with the electroporation process.<sup>80</sup> At this point the cells can be aliquoted to prevent unnecessary freeze thaw cycles. The next step is to undergo either of the transformations dependant on how the cells were prepared. For the heat shock process, initially the cells are cooled in ice for up to 30 minutes and then mixed with DNA that determines the protein being induced.<sup>81</sup> The cells are then heated between 37 to 42 °C for approximately 30 seconds and then placed back in the ice.<sup>81</sup> For electroporation the competent cells are mixed with the relevant DNA and for a short period of time are exposed to an electric field.<sup>82</sup> Usually a higher voltage is used initially which decays over a set period of time leading to the formation of pores in the cell membrane allowing DNA to enter.<sup>83</sup> The *E. coli* cells are then cultured to increase cell count and antibiotic resistances. The protein being induced is dependent on the DNA introduced prior to culturing and a large group of these cells affected by the DNA are known as clones.<sup>84</sup> *E. coli* is chosen due to its simplicity and speed of growth and low

cost.<sup>85</sup> Many issues can occur throughout this process including unfolding or improper folding of proteins (causing inactivity), reduced growth of host and even no protein formed at all.<sup>86</sup> One benefit of this method is the enzyme can be expressed with a fusion tag such as histidine, providing multiple uses such as increased expression and ease of purification.<sup>87</sup> Large quantities of enzyme and metabolites can be formed utilising this technique however it is frequently observed where proteins formed are unfolded or insoluble, preventing their use.

Post transitional protein modifications have also been studied which further diversifies the proteins found within the human body, and have been observed to provide a wide variety of effects such as increasing cell viability or affecting enzymatic activity.<sup>88</sup> Glycosylation is a post translation modification associated with 50% of all proteins which is further linked with increased enzyme activity.<sup>89</sup> For example, aspartic protease cathepsin E suffered reduced activity when *N*-glycans were enzymatically cleaved<sup>89</sup>. These complex modifications are not provided utilising the commonly used *E. coli* host.

## **Liver cell incubations**

Liver cell incubations have been widely applied to the synthesis of physiologically relevant metabolites as they contain both the enzymes and co-factors that metabolise compounds upon entering the body.<sup>90</sup> Due to the increasing commercial availability of hepatocytes their research and understanding is increasing quickly, leading to their wide use and are now described as the gold standard method for metabolic studies.<sup>91</sup> This method involves directly incubating the substrate with the chosen hepatocytes whilst varying external parameters such as temperature and incubation time.<sup>92, 93</sup> Due to the extensive amount of research the capabilities and negatives of this method are

widely available and methods of bypassing them are currently being researched.<sup>94, 95</sup> For example, the gold standard method hepatocytes suffer from limited availability leading to increased costs. Due to this a variety of different methods have been employed to increase the longevity of these cells.<sup>96, 97</sup> One of which is the use of cryogenic freezing alongside the use of cryo-protecting compounds such as Dimethyl siloxane (DMSO), albumin, fetal calf serum (FCS) and polyvinyl pyrrolidone.<sup>98-101</sup> Despite this low availability, hepatocytes advantages heavily outweigh this cost as they contain all metabolising enzymes allowing for a direct comparison to those formed within the liver.<sup>94</sup> The overall focus in the literature shows that almost all studies have been utilised for CYP based metabolism and very little attention has been given to any of the conjugative enzymes.<sup>94</sup> Liu *et al.* published a protocol for the isolation of hepatocytes from a liver and low yields were observed.<sup>102</sup>

Human hepatic cell lines have also been utilised for the synthesis of metabolites, typically formed *via* tumour tissue and genetic engineering of human liver cells leading to them being considerably more available than the previously mentioned gold standard, and methods have been employed to further optimise these methods.<sup>103</sup> However, hepatic cell lines suffer from very low drug metabolising enzyme concentrations.<sup>94</sup> Nagarajan *et al.* focussed on comparing a variety of different cell types to mimic *in vivo* formation of metabolites.<sup>104</sup> This study suggested that, dependent on the cell types used, potentially different products can be formed, and dependant on the mode of metabolism a different cell type also provides comparable metabolism to those naturally observed *in vivo*. Whilst these methods are effective in the determination of metabolites formed *in vivo*, a large amount of optimisation is required for an accurate representation as in current tests metabolites that are not naturally observed are also frequently seen.<sup>105</sup> Also, comparatively to the s9 fractions,

this method involves incubating the respective substrate with the hepatocytes directly. Due to this, similar issues are found including difficult separations and products inhibiting enzymatic activity.<sup>106</sup> Also, because this method simulates *in vivo* metabolism using comparatively low enzyme concentrations a wide variety of metabolites are formed.<sup>107</sup> This does not allow for a simple synthesis of these products in high quantities and would necessitate a complex separation from similarly structured metabolites whilst also removing co-factors and enzymes. This makes the collection of a singular product increasingly difficult.<sup>108</sup> If multiple products are obtained the determination of a specific metabolite's beneficial and toxicological effects is not simply available. This can cause delays with regards to drug testing and development, which is especially important as in some cases metabolites can have a detrimental effect on a person's health. For example, thalidomide was used as an anti-emetic for a variety of conditions in pregnant women.<sup>109</sup> One of the two isomers that naturally interconverts under biological conditions had detrimental effects, causing birth defects and in some cases death. The mechanism involved is unclear, but the metabolites are currently under investigation.<sup>110</sup>

## **Liver microsomes**

Liver microsomes are subcellular fractions similar to s9 fractions which contain membrane bound xenobiotic metabolising enzymes such as CYP, UGT and SULT (the three enzymes focused on in this thesis).<sup>35, 111, 112</sup> Due to their ease of preparation, use and storage these fractions are considerably cheaper than the liver cell models. As with liver cell methods, the donor's individual metabolomic characteristics are observed within the fraction.<sup>91</sup> To bypass this, microsomes from a variety of different donors are pooled together to minimize this individuality effect on overall

measurements.<sup>113</sup> Due to their low stability these are readily frozen at -80 °C and studies have shown they can be frozen and thawed at least 10 times with no significant effect on metabolic activity.<sup>114</sup> Comparatively to the previous enzymatic methods direct incubation with substrate and co-factor (if required) is the preferred method for screening of potential drug candidates and their metabolites, especially when focussing on phase I metabolism. Typically these microsomal incubation experiments are limited to an hour due to optimal enzymatic conditions.<sup>115</sup> Due to their ease of access typically microsomes are tested before utilising hepatocytes to prevent large costs for non-pharmacologically relevant compounds.<sup>116</sup> Studies have shown that CYP activities throughout the two methods are comparable, and no significant difference is observed but conjugative enzymes such as UGT are not comparable. This is frequently bypassed *via* the incubation of additional external co-factors.<sup>117</sup> The use of microsomes have been typically hampered by their inherently low yields and the need for a complex purification technique, as demonstrated by Tuffal *et al.* in which direct incubation with human platelets very little product was found and only one of the four tested substrates were quantifiable.<sup>118, 119</sup>

#### **1.4. Microfluidics**

Within the pharmaceutical sciences, miniaturised devices can be utilised for speeding up the overall drug development process.<sup>120</sup> As microfluidics works *via* the manipulation of considerably lower volumes than alternative methods, a wide variety of advantages have been noted for effective drug development; including small surface area to volume ratios allowing more interactions between enzyme and cofactor/substrate, lower volumes leading to lower amounts of expensive biological

reagents used (such as enzymes and cofactors), continuous flow through preventing product inhibition of the enzyme compared to other large scale enzyme systems alongside high mass and heat transfer, whilst also allowing excellent control for all experimental parameters and reduction in overall reaction times.<sup>121</sup> For example, Vickerman *et al.* developed a device for 3D cell culture allowing for time dependant drug delivery whilst controlling surface stress, interstitial flow and culture scaffold properties. Along this Uddin *et al.* developed an ELISA integrated microfluidic device which reduced reaction times of each step to less than 15 minutes whilst still providing an increased limit of detection.<sup>122</sup> Although not an enzymatic application, exquisite parameter control was utilised by Thiele *et al.*, which used a zig-zag single channel device for the formation of gold nanocubes.<sup>123</sup> Gold nanocubes are difficult to obtain in a uniform and with sufficient yields simultaneously. The parameters altered included: precise incubation time, solvent concentration variation, altering counter ions and volume alterations. Finally, product inhibition was completely removed for the enzyme alcohol dehydrogenase. Current state of the art microfluidic devices is described in Table 1.1.

Table 1.1: Descriptions of current state of the art microfluidic devices and their applications.

Microfluidic approach	Definition	Applications
Droplet based	Involves the formation of droplets utilising either passive or active methods. The former utilises specific channel designs such as T junctions or flow focussing and the latter utilising an external factor usually an electric field <sup>124</sup>	Targeted drug delivery <sup>125-127</sup> Single cell analysis <sup>128-130</sup> Emulsifiers synthesis <sup>131-133</sup> Electrophoresis <sup>134, 135</sup>
Inertial	Inertial microfluidics utilises hydrodynamic forces using a variety of different channel designs which focuses particles into specific positions under specific parameters <sup>136</sup>	Miniaturisation of HPLC systems <sup>137</sup> Cell/particle sorting <sup>138-141</sup> DNA isolation <sup>142</sup> Cancer detection <sup>143-145</sup>
Paper based	Paper based devices involve the use of hydrophobic barriers on paper for point of care analysis <sup>146</sup>	ELISA <sup>147-149</sup> Pathogen detection <sup>150-152</sup> Biosensing <sup>153-155</sup>
Electrode containing devices	Electrode can be implemented within a microfluidic device to facilitate electrochemical redox reactions <sup>156</sup>	Biosensing <sup>157-159</sup> Mimicking metabolism <sup>160-162</sup>
Tissue/Organ-on-a-chip	Tissue on a chip devices involve simulating the microenvironment found within the tissue/organs natural environment	Modelling a wide variety of biological systems: <ul style="list-style-type: none"> <li>• Pulmonary edemas<sup>163</sup></li> <li>• Viral infections<sup>164</sup></li> <li>• Synthesis of liver specific proteins<sup>165, 166</sup></li> <li>• Drug induced kidney nephrotoxicity<sup>167</sup></li> <li>• Wound healing, skin aging and repair<sup>168</sup></li> </ul>
Miscellaneous	Any other device types that don't fit into a specific category. <i>I.e.</i> , single channel devices, devices containing membrane filters etc.	PCR <sup>169, 170</sup> Immunoassay <sup>171-173</sup> Traditional synthesis <sup>174, 175</sup> Enzymatic reactions <sup>176-178</sup>

When designing a microfluidic device for a specific purpose, the material in which the device is fabricated is vital to ensure compatibility between the support, the immobilisation technique and the enzyme itself<sup>179</sup>. Dependant on the material the device is made out of the fabrication method significantly differs between polymer and glass based devices.<sup>180</sup>

### **1.5. Fabrication of microfluidic devices**

Glass microfluidic devices offer some benefits over polymer based devices including higher reusability (after removal of immobilised enzyme), higher rigidity, superior optical transparency, increased thermal stability, high biocompatibility and are inert to the many liquids typically used in enzyme chemistry.<sup>181, 182</sup> Tatsuro *et al.* developed a thin layered microfluidic device to utilise the transparency and biocompatibility of glass and gain a time based fluorescent measurement of fluorescein to facilitate c-reactive protein detection utilising an ELISA reaction.<sup>183</sup> Mazio *et al.* developed a reusable device with snap fitting of commercially available inserts.<sup>184</sup> These alterations allow this device to be reusable for a variety of different commercially available inserts for air liquid interface facilitating tissue oxygenation and feeding of bronchial cystic fibrosis cells. The ability to remove and replace these inserts significantly improve this devices reusability for the culturing of these cell types.<sup>184</sup>

For the fabrication of microfluidic devices the majority of microstructures in glass are created using a wet etching technique.<sup>185</sup> This involves coating clean dry devices in a photoresist *via* spin-coating.<sup>186</sup> These are then soft baked for 30 minutes at 90 °C, then covered in a photomask containing the design and exposed to UV radiation through the mask and rinsed with DI water.<sup>187</sup> Devices are then placed in hydrofluoric

acid solution (HF) to the desired etching depth. After removing from the HF solution, the devices are rinsed with deionised water and the photoresist is removed *via* solvent (*i.e.*, acetone), this process is illustrated in Figure.1.3. Prior to binding the device to a glass base plate, it is necessary to introduce the inlet and outlet holes for the device. These are typically drilled *via* a diamond drill, different drill bit sizes are available depending on the method of interfacing (*i.e.*, capillary or tubing).<sup>188</sup> The etched glass can then be bound to the glass plate using heat press at a temperature over 400 °C and a pressure of around 0.05 MPa (Figure.1.3).<sup>189</sup> For an irreversible bonding this involves heating the two pieces of glass whilst simultaneously placing pressure.<sup>181</sup> At reduced temperatures (100 °C) a reversible binding is observed, this can be bypassed *via* the use of an intermediate which can facilitate further interactions between the two glass plates. Examples of these include epoxy 2:1 resin, thin adhesive tape and sodium silicate.<sup>190-192</sup> Although these are all viable, the required strength of the device alters with differing pressures within the device when it is used. If a reduced pressure is utilised, then a less effective binding is acceptable such as the thin adhesive tape. Although these are available, extra care must be taken when using them as they can yield a non-homogeneous binding leading to leaking devices.<sup>193</sup>

Although these devices can be cheap to make, there is a wide variety of expensive equipment and solvents necessary for their fabrication; including a furnace and heat press.<sup>194</sup> Unless an area of research has a specialised microfluidic department, it is unlikely these pieces of equipment will be available, although there are commercial suppliers of microfluidic devices available.

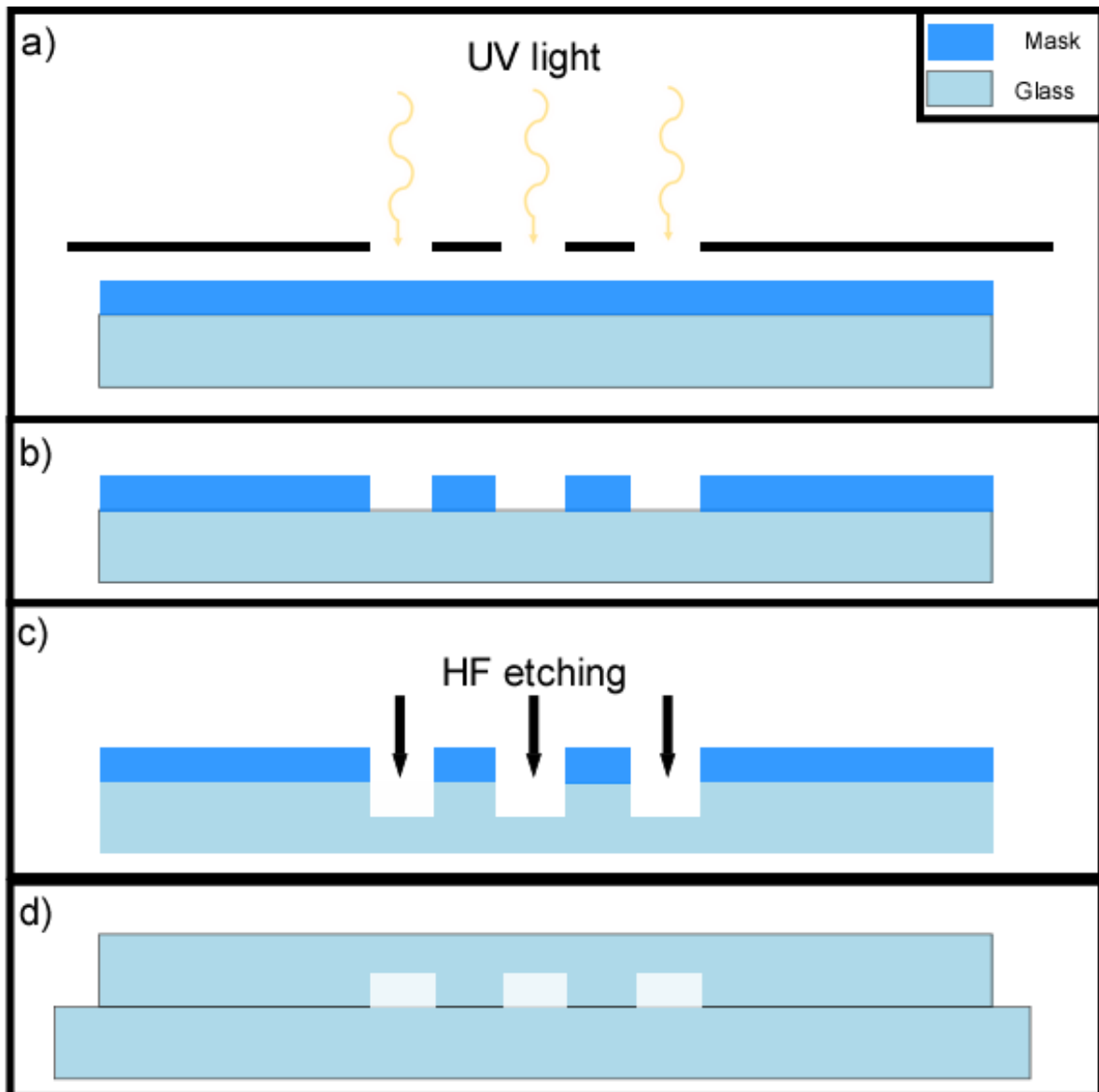


Figure.1.3 Schematic detailing the creation of a microfluidic device using the wet etching technique. This process consists of UV patterning of mask (a), removal of the unbaked mask (b) HF etching of the design onto a glass plate (c) and bonding the patterned glass on to a glass base plate containing the microstructures.

When fabricating a glass microfluidic chip, a wide variety of parameters need to be considered prior to deciding on a design. The schematic or overall design of the device has a significant impact on the surface area to volume ratio as described previously. Three different design types have been of frequent application for the formation of metabolic products.

The mixer based devices have been applied differently to the other three devices as typically a non-immobilised enzyme is flowed through one of the inlets and a substrate is flowed through the other containing the co-factor if necessary.<sup>195</sup> Clark *et al.* cultured preadipocytes on a glass coverslip and both Amplex Red (fluorescent dye) and enzymes (Glycerol kinase, glycerol phosphate oxidase and horseradish peroxidase) were flowed through the device simultaneously leading to mixing allowing glycerol secretion measurements.<sup>196</sup> These devices allow for the needed trial and error-based approach when using free enzymes, as there is no significant clean-up process needed. One of the main benefits of this method is due to the available control of the flowrate/injection rate for both the substrate and the enzyme itself; allowing for a much higher control of enzyme interactions between both co-factor and substrate.<sup>197</sup> One of the major disadvantages of this method is in the loss of expensive biologically active reagents such as the enzyme itself and its respective co-factor. Alongside this, a complex separation is usually required due to the biological matrix that is formed upon collecting effluent due to a mixture of both enzyme, cofactor and substrate forming; which is comparable to incubation methods.<sup>198</sup> Due to these constraints certain short lived products are not observed, thus preventing any further testing or determination of these products.<sup>199</sup> Although the downfalls of these devices largely hinder their use for any significant singular product formation they are still widely applicable in cases where the product can be monitored within the device.<sup>200</sup>

The vast majority of studies utilise one of either wall coated, packed or monolithic devices where utilising enzymes immobilisations is optimal.<sup>201</sup> Wall coated methods focus on immobilising the enzyme directly on to the surface of the device, packed devices are typically filled with particles in which the enzyme can be loaded in order

to increase the surface area to volume ratio, and lastly monolithic devices where the enzyme is either immobilised or trapped within the porous matrix. Trypsin has been frequently observed to be immobilised within a monolithic matrix for the digestion of peptides and a mixture of proteins.<sup>202</sup> Amalia *et al.* conducted an interesting study, in which an organic-polymer based monolithic column for the digestion of proteins. The monoliths surface allowed simultaneous digestion and chiral separation which was directly connected to a HPLC facilitating in-line analysis.<sup>203</sup>

The three previously mentioned devices can be further modified with the original being described as wall coated (where an enzyme is directly immobilised on the surface of the device), packed (where the device is filled with particles in which the enzyme is immobilised on to) and utilising a monolith within the device channels.<sup>121</sup> Wall coated were utilised throughout this thesis due to their considerably lower complexity, easy of cleaning, and reusability,

Wall coated devices focus on immobilising the enzyme onto the surface of the device either *via* surface modification or direct immobilisation.<sup>121</sup> There are a variety of different device structures that have been utilised for chemical reactions. The major types are described as single channel (Figure1.4a) and multichannel (inlet and outlet connected by multiple parallel splitting channels, Figure1.4b).

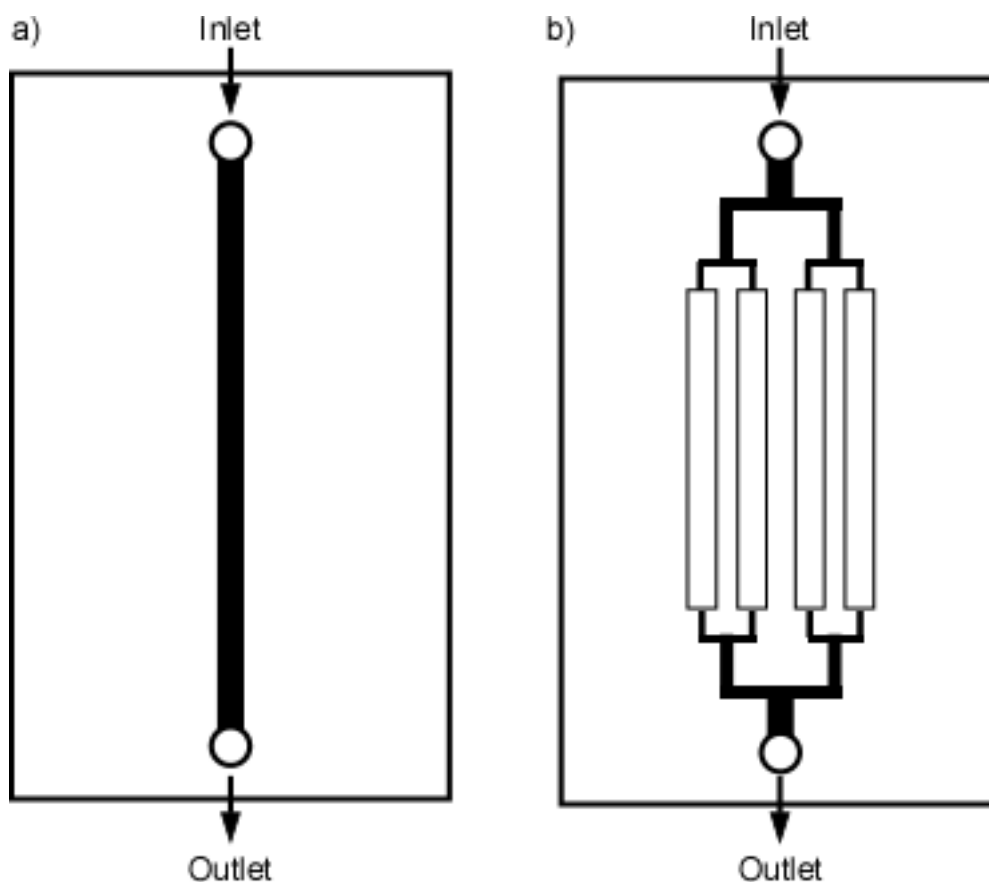


Figure 1.4: Depictions of two different microfluidic device structures a single channel/serpentine (a) and a multichannel (b)

Serpentine devices can be long or short, dependant on the experimental needs, and long channels can be placed onto a smaller device by winding around the glass.<sup>204</sup>

Parallel devices contain a splitting in which the devices converge at a single point which effectively multiplies the immobilisation volume.<sup>205</sup>

Most changes made with either of these designs focus on altering the dimensions of the channels *i.e.*, widening or tightening the flow path. The altering of channel dimensions with regard to enzymatic synthesis can have a large impact on the overall amount of product formed as it will reduce or increase the amount of interactions between the enzyme and co-factor/substrate increasing overall potential yield. For example, Kwapiszewski *et al* conducted a study on the effect surface area to volume ratio for the detection of fluorescein using optical fibres yielding one magnitude higher

sensitivity than a standard cuvette. Due care needs to be taken when designing thinner devices, as one frequently observed problem that needs to be bypassed is an increase in back pressure.<sup>206</sup> If too much back pressure occurs, very little to no flow through is observed and the method of integration from inlet to substrate becomes much more important (a weakly bound interface can become disconnected from the device).<sup>207</sup> In order to further improve the use of microfluidic devices for enzymatic compatibility immobilising the enzyme is used to create a physical attachment between the enzyme and immobilisation surface.

## **1.6. Application of microfluidics to metabolomics**

Microfluidic devices have been frequently applied for metabolomic studies. Utz *et al.* have developed an NMR probe that can incorporate microfluidic devices.<sup>208</sup> This was utilised to conduct studies on a single cell cancer spheroid that allowed for a constant time study of metabolic product formation by NMR analysis without the need for a consistent flow through method or extraction of L-lactic acid. A comparison over 2 days showed that spheroids (3D structures made of an aggregation of cells) provided 2.5 to 3 times less product formation in the case of D-glucose and L-Lactic acid consumption potentially due to less viable (live) cells in the spheroids, or different behaviour of the cells in a spheroid in comparison to those in a cultured monolayer.

Midwoud *et al.* created a microfluidic device enabling small scale tissue drug based metabolism utilising a PDMS membrane allowing for breathability for the necessary oxygen and CO<sub>2</sub> and allow for maintaining the optimum biological environment.<sup>209</sup> Continuous flow of media prevents a loss of growth due to a lack of required nutrients as fresh media is constantly being supplied. The study utilised four different test

substrates 7-ethoxycoumarin, 7-hydroxycoumarin testosterone and lidocaine which are all liable to undergo both phase I and phase II metabolism. It was observed that conjugative metabolism was still functional over an 8-hour timeframe for intestine and for 24-hour timeframe for liver cells utilising HPLC analysis *via* UV detection. Oxidative metabolites decreased over the same timeframe and was attributed due to no endogenous compounds within the media preventing continuous expression of the required enzymes.

Cells have been cultured directly within a microfluidic device, in both 2D and 3D. For example, in most cases 2D provide similar results to those in the natural 3D environment, cells in the 3D environment yield a higher resistance to anti-cancer drugs providing a false positive, when upon development the anti-cancer effect is no longer observed.<sup>210</sup> Marinkovic *et al.* measured metabolic landscapes in monolayer colonies of yeast cells for both single cells and a structured population, yielding consistent, reproducible glucose gradients as expected based on other non-microfluidic studies.<sup>211</sup> For the 3D cell culturing Frisk *et al.* attempted to bridge the gap between organ/tissue culture and 2D methods by using synthetic gels.<sup>212</sup> This study yielded the expected calcein gradient showing that staining is available alongside metabolism whilst maintaining cell viability within this synthetic matrix.

The immobilisation of both CYP and UGT microsomes *via* biotinylation onto a streptavidin functionalised surface has been carried out by Kiiski *et al.*<sup>213, 214</sup> In which it was observed that comparable high activity was observed both initially for the metabolism of Luciferin for CYP and 8-hydroxyquinoline or zidovudine for UGT. Both of which were aimed towards time-dependant concentration gradients for studies of

substrate co-factor and inhibitors and time-based enzyme function studies. Biotinylated human liver microsomes and a streptavidin modified microfluidic device allowed for the determination of alamethicin effects on reaction velocity and the causes that effect. This demonstrated that the alamethicin removed the mass transfer barrier, which is not necessary when utilising flow through conditions. Whilst these inhibition and enzyme studies are necessary for the understanding of enzyme mechanics, it has not been tested for the synthesis of a bulk singular product nor provide any pharmacological understanding of the beneficial or toxic effects of the metabolites of a compound.

Despite the documented uses of microfluidic devices utilising immobilised enzyme devices, there are still a variety of different applications that have not been fully realised, such as bulk synthesis of metabolic products to allow for further pharmacological studies (the aim of this thesis).

## **1.7. Enzyme immobilisation techniques**

Immobilising an enzyme provides many advantages over free enzymes, including increased structural and thermal stability, simpler extraction of both enzymes and products enzyme reusability, continuous enzymatic conversion, efficient reaction halting and ability to manipulate reactor design.<sup>120</sup> The methods for immobilising enzymes are typically divided into three categories. These categorise into (a) binding the enzyme onto a physical surface utilising physical or chemical interactions (b) entrapping the enzyme within a highly porous matrix and (c) crosslinking the enzyme together to form an aggregate or crystal.<sup>120</sup> Binding the enzyme *via* physical and

chemical interactions is further split into two categories non-covalent and covalent binding.<sup>215</sup> All of these categories and subcategories are visualised in Figure 1.5.

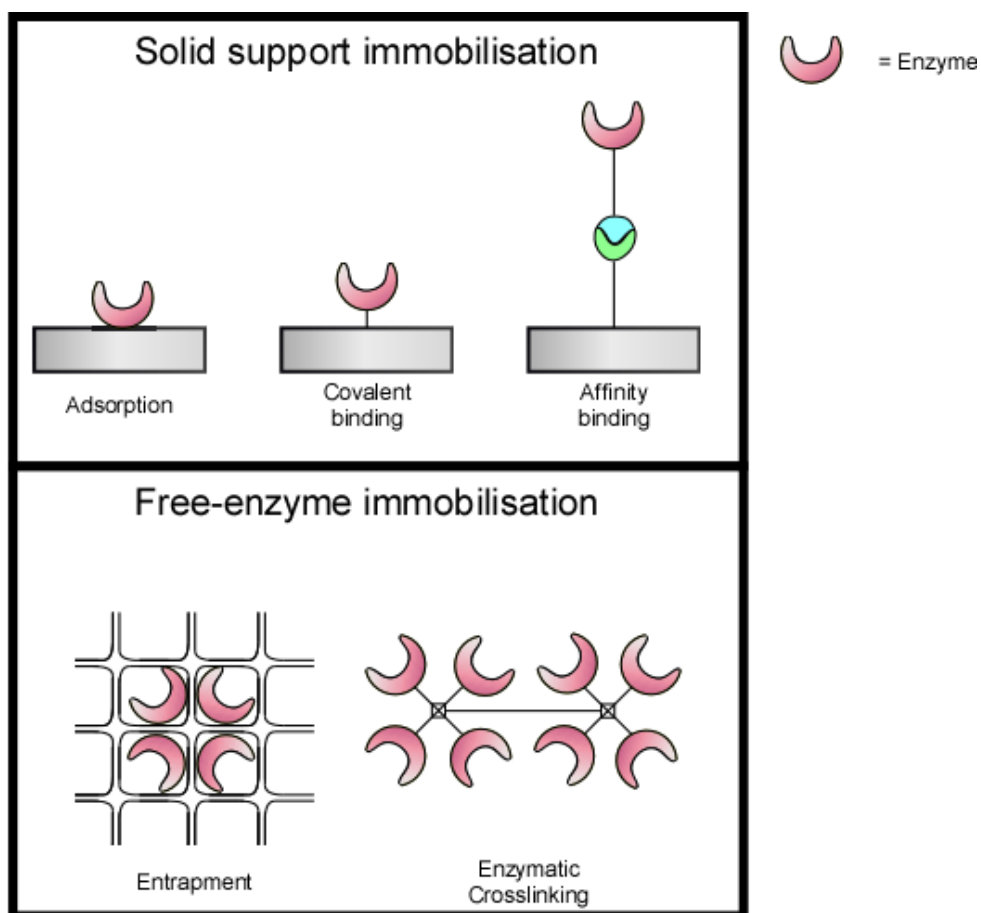


Figure 1.5: Visualised enzyme immobilisation methods.

Covalent bonding (the technique utilised throughout this thesis) provides an irreversible structure bypassing the leaching observed with the non-covalent binding.<sup>216</sup> A higher understanding and thorough research is required when immobilising covalently due to the conditions required potentially leading to inactivation and/or denaturing of the enzyme.<sup>217</sup> It is routinely noticed that a loss of enzymatic activity of even up to 70% is not uncommon upon covalently binding a compound to a physical support.<sup>217</sup> Covalent binding typically utilises common functional groups naturally found on an enzyme ( $\text{NH}_2$  and  $\text{COOH}$ ) and a modified surface bypassing the need to modify the enzyme potentially causing deactivation.<sup>218</sup>

One frequently used method involves amination of a silica support with subsequent glutaraldehyde addition yielding a carboxylic acid to amino reaction producing a highly strong bond.<sup>219</sup> Due to the number of amino groups within an enzyme in some cases the active site immobilises to the silica support, rendering it inaccessible to substrates preventing any product formation.<sup>220</sup> Due to a lack of control it is almost impossible to yield a heterogeneous array of immobilised enzymes that do not get inactivated by this process<sup>221</sup> and so significant differences can be found between catalytic runs.

Each of these different techniques have their own inherent benefits and deficits. Although extensive research has been conducted, no generic method that can be utilised for the synthesis of metabolites in sufficient quantities viable for standards. These advantages and disadvantages are described in Table 1.2.

Table 1.2: Comparison of advantages and disadvantages of different immobilisation techniques.

<b>Immobilisation technique</b>	<b>Advantages</b>	<b>Disadvantages</b>
Adsorption	<ul style="list-style-type: none"> <li>• Low binding energy</li> <li>• No structural changes</li> <li>• High catalytic activity</li> <li>• Simple</li> <li>• Cost-effective</li> <li>• Allows recyclability of expensive proteins</li> </ul>	<ul style="list-style-type: none"> <li>• High likelihood of enzyme leaching</li> </ul>
Covalent binding	<ul style="list-style-type: none"> <li>• Irreversible covalent bond prevents enzyme leaching</li> <li>• Increased thermal and structural stability</li> <li>• Extensive literature and research on different protocols utilising different solid supports to enable the use for a wide variety of enzymatic systems</li> <li>• Simple</li> </ul>	<ul style="list-style-type: none"> <li>• Strong covalent bond can lead to inactivity by altering an enzymes active sites</li> <li>• Loss of activity due to lack of immobilisation spatial control</li> <li>• Enzyme leaching in aqueous conditions</li> </ul>
<b>Immobilisation technique</b>	<b>Advantages</b>	<b>Disadvantages</b>
Affinity binding	<ul style="list-style-type: none"> <li>• Strong binding energy</li> <li>• Surface is highly selective towards the enzyme</li> <li>• Controlled orientation</li> </ul>	<ul style="list-style-type: none"> <li>• Enzyme structure must be altered to contain the affinity tag potentially reducing/removing activity</li> </ul>
Entrapment	<ul style="list-style-type: none"> <li>• Increased complexity with determining matrix viability</li> <li>• Increased thermal stability</li> <li>• Increased enzyme reusability</li> </ul>	<ul style="list-style-type: none"> <li>• Lack of robustness</li> <li>• Increased likelihood of enzyme leaching</li> </ul>
Crosslinking	<ul style="list-style-type: none"> <li>• Simple</li> <li>• Activity of free enzyme retained</li> <li>• Carrier free</li> <li>• Thermal stability</li> <li>• Solvent tolerant</li> </ul>	<ul style="list-style-type: none"> <li>• Enzyme of significant purity required</li> <li>• Costly</li> </ul>

The method utilised in this thesis is *via* covalent binding of the enzyme onto a glass surface using a 3-aminopropyl trimethoxysilane-glutaraldehyde linkage onto the NH<sub>2</sub> groups naturally observed within the enzymes structure.

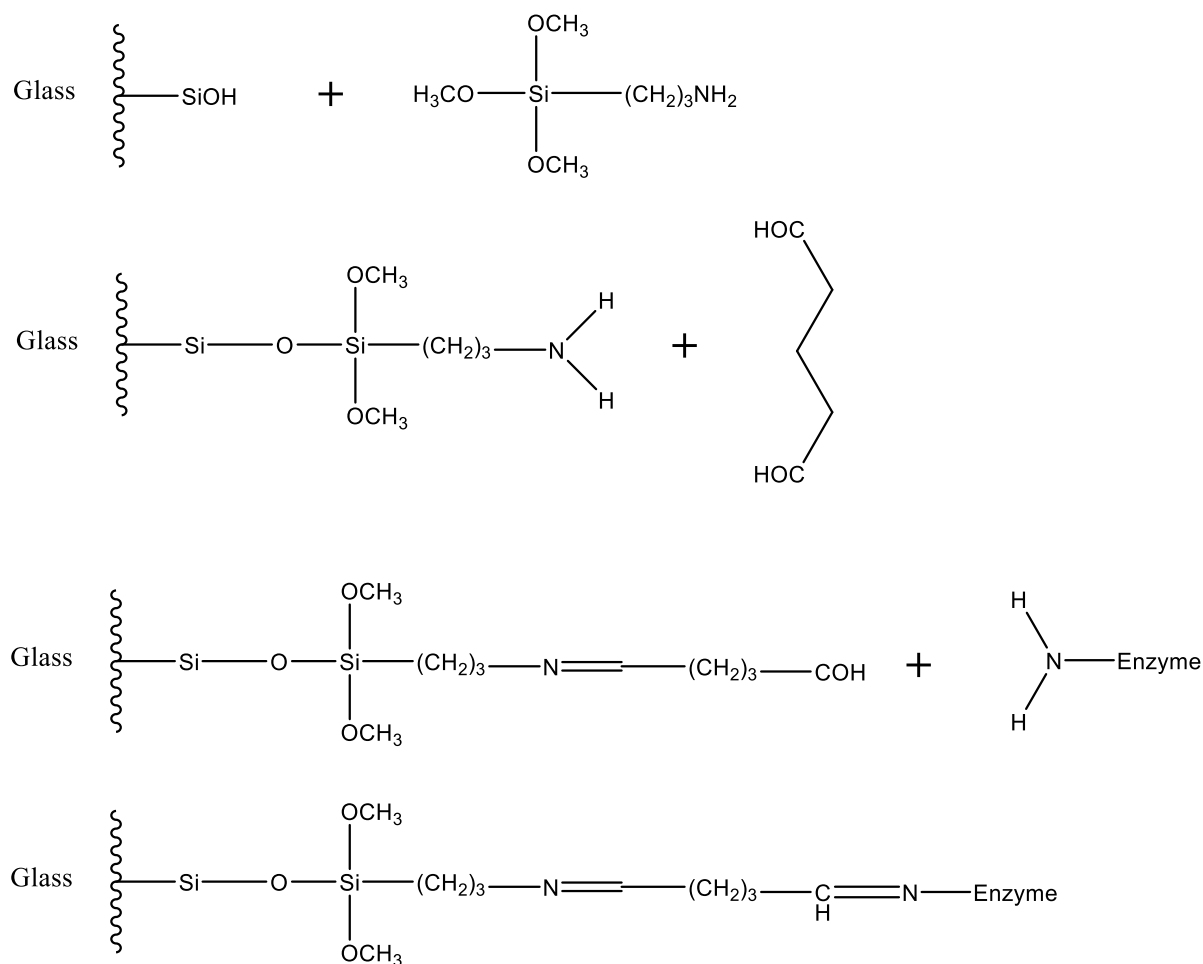


Figure 1.6: Reaction scheme for the immobilisation of enzymes utilising the frequently used silanisation followed by glutaraldehyde reaction.

In summary, there are a wide variety of different immobilisation techniques with covalent offering the most versatility due to the functional groups utilised in the reaction being widely available in all human enzymes.

## 1.8. Applied immobilisation of microsomal enzymes

The vast majority of studies that utilise the immobilisation of drug-metabolising enzymes have focused on CYP isoforms whilst the conjugative enzymes have had considerably less research.<sup>222, 223</sup> CYP-based reactors have been utilised for a variety of applications including; biosensors and biocatalytic synthesis.<sup>224-227</sup> Due to CYP's need for an electron donor, the use of electrodes as a surface for enzyme immobilisation has been conducted, allowing it to provide electrons directly to the CYP isoforms respective active site.<sup>228</sup> However, many issues have arisen that require a complex array of electrode materials surface modifications and immobilisation techniques to allow for catalytic activity.

Shumyantseva *et al.* focussed on measuring CYP catalytic activity on a variety of different electrochemical techniques namely cyclic voltammetry, square wave voltammetry and amperometry utilising a gold electrode, gold nanoparticles and a membrane-like synthetic surfactant (didodecyldimethylammonium bromide).<sup>229</sup> This allowed the determination of multiple antioxidants (mexidol, ethoxidol, cytochrome c and L-carnitine) effects on cytochrome P450's catalytic activity, with ethoxidol increasing by over 110% for three different CYP isoforms (CYP3A4, CYP2C9, CYP2D6) With the nanoparticles and surfactant increasing enzyme stability and longevity. Mie *et al.* noted that due to CYP's microsomal structure having hydrophobic regions that a hydrophobic electrode surface would likely yield optimum immobilisation.<sup>228</sup> Upon further study this was proven correct in regard to the majority substrates with an anomaly aminoethanethiolate which yielded no measurement on the voltammogram which was stated to be due to the saturated alkanethiolate, not providing sufficient conductivity preventing electron transfer.<sup>228</sup> It was hypothesised

that this technique can be utilised for drug research and as a biosensor dependant on the substrate.<sup>228</sup>

Affinity binding was utilised for immobilisation and purification of enzymes with affinity tags by Zhou *et al.* These affinity tag proteins were formed *via* plasmid and DNA manipulation under physiological conditions by utilising the bacterial overexpression method described previously in section 1.3.<sup>230</sup> The use of chitin as an affinity substrate increased the availability of this method due to its low cost with both the affinity substrates and the lack of cooling needed with low reaction times (30 minutes) when compared to similar methods.<sup>230</sup> As only a small modification was made on the enzyme and only 60% of the enzymes initial activity was observed, this was not comparable to alternative methods in which nearly 100% activity was retained<sup>230</sup>. However, without the immobilisation, a lack of activity longevity and stability was noted.

In the respect of covalent enzyme attachment, Hassan *et al.* studied the covalent attachment of glucoamylase to gel beads.<sup>231</sup> This covalent linkage focussed on functionalising the beads with an aminated group, further modified using glutaraldehyde which spontaneously reacts with the amino groups within the enzymes structure. Upon immobilising it was noted that both the pH and temperature retained their optima, with an observed increase in stability over an acidic range in the former and the latter retaining its optima but with a wider range varied by  $\pm 10$  °C. Most importantly, as with the other optimisation methods, a much higher reusability of the enzyme was found, with no measurable loss after 11 cycles.

Entrapment was utilised by Sharma *et al.* using a calcium agar gel. They immobilised within agar beads by dissolving  $\alpha$ -amylase within molten agar at 45 °C. Hydrogel

beads were then formed using a syringe into distilled water and required drying for 48 hours. Upon testing these hydrogel beads no large effect on thermal or pH optima; alongside no additional thermal stability.<sup>232</sup> This method is an improvement compared to previous entrapment studies which utilise calcium chloride/agar matrix, as their structural integrity was largely affected by the environments necessary for enzymatic conversion thus causing enzyme leaching with 78% residual activity after 6 uses. Zhu *et al.* observed only 55.1% of bovine liver catalase initial activity after only 3 uses.<sup>233</sup> Huang *et al.* attempted to bypass this loss by utilising a hybrid of both organic and inorganic materials with aluminium oxide boehmite and alginate which reduced leaching considerably where after 12 cycles 87% of initial activity was remaining. Despite this, the overall activity over the free enzyme was extremely reduced at 7%.<sup>234</sup> Techniques have been developed to allow the extraction of the enzyme and matrix from the products formed utilising magnetic beads but due to the significantly reduced reusability or activity compared to free enzymes there industrial use has been hindered by this leaching and reusability issue.<sup>235</sup> It was theorised that this immobilisation technique can be applied for the treatment of biological waste from food processing industries.<sup>235</sup>

Finally, Cao *et al.* used enzyme aggregates of penicillin G acylase for the formation of enzyme crystals alternatively to pure enzyme in order to ensure the superstructure formed in the aggregation process is retained. This theoretically allowed for an increased activity in comparison to its predecessor (aggregates), whilst bypassing the issues with aggregates in which aqueous solutions causes the enzyme to redisperse. The activity of this crystallised aggregate was determined by measuring the synthesis of ampicillin *via* crystallisation at its isoelectric point. The development of this method yielded comparable activity to the enzyme in solution, yielding approximately 50%

higher activity than crystalized enzymes that have undergone crosslinking which was in turn only slightly more effective than the crosslinked enzymes in their original state.<sup>236</sup> Another example by Schnepfel *et al.* utilises a multienzyme cascade reaction system starting with halogenase, to tryptophanase and finally monooxygenase to convert L-tryptophan to di-bromoindigo. This yielded a conversion of approximately 46%.

The application of all of these techniques have been either for the determination of which metabolic products are formed naturally, as a biosensor or for the determination of properties such as rate of formation.

Whilst all of these techniques have the potential for the synthesis of metabolic products, the applications above currently suffer from enzyme leaching, inactivation and low enzyme loading. Each of these issues leads to either a complete lack of product formed or the complex biological matrix that the method attempts to bypass by immobilising the enzyme is still formed. Covalent bonding (the chosen technique for this thesis) yields the least deficits in which leaching at lower flow rates have been observed to be minimal.<sup>237</sup>

An overview of the current metabolite synthesis techniques utilising microfluidic devices has been detailed in Table 1.3

Table 1.3: Description of metabolic studies utilising microfluidics.

Methodology	Enzymes activity assessed (Source of enzyme utilised)	Applications
Human liver microsomes immobilised on magnetic bead (biotin/streptavidin) utilising electrodes to control the sample droplet <i>via</i> an electrowetting technique <sup>238</sup>	<ul style="list-style-type: none"> <li>• CYP1a1</li> <li>• CYP1a2</li> <li>• CYP2a6</li> <li>• CYP3a4</li> </ul> (Liver biopsies)	<ul style="list-style-type: none"> <li>• Liver disease diagnoses</li> <li>• Development of personalised drug dosing</li> </ul>
Methodology	Enzymes activity assessed (Source of enzyme utilised)	Applications
Liver slices within a PDMS microchamber connected to two porous membranes to allow the constant flow of media which was directly coupled to a HPLC system <sup>239</sup>	<ul style="list-style-type: none"> <li>• CYP7a1</li> </ul> (Liver slices)	<ul style="list-style-type: none"> <li>• Mimic first pass metabolism</li> <li>• Study drug induced toxicity</li> </ul>
Microfluidic paper-based lateral flow assay focussed on the rapid screening of the metabolism of xenobiotics. The device contains three zones sequentially are enzyme reaction zone, a separation zone and a detection zone <sup>240</sup>	<ul style="list-style-type: none"> <li>• CYP2a6</li> </ul> (Human liver microsomes)	<ul style="list-style-type: none"> <li>• Examination of drug-drug and drug-chemical interactions</li> </ul>
Microfluidic device consisting of 8 parallel channels each of which interfaced with electrode arrays <sup>241</sup>	<ul style="list-style-type: none"> <li>• CYP1b1 (Supersomes)</li> <li>• NAT</li> <li>• epoxide hydrolase (S9 fraction)</li> </ul>	<ul style="list-style-type: none"> <li>• Detection of reactive metabolites</li> <li>• Determination of damage to DNA provided by reactive metabolites</li> </ul>
Microfluidic device featuring two layers linked by a porous. Four different cell types were co-cultured in the top layer small molecules pass through the membrane into the bottom layer. This layer was collected after 24 hours to allow metabolite analysis <i>via</i> UPLC-MS <sup>242</sup>	<ul style="list-style-type: none"> <li>• Various CYP enzymes</li> </ul> (Human hepatocytes)	<ul style="list-style-type: none"> <li>• Drug screening</li> </ul>
Hepatocytes directly cultured onto patterned fibres which are integrated within a multilayer microfluidic device <sup>243</sup>	<ul style="list-style-type: none"> <li>• CYP3a1</li> <li>• CYP2c11</li> </ul> (Primary rat hepatocytes)	<ul style="list-style-type: none"> <li>• Test model for the evaluation of <i>in vitro</i> drug metabolism</li> <li>• Drug clearance modelling</li> </ul>

Microfluidic device featuring a series of electrodes for precise droplet control directly integrated to a time of flight mass spectrometer <sup>244</sup>	<ul style="list-style-type: none"> <li>• CYP1a2 (Recombinant enzyme)</li> </ul>	<ul style="list-style-type: none"> <li>• Preclinical drug discovery and development</li> </ul>
Microfluidic device featuring a winding channel with human liver microsomes immobilised within a hydrogel leading to a channel contain cultured cells to allow the determination of cytotoxicity and finally a solid phase extraction (SPE) fabricated channel. The outlet of the device was directly connected to a time of flight mass spectrometer to allow metabolite determination <sup>244</sup>	<ul style="list-style-type: none"> <li>• Various CYP450 isoforms (Microsomes)</li> </ul>	<ul style="list-style-type: none"> <li>• Drug metabolite determination</li> <li>• Cytotoxicity measurements</li> </ul>
<b>Methodology</b>	<b>Enzymes activity assessed</b>	<b>Applications</b>
Microfluidic device containing a square pillar array to mimic liver lobule intervals found <i>in vivo</i> . Valves were added to the device in order to allow precise control of cell loading <sup>245</sup>	<ul style="list-style-type: none"> <li>• CYP1a1</li> <li>• CYP1a2</li> <li>• Various UGT isoforms (Cultured HepG2 cell lines)</li> </ul>	<ul style="list-style-type: none"> <li>• Liver tissue engineering</li> <li>• Drug screening</li> <li>• Prediction of therapeutic effects of new compounds</li> </ul>
Co-cultures of both hepatocytes and non-parenchymal cell co-cultures using a Hurel biochip which contains four compartments. A liver compartment to facilitate metabolism, a lung compartment which represents the targeted tissue, a fat site which facilitates the accumulation of hydrophobic xenobiotics and a compartment that mimics a non-metabolism, non-accumulation site <sup>246</sup>	<ul style="list-style-type: none"> <li>• CYP3a4</li> <li>• CYP1a2</li> <li>• CYP2c19 (Hepatocytes)</li> </ul>	<ul style="list-style-type: none"> <li>• Drug metabolite determination</li> </ul>
Enzyme was immobilised within a porous monolith and placed within a microfluidic device interfaced to electrodes to allow droplet control <sup>247</sup>	<ul style="list-style-type: none"> <li>• CYP1a2 (Recombinant enzyme)</li> </ul>	<ul style="list-style-type: none"> <li>• Preclinical drug discovery</li> <li>• Drug development</li> </ul>
Human liver microsomes were immobilised within a microfluidic device containing an array of micropillars in a singular channel device <i>via</i> a biotin/streptavidin linkage <sup>248</sup>	<ul style="list-style-type: none"> <li>• Various UGT isoforms (Human liver microsomes)</li> </ul>	<ul style="list-style-type: none"> <li>• Inhibition determination</li> <li>• Timepoint measurements of substrates/cofactors and inhibitors</li> </ul>
A multichannel device with 6 parallel channels and a cell culture chamber in which a card slot is attached allowing an automated sampler to collect and analyse potential products real time <sup>249</sup>	<ul style="list-style-type: none"> <li>• Various UGT isoforms (Cultured HepG2 cell lines)</li> </ul>	<ul style="list-style-type: none"> <li>• Anticancer effect determination</li> <li>• Determination of alternative reaction pathways <i>in vivo</i></li> </ul>
HPLC column packed with immobilised enzyme <sup>250</sup>	<ul style="list-style-type: none"> <li>• Various UGT isoforms (Microsomes)</li> </ul>	<ul style="list-style-type: none"> <li>• Determination of metabolic products formed <i>in vivo</i>.</li> </ul>

		<ul style="list-style-type: none"> <li>• Determination of enzymatic catalysis parameters</li> </ul>
HPLC column packed with immobilised enzyme <sup>251</sup>	<ul style="list-style-type: none"> <li>• Various UGT isoforms (microsomes)</li> </ul>	Determination of active UGT isoforms
Enzyme encapsulated in a solgel matrix within a capillary column <sup>252</sup>	<ul style="list-style-type: none"> <li>• Various UGT isoforms (microsomes)</li> </ul>	<ul style="list-style-type: none"> <li>• Enzyme inhibition studies</li> </ul>
Enzymes were immobilised onto magnetic beads via biotin/streptavidin bonding and placed within individual compartments to allow sequential metabolism <sup>253</sup>	<ul style="list-style-type: none"> <li>• CYP3a4</li> <li>• UGT2b7 (supersomes)</li> </ul>	<ul style="list-style-type: none"> <li>• Identification of naturally forming metabolites</li> <li>• Small scale synthesis</li> <li>• Study cascade metabolism of xenobiotics</li> </ul>

As can be seen in Table 1.3, there has been an extensive amount of research on cytochrome P450 enzymes within a microfluidic device for a variety of different applications. However, the sole focus of these studies is typically on the determination of mechanistic properties of complex mixtures of enzymes rather than isozymes (as detailed in Table 1.3), on cytotoxicity studies and the prediction of metabolites formed *in vivo*. Contrary to CYP, UGT facilitated reactions within a microfluidic device have only been attempted a limited number of times and. The previous studies yielded promising results with the potential of immobilized enzymes as a synthetic method, but these have as of yet not been applied.

## 1.9. Aims of thesis

The aim of this thesis was to develop a method that has the potential to synthesise metabolic products in bulk, bypassing the issues with previous methods (low yields and separating the products from a complex biological matrix). The specific aims of this thesis are:

- The optimisation of an analytical technique for each of the substrates and products utilised throughout this thesis (resorufin, resorufin- $\beta$ -D-glucuronide, *p*-nitrophenol, *p*-nitrophenyl sulfate and 7-ethoxyresorufin).

- Development and initial optimisation of an UDP-glucuronosyl transferase (UGT1a1) immobilised microfluidic device that allows for the synthesis of a glucuronide conjugated metabolite (resorufin glucuronide)
- Development and optimisation of a sulfotransferase (SULT1a1) immobilised microfluidic device that allows for the synthesis of sulfate conjugated metabolite (resorufin sulfate and *p*-nitrophenyl sulfate)
- Initial development of a Cytochrome P450 (CYP1a1) immobilised microfluidic device that has the potential to allow for the synthesis of CYP facilitated metabolic product (resorufin)

## 1.10. Gap in the field

To the authors' knowledge the previous methods for metabolic studies have focused on the measurement of rate and determination of which specific metabolites are formed and their effects on the human body. There is a significant gap in this field where the synthesis of specific human metabolites of drugs that can simply be used for *in vitro* mechanistic studies (or as analytical standards) has yet to be explored. The current lack of availability of drug metabolites in sufficient quantities for *in vitro* testing, means that *in vitro* testing of drugs and drug-candidates has limited predictivity of *in vivo* action, due to a lack of integration of drug metabolism into these model systems. Addressing this limitation by synthesising usable quantities of stable drug metabolites would represent a significant step in improving *in vitro* predictivity for *in vivo* drug action or toxicity. This is a frequently observed problem in the study of polyphenolic compounds, in which contradictory information has been observed when determining their beneficial or toxicological effects. Lewandowska *et al.* created an overview of metabolism and bioavailability of polyphenols in which contradictory results have been reported.<sup>254, 255</sup> This could potentially be due to metabolism having an effect on a specific polyphenols' bioactivity with regards to beneficial and toxicological effects (reducing or increasing). In some cases a certain metabolite may be formed in which an antioxidative affect has been observed but different metabolites can be formed dependant on a specific persons metabolic profile.<sup>256</sup> Many polyphenols are highly metabolised within the liver whereas, in live animal/human testing, the focus is predominantly on the unmetabolized compound. It is also worth noting that in some studies unrealistic exposure concentrations are tested. Therefore, a method that

allows for the production of the metabolised products is vital for effective nutraceutical and pharmaceutical understanding and development.

## 2. Experimental

This section describes the relevant chemicals and materials, instrumentation, methods and analytical procedures.

### 2.1. Chemicals and materials

Chemicals and materials used throughout this thesis are described in tables Table 2.1 and Table 2.2. Equipment used is detailed in Table 2.3

Table 2.1: Commercially available solvents and reagents used throughout this research.

Reagent/solvent	Supplier	Details
<b>Hydrogen peroxide (30%)</b>	Thermo Fisher Scientific, Vantaa, Finland	Piranha solution for cleaning devices
<b>Sulfuric acid (95%)</b>	Honeywell, Morris Plains, USA	
<b>Araldite® 2014-2 Two Component Epoxy paste</b>	Araldite, Basel, Switzerland	Device interfacing to syringe pump
<b>Sodium hydroxide (98%)</b>	Thermo Fisher Scientific, Vantaa, Finland	Device cleaner
<b>Methanol (99.6%)</b>	Thermo Fisher Scientific, Vantaa, Finland	Dissolve epoxy resin
<b>(3-Aminopropyl) trimethoxysilane (APTMS) (97%)</b>	Sigma Aldrich, Poole, UK	Silanising agent

<b>Ethanol</b> (99.5%)	Sigma Aldrich, Poole, UK	Diluent for APTMS
<b>Glutaraldehyde</b> (25%)	Sigma Aldrich, Poole, UK	Functionalisation of microfluidic device
<b>Sodium phosphate monobasic</b> (99%)	Sigma Aldrich, Poole, UK	Phosphate buffer
<b>Sodium phosphate dibasic</b> (99%)	Sigma Aldrich, Poole, UK	
<b>Resorufin</b> (95%)	Sigma Aldrich, Poole, UK	Initial substrate
<b>P-Nitrophenol</b> (99%)	Sigma Aldrich, Poole, UK	
<b>7-Ethoxyresorufin</b> (95%)	Sigma Aldrich, Poole, UK	
<b>Resorufin Glucuronide</b>	Sigma Aldrich, Poole, UK	Product formed <i>via</i> UGT1a1
<b>P-nitrophenyl sulfate</b> (95%)	Sigma Aldrich, Poole, UK	Product formed <i>via</i> SULT1a1
<b>Methanol</b> (LC-MS quality)	Thermo Fisher Scientific, Vantaa, Finland	Mobile phase in LC-TQ-MS
<b>Water</b> (LC-MS quality)	Thermo Fisher Scientific, Vantaa, Finland	

<b>Formic Acid (98-100%)</b>	Chem Solute®, Renningen Germany	
----------------------------------	------------------------------------	--

Table 2.2: Commercially available enzyme system used in this study.

Enzyme	Supplier	Details
<b>UGT1a1 supersomes</b>	Corning, Wiesbaden, Germany	Enzymes utilised for immobilisation and static reactions
<b>SULT1a1 supersomes</b>	Santa Cruz Biotechnology, California, USA	
<b>Cypexpress CYP1a1</b>	Sigma Aldrich, Poole, UK	
<b>CYP1A1 supersomes</b>	Corning, Wiesbaden, Germany	

Table 2.3: Equipment used throughout this research.

Equipment	Supplier	Details
<b>Starlab 96 v-well microplate</b>	Starlab, Milton Keynes, UK	Fluorescence based analysis of resorufin
<b>BMG Labtech FLUOstar Omega platereader</b>	BMG, Aylesbury, UK	Fluorescence measurements of resorufin
<b>Shimadzu Nexera X2</b>	Shimadzu, Kyoto, Japan	LC-TQ-MS
<b>Shim-pack GISS HP (C18) column</b>	Shimadzu, Kyoto, Japan	
<b>Shimadzu CTO-20AC oven</b>	Shimadzu, Kyoto, Japan	

<b>Shimadzu Nexera X2 SIL-30AC autosampler</b>	Shimadzu, Kyoto, Japan	
<b>Heracell 150 Incubator</b>	Thermo Fisher Scientific, Vantaa, Finland	Temperature studies for metabolism
<b>The Harvard Apparatus Pump 11</b>	Harvard Apparatus, Massachusetts, USA	Interfaced to microfluidic device for substrate flow
<b>PTFE Teflon tubing (1.58 mm OD x 0.3 mm ID)</b>	Sigma Aldrich, Poole	Interface from syringe pump to capillary
<b>Syringe to tubing adaptor</b>	Kinesis, Colmworth, UK	
<b>Fused silica capillary (100 µm ID x 363 µm OD)</b>	Sigma Aldrich, Poole, UK	Interface from PTFE Teflon tubing to microfluidic device

## 2.2. Device designing, preparing, interfacing and cleaning

The device designing and preparation was conducted in house by Alex Iles using the following method: Two different flowthrough devices were designed on AutoCAD based on previous studies, being a split channel and a serpentine.<sup>257</sup> These devices were developed using a wet etching technique. Glass devices were etched onto 10 mm thick glass wafer coated with a chromium and a photoresist layer utilising a technique called contact mask lithography (Schott B270, Tellic, USA). The device was

patterned using UV light and chrome etching prior to wet etching using hydrofluoric acid to a depth of 30  $\mu\text{m}$ . Inlet and outlet holes were then drilled using a CNC drill (Datron M7) into another 10 mm thick Schott B270 glass cover plate. These were then aligned and thermally bonded. These two devices are depicted in Figure 2.1a-d.

As these devices are reused prior to every use they were cleaned by placing in methanol overnight (~16 hours) removing any excess glue and placed in a furnace overnight, ashing any excess glue. The devices were filled with milliQ water and immersed in piranha solution (sulfuric acid and hydrogen peroxide in a 3:1 ratio). These were then immersed in milliQ water and sonicated for a minimum 15 minutes. Fused silica capillary (100  $\mu\text{m}$  ID x 363  $\mu\text{m}$  OD) was glued to both the inlet and outlet holes using araldite 2:1 epoxy resin and was interfaced to a syringe pump (NE-4000) *via* PTFE Teflon tubing (0.3 mm ID x 1.5 mm OD) and a luer lock as depicted in Figure 2.2.

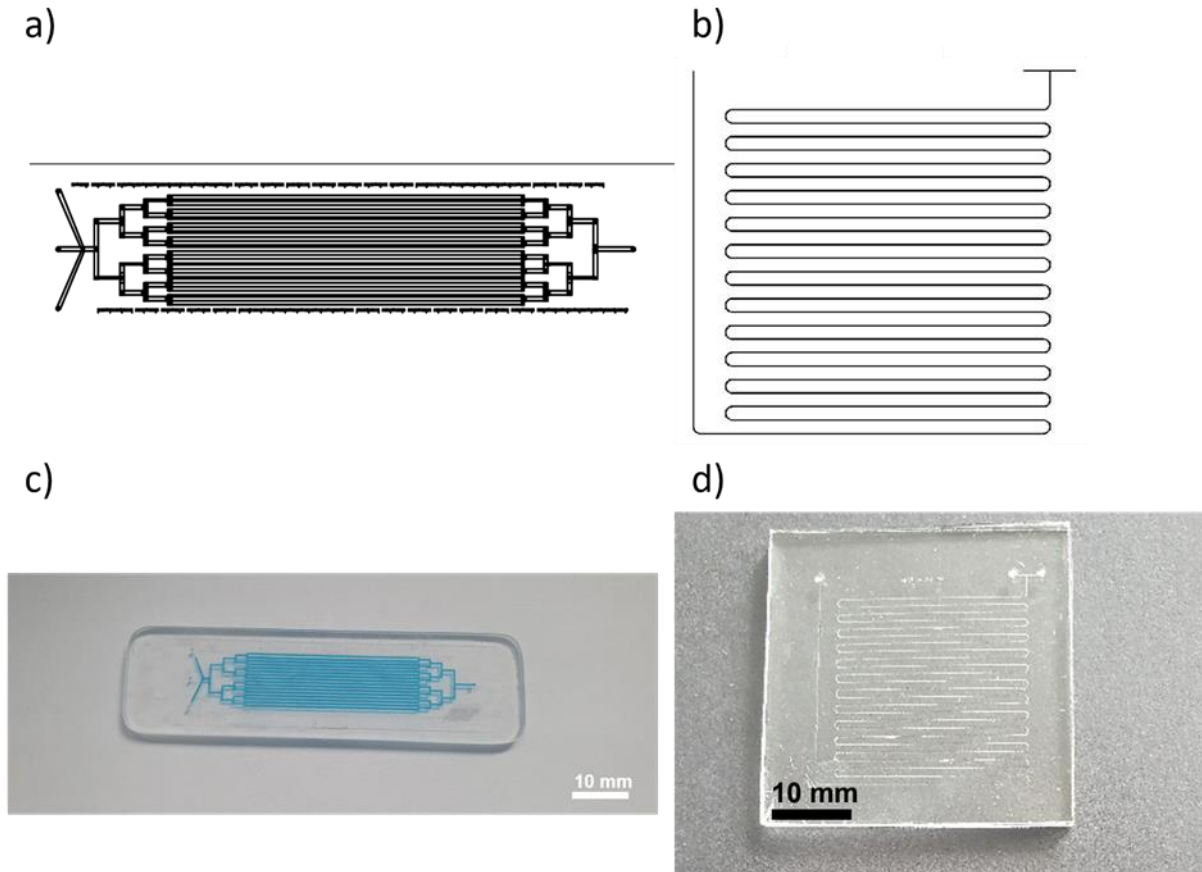


Figure 2.1 AutoCAD schematics for both a parallel (a) and a serpentine device (b), with a photograph of each respectively (c-d).

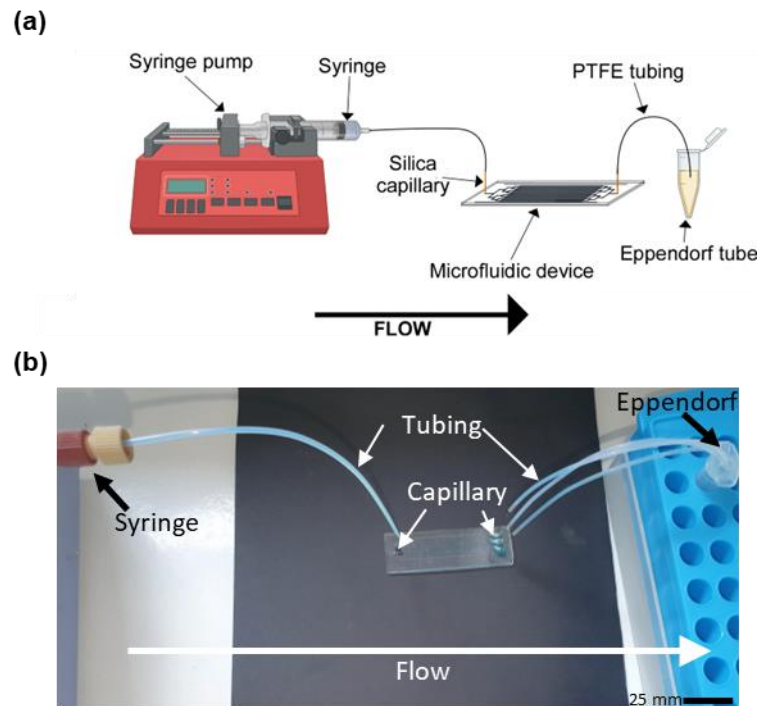


Figure 2.2 Representative schematic of the interfaced microfluidic device starting with the syringe pump with 1 mL syringe connected to PTFE tubing placed into the glued silica capillary

of the microfluidic device and ending at the collection Eppendorf tube (a) and a photograph of this setup (b).

### 2.3. Microfluidic substrate metabolism

Both sodium hydroxide (0.1 M, 3x1 mL), then methanol (3x1 mL) was flowed through the device. (3-Aminopropyl) trimethoxy silane (5% v/v in ethanol) was incubated in the device at room temperature for 5 minutes to facilitate silanisation. This was washed out with methanol (3x1 mL). The device was placed in an oven at 60 °C for one hour. The next step was further functionalisation by flowing glutaraldehyde (5% v/v in 0.1 M phosphate buffer, pH 7.4) at 3  $\mu\text{L min}^{-1}$  for one hour. The final step of immobilisation was then to fill the channel with enzyme solution (UGT1a1 at 0.15 mg mL<sup>-1</sup>, and SULT1a1/CYP1a1 at 10 ng mL<sup>-1</sup>) solution and left in the fridge overnight. This reaction is depicted in **Error! Reference source not found.**

The enzyme immobilised device was then washed out with phosphate buffer (0.1 M, pH 7.4). Resorufin, *p*-nitrophenol or 7-ethoxyresorufin (100  $\mu\text{M}$ ), and respective co-factor (UDP-GA, PAPS or NADPH at 100  $\mu\text{M}$ ) were flowed through both devices at varying flow rates (0.1, 0.5 and 1  $\mu\text{L min}^{-1}$ ) at room temperature (20  $\pm$  2 °C) with collecting and freezing upon collection of 12  $\mu\text{L}$  per sample over varying periods of time dependant on flow rate. To facilitate temperature studies longer tubing was used to allow the device to be within an incubator set to the respective temperatures (30 and 37 °C). Control reactions were conducted by omitting co-factor from the initial substrate mixture and an alternative unreactive enzyme (triosephosphate isomerase) to the substrates used was also immobilised.

## 2.4. Conventional static metabolism

Resorufin/7-ethoxyresorufin (10  $\mu\text{L}$ , 100  $\mu\text{M}$ ) and respective co-factor (UDP-GA or PAPS and NADPH respectively at 100  $\mu\text{M}$ ) was added to 2  $\mu\text{L}$  of enzyme solution (UGT1a1 at 0.15  $\text{mg mL}^{-1}$ , and SULT1a1/CYP1a1 at 10  $\text{ng mL}^{-1}$ ) and incubated in a microwell plate at 37  $^{\circ}\text{C}$  for 2 hours. A calibration curve for resorufin was then added to this plate and analysed as below.

## 2.5. Fluorescence analysis of resorufin

A calibration curve was created using 10  $\mu\text{L}$  of resorufin from 100  $\mu\text{M}$  diluted sequentially two-fold 16 times in phosphate buffer (0.1 M, pH 7.4) implemented into a Starlab 96 v-well microplate. Fluorescence intensity was then measured through the bottom optical using a BMG Labtech FLUOstar Omega plate reader set to 544 nm  $\lambda_{\text{ex}}$  and 590 nm. Concentrations of resorufin within a sample was also measured and a concentration of resorufin remaining was determined using a new calibration curve alongside each set of analysed samples.

## 2.6. LC-TQ-MS analysis of substrates and expected products

All substrates and products used in these studies were injected at 10  $\mu\text{L}$ (resorufin, resorufin glucuronide, *p*-nitrophenol, *p*-nitrophenyl sulfate) at 100  $\mu\text{M}$  in phosphate buffer (0.1 M, pH 7.4), was injected into LCMS as described in Table 2.4 and Table 2.5.

For resorufin glucuronide within a sample an extraction was necessary in which, C18 zip tips were added to a pipette set to 10  $\mu\text{L}$  which was then wetted by implementing

10 $\mu$ L of 50% methanol in water twice. The tip was then equilibrated by implementing 10 $\mu$ L of 0.1% TFA in water and discarding twice. 10 $\mu$ L of sample was implemented into the C18 tip and aspirated 10 times sample and left within the tip for 5 minutes. Tip was then rinsed with 10  $\mu$ L of MilliQ water and discarding solvent twice. Sample was then extracted into a HPLC vial from the C18 tip using 10  $\mu$ L of methanol followed by injection into the LCMS. All other substrates and samples were directly injected using the settings described in Table 2.4 with the gradient depicted in Figure 2.4. Substrates and samples were analysed using a Shimadzu Nexera X2 series LC (Kyoto, Japan) equipped with a Shimadzu Nexera X2 SIL-30AC autosampler linked to a Shimadzu 7060 TQ-MS (typical TQ-MS drawn in Figure 2.3). Data acquisition and processing was performed by LabSolutions™ 5.93 software. A Shim-pack GISS C18 column (50 mm x 2.1 mm, 1.9  $\mu$ m) was utilised to achieve chromatographic separation.

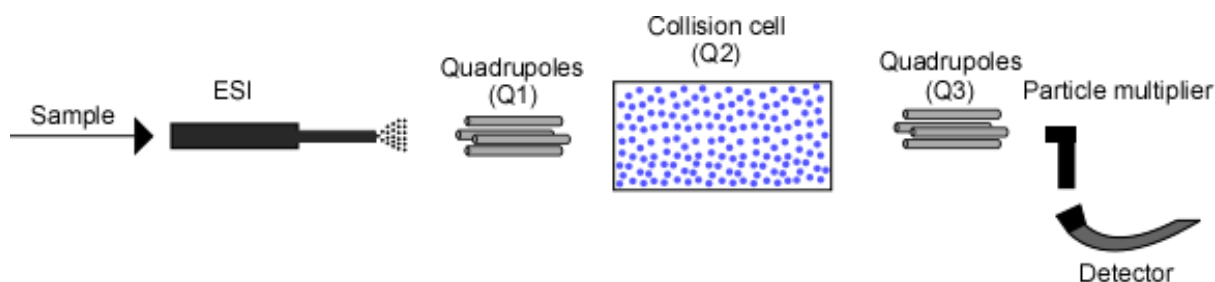


Figure 2.3: Schematic of a typical LC-TQ-MS equipped with an ESI.

Table 2.4: Experimental setup for the LC-TQ-MS of substrates throughout this research

<b>Column</b>	<b>Shim-pack GISS HP (C18)</b>	
<b>Oven temperature</b>	40 °C, Shimadzu CTO-20AC	
<b>Injection volume</b>	10 $\mu$ L	
<b>Eluent A</b>	0.1 % Formic Acid in Water	
<b>Eluent B</b>	0.1% Formic Acid in Methanol	
<b>Composition A: B</b>	<b>Time (min)</b>	<b>A: B</b>
	0	95:5

	3 10 20 22 25	95:5 25:75 25:75 95:5 95:5
<b>Flow rate</b>	0.5 ml min <sup>-1</sup>	
<b>Autosampler</b>	Shimadzu Nexera X2 SIL-30AC	
<b>Spray voltage</b>	2.32 kV	
<b>Capillary temperature</b>	250 °C	

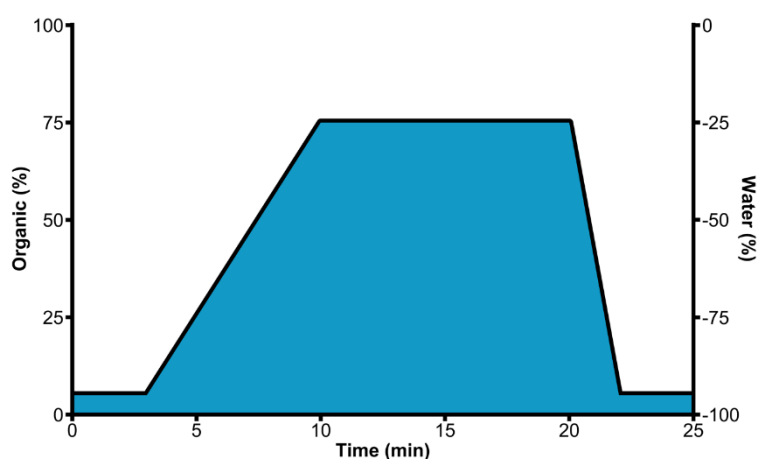


Figure 2.4 Graphical representation of gradient utilised for the separation of products and substrates formed throughout this study.

Four different scans were optimised for each analysed compound (Q1 scan, product ion scan, precursor ion scan and MRM scan) and the settings for each are described in Table 2.5. All samples were analysed in negative mode with the exception of 7-ethoxyresorufin which was in positive mode due to increased sensitivity and reduced background noise.

Table 2.5: Experimentally determined scans for the analysis of each substrate or product used throughout this research.

<b>Compound</b>	<b>Type of scan</b>	<b>Product/ Precursor mass (m/z)</b>	<b>Retention time (min)</b>
<b>Resorufin</b>	Product ion scan	212	9.8
	Precursor ion scan	155	
	MRM	212>155	
<b>Resorufin glucuronide</b>	Product ion scan	388	8.0
	Precursor ion scan	212	
	MRM	388>212	
<b>p-Nitrophenol</b>	Product ion scan	138	8.7
	Precursor ion scan	108	
	MRM	138>108	
<b>Nitrophenyl Sulfate</b>	Product ion scan	218	6.9
	Precursor ion scan	138	
	MRM	218>138	
<b>7-Ethoxy resorufin</b>	Product ion scan	242	11.0
	Precursor ion scan	212	
	MRM	242>214	

## 2.7. Statistical analysis

Normal distribution and homogeneity for the data was assessed using a Shapiro-Wilk test and Levene test respectively using SPSS version 28.0. Parametric data was analysed using a One-way ANOVA with Bonferroni post hoc test. All samples that statistical analysis was undergone were analysed in triplicate. Values of  $p < .05$  were

significant. Figures were denoted with significance stars \*, \*\* and \*\*\* indicating  $<0.05$ ,  $<0.01$  and  $<0.001$  respectively.

### **3. Optimisation of mass spectrometry for the determination of phase II metabolites and their precursors *via* LC-TQ-MS**

#### **3.1. Introduction**

Many analytical techniques for resorufin are based on the compound's highly fluorescent nature. These include fluorescence spectroscopy and fluorescence plate reader-based methods.<sup>62, 258-261</sup> The amount of resorufin in a sample can be quantified by comparison to a calibration curve, and the conversion of resorufin can be measured as a loss of fluorescence. However, this approach has limitations, since the reduction in fluorescence only confirms the loss of resorufin from the sample but does not measure the formation of a specific reaction product. Thus, it is not possible to determine exactly which products are formed, which is particularly desired when studying more complex substrates that can result in a variety of isomers and/or multiply conjugated compounds.

Mass spectrometry is well suited to study product formation. It is widely used in synthetic chemistry and has also been applied for the analysis of naturally formed metabolites.<sup>262, 263</sup> However, many studies so far have focussed on the rate at which resorufin is metabolised rather than aiming at measuring a specific product formed. Methods for the separation of resorufin from its respective metabolites are generally lacking with the majority of them focussing on the use of UPLC. LC-TQ-MS is particularly applicable for metabolite identification due to the integration of a chromatographic separation with compound identification via MS-MS fragmentation

and can allow for potential visualisation of short-lived products and intermediates. This gives significantly more confidence in the data obtained alongside some structural insight.

A Q1 scan measures any ions passing through the first quadrupole (Q1) allowing for depiction of any ionisable compounds within a solution. A Q3 scan measures any fragmented compounds after entering the collision cell the Q1 is not used in this scan and the Q3 allows any ions to enter the detector. A Q1 and Q3 single ion monitoring scan (SIM) only lets one specific  $m/z$  to the detector. This increases the overall sensitivity but does not provide any characteristics of the analyte. The product ion scan is vital for metabolite identification as it provides much more characteristic information that allows for a direct comparison to a known compound. This involves setting the Q1 to a specific  $m/z$  (comparable to the SIM and typically the parent ion of the analyte) but allows for any ions to enter the detector after entering the collision cell, this enables visualising of each ionised fragment that is formed. Precursor ion scan effectively does the reverse in which Q3 is set to a specific ion and only shows ions that caused this fragment to be formed. Multiple reaction monitoring (MRM) is the most sensitive of these scans but requires both the parent ion  $m/z$  and the  $m/z$  of a fragment formed. As both Q1 and Q3 are set to a defined  $m/z$  value no scanning is required, thus increasing the overall intensity. The final scan, neutral loss, measures any ions that enter Q1, and a specific mass is lost upon fragmenting in the collision cell and measured by Q3. This is also beneficial for determining metabolites and can be used to differ between multiply conjugated products. These scans have their own benefits and applications as described in Table 3.1.

*Table 3.1: Settings for different scans on LC-TQ-MS and their applications. Q1 and Q3 scan measure all ions that enter their respective detector, Q1 and Q3 SIM measure a specific  $m/z$  entering the respective detector, product ion scan measures fragments of a specific known parent ion, precursor ion scan measures from a fragment back and determines previous*

fragments and parent ions, MRM measures a specific fragmentation from both the parent ion to a known fragment ion and a neutral loss scan which measures all masses that 80 mass units are lost between the Q1 and Q3 detectors.

Scan	Q1 setting	Q3 setting	Application
<b>Q1 scan</b>	Entire m/z range	N/A	Determining parent ions/finding contaminants
<b>Q3 scan</b>	N/A	Entire m/z range	Determining parent ions allowing for fragmentation
<b>Q1 SIM</b>	Single m/z	N/A	Calibration curves of a known
<b>Q3 SIM</b>	N/A	Single m/z	Calibration curves of a known
<b>ProIS</b>	Single m/z	Entire m/z range	Can allow the determination of the structure of the parent ion. Identify fragmentations which can be used for quantification by MRM.
<b>PreIS</b>	Entire m/z range	Set to a single m/z	Confirmation of specific functional groups
<b>MRM</b>	Single m/z	Single m/z	Trace detection and calibrations of known compounds
<b>Neutral loss scan</b>	Entire m/z range	Entire m/z range	Detection of characteristic fragmentations, <i>i.e.</i> , sulfation loss of 80 m/z units

### 3.2. Methods

#### Optimisation of fragments and collision energy

Resorufin, resorufin glucuronide, nitrophenol, nitrophenyl sulfate and 7-ethoxyresorfin (10  $\mu$ L at 1  $\mu$ M) were injected into an LC-TQ-MS system with the column removed. Q1 scans, product ion scans, MRM scans and optimisation for collision energy were applied in turn. Initially the parent/major ions were determined in both positive and negative mode using the Q1 scan irrespective of the analytes' inherent structure, and the fragments 58 remained were optimised using the inbuilt LabSolutions software's function "optimisation for collision energy". Throughout the initial optimisation the

column was removed and 10  $\mu\text{L}$  of resorufin (1  $\mu\text{M}$ ) was injected to directly into the MS. This bypassed long retention times whilst optimising the scans and also reduced solvent use. The approach was also followed for all single compound analysis. Determining a compound's parent/major ions was necessary for further optimisation, as the next step being a product ion scan requires setting the Q1 to its measured value to see which fragments are formed which in turn are applied within the MRM scan. Finally, the scan yielding the highest intensity and most visible peak was chosen in order to yield the highest sensitivity. The initial predicted m/z found for each analyte were their parent ions, either 1 m/z more or less depending on whether positive or negative mode was utilised. With the chosen analytes both the sulfates and glucuronides have an expected neutral loss of 80 m/z and 176 m/z, respectively.<sup>264</sup>

## Isocratic flow

The same concentration (100  $\mu\text{M}$ ) of both resorufin and resorufin glucuronide were analysed in both positive and negative mode using an isocratic flow as described in Table 3.2. The isocratic method was developed based on a similar study by Johansson *et al.* but further developed *via* previous studies on a HPLC equipped with a fluorescence and absorbance detector (data not shown).<sup>265</sup>

Table 3.2 Liquid chromatography and HPLC parameters and conditions for the analysis of metabolites

Column	Shim-pack GISS HP (C18)
Oven temperature	40 °C, Shimadzu CTO-20AC
Injection volume	10 $\mu\text{L}$
Eluent A	0.1 % Formic Acid in Water
Eluent B	0.1% Formic Acid in Acetonitrile
Composition A: B	30:70
Flow rate	0.5 ml min <sup>-1</sup>
Autosampler	Shimadzu Nexera X2 SIL-30AC
Spray voltage	2.32 kV
Capillary temperature	250 °C

## Gradient flow

In turn all substrates, resorufin, resorufin glucuronide, nitrophenol, nitrophenyl sulfate and 7-ethoxyresorufin, were studied using the gradient method described in Table 3.3 at 100  $\mu$ M. This gradient method was initially developed to allow the removal of any unwanted highly hydrophilic compounds, such as the substituents of the phosphate buffer used and the slow increase in polarity will allow for the separation of similar structured metabolites and precursors. A visualised gradient is shown in Figure 3.1.

*Table 3.3: Isocratic mode parameters utilised for both positive and negative mode.*

Column	Shim-pack GISS HP (C18)
Oven temperature and controller	40 °C, Shimadzu CTO-20AC
Injection volume	10 $\mu$ L
Eluent A	0.1 % Formic Acid in Water
Eluent B	0.1% Formic Acid in Acetonitrile
Time	Composition A: B
0 min	95:5
3 min	95:5
10 min	25:75
20 min	25:75
22 min	95:5
25 min	95:5
Flow rate	0.5 ml min <sup>-1</sup>

Autosampler	Shimadzu Nexera X2 SIL-30AC
Spray voltage	2.32 kV
Capillary temperature	250 °C

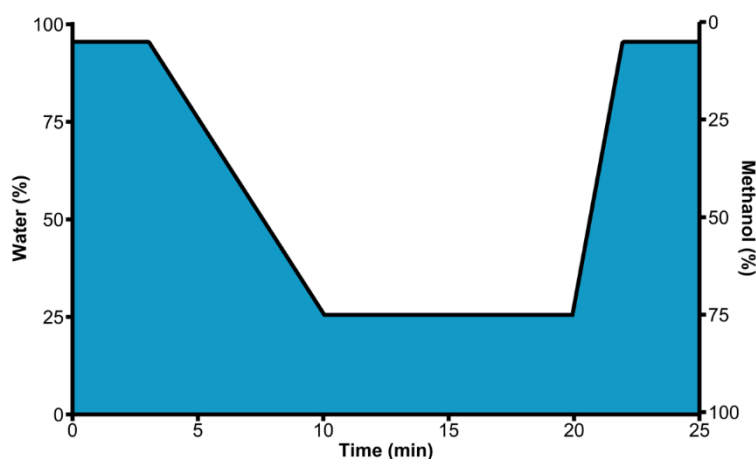


Figure 3.1: Visualisation of gradient used for LC-MSMS analysis.

### 3.3. Results and Discussion

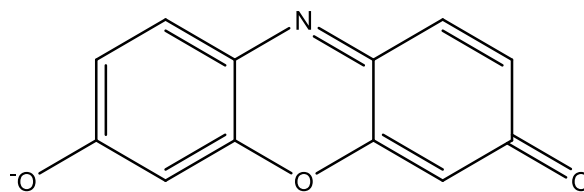
#### Resorufin

##### Q1 scan

A Q1 scan measures all ions that pass through the initial quadrupole. This approach minimises in-source fragmentation and does not include collision induced fragmentation that can occur within the collision cell in Q2 prior to entering Q3. A schematic of a general TQ-MS is shown in Figure 2.3. The parent ions of resorufin are shown in Figure 3.2. A Q1 scan was conducted on resorufin in positive mode (Figure 3.3a) and negative mode (Figure 3.3b). Both feature a large peak containing all masses entering the detector in a single trace at the beginning of the scan. The mass spectra of these peaks show the expected parent ions for resorufin, 214 m/z for positive mode (Figure 3.3c) and 212 m/z for negative mode (Figure 3.3d), respectively.

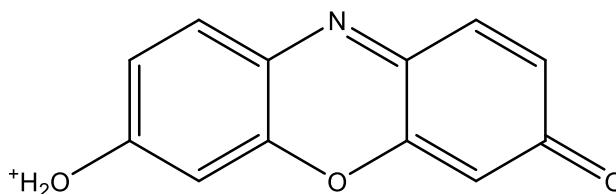
These parent ions were taken forward for MS-MS analysis to determine the fragments formed.

a)



Resorufin negative ion  
Molecular Weight: 212.18

b)



Resorufin positive ion  
Molecular Weight: 214.20

Figure 3.2: (a) Structure of expected resorufin negative ion and (b) the positive ion (b).

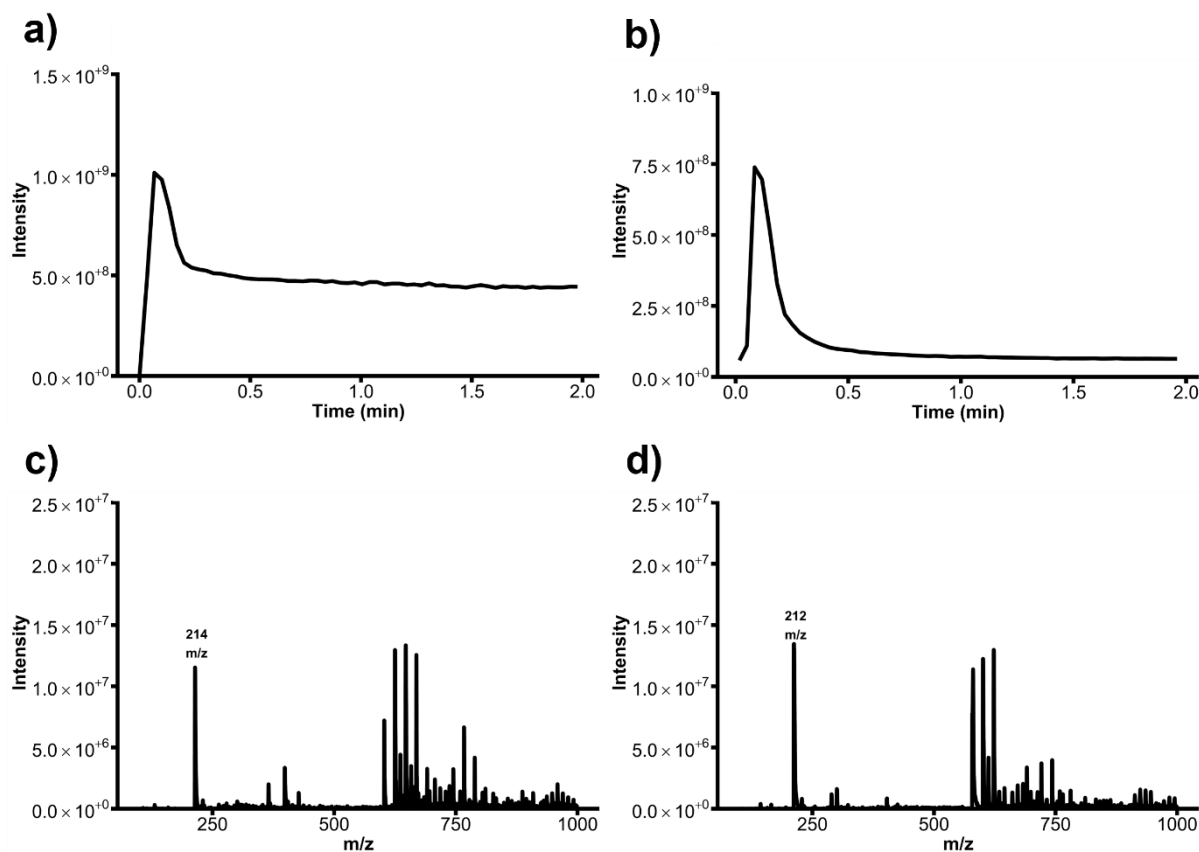


Figure 3.3 (a) Signal traces from injection of resorufin into the MS obtained in positive mode and (b) negative mode using a Q1 scan. (c) Mass spectrum of the area under the peak in (a), and (d) under the peak in (b).

### Product ion scan

During a product ion scan, Q1 is set to a predetermined m/z and all fragmentations formed within the collision cell from that m/z are passed to the second quadrupole (Q3). Here, Q1 was set to 214 m/z in positive mode (Figure 3.4a) and 212 m/z in negative mode (Figure 3.4b). The mass spectra from the signal peaks in both positive mode (Figure 3.4c) and negative mode (Figure 3.4d) yielded multiple fragments. The expected major ions found for negative mode were 214, 186 and 103 m/z, and for positive mode 212, 155 and 118 m/z as found using CFM-ID fragmentation prediction software.<sup>266-270</sup>

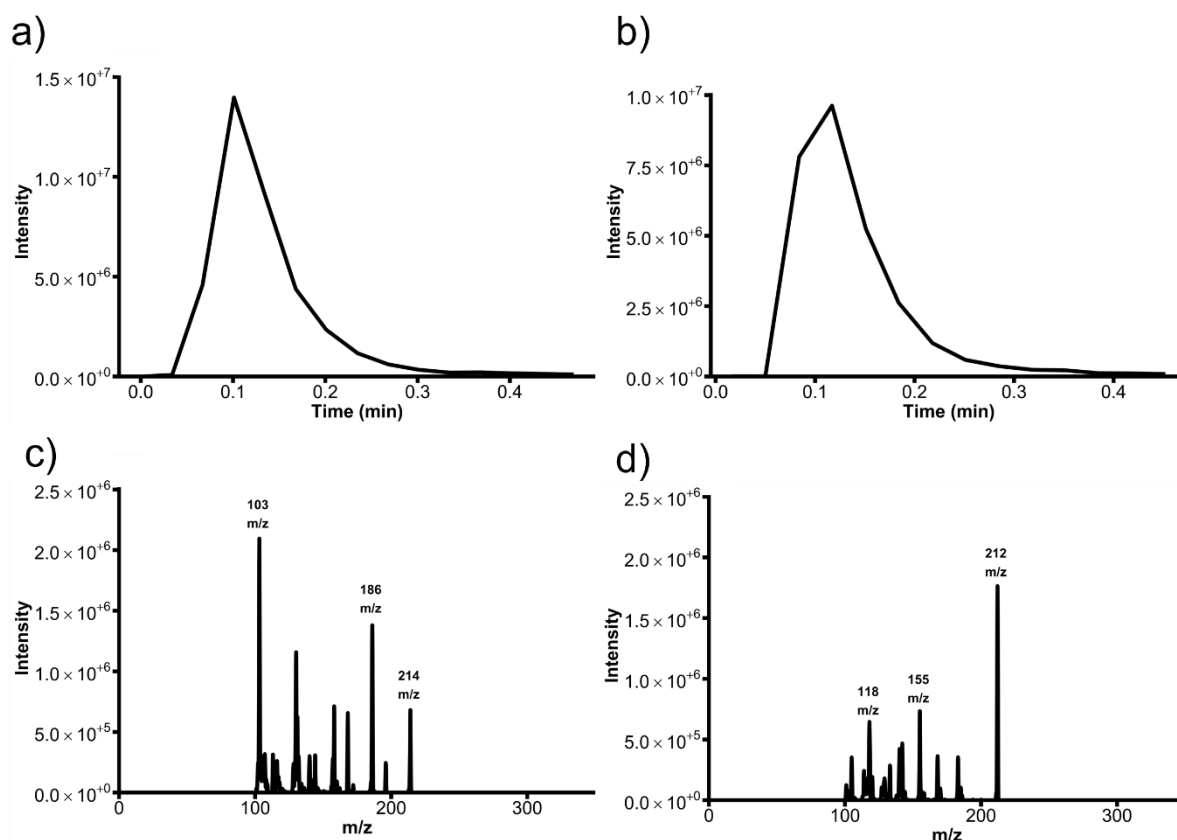


Figure 3.4: (a) Signal traces from injection of resorufin into the MS obtained in positive mode and (b) negative mode using a product ion scan. (c) Mass spectrum of the area under the peak in (a). (d) Mass spectrum of the area under the peak (b).

### Multiple reaction monitoring (MRM) scan

The next step was to conduct a multiple reaction monitoring (MRM) scan to show that these fragments are due to fragmentation from the pre-determined parent ion and not any potential contaminations within the resorufin standard whilst also providing a large increase to intensity. During an MRM scan, both quadrupole 1 and quadrupole 3 are set to a specific m/z. Both of these m/z were previously determined from the Q1 scan and the product ion scan, with significant peaks produced in positive mode being the identified transitions at 214>186 m/z (Figure 3.5a) and a 214>103 m/z (Figure 3.5a). Comparatively, the transitions in negative mode, 212>108 m/z (Figure 3.5c) and 212>155 m/z (Figure 3.5d) should provide peaks based on the mass spectrum in

Figure 3.4. The chosen fragmentations from the section above was applied to an MRM scan.

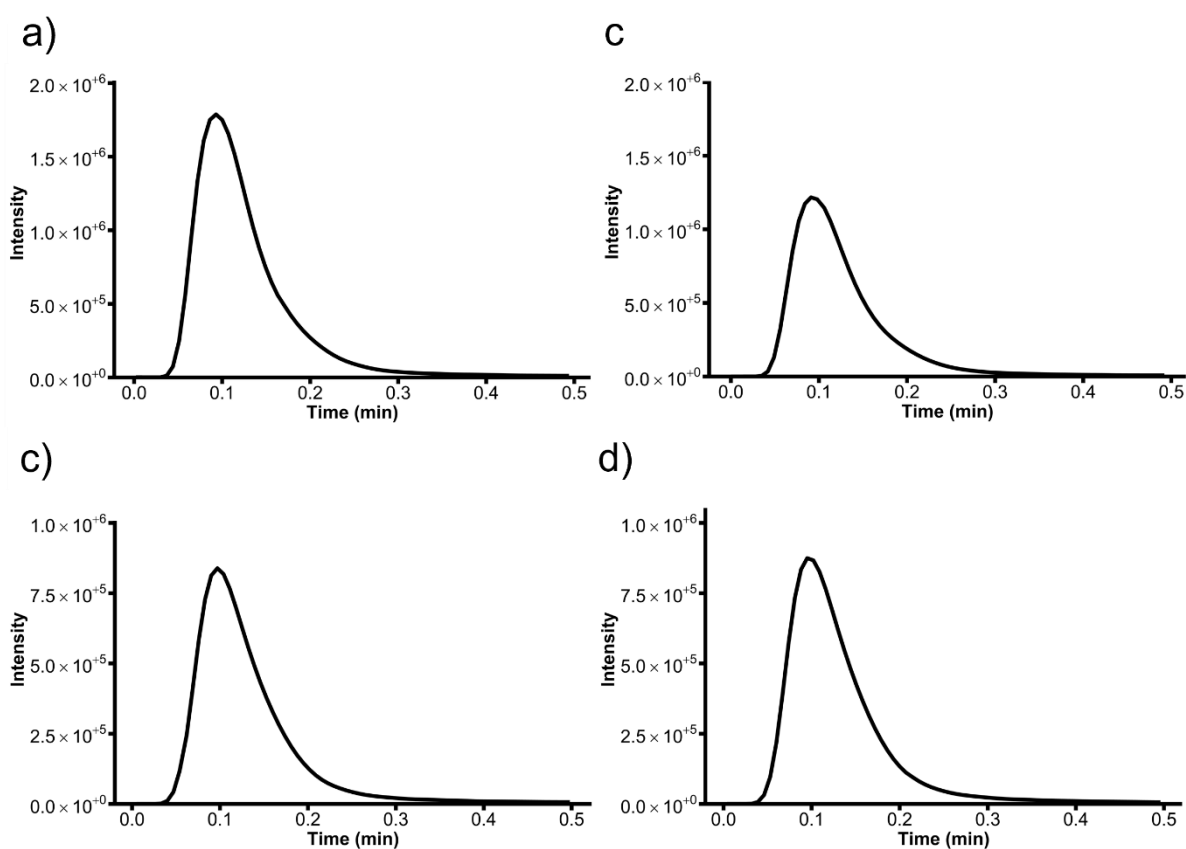


Figure 3.5: (a) Signal traces from injection of resorufin into the MS obtained in positive mode set to 214>103 and (b) 214>186 m/z and in negative mode (c) 212>108 m/z and (d) 212>155 m/z.

All four of these spectra provided a peak in the MRM scan so all of the fragmentations were carried forward to determine the optimum fragmentation. This was the fragmentation that provided the highest intensity and peak area as this provided a higher signal over the background at a comparable concentration, allowing for an improved sensitivity. With these transitions being, 214>103 m/z (Figure 3.5a) or 214>186 (Figure 3.5b) for positive mode, and 212>118 (Figure 3.5c) or 212>155 m/z (Figure 3.5d) for negative mode. The optimum of either of these scans can be used dependant on the respective conjugated moiety's optima, preventing a loss of instrument sensitivity when utilising both positive and negative mode simultaneously.

In turn, determining which of these scans yielded the highest intensity was the next step.

### *Optimisation of collision energy*

The LabSolutions software on the mass spectrometer provides an option to optimise the collision energies for a specific MRM. The collision energy has a large effect on determining the degree of fragmentation the molecule entering the collision cell undergoes. Therefore, optimising the collision energy has a significant effect on the fragment ions that are measured. A lower collision energy may not ionise the compound, and a higher collision energy may significantly fragment the molecule before it enters the detection region. Both a broad and an in-depth collision energy optimisation was conducted on the previously determined  $m/z$  transitions in positive mode at  $214 > 103$  (Figure 3.6a-b, respectively) ,  $214 > 186$  (Figure 3.6c-d respectively) and negative mode at  $212 > 108$  (Figure 3.6e-f respectively) and  $212 > 155$   $m/z$  (Figure 3.6g-h) for negative mode measurements in order to increase the overall sensitivity of the method.

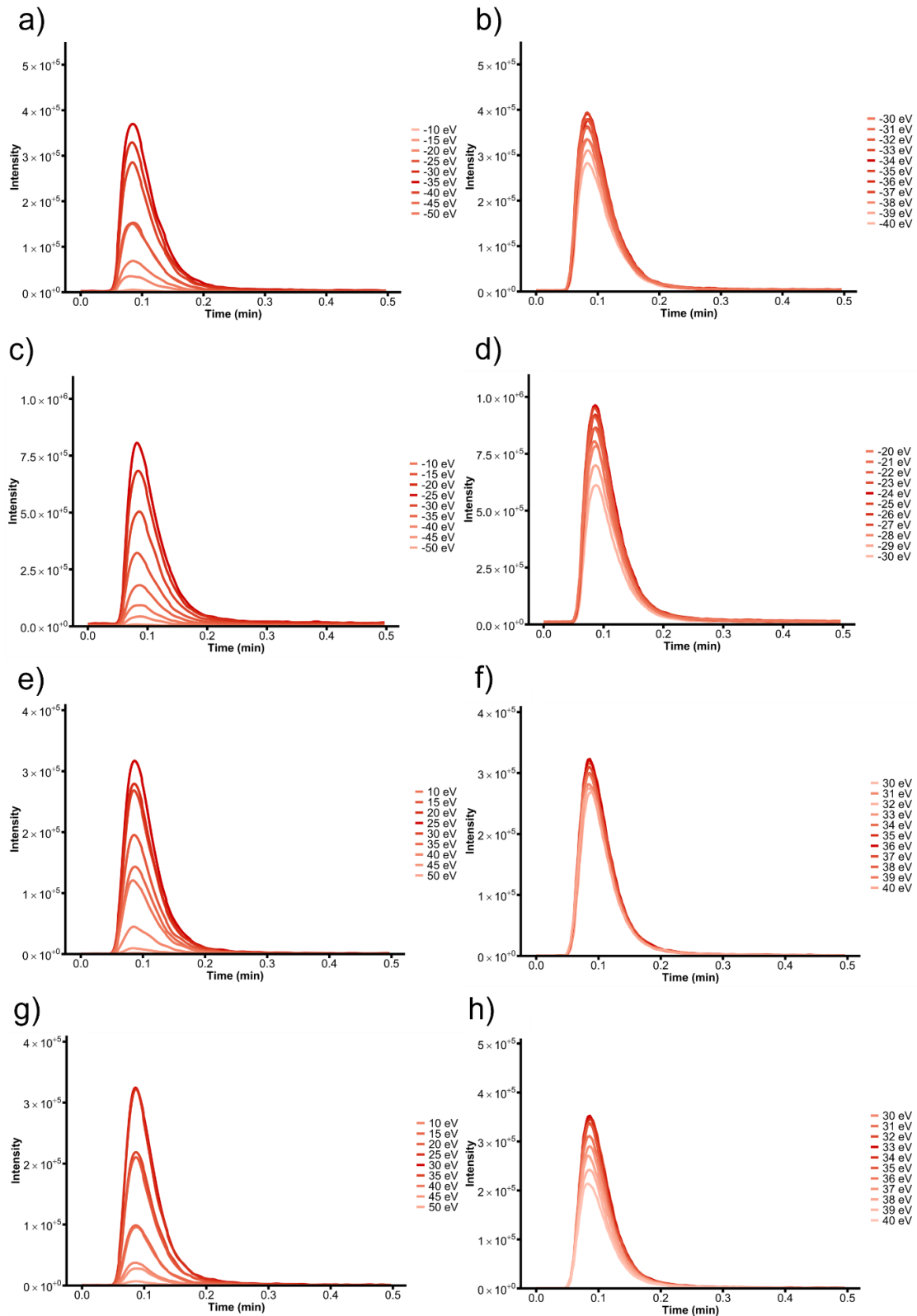


Figure 3.6: (a) Signal traces from injection of resorufin into the MS optimising the collision energy for the fragmentation in positive mode set to  $214 > 103$   $m/z$  using a broad scan and (b) a detailed scan between  $-30$  to  $-40$  eV and  $214$  to  $186$   $m/z$  using (c) a broad scan and (d) a detailed scan between  $-20$  to  $-30$  eV. In negative mode it was set to  $212 > 118$   $m/z$  using (e) a broad scan and (f) a detailed scan between  $30$  to  $40$  eV and  $214 > 186$   $m/z$  using (g) a broad scan and (h) a detailed scan between  $30$  to  $40$  eV.

The figures above are in pairs (a/b, c/d, e/f and g/h) with the former being a broad scan varying between 10 to 50 or -10 to -50 eV (with intervals of 5 eV) dependant on the mode of the detector and the latter being an in-depth scan. The mass spectrometer automatically determined the optimum collision energy dependant on the peak area of the resulting spectrum and applied it to the method being used. These four different optimised spectrum 214>103 (Figure 3.6a-b), 214>186 (Figure 3.6c-d) using positive mode and 212>118 (Figure 3.6e-f), 212>155 m/z (Figure 3.6g-h) for negative mode, were compared and the fragmentations 214>186 and 212>155 yielded a larger peak than their respective mode counterpart. The optimum collision energy for these scans is described in Table 3.4

*Table 3.4: Measured optimum collision energy (eV) for resorufin at all tested fragmentations.*

<b>Fragmentation (related in Figure 3.6)</b>	<b>Optimum collision energy</b>
214>103 m/z (a/b)	-34 eV
214>186 (b/c)	-24 eV
212>118 (d/e)	36 eV
212>155 (f/g)	33 eV

## **Resorufin glucuronide**

### *Q1 scan*

The parent ions of resorufin glucuronide are shown in Figure 3.7. A Q1 scan was used to determine the parent/major ions as previously described in the section 1.3 for resorufin glucuronide in both positive mode (Figure 3.8a) and negative mode (Figure 3.8b).

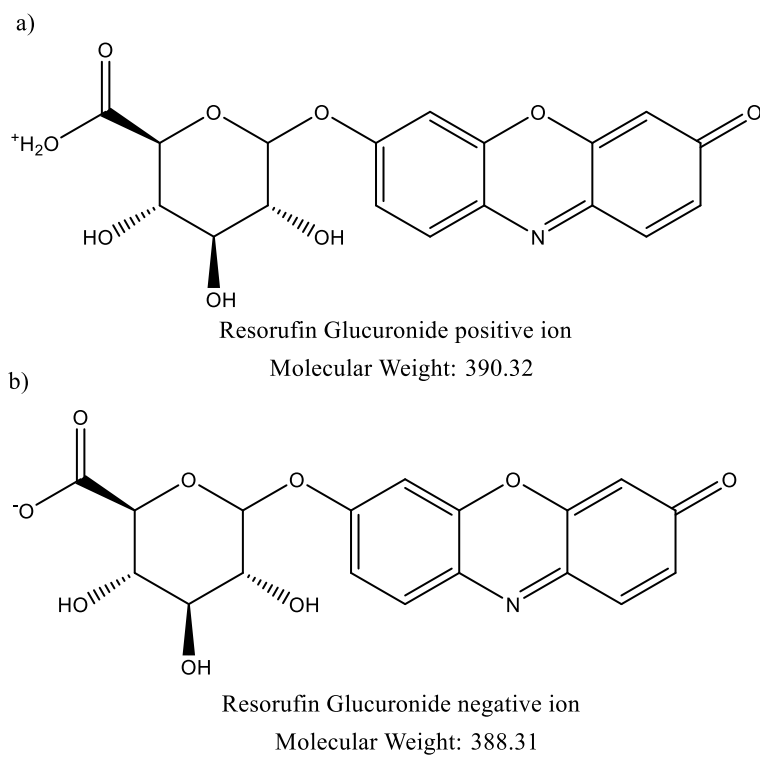


Figure 3.7: (a) Expected parent ions for resorufin glucuronide for both positive and (b) negative mode.

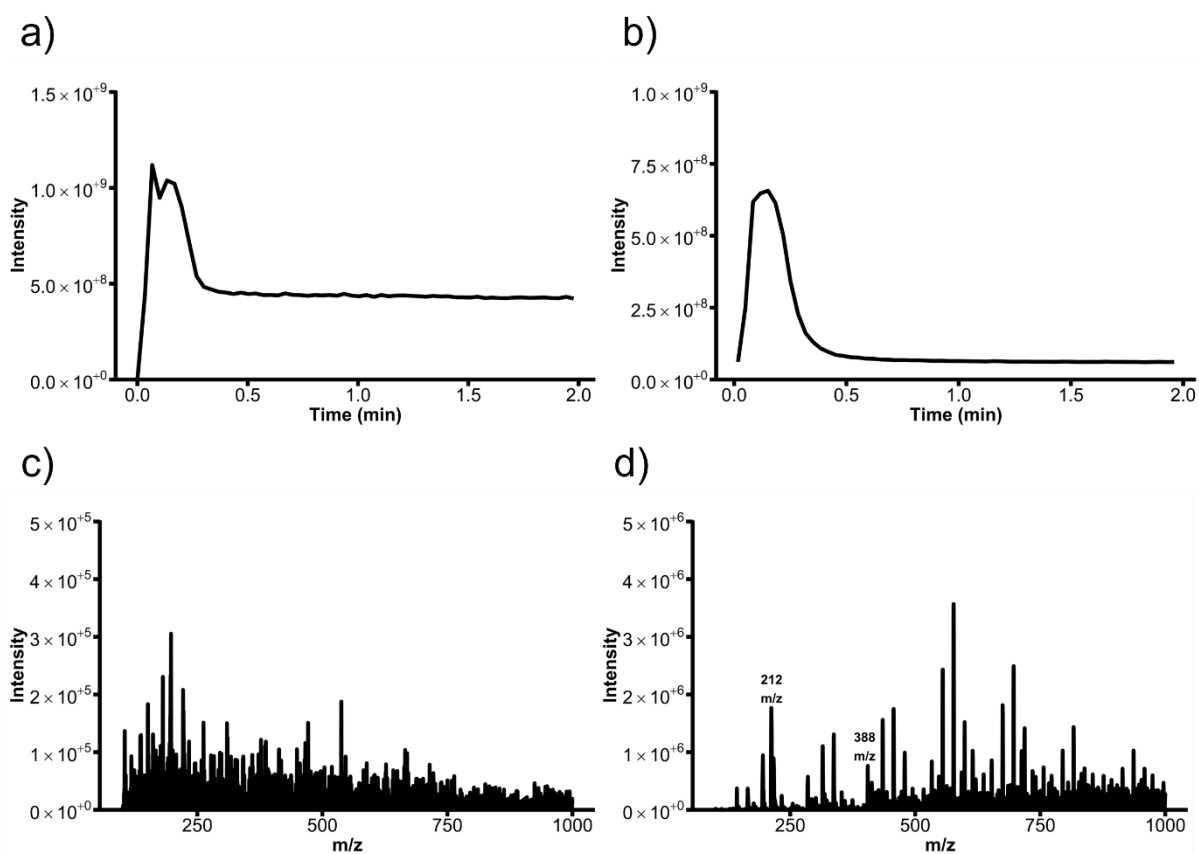


Figure 3.8: (a) Signal traces from injection of resorufin glucuronide into the MS obtained in positive mode and (b) negative mode using a product ion scan. (c) Mass spectrum of the area under the peak in (a). (d) Mass spectrum of the area under the peak (b).

The areas under the peaks observed for the Q1 scan of resorufin glucuronide in both positive mode (Figure 3.8a) and negative mode (Figure 3.8b) to find the parent/major ion to allow further optimisations (Figure 3.8c and d respectively). A very small mass of 383 m/z was observed in positive mode, and in negative mode the expected parent ion was found at 388 m/z. These two masses were carried forward into the product ion scan. Alongside these two masses, a third was found at 212 m/z which is likely to be due to resorufin, with a common glucuronide loss of 176 mass units prior to entering the detector. Thus, was not carried forward for further optimisation.

## Product ion scan

Similarly to the resorufin section, both positive and negative mode product ion scans were applied to allow determination of which fragments are formed upon undergoing collision induced fragmentation. As only one mass was visible in each mode, they were both implemented into a product ion scan to measure which fragments are observed and viable for MRM scans. The precursor ions selected for this scan were determined in the Q1 scan, 383 m/z in positive mode (Figure 3.9a&c) and 388 m/z in negative mode (Figure 3.9b&d).

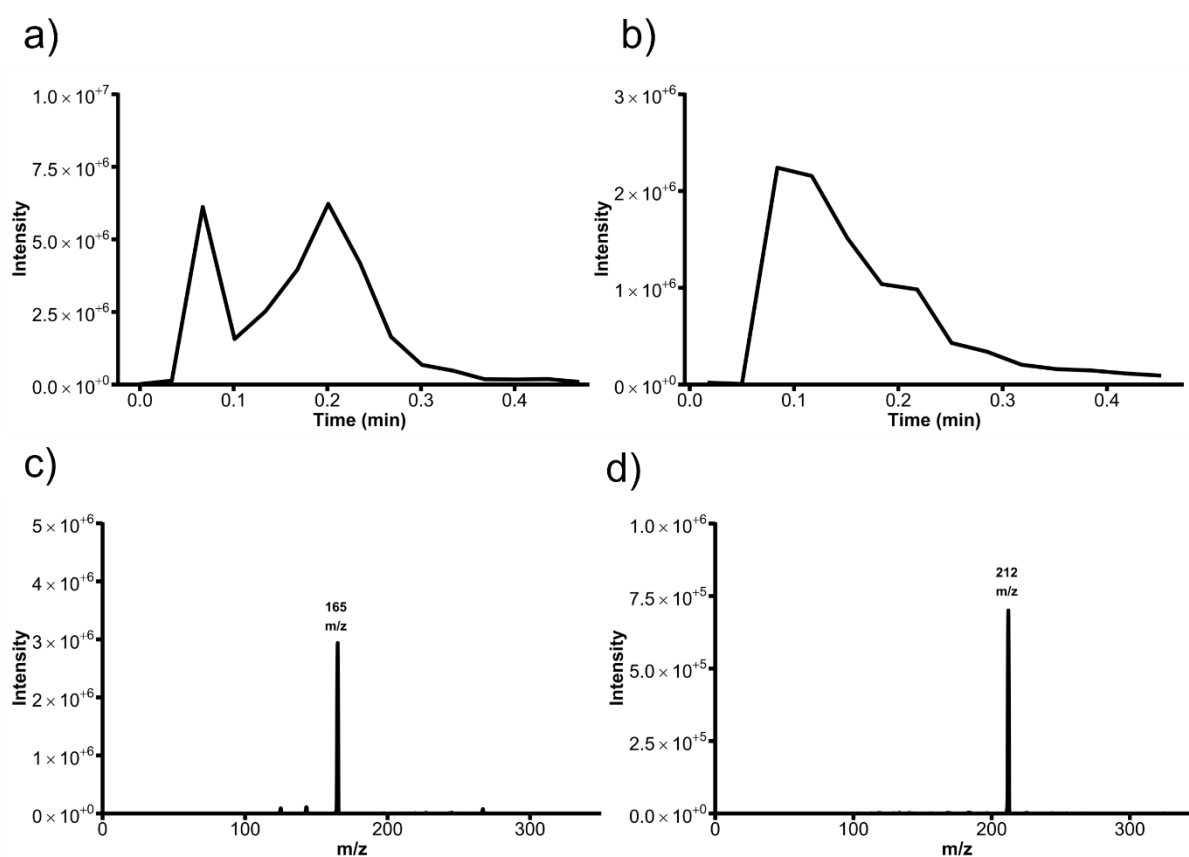


Figure 3.9: (a) Signal traces from injection of resorufin glucuronide into the MS obtained in positive mode at 383 m/z and in (b) negative mode at 388 m/z. (c) Mass spectrum of the area under the peak in (a). (d) Mass spectrum of the area under the peak (b).

The positive mode product ion scan chromatogram (Figure 3.9a) unexpectedly showed two peaks, only one of which provided a large singular mass differentiable

from the background (Figure 3.9c) which was 165 m/z. Whereas, the negative mode chromatogram (Figure 3.9b) provided an expected singular large peak. This singular peak provided the expected mass fragment at 212 m/z (Figure 3.9d). These fragmentations (383>165 and 388>212 m/z) were then implemented into an MRM scan to ensure they were measured by the detector.

### *MRM scan*

The MRM scan for both 383>165 and 388>212 for the same motivations as mentioned previously is shown in Figure 3.10.

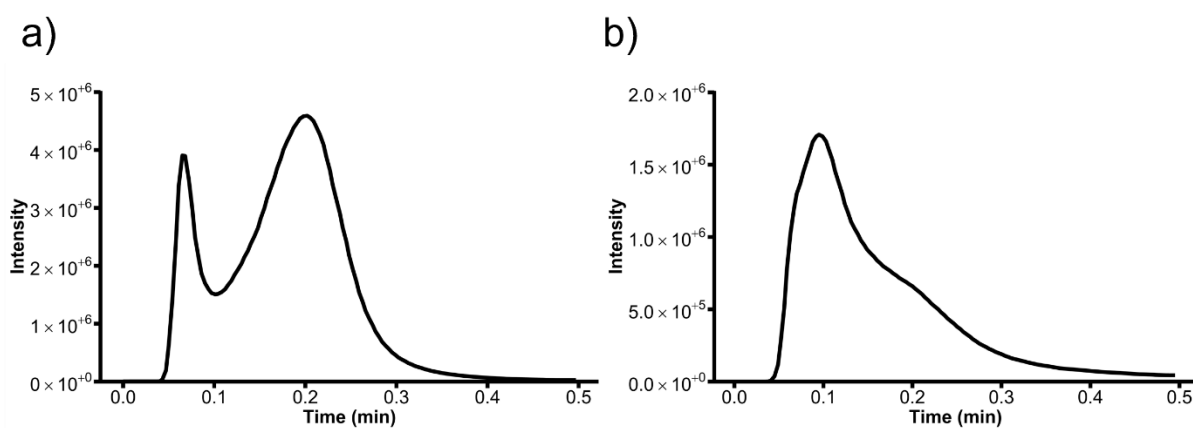


*Figure 3.10: (a) Signal traces from injection of resorufin glucuronide into the MS obtained in positive mode set to 383>165 m/z and (b) negative mode set to 388>212 m/z using an MRM scan.*

As expected both spectra provided peaks, with the positive mode MRM providing two peaks (Figure 3.10a) and the negative mode yielding one large peak (Figure 3.10b), both of which comparable to their respective product ion scans in Figure 3.9. Both peaks were investigated in order to determine which provided the highest sensitivity. This involved determining which provided the least broad peak, the largest intensity value, and the largest peak area. Although, prior to optimisation the transition from 383>165 m/z provides a double peak which may affect its overall applicability.

## Optimisation of collision energy

The same optimisation as previously conducted for resorufin was used on the two precursor to fragment transitions, 383>165 (Figure 3.11a) and 388>212 m/z (Figure 3.11b).

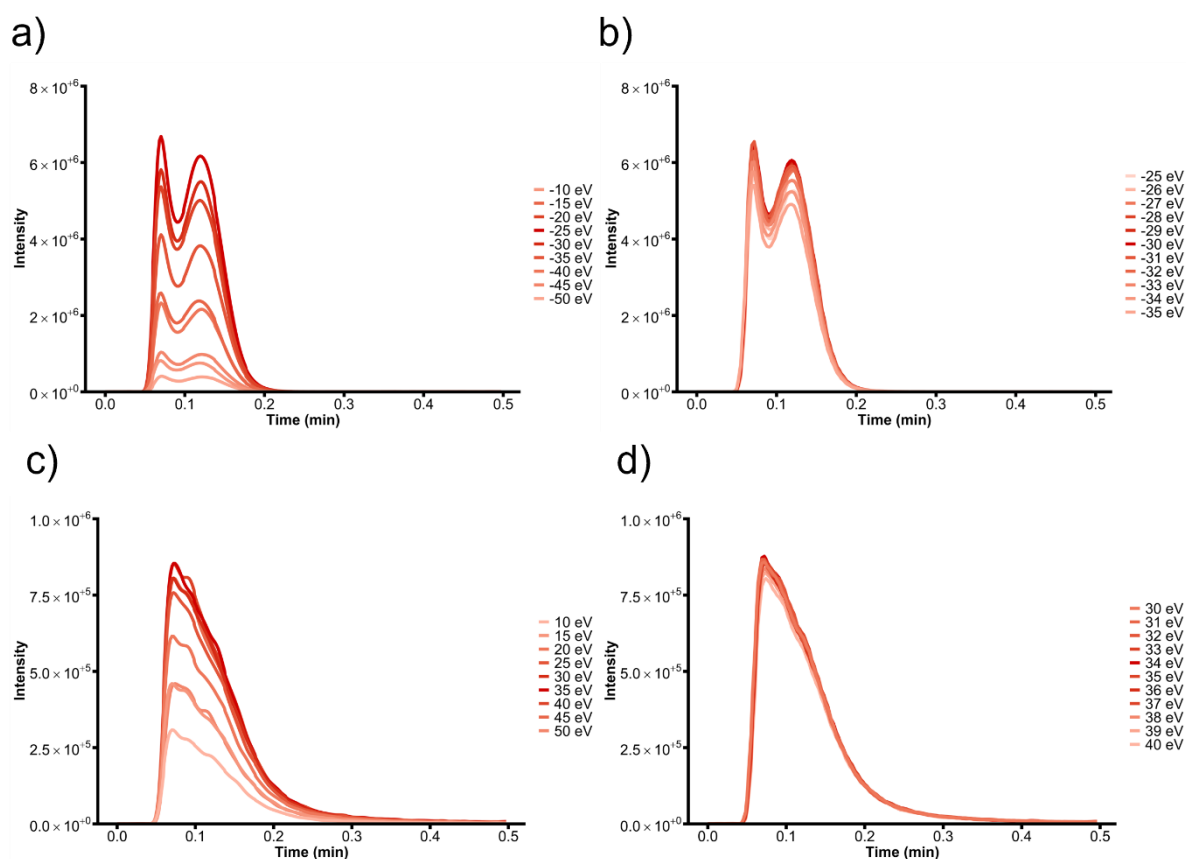


Figure 3.11: (a) Signal traces from injection of resorufin glucuronide into the MS optimising the collision energy for the fragmentation in positive mode set to 383>165 m/z using a broad scan and (b) a detailed scan between -25 to -35 eV and in negative mode set to 388>212 m/z using (c) a broad scan and (d) a detailed scan between 30 to 40 eV.

The broad scans for both positive (Figure 3.11a) and negative mode (Figure 3.11c) were automatically analysed by the LabSolutions software and applied to the in detailed scans (Figure 3.11b and Figure 3.11d respectively). Determining that a point between 25 and 35 eV would yield the optimum fragmentation in positive mode (Figure 3.11b) and 30 to 40 eV in negative mode (Figure 3.11d). Both of these fragmentations

provided a peak. However, as with previously the transition from 388>212 yielded a singular peak with an optimum collision energy of 34 eV (Figure 3.11d), and 383>165 provided 2 peaks at its optimum collision energy of 30 eV (Figure 3.11b). The optimum collision energies for these scans are described in Table 3.5. The next step was optimising the separation between these two compounds, resorufin and resorufin glucuronide.

*Table 3.5: Measured optimum collision energy (eV) for resorufin glucuronide at all tested fragmentations.*

Fragmentation (relation to Figure 3.11)	Optimum collision energy
383>165 (a/b)	-30 eV
388>212 (c/d)	34 eV

## **Mixture of resorufin and resorufin glucuronide**

Conducting a run with the column implemented by injecting a mixture of both analytes (10 µL of 1 µM) was then necessary. As once metabolised both product and precursor may be contained within the effluent being measured. Although it is not necessary when using LCMS-MS to separate analytes, this was a large focus on the optimisation of these compounds due to the metabolism focus throughout the rest of this thesis. Typically, a substrate undergoing metabolism will not yield one single substrate and determining which one is formed is difficult.

### *HPLC isocratic separation of resorufin and resorufin glucuronide*

In order to detect a mixture of resorufin and resorufin glucuronide simultaneously an isocratic method was conducted using standards and is described below (Table 3.6), these scans and calibration curves for positive (Figure 3.12) and negative mode

(Figure 3.13). Equal volumes (10  $\mu\text{L}$ ) of resorufin and resorufin glucuronide (100  $\mu\text{M}$ ) were mixed and then directly injected and analysed using the detector parameters optimised through Resorufin and Resorufin glucuronide sections.

*Table 3.6: LCMS parameters for isocratic method.*

Column	Shim-pack GISS HP (C18)
Oven temperature	40 °C, Shimadzu CTO-20AC
Injection volume	10 $\mu\text{L}$
Eluent A	0.1 % Formic Acid in Water
Eluent B	0.1% Formic Acid in Acetonitrile
Composition A: B	30:70
Flow rate	0.5 ml min <sup>-1</sup>
Autosampler	Shimadzu Nexera X2 SIL-30AC
Spray voltage	2.32 kV
Capillary temperature	250 °C

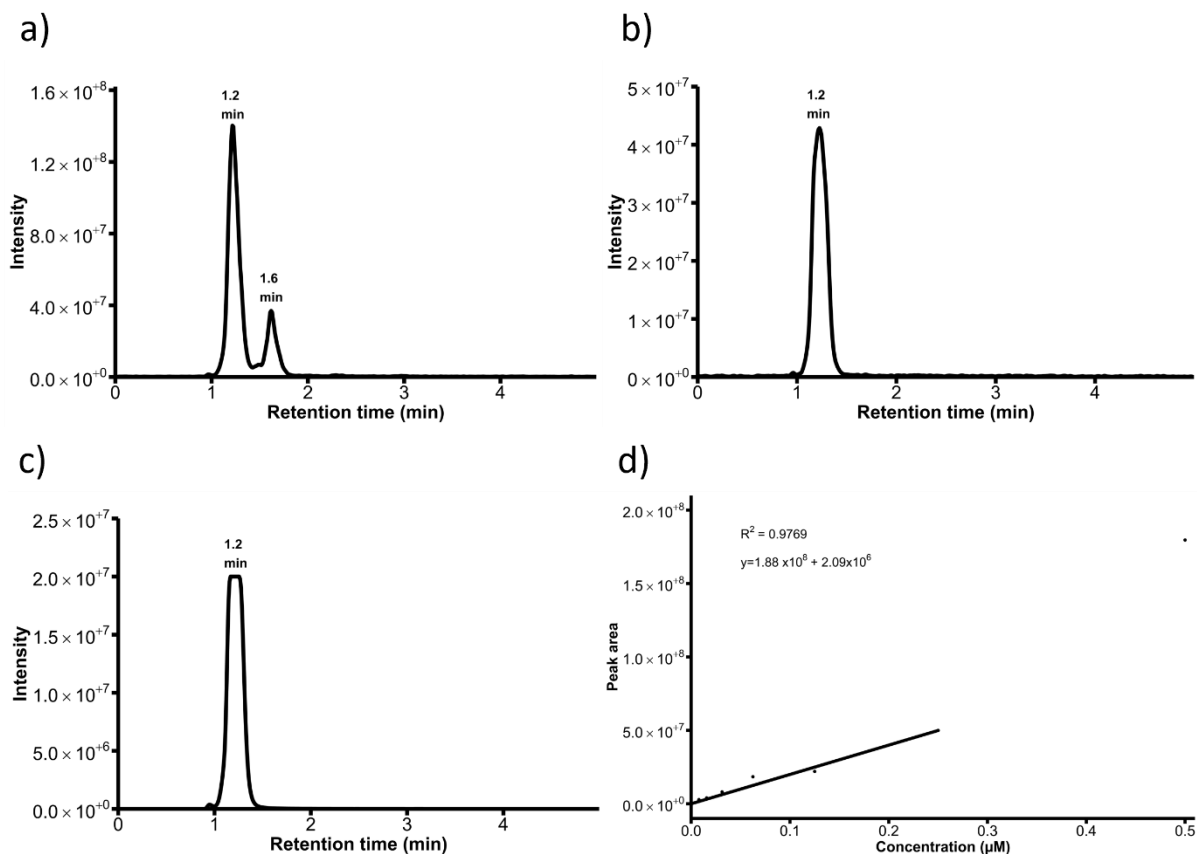


Figure 3.12: (a) Signal traces from injection of a mixture containing resorufin and resorufin glucuronide into the LC-TQ-MS in positive mode obtained in precursor ion scan set to 214 m/z, (b) a product ion scan set to 383 m/z mode and (c) an MRM scan at 383>165 m/z with (d) a calibration curve created using data shown in (a), line of best fit only up to 0.25  $\mu\text{M}$  as this is the linear portion of the graph.<sup>9</sup>

Two of the tested scans yielded large peaks for both compounds within the precursor ion scan at 214 m/z (Figure 3.12a) and the previously optimised MRM set to 383>165 m/z (Figure 3.12c) and a singular peak was found utilising a product ion scan set to 383 m/z. These showed very little separation between the peaks and linearity was only observed up to 0.25  $\mu\text{M}$  whilst providing an  $R^2$  of 0.9769 (Figure 3.12d).

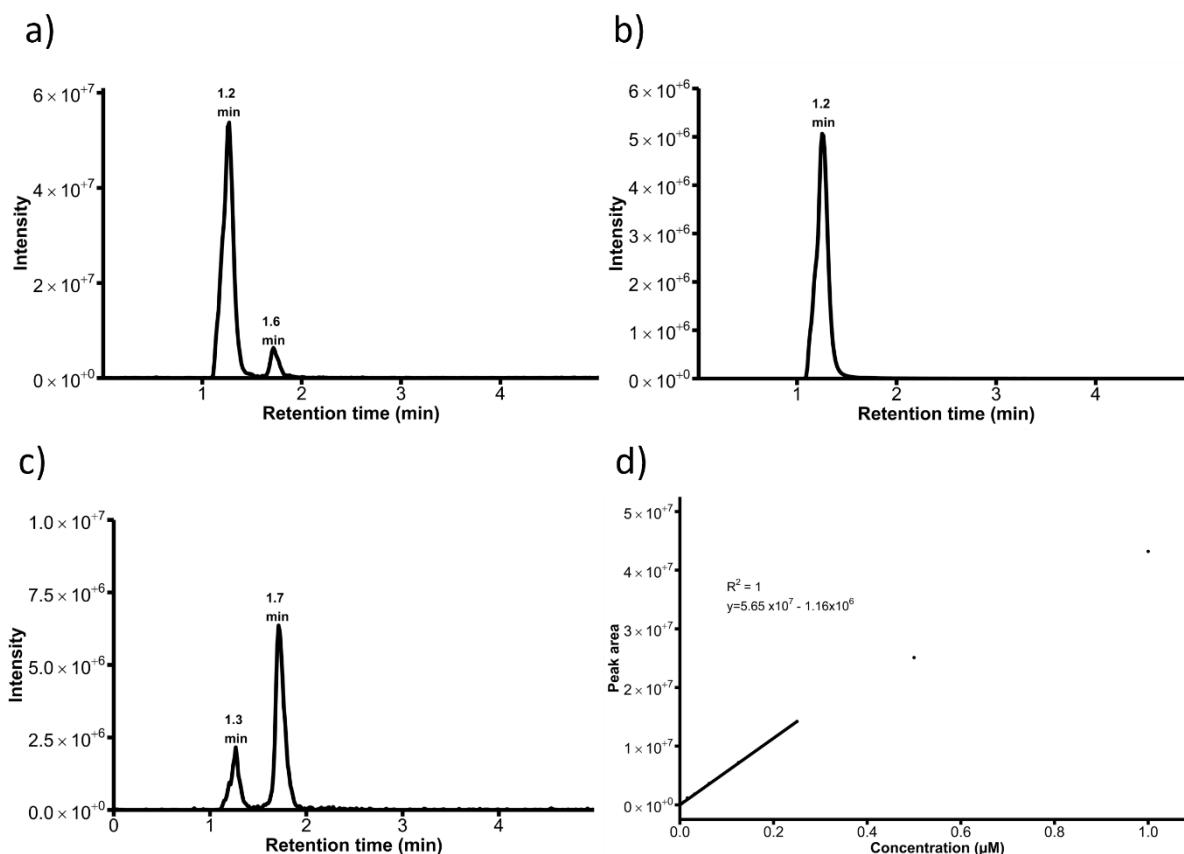


Figure 3.13: (a) Signal traces from injection of a mixture containing resorufin and resorufin glucuronide into the LC-TQ-MS in negative mode obtained in precursor ion scan set to 212  $m/z$ , (b) an MRM scan set to 388>212> $m/z$  and (c) a product ion scan set to 212  $m/z$  mode and with (d) a calibration curve created using data shown in (a) with concentration varying from 100  $\mu M$  to 15.6 nM in serial dilution by half, line of best fit only goes up to 0.25  $\mu M$  as this is the linear portion of the graph.

Similarly to the positive mode, three different scans were compared to determine the amount of separation between these two compounds and a comparable amount of separation was observed. The linear range for these logarithmic concentrations was also up to 0.25  $\mu M$  with an  $R^2$  of 1.00 but no linearity is measured beyond this point, as shown in Figure 3.13.

As can be seen from the chromatograms in both positive (Figure 3.12) and negative mode (Figure 3.13) the resorufin glucuronide peak was observed at 1.2 min with the resorufin peak at 1.6 mins yielding very little resolution. Due to this low resolution, the calibration curve in positive mode provides some linearity, severely hindering this

method at higher concentrations due to the potential for overlap between the two peaks. For negative mode a much higher correlation of data is found with an  $r^2$  of 0.9769 for positive mode (Figure 3.12d) and an  $r^2$  of 1.00 on negative mode (Figure 3.13d) both of which only linear until 0.25  $\mu\text{M}$ . This is not optimal for the determination of concentration of resorufin glucuronide within a sample collected throughout this thesis, due to its potential concentration up to 100  $\mu\text{M}$  prior to dilution. There is a large potential for improvement with the resolution of these two compounds. Using a gradient could also potentially allow for increased separation between the matrix and the two analytes themselves, which may also improve the linearity of the calibration curves.

### *Gradient HPLC separation of resorufin and resorufin glucuronide*

Due to the constraints of the isocratic method, the gradient method described below (Table 3.7) was tested using the same scans as previously (Figure 3.14a-c) with a calibration curve to allow for product quantification (Figure 3.14d). Negative mode was continued through all subsequent experiments due to an improved peak shape and reduced peak tailing.

*Table 3.7: LCMS parameters for gradient method.*

Column	Shim-pack GISS HP (C18)
Oven temperature and controller	40 °C, Shimadzu CTO-20AC
Injection volume	10 $\mu\text{L}$
Eluent A	0.1 % Formic Acid in Water
Eluent B	0.1% Formic Acid in Acetonitrile
Time	Composition A: B

0 min	95:5
3 min	95:5
10 min	25:75
20 min	25:75
22 min	95:5
25 min	95:5
Flow rate	0.5 ml min <sup>-1</sup>
Autosampler	Shimadzu Nexera X2 SIL-30AC
Spray voltage	2.32 kV
Capillary temperature	250 °C

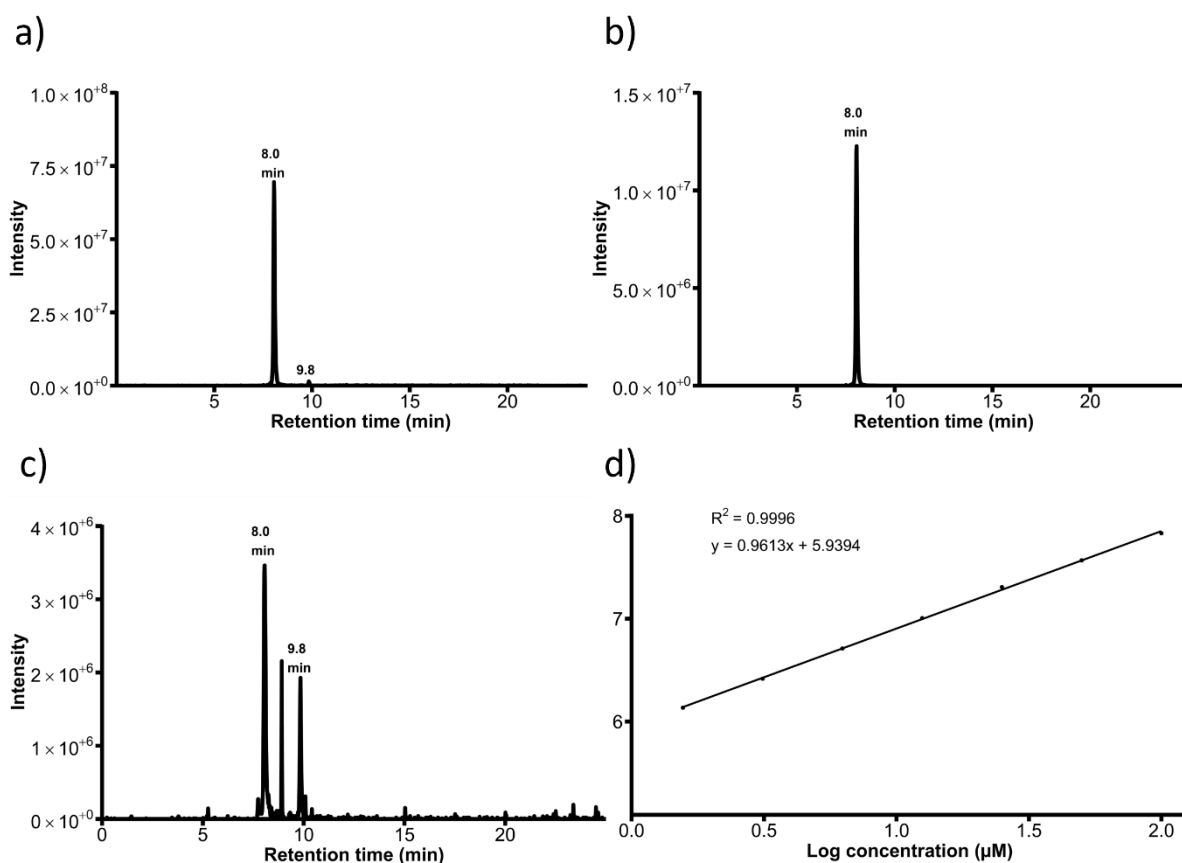


Figure 3.14: (a) Signal traces from injection of a mixture containing resorufin and resorufin glucuronide into the LC-TQ-MS in negative mode obtained in precursor ion scan set to 212 m/z, (b) an MRM scan at 388>212 m/z and (c) a product ion scan at 212 m/z with (d) a

*calibration curve created using data shown in (a) with varying concentration from 100  $\mu$ M to 15.6 nM in serial dilution.*

The precursor ion scan (Figure 3.14a) and product ion scan (Figure 3.14b), both of which were set to 212 m/z, showed a much higher resolution between resorufin glucuronide's (8.0 mins) and resorufin's (9.8 mins) respective retention time alongside comparable linearity between concentration of resorufin glucuronide and peak area, with an  $r^2$  of 1 in the negative mode isocratic method (Figure 3.13d) and 0.9996 in the equivalent gradient method (Figure 3.14d). However, the maximum linear point on the calibration curve for the isocratic method was found at 0.25  $\mu$ M, and the gradient did not show plateauing even at 100  $\mu$ M. Due to the highly improved separations and largely improved upper limit, higher concentrations could be measured due to the improved gap in retention times whilst also allowing a more accurate confirmation of product formation.

This method was carried forward for all subsequent experiments as sufficient separation and sensitivity was found within the expected range of product formed.

## **Nitrophenol**

Initially, the intention was to focus on the metabolism or formation of resorufin utilising the three enzymes (UGT1a1, SULT1a1 and CYP1a1). However, upon further analysing standards for resorufin, a resorufin sulfate like peak was found at the expected retention time. Due to the lack of availability for a resorufin sulfate standard, a true confirmation of product formation would not be viable using resorufin as a substrate. Due to this, another commonly utilised substrate for the formation of sulfated compounds was used being nitrophenol into nitrophenyl sulfate.

Nitrophenol is a commonly used metabolite for sulfated metabolites due to its reactively available hydroxyl group and ease of measurement in mass spectrometry. This compound was used to show that the synthesis of nitrophenyl sulfate was viable within the devices shown in section 2.2. The determination of optimum parameters for the measurement of this compound in LC-TQ-MS was also necessary for a proof of product formation upon enzymatic conversion.

### Q1 scan

The parent ions of *p*-nitrophenol are shown in Figure 3.15. A Q1 scan in both positive mode (Figure 3.16a) and negative mode (Figure 3.16b) was used to determine parent and major ions as mentioned previously in the resorufin section. The next step was optimising the separation between these two compounds, *p*-nitrophenol and *p*-nitrophenyl sulfate.

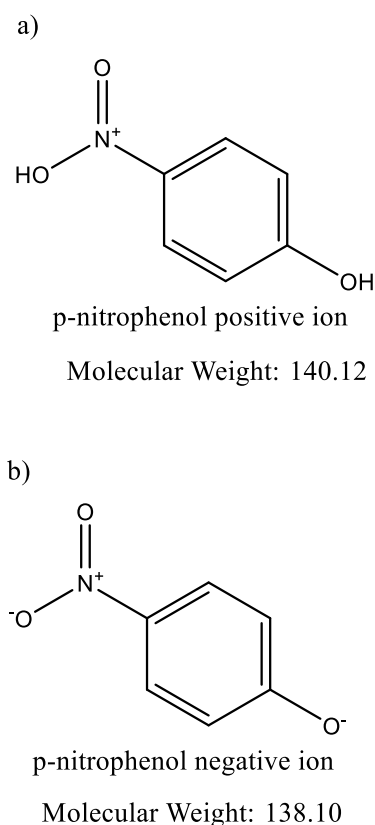


Figure 3.15: (a) Expected parent ions for *p*-nitrophenol for both positive and (b) negative mode.

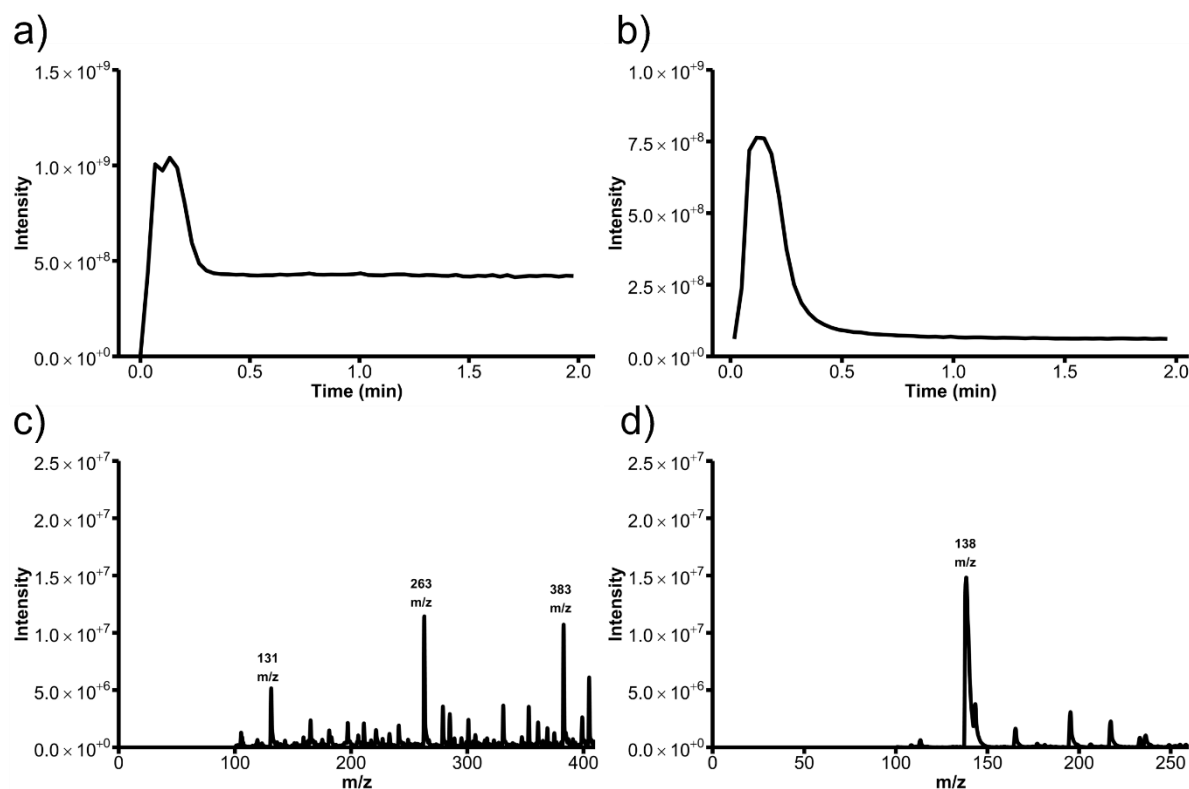


Figure 3.16: (a) Signal traces from injection of *p*-nitrophenol into the MS obtained in a Q1 scan in both positive mode and in (b) negative mode. (c) Mass spectrum of the area under the peak in (a) and (d) Mass spectrum of the area under the peak (b).

For both positive mode (Figure 3.16a) and negative mode (Figure 3.16b) one large peak was observed; the average spectrums under these peaks are shown in Figure 3.16c and d respectively. As shown in Figure 3.16c, no specific relevant fragment stands out or has a large intensity, but in Figure 3.16a large *m/z* at 138 was found. This mass is likely due to be the parent ion for *p*-nitrophenol as its molecular mass is  $139 \text{ g mol}^{-1}$ . In order to determine the common fragmentations, a product ion scan was needed which in turn will allow for a proof of product due to the specific fragments undergone by nitrophenol and its respective sulfated metabolite nitrophenyl sulfate in a mixture.

## Product ion scan

A product ion scan for 138 in negative mode (Figure 3.17) was then conducted to determine the fragmentations that are observed from the masses determined in the Q1 scan.

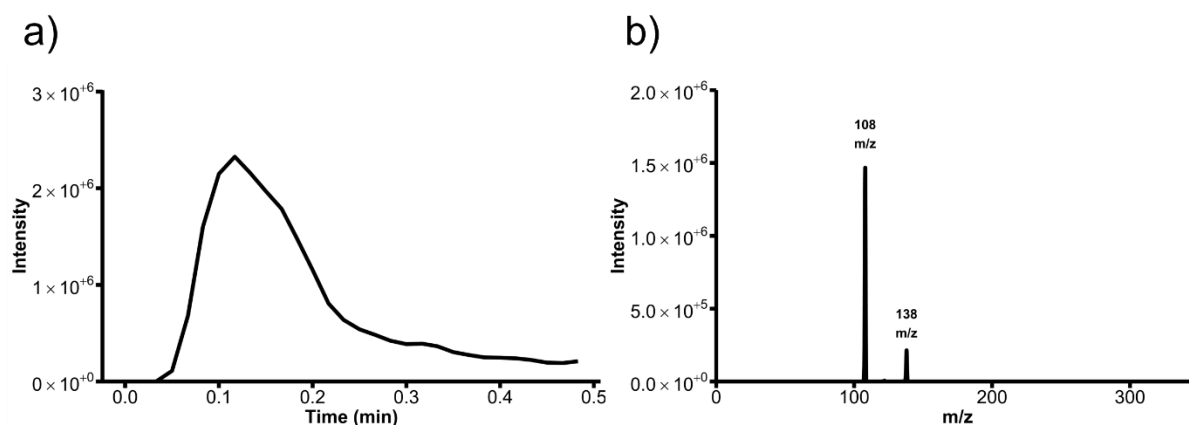


Figure 3.17: (a) Signal traces from injection of nitrophenol into the MS obtained negative mode using a product ion scan set to 138 m/z and the mass spectrum of the area under the peak in (a).

A single large peak was observed in the chromatogram for product ion scan set to 138 m/z (Figure 3.17a) and the area under this curve was used to create Figure 3.17b. Which shows the parent ion for nitrophenol (138 m/z) as well as a potential fragment ion at 108 m/z. In order to further test this fragment MRM was measured.

## MRM scan

An MRM scan for the observed transition at 138>108 (Figure 3.18) was conducted on the same standard (nitrophenol) to determine if this specific fragmentation was measured.

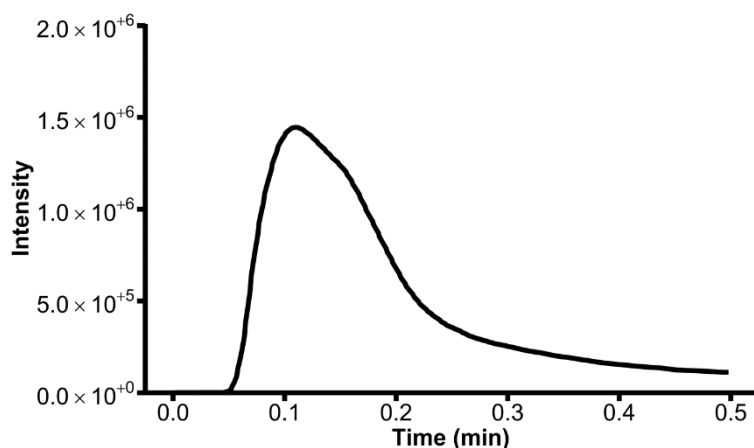


Figure 3.18: Signal traces from injection of nitrophenol into the MS obtained in negative mode using an MRM set to 138>108 m/z.

The MRM scan for 138>108 (Figure 3.18) yielded a large singular peak as expected. The next step was to undergo fragment optimisation using the inbuilt optimisation setting on the Shimadzu LabSolutions software.

### Optimisation of collision energy

The optimisation method on the Shimadzu LabSolutions software (Figure 3.19) was applied to the previously determined MRM scan (Figure 3.18).

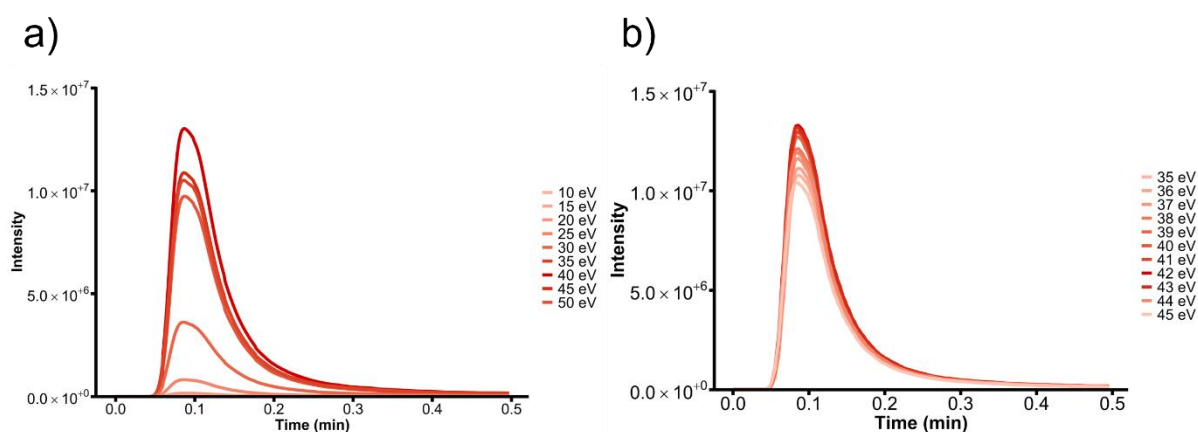


Figure 3.19: (a) Signal traces from injection of nitrophenol into the MS optimising the collision energy for the fragmentation in negative mode set to 138>108 m/z using a broad scan and (b) a detailed scan between 35 to 45 eV.

A broad optimisation for the transition from 138>108 m/z (Figure 3.19a) with varying collision energy between 10 and 50 eV determined that a point between 35 and 45 eV provided the highest peak area and intensity, and then automatically measured a detailed fragmentation (Figure 3.19b) between these points and determined that the optimum collision energy was found to be 37 eV. Determination of retention time using the method described for resorufin and resorufin glucuronide was then followed.

### *Retention time determination*

The retention time was then determined using the gradient method described in Table 3.7 and is shown in Figure 3.20.

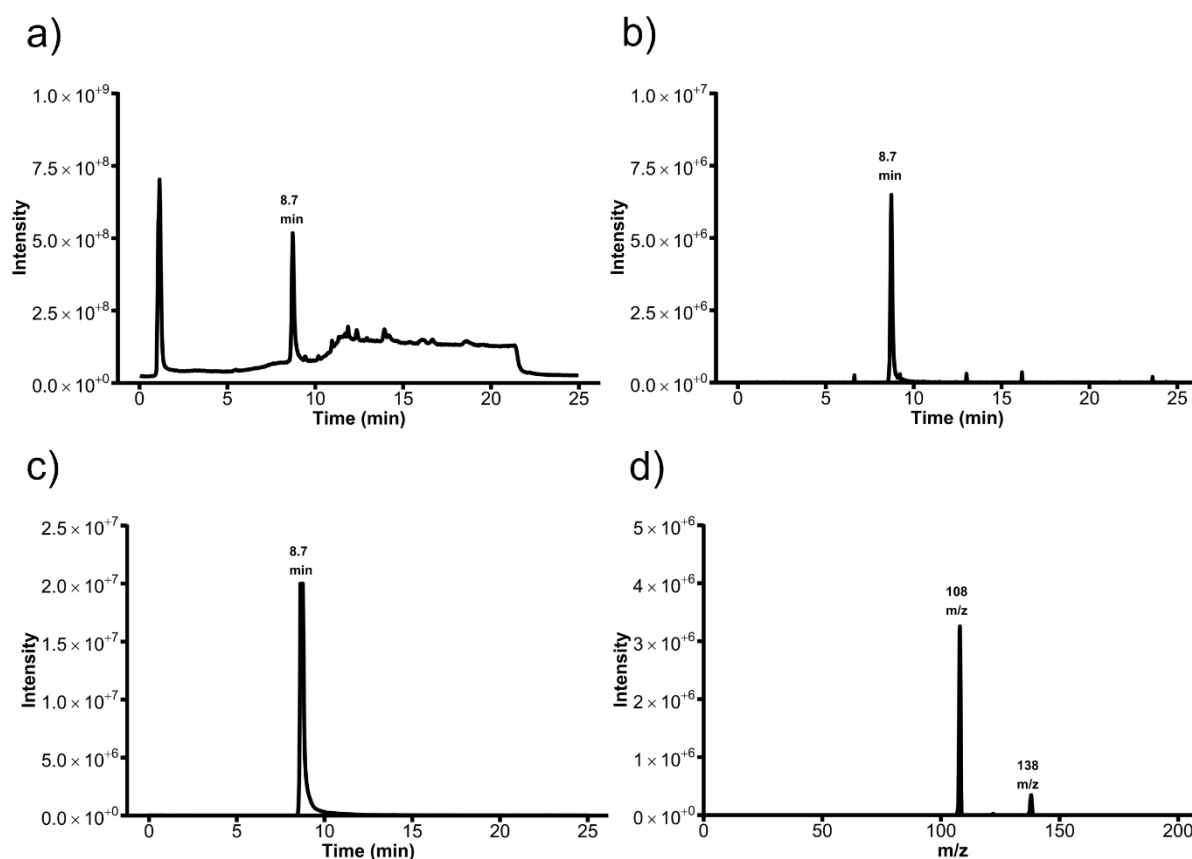
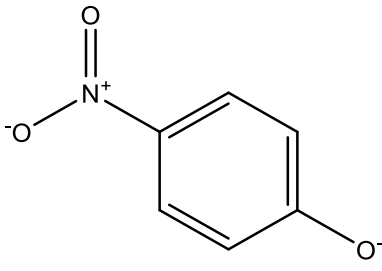
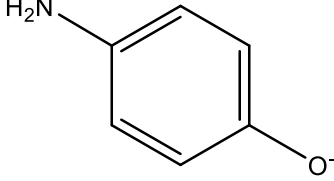


Figure 3.20: (a) Signal traces from injection of nitrophenol into the MS obtained in negative mode using a Q1 scan, (b) a product ion scan set to 138 m/z (c) an MRM scan set to 138>108 m/z and (d) Mass spectrum of the area under the peak (b).

The retention time for nitrophenol was determined to be 8.7 minutes in all scans optimised previously within this section, Q1 scan (Figure 3.20a), product ion scan (Figure 3.20b) and MRM (Figure 3.20c). This was confirmed by comparing the product ion scan in the optimisation section (Figure 3.17b) to that measured under this retention time (Figure 3.20d).

The mass spectrum of *p*-nitrophenol was also measured by Han *et al* (2008). finding three major peaks were formed in positive mode, the parent ion 139 m/z, a peak at 109 m/z and another at 65 m/z<sup>271</sup>. This is similar to the findings from the spectrum measured in this study. However, the peak at 65 m/z was not measured due to the detector being set to scan between 100 and 1000 m/z. The expected fragmentations based on common fragmentation pathways are shown in Table 3.8

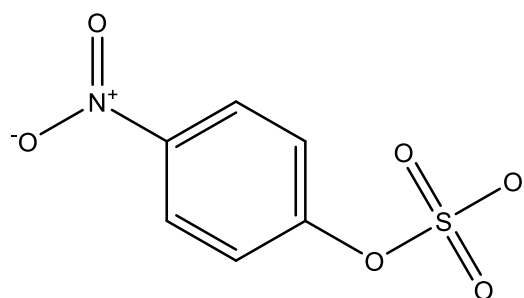
Table 3.8: Summary of expected fragments for *p*-nitrophenol based on common fragmentation pathways simulated using CFM-ID.<sup>266-270</sup>

Mode	Expected loss (m/z)	Molecular weight (g mol <sup>-1</sup> )	Expected molecule
Negative	0	138	
Negative	30	108	

## Nitrophenyl sulfate

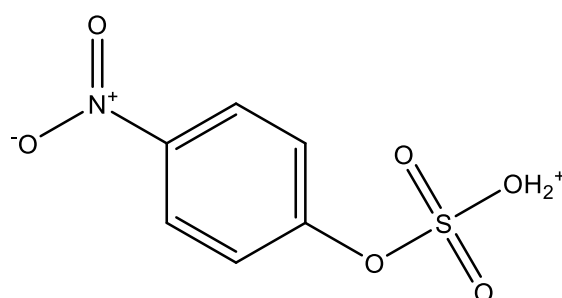
### Q1 scan

The parent ions of *p*-nitrophenol are described in Figure 3.21. As previously carried out in the resorufin analysis, in order to determine the major masses and/or the parent ion, a Q1 scan was conducted on nitrophenyl sulfate in positive mode (Figure 3.22a) and negative mode (Figure 3.22b).



p-nitrophenyl sulfate negative ion

Molecular Weight: 218.16



p-nitrophenyl sulfate positive ion

Figure 3.21: (a) Expected parent ions for *p*-nitrophenyl sulfate for both positive and (b) negative mode.

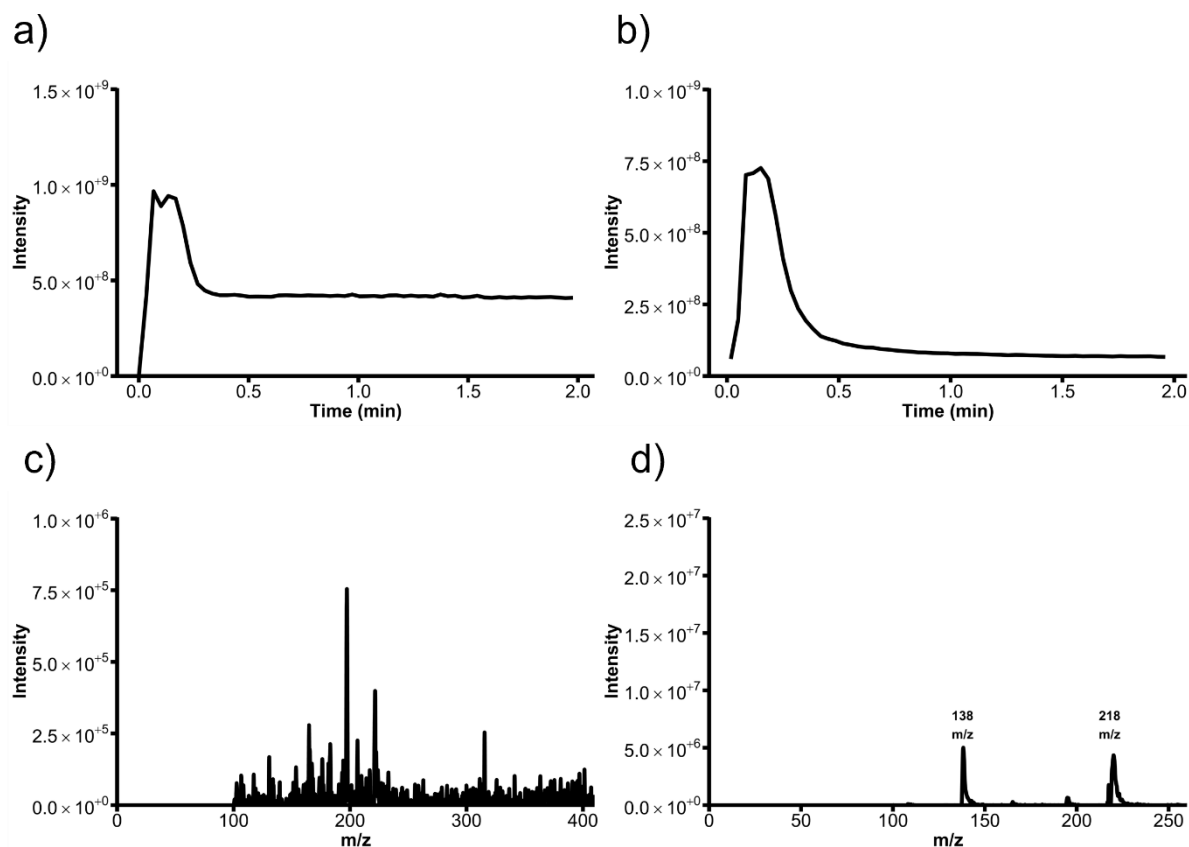


Figure 3.22: (a) Signal traces from injection of nitrophenyl sulfate into the MS obtained using a Q1 scan in positive mode and (b) negative mode. With (c) Mass spectrum of the area under the peak in (a). (d) Mass spectrum of the area under the peak (b).

No peak was observed in positive mode and the expected parent ion was not observed in the mass spectrum (Figure 3.22a&d). Whereas a large singular peak was observed in negative mode (Figure 3.22b).

By visualising the masses for the areas under the curve it was possible to observe the parent/major ions for nitrophenyl sulfate. In positive mode no specific ion was obviously relevant (Figure 3.22c). Due to nitrophenyl sulfates molecular mass of 219  $\text{g mol}^{-1}$ , the expected ion for negative mode was 218  $\text{m/z}$  which was found alongside the mass 138  $\text{m/z}$  (Figure 3.22d). The mass at 138  $\text{m/z}$  is likely to be due to in source fragmentation, as it is what would be expected for the loss of the sulfate ion and is the same as that which was seen for *p*-nitrophenol.

## Product ion scan

As previously, a product ion scan was conducted in order to determine the likely fragments for MRM using the parent ion for nitrophenyl sulfate 218 m/z (Figure 3.23).

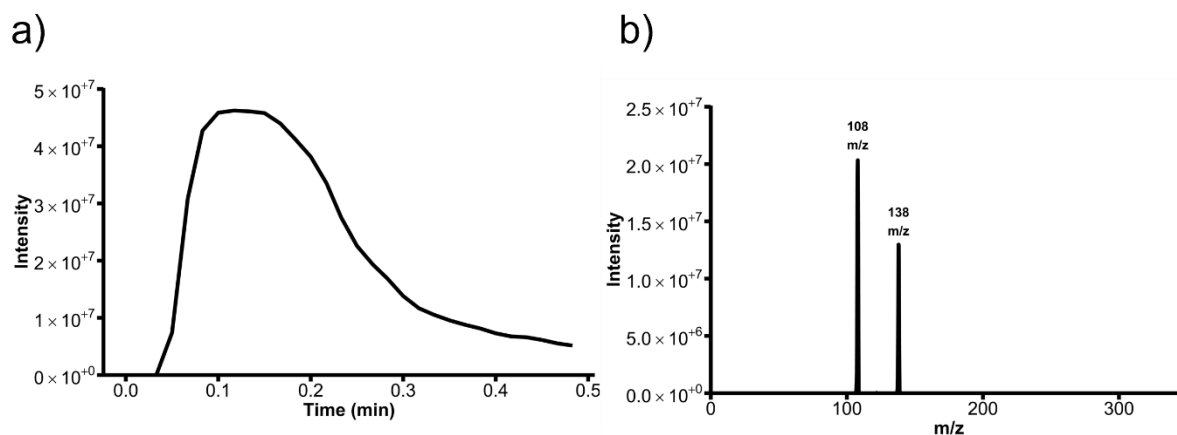


Figure 3.23: (a) Signal traces from injection of nitrophenyl sulfate into the MS obtained in negative mode using a product ion scan at 218 m/z and (b) Mass spectrum of the area under the peak in (a).

A large singular peak was found as expected (Figure 3.23a). As expected, the spectrum under the curve (Figure 3.23b) showed the masses found upon fragmentation are 138 and 108 m/z. 138 m/z is likely to be due to a loss of the sulfate ion, and 108 m/z is likely to be due to further fragmentation of the nitrophenol ion as it concurs with that observed previously in the nitrophenol optimisation section (Figure 3.17d). An MRM fragmentation was then used to ensure these masses were measured by the detector. The expected fragmentations are described in Figure 3.24.

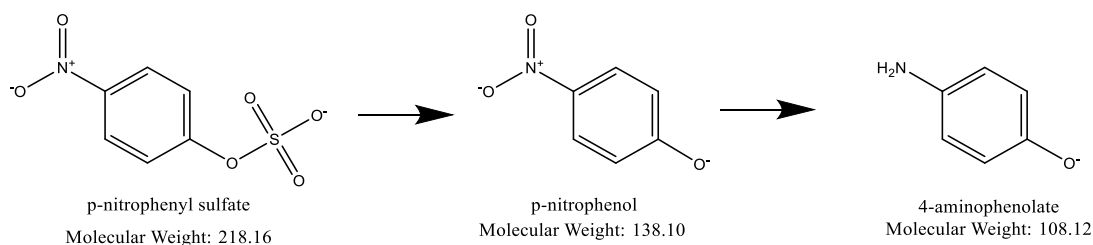


Figure 3.24: Parent ion (p-nitrophenyl sulfate<sup>-</sup>) and the expected fragmentations

## MRM scan

An MRM (Figure 3.25) was conducted on the observed fragmentations of nitrophenyl sulfate to ensure the fragmentations provided a peak as expected.

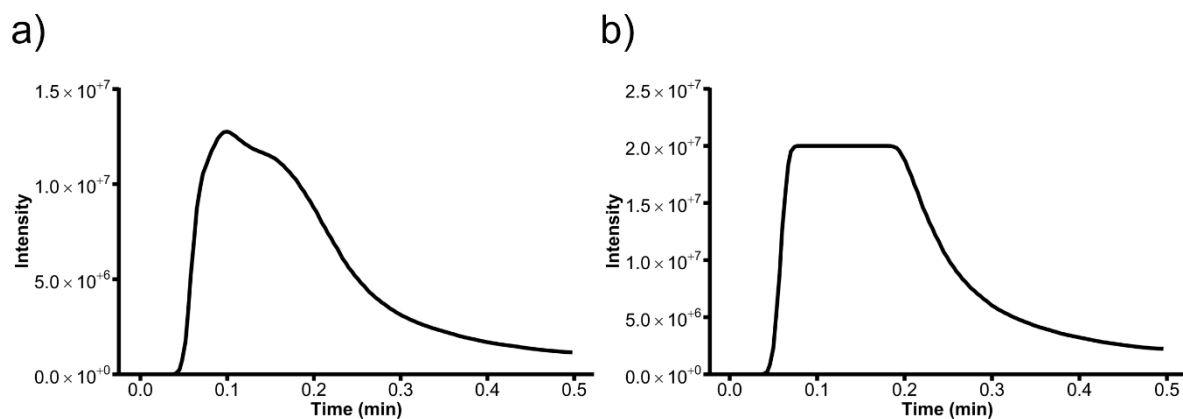


Figure 3.25: (a) Signal traces from injection of nitrophenyl sulfate into the MS obtained negative mode using an MRM scan at 218>108 and (b) 218>138 m/z at 383 m/z.

As both fragmentations (218>138 and 138>108) provided a peak they were carried forward for optimisation of the collision energy. The MRM fragmentation for 218>138 m/z saturated the detector so would provide the highest overall sensitivity at these settings. However, upon undergoing collision energy optimisation the fragmentation for 218>108 may yield a higher sensitivity.

### Optimisation of collision energy

The collision energy for these fragmentations was then optimised for both fragmentations (Figure 3.26) using the inbuilt function on the Shimadzu LabSolutions software.

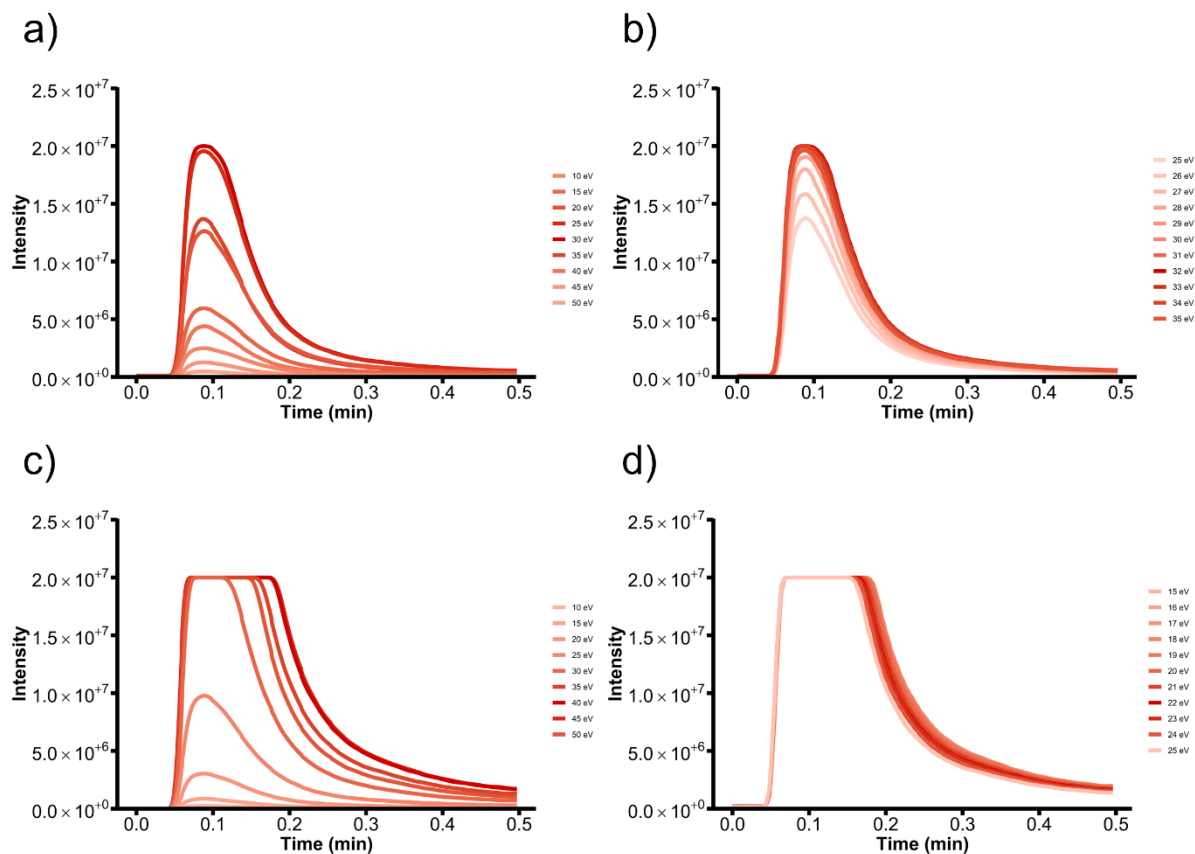


Figure 3.26: (a) Signal traces from injection of nitrophenyl sulfate into the MS optimising the collision energy for the fragmentation in negative mode set to  $218 > 108$  m/z using a broad scan and (b) a detailed scan between 25 to 35 eV and  $218 > 138$  m/z using (c) a broad scan and (d) a detailed scan between 15 to 25 eV.

As can be seen from the chromatogram, the optimum fragmentation is 218 to 138 m/z with its optimum collision energy at 23 eV as this saturated the detector (Figure 3.26a-b). Whereas the fragmentation from 218 to 108 m/z has a much lower intensity and did not saturate the detector (Figure 3.26c-d). Due to the extreme sensitivity, optimising the fragmentation from 218 to 138 m/z using a lower concentration was not necessary as the expected amounts of product were approximately equivalent concentration to that of the concentration implemented within this scan. The determination of retention time upon being implemented with the same gradient method as all previous analytes was the next step.

## Retention time determination

The retention time was then determined using the gradient parameters described in Table 3.7 for the separation and proof of product formed for comparison with *p*-nitrophenol and is shown in Figure 3.27.

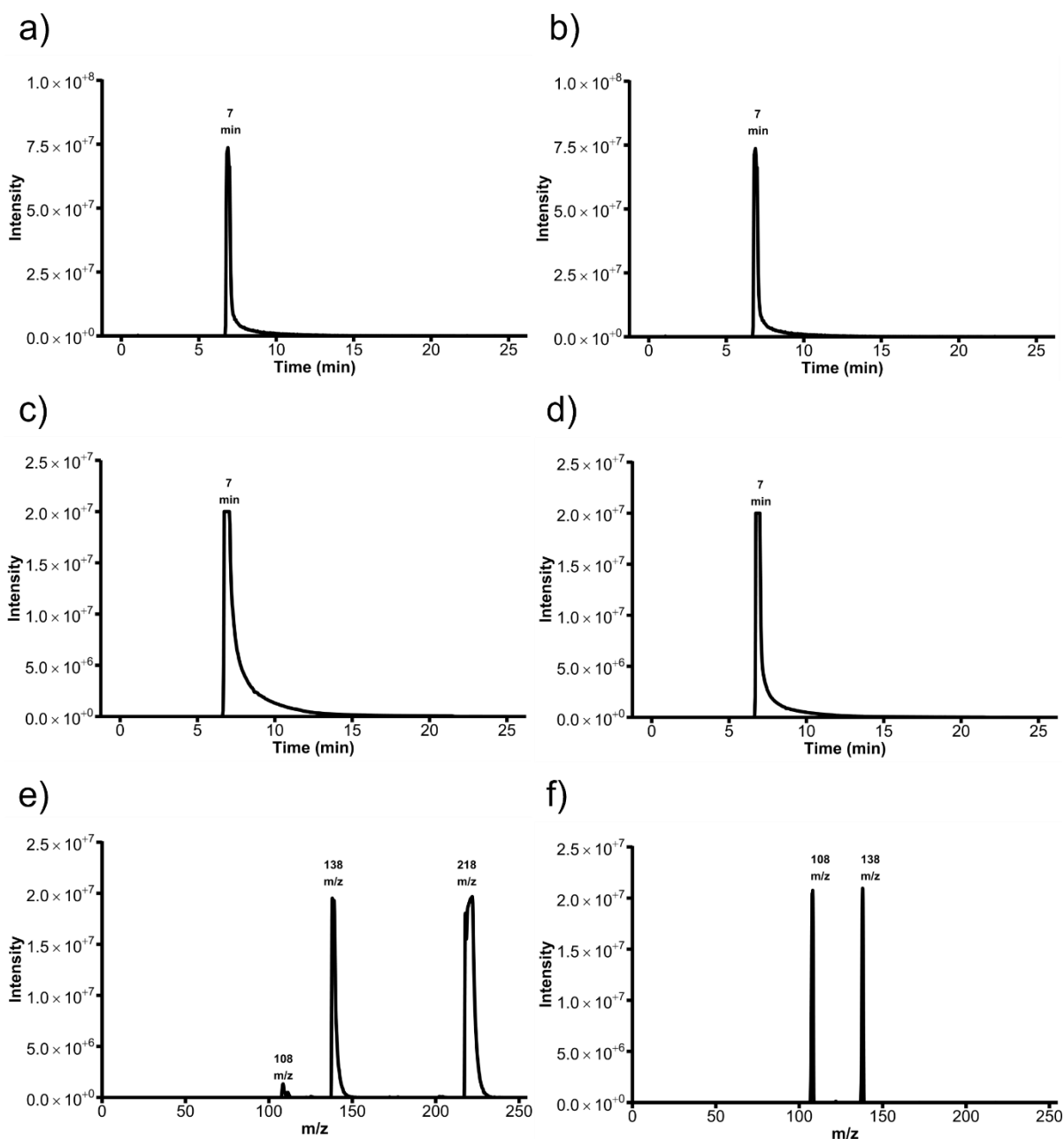
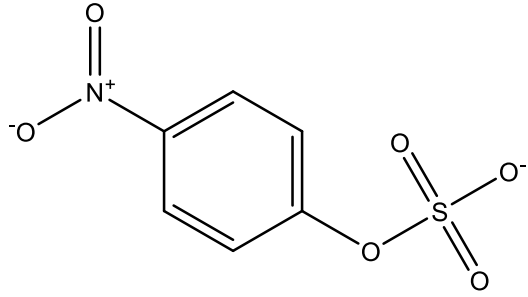
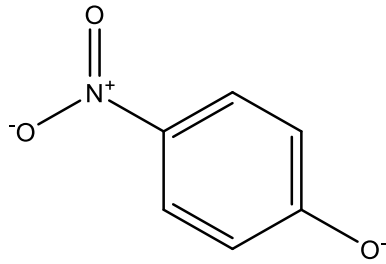


Figure 3.27: (a) Signal traces from injection of nitrophenyl sulfate into the MS obtained in negative mode using a Q1 scan, (b) a product ion scan at 218 m/z, (c) an MRM scan at 218>108 m/z and (d) 218>138 m/z, I Mass spectrum of the area under the peak in (a) and (f) the area under the curve in (b).

The retention time for nitrophenyl sulfate was 7 minutes in all of the scans conducted, *i.e.*, Q1 scan (Figure 3.27a), product ion scan at 218 m/z (Figure 3.27b) and MRM scans set to both 218>108 (Figure 3.27c) and 218>138 m/z (Figure 3.27d). Comparatively to the separation between resorufin glucuronide and resorufin, based on the retention times of the respective compounds, high separation was found from *p*-nitrophenol at 8.7 minutes (Figure 3.20) alongside the scans for the area under the curves for both Q1 (Figure 3.27e) and product ion scan (Figure 3.27f) are comparable to those found in the optimisation section (Figure 3.23). This finding allows for proof of substrate remaining and product confirmation, alongside the alternative scans that were used throughout this optimisation.

The mass spectrum of *p*-nitrophenyl sulfate was also measured by Draper *et al* (1989), finding two major peaks formed one of which being 218 m/z and the other being 139 m/z<sup>272</sup>. This is comparable to what was found in this study, although one further fragment was found at 108 m/z in this research. The expected fragments for *p*-nitrophenyl sulfate are shown in Table 3.9

Table 3.9: Summary of expected fragments for *p*-nitrophenyl sulfate based on common fragmentation pathways simulated using CFM-ID.<sup>266-270</sup>

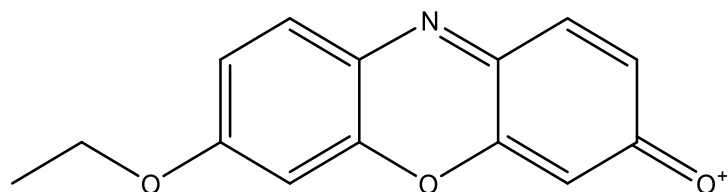
Mode	Expected loss (m/z)	Molecular weight (g mol <sup>-1</sup> )	Expected molecule
Negative	0	218	 The structure shows a benzene ring with a nitro group (-NO <sub>2</sub> ) at the top position and a sulfate group (-OSO <sub>3</sub> <sup>-</sup> ) at the para position (bottom). The nitro group is represented as a nitrogen atom with a positive charge bonded to two oxygen atoms, one of which is double-bonded. The sulfate group consists of a sulfur atom bonded to four oxygen atoms, one of which is single-bonded to the benzene ring and carries a negative charge.
Negative	80	138	 The structure shows a benzene ring with a nitro group (-NO <sub>2</sub> ) at the top position and an oxygen atom with a negative charge (-O <sup>-</sup> ) at the para position (bottom). The nitro group is represented as a nitrogen atom with a positive charge bonded to two oxygen atoms, one of which is double-bonded.

## 7-Ethoxyresorufin

For the final enzymatic reaction studied in this thesis, CYP1A-mediated diacylation of 7-ethoxyresorufin into resorufin, the optimum parameters for the measurement of 7-ethoxyresorufin was required. LC-TQ-MS detection of resorufin had been previously optimised as described above.

### Q1 scan

The expected parent ion of 7-ethoxyresorufin is shown in Figure 3.28. A Q1 scan of 7-ethoxyresorufin was conducted in both positive mode (Figure 3.29a) and negative mode (Figure 3.29b) in order to determine major peaks and/or the parent ion.



7-Ethoxy resorufin positive ion

Molecular Weight: 241.25

Figure 3.28: Expected parent ions for 7-ethoxyresorufin for positive mode.

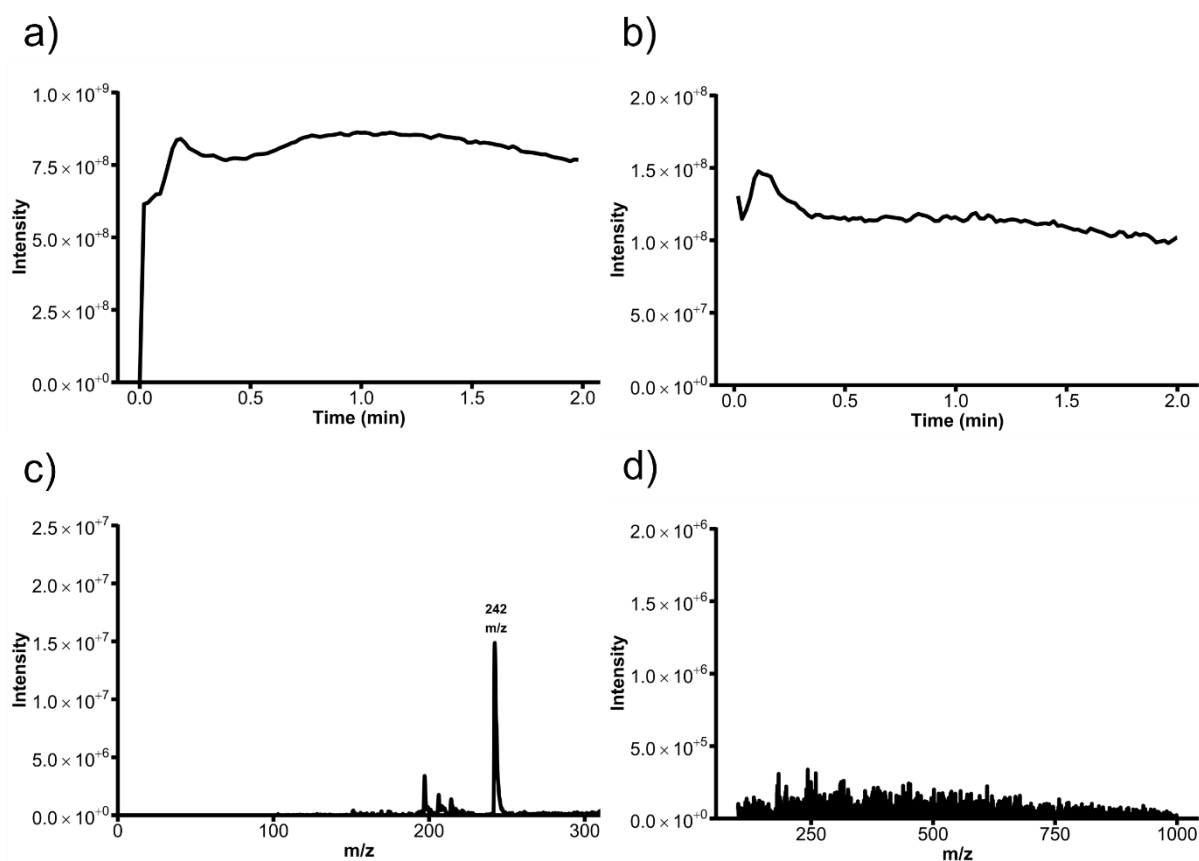


Figure 3.29: (a) Signal traces from injection of 7-ethoxyresorufin into the MS obtained in a Q1 scan in positive mode (b) negative mode with the (c) Mass spectrum of the area under the peak in (a) and (d) Mass spectrum of the area under the peak (b).

The HPLC spectrum for both positive mode (Figure 3.29a) and negative mode (Figure 3.29b) show a small singular peak. However, for positive mode its respective mass spectrum showed the expected parent ion of 242 m/z due to its molecular weight of 241 m/z, whereas no large peak was found in the negative scan (d). Comparably to the previous analytes the next step was to conduct a product ion scan.

### *Product ion scan*

A product ion scan set to the previously observed parent ion, 241 m/z (Figure 3.30) was conducted in order to determine which fragmentations occur for further use in MRM scans.

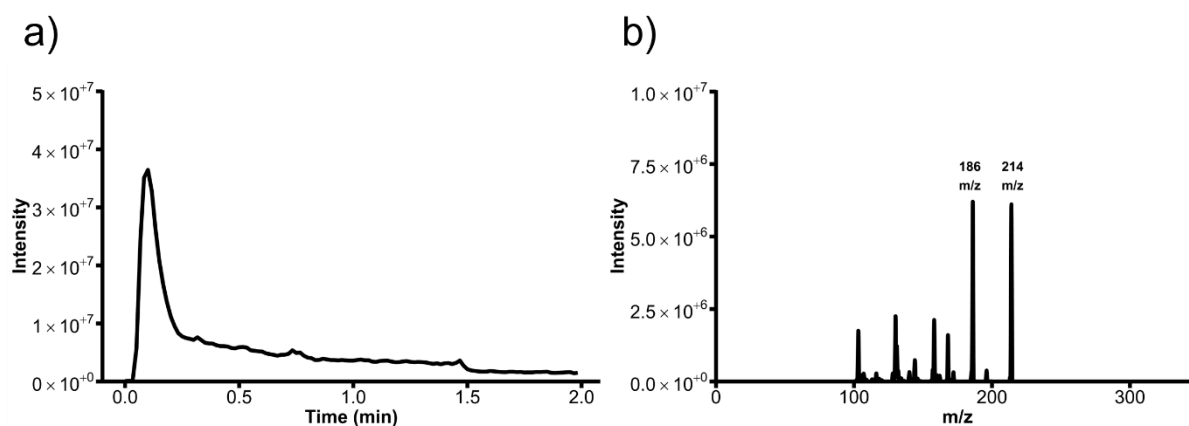


Figure 3.30: (a) Signal traces from injection of 7-ethoxyresorufin into the MS obtained in positive mode at 242 m/z with the (b) mass spectrum of the area under the peak in (a).

The HPLC chromatogram for 7-ethoxyresorufin (Figure 3.30a) showed a singular large peak and the resulting mass spectrum provided multiple different fragmentation points, the larger two being 242>214 and 242>186 m/z (Figure 3.30b). An MRM scan was

then conducted in order to determine if these fragmentations provide a peak much higher than that of the background within expected levels post enzymatic conversion.

### *MRM*

An MRM scan was conducted in order to determine whether the fragments provide a peak as expected, these are shown in Figure 3.31.

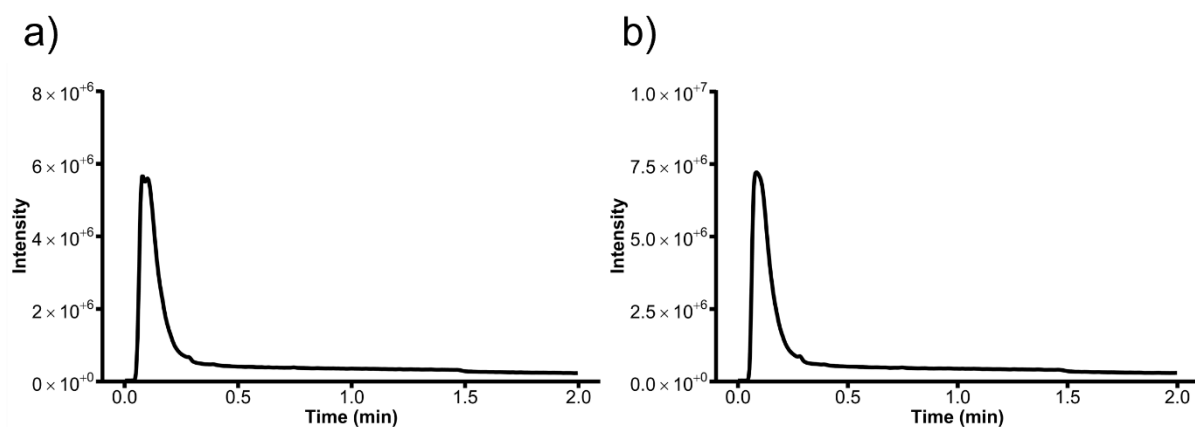


*Figure 3.31: (a) Signal traces from injection of 7-ethoxyresorufin into the MS obtained in positive mode using an MRM scan at 242>186 m/z and (b) 242>214 m/z.*

As can be seen both of these fragmentations, 242>186 m/z (Figure 3.31a) and 242>214 m/z (Figure 3.31b) provided a peak allowing an optimisation on these to be carried out.

## Optimisation of collision energy

The inbuilt optimisation of collision energy method was then used to optimise the fragmentations 242>186 m/z and 242>214 m/z (Figure 3.32).

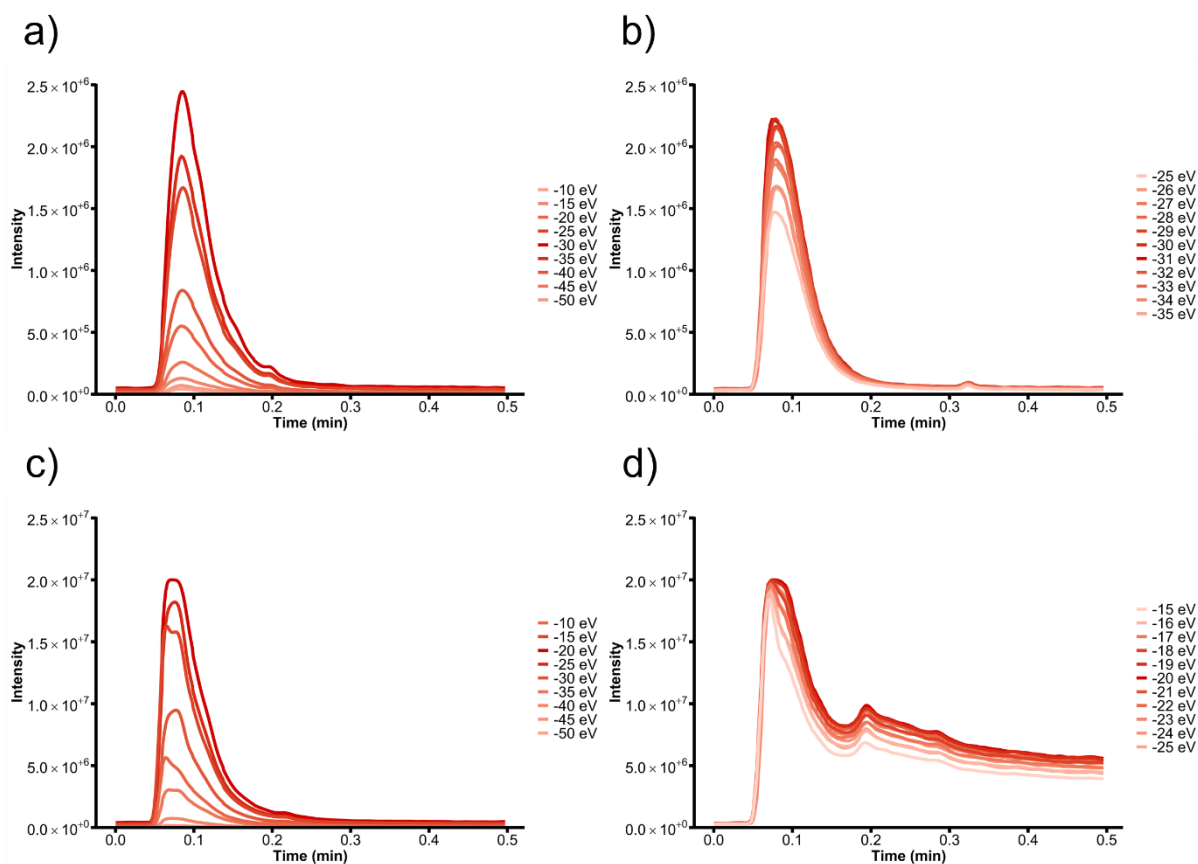


Figure 3.32: (a) Signal traces from injection of 7-ethoxyresorufin into the MS optimising the collision energy for the fragmentation in positive mode set to 242>186 m/z using a broad scan and (b) a detailed scan between -25 to -35 eV and 242 to 214 m/z using (c) a broad scan and (d) a detailed scan between -15 to -25 eV.

These spectrum were measured in both a broad scan varying from -10 to -50 eV for the two previously measured collisions 242>186 m/z (Figure 3.32a) and 242>214 m/z (Figure 3.32c) and a detailed scan (Figure 3.32b and d respectively) which range is dependent on the highest peak area measured in the broad scan. For the fragmentation 242>186 the optimum was determined between 25 and 35 eV and for 242>214 between 15 and 25 eV, which was further optimised to -31 and -20 eV respectively. Upon comparing the relative peak areas and intensity for both

fragmentations (Figure 3.32b and d) the fragmentation of 242>214 provides a 10 times higher intensity and peak area.

### *Retention time determination*

The retention time for 7-ethoxyresorufin (Figure 3.33) was determined using the gradient method optimised previously and described in Table 3.7.

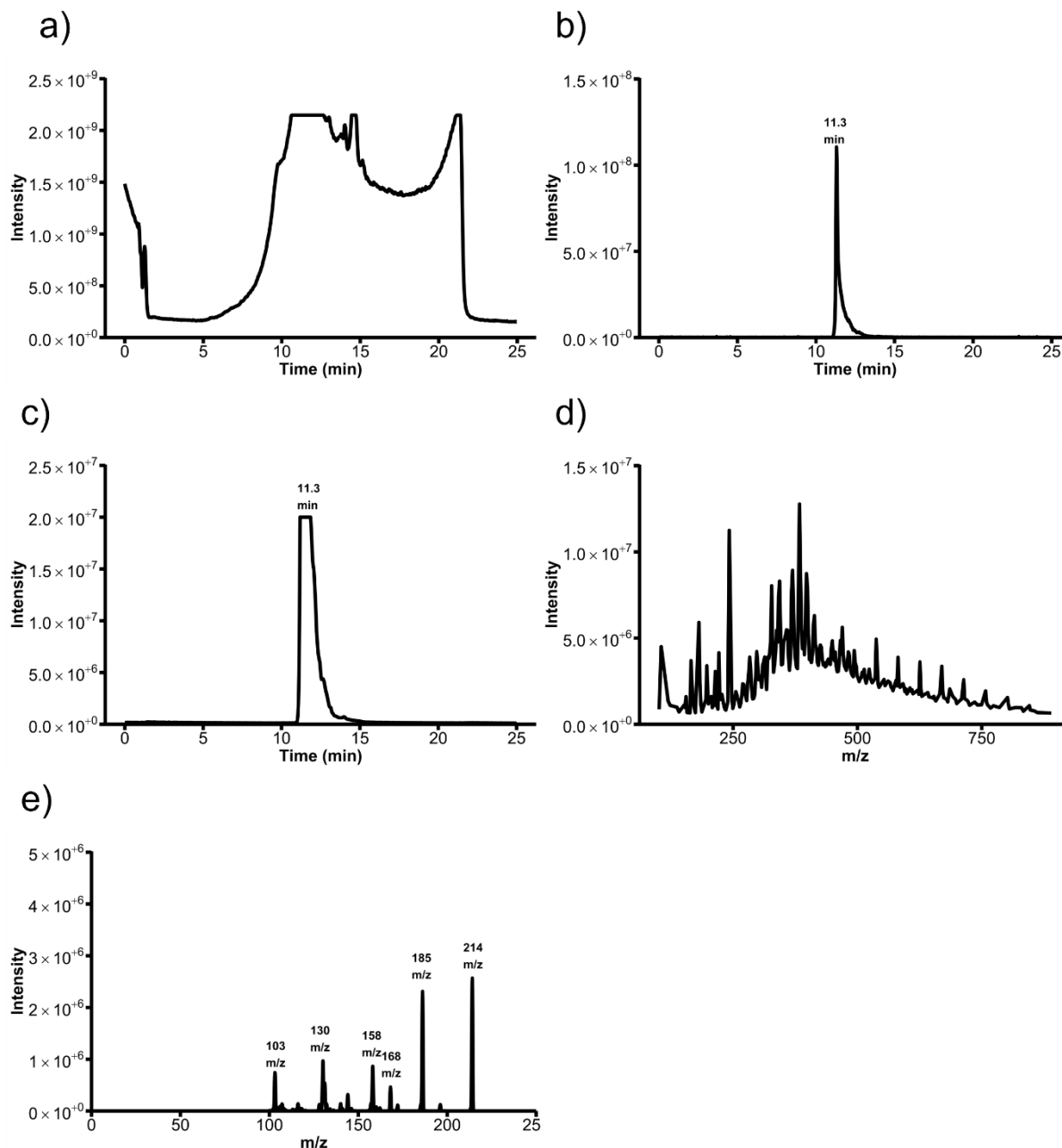


Figure 3.33: (a) Signal traces from injection of 7-ethoxyresorufin into the MS obtained in positive mode using a Q1 scan (b) a product ion scan set to 242 m/z (c) and an MRM set to 242>214 m/z (d) Mass spectrum of the area under the peak in (a) (e) Mass spectrum of the area under the peak (b).

As can be seen in these all of the conducted scans, Q1 scan (Figure 3.33a), product ion scan set to 242 m/z (Figure 3.33b) and an MRM scan set for the optimised collision 242>214 m/z (Figure 3.33c), the retention time of 7-Ethoxyresorufin was found to be 11.3 minutes which is sufficiently separated from resorufin at 9.8 minutes (Figure

3.14). The Q1 scan did not yield the expected parent ion. However, the product ion scan (Figure 3.33e) provided multiple fragmentations compared to those found within the product ion scan (Figure 3.30). These product ion scan fragments can be further applied to sample scans in order to further prove 7-Ethoxyresorufin was found within the sample.

### 3.4. Comparison between isocratic and gradient

Two different HPLC methods have been tested, an isocratic method and a gradient method. The isocratic method found very little separation and a much lower resolution as shown in Figure 3.13. Whereas the gradient method provided much higher resolution (Figure 3.14) allowing for more accurate substrate confirmation and a higher sensitivity. Resolution for all separations used throughout these studies were calculated between these compounds using Equation 1 and is shown in Table 3.10.

*Equation 1: Calculation for the resolution between peaks within a spectrum*

$$Resolution = \frac{tr_2 - tr_1}{0.5 \times (W_2 + W_1)}$$

Where  $tr$  is the retention time of a peak in minutes and  $W$  is the width of the peak in minutes.

*Table 3.10: Resolutions calculated for all optimised separations using Equation 1.*

Substrate	Product	Resolution
Resorufin (isocratic)	Resorufin glucuronide (isocratic)	1.05
Resorufin (gradient)	Resorufin glucuronide (gradient)	2.46
<i>p</i> -Nitrophenol	<i>p</i> -Nitrophenyl sulfate	2.10
7-Ethoxyresorufin	Resorufin	14.44

The optimum scans along with their parameters that were determined throughout this section are found below in Table 3.11.

Table 3.11: Summary of obtained optimum collision energies for fragmentations.

Substrate	Mode	Fragmentation (m/z)	Optimised collision energy (eV)
Resorufin	Positive	214>103	-35
	Positive	214>186	-25
	Negative	212>118	36
	Negative	212>155	33
Resorufin glucuronide	Positive	383>165	-20
	Negative	388>212	34
<i>p</i> -nitrophenol	Negative	138>108	42
<i>p</i> -nitrophenyl sulfate	Negative	218>108	33
	Negative	218>138	22
7-Ethoxyresorufin	Positive	242>186	-31
	Positive	242>214	-22

The scans optimised and described throughout this section were applied to the gradient method for future analysis of their respective samples and blanks.

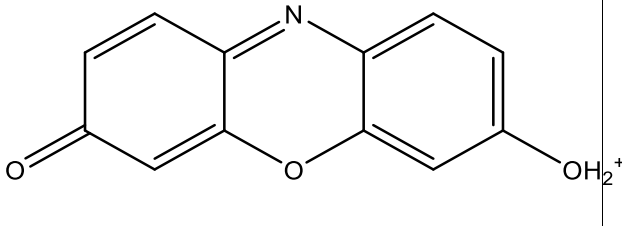
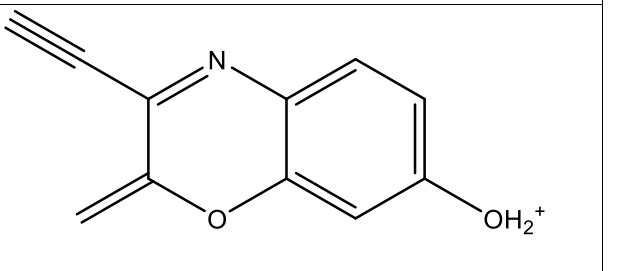
### 3.5. Discussion

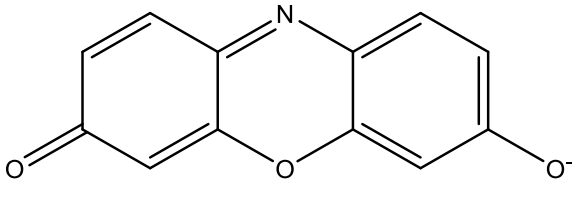
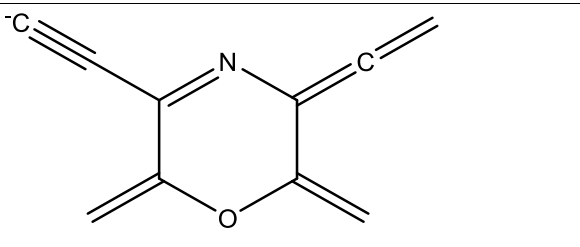
A method to detect compounds that have been frequently used in literature for the metabolism-based studies has been optimised throughout this chapter. The studies that have used these compounds frequently rely on a fluorescence-based analysis, to take advantage of the highly fluorescent nature of resorufin, the pH utilised was optimal for both the enzyme and the substrate. Although this is a viable method for

quantification of metabolites formed, it is not the optimal in most cases due to the different synthetic routes and isomers that can be formed upon undergoing the majority of metabolic methods. To the authors' knowledge there is very little research into the measurement of these compounds utilising LC-MS in conjunction. However, there has been research on each of these compounds independently. No studies have focussed on the fragmentation of these compounds making a simple mimicable method not available for analysts.

The mass spectrum of resorufin was measured by Yu *et al.* (2003) finding two major fragments were formed in positive mode one of which being the parent ion at 214 m/z and the other being a peak at 186 m/z. This was also comparable to that which was found in this study.<sup>273</sup> The structures expected based on fragmentation patterns for both resorufin and resorufin glucuronide are shown in Figure 3.11 and Figure 3.12 respectively.

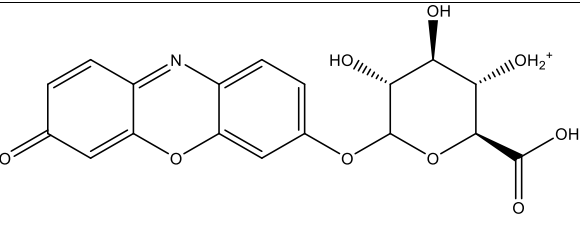
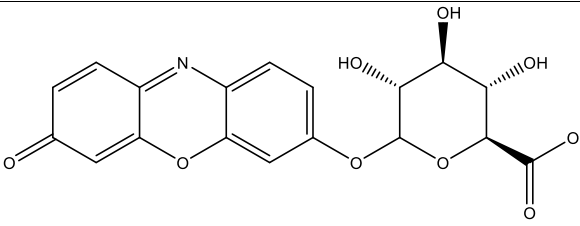
Table 3.12: Summary of expected fragments for resorufin based on common fragmentation pathways simulated using CFM-ID.<sup>266-270</sup>

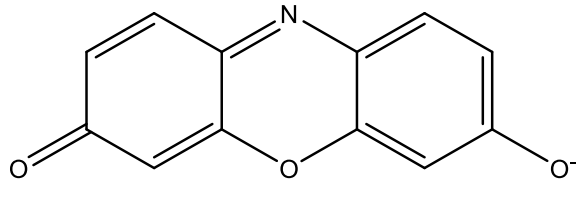
Mode	Expected loss (m/z)	Molecular weight (g mol <sup>-1</sup> )	Expected molecule
Positive	0	214.2	
Positive	28	186.2	

Negative	0	212.2	
Negative	57	155.2	

The mass spectrum of resorufin glucuronide was also measured by Wang *et al* (2015) finding two major peaks were formed in positive mode the parent ion at 390 m/z and a mass at 214 m/z.<sup>274</sup> The latter is likely to be due to the loss of the glucuronide group. The specific fragmentation of glucuronide functionalised molecules in mass spectrometry has been widely documented with the loss of 176 mass units.<sup>275</sup> The equivalent is also true for negative mode with a two-mass unit difference due to the charge.

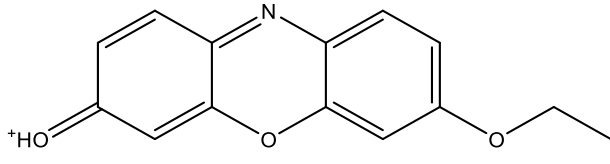
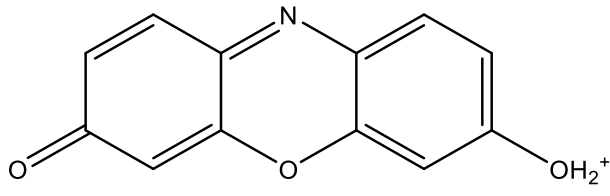
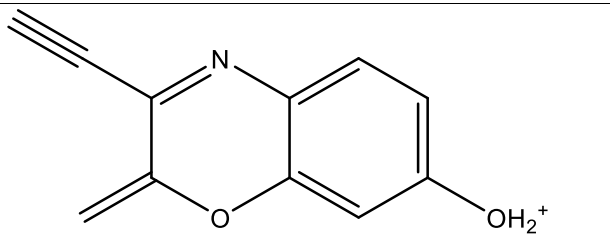
Table 3.13: Summary of expected fragments for resorufin glucuronide based on common fragmentation pathways simulated using CFM-ID.<sup>266-270</sup>

Mode	Expected loss (m/z)	Molecular weight (g mol <sup>-1</sup> )	Expected molecule
Positive	0	390	
Negative	0	388	

Negative	176	212	
----------	-----	-----	--

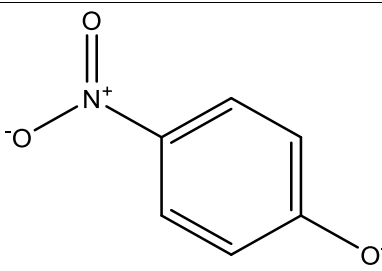
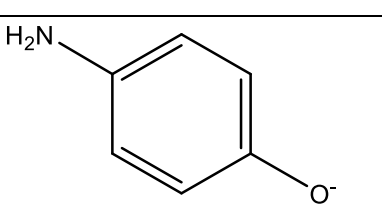
The mass spectrum of 7-ethoxyresorufin was also simulated using CFM-ID finding two major peaks were formed in positive mode one of which being the parent ion at 242 m/z and the other being at 214 m/z. It is likely the 214 m/z is a resorufin peak due to the loss of the ethane group during fragmentation. This is also comparable to that which was found in this work. The expected fragmentations for 7-ethoxyresorufin are shown in Table 3.14.

Table 3.14: Summary of expected fragments for 7-ethoxyresorufin based on common fragmentation pathways simulated using CFM-ID.<sup>266-270</sup>

Mode	Expected loss (m/z)	Molecular weight (g mol <sup>-1</sup> )	Expected molecule
Positive	0	242.2	
Positive	28	214.2	
Positive	56	186.2	

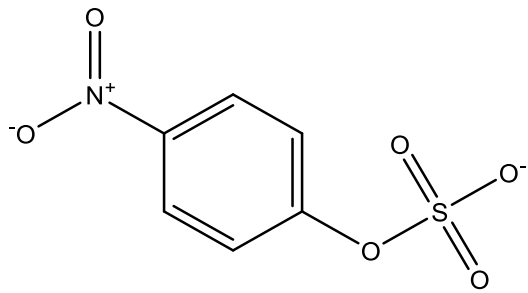
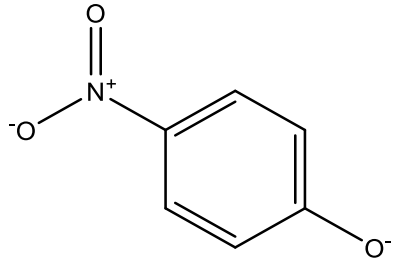
The mass spectrum of *p*-nitrophenol was also measured by Han *et al.* (2008) finding three major peaks were formed in positive mode, the parent ion 139 m/z, a peak at 109 m/z and another at 65 m/z.<sup>271</sup> This is similar to which was found from the spectrum measured in this study. However, the peak at 65 m/z was not measured due to the detector being set to scan between 100 and 1000 m/z. The expected fragmentations based on common fragmentation pathways are shown in Table 3.15.

Table 3.15: Summary of expected fragments for *p*-nitrophenol based on common fragmentation pathways.

Mode	Expected loss (m/z)	Molecular weight (g mol <sup>-1</sup> )	Expected molecule
Negative	0	138	
Negative	30	108	

The mass spectrum of *p*-nitrophenyl sulfate was also measured by Draper *et al.* (1989) finding two major peaks formed one of which being 218 m/z and the other being 139 m/z.<sup>272</sup> This is comparable to what was found in this study, although one further fragment was found at 108 m/z in this research. The expected fragments for *p*-nitrophenyl sulfate are shown in Table 3.16.

Table 3.16: Summary of expected fragments for *p*-nitrophenyl sulfate based on common fragmentation pathways.

Mode	Expected loss (m/z)	Molecular weight (g mol <sup>-1</sup> )	Expected molecule
Negative	0	218	 The structure shows a benzene ring with a nitro group (-NO <sub>2</sub> ) at the top position and a sulfate group (-OSO <sub>3</sub> <sup>-</sup> ) at the para position (bottom). The nitro group is represented as a nitrogen atom with a positive charge and two oxygen atoms, one double-bonded and one single-bonded. The sulfate group consists of a sulfur atom double-bonded to two oxygen atoms and single-bonded to two others, one of which is the oxygen atom connecting to the benzene ring.
Negative	80	138	 The structure shows a benzene ring with a nitro group (-NO <sub>2</sub> ) at the top position and an oxygen atom at the para position (bottom). The nitro group is represented as a nitrogen atom with a positive charge and two oxygen atoms, one double-bonded and one single-bonded. The oxygen atom at the para position has a negative charge, representing the phenoxide fragment.

Throughout all of the optimisations found within this chapter, all of those observed were fully comparable to those that are expected utilising a fragmentation prediction software called CFM-ID, showing that these are the correct fragmentations for the respective analytes. This, in conjunction with the expected retention times based on their polarities, shows that these peaks are indeed caused by the expected compounds.

### **3.6. Conclusion**

This section has described the optimisation of mass spectrometry and separation for resorufin and its respective metabolites/precursor (7-ethoxyresorufin and resorufin  $\beta$ -D glucuronide) and nitrophenol with its sulfated metabolite nitrophenyl sulfate. This is important as it represents a method for identifying the expected reaction products from both oxidative and conjugative metabolism reactors. The use of LC-TQ-MS provides some structural confirmation, as well as offering a high degree of sensitivity and selectivity. The optimisation of collision energies will allow for much more sensitive measurements due to the increased amount of fragmentation upon entering the collision cell. Through the optimisation of a chromatographic method, a gradient (illustrated in Figure 3.1) method will be used, offering superior separation than the isocratic method tested in this study.

## 4. Optimisation of the synthesis of naturally occurring metabolites using UGT1a1

### 4.1. Introduction

The synthesis of naturally circulating metabolites has been of large interest for the determination of nutraceuticals and drugs with specific beneficial and toxicological effects on the human body. The motivations and methods for these have been described in detail in section 1.3.

UGT enzymes, found within the endoplasmic reticulum of a living organisms' cells, are one of the common elimination pathways for most xenobiotics.<sup>276</sup> They transform small non-polar molecules into larger polar molecules, allowing for easier excretion by the kidneys into bile or, in the majority of cases, urine mostly *via* glomerular filtration.<sup>277</sup> UGT enzymes have specific but overlapping substrate specificities.<sup>276</sup> For example, UGT1a1 is the only isoform that conjugates bilirubin, allowing for its excretion.<sup>278</sup> In contrast, acetaminophen is metabolised into acetaminophen glucuronide *via* one of four different UGT isoforms (UGT1a1, UGT1a6, UGT1a9, UGT2B15).<sup>23</sup> All UGT isoforms catalyse the formation of oxygen, nitrogen and sulphur linked glucuronide metabolites.<sup>49</sup> The therapeutic and toxicological effects of conjugated metabolites often differ from the parent molecule.<sup>279</sup> Xenobiotics that have undergone glucuronidation are usually inert and non-toxic.<sup>213</sup> However, some compounds have been found to have an increased therapeutic or toxicological effect. For example,

morphine is naturally metabolised into M6G and M3G, with the former providing the analgesic effect and some of the side effects are attributed to the latter.<sup>42</sup> A compound's metabolite may have an increased toxicity, detrimentally affecting a person's health, for example acyl glucuronides.<sup>280</sup> Thus, determining the beneficial and toxicological effects of drug metabolites prior to human testing is vital for effective drug development.<sup>281, 282</sup> However, testing these metabolites is difficult due to their current lack of availability.<sup>29</sup> For example, the glucuronide metabolite of quercetin, quercetin 3-O-glucuronide, is currently not available for purchase. An isomer of this, quercetin 3-glucuronide is commercially available, however this is a plant metabolite, and may not replicate the pharmacology of the human metabolite. Due to the potential difference in pharmaceutical and toxicological effects between the 3-O-glucuronide and the 3-glucuronide, testing the naturally formed metabolite is currently difficult. This demonstrates a requirement for a method that allows for the synthesis of glucuronic metabolites of drugs and xenobiotics, to allow for the determination of therapeutic effects of both parent compounds, and metabolites.

The current methods for synthesising glucuronide metabolites are described in detail in section 1.3 and summarised in the discussion below. The main purpose of these methods is for the identification of drug metabolites, rather than producing sufficient quantities for use in pharmacological investigations.

Microfluidic devices have already been combined with these methods and studied for the formation of naturally circulating metabolites. Immobilising the enzymes and liver cell microsomes is a common method for the determination of metabolites formed *in vivo*.<sup>121</sup> A variety of different immobilisation techniques and surfaces have been tested, including studies using a liver slice combined with a breathable membrane within a microfluidic device.<sup>283</sup> However, the aim of these methods has been the determination

of metabolites and not the synthesis of a pure product. These published approaches demonstrate that microfluidic systems are a viable option for the synthesis of metabolites and may be applicable for the synthesis of a pure product.

In this chapter, the development and optimisation of a microfluidic reactor with the immobilisation of UGT1a1 for the synthesis of metabolites *via* glucuronidation reactions naturally occurring in the human will be described. This will include optimisation of flow rate, temperature and then comparing against optimal batch conditions frequently used in literature. Initially, transformation is studied by reduction in fluorescence from a fluorescent starting product. Finally, the metabolic reaction product is confirmed with specific LC-TQMS methods.

## **4.2. Experimental procedure**

### **Determination of resorufin concentration**

A calibration curve for resorufin was created by serial dilution of an initial concentration of 100  $\mu\text{M}$ . The dilution was carried out sixteen times by half in a V-shaped 96-well microplate (STARLAB). Fluorescence intensity was measured using a microplate reader set to 544 nm ( $\lambda_{\text{ex}}$ ) and 590 nm ( $\lambda_{\text{em}}$ ) as optimised in the UGT section, Plate reader analysis.

## Determination of resorufins fluorometric properties

An absorbance scan varying from 200-800 nm was conducted on both resorufin and resorufin glucuronide (100  $\mu\text{m}$ ) using a Jenway 7315 spectrometer equipped with a xenon lamp. An excitation scan was conducted for resorufin solely with  $\lambda_{\text{em}}$  to 586 nm. Then an emission scan was conducted with  $\lambda_{\text{ex}}$  set to 572 nm.

## Fabrication of microfluidic devices

Two different designs created on AutoCAD (Figure 2.1) were compared. Device design A included a splitting channel network featuring 16 parallel channels and design B included a long single serpentine channel. The channels in chip design A were 50 mm long, 300  $\mu\text{m}$  wide and a depth etched to 30  $\mu\text{m}$ . This equates to a surface area to volume ratio  $>5000 \text{ m}^{-1}$ . At a flow rate of  $0.1 \mu\text{L min}^{-1}$  the residence time was 72 minutes. The channel in device B, the serpentine was 667 mm long, 75  $\mu\text{m}$  wide and etched to a depth of 30  $\mu\text{m}$ . Equating to a surface area to volume ratio of  $150 \text{ m}^{-1}$ . At a flow rate of  $0.1 \mu\text{L min}^{-1}$  the residence time was 15 minutes.

These two devices were fabricated in glass. These designs were printed on a photolithographic mask (JD Phototools) and transferred *via* photolithography onto glass (Schott B270, Tellic USA) containing a photoresist and chromium layer. Devices were etched utilising hydrofluoric acid (49%) and access holes were drilled *via* a CNC machine (Datron). Devices were bonded *via* thermal fusion at  $585 \text{ }^\circ\text{C}$ . Pictures of both Design A and B are shown in Figure 2.2.

Prior to each use the devices were submerged and cleaned with piranha solution (95% sulfuric acid and 30% hydrogen peroxide in a 3:1 ratio) for 2 hours. The devices were

then sonicated in water to extract any piranha solution remaining within the channels and left to dry. Silica capillaries were then placed in the inlet and outlet holes and glued using epoxy resin 2:1 and left to cure overnight, allowing the device to interface to a 1 mL syringe *via* PTFE tubing.

### **Immobilisation of UGT supersomes**

For both the serpentine and the parallel device initially sodium hydroxide (0.1 M, 3 x 1 mL) was hand pumped through the device. This was followed by methanol (3 x 1 mL) and then the devices were left in the oven for 1 h at 60°C to dehydrate the surface of the channels a solution of (3-aminopropyl) trimethoxy silane (5% v/v in ethanol) was introduced into the device and left for 5 minutes. Next glutaraldehyde (5% v/v in 0.1 M phosphate buffer, pH 7.4) was pumped through the device using a syringe pump for one hour at 3  $\mu\text{L min}^{-1}$ . Finally, the device was filled with UGT1a1 supersomes (0.15 mg mL<sup>-1</sup>) and left in the fridge at 4 °C overnight and then rinsed out with phosphate buffer (0.1 M, pH 7.4).<sup>284</sup> Metabolic conversions within the device were studied using resorufin (100  $\mu\text{M}$ ) as a substrate alongside the necessary co-factor (UDP-GA at 100  $\mu\text{M}$ ) using varying flow rates using an NE-4000 syringe pump (0.1, 0.5 and 1  $\mu\text{L min}^{-1}$ ).

### **Metabolism of test substrates**

Resorufin is a fluorescent compound that upon undergoing UGT facilitated metabolism leads to the formation of resorufin glucuronide. Resorufin is a highly fluorescence molecule with a  $\lambda_{\text{ex}} = 572$  and  $\lambda_{\text{em}} = 583$  nm. This loss of fluorescence forms the basis for determining the amount of metabolism formed by the microfluidic devices.

Resorufin (100  $\mu\text{M}$ ) was pumped through the enzyme immobilised devices, effluent was collected, and fluorescence intensity was utilised to quantify product formation using a calibration curve varying from 0 – 100  $\mu\text{M}$ . Flow rates of 0.1, 0.5 and 1  $\mu\text{L min}^{-1}$  were investigated in both chip designs A and B with immobilised UGT1a1 supersomes. For experiments where temperature was altered, devices were incubated at room temperature ( $20 \pm 2$   $^{\circ}\text{C}$ , variation measured utilising a thermometer every time effluent was collected), 30 and 37  $^{\circ}\text{C}$  in a  $\text{CO}_2$  incubator (BB15, Thermo Scientific) with a run time of 2 hours. For a comparison to static reactions, 2  $\mu\text{L}$  of UGT1a1 supersomes ( $0.15 \text{ mg mL}^{-1}$ ) was added to 10  $\mu\text{L}$  of resorufin (100  $\mu\text{M}$ ) with co-factor UDP-GA (100  $\mu\text{M}$ ) and left to incubate at 37  $^{\circ}\text{C}$ . Control reactions were carried out where the co-factor (UDP-GA) or the UGT1a1 supersome was not immobilised. Devices were also prepared with immobilising the enzyme triosephosphate isomerase ( $0.15 \text{ mg mL}^{-1}$ ) as an alternative reaction that was expected to yield no reduction in fluorescence, due to having no reactivity towards resorufin. These were conducted to confirm that both the correct enzyme and co-factor are required to obtain a reduction of fluorescence.

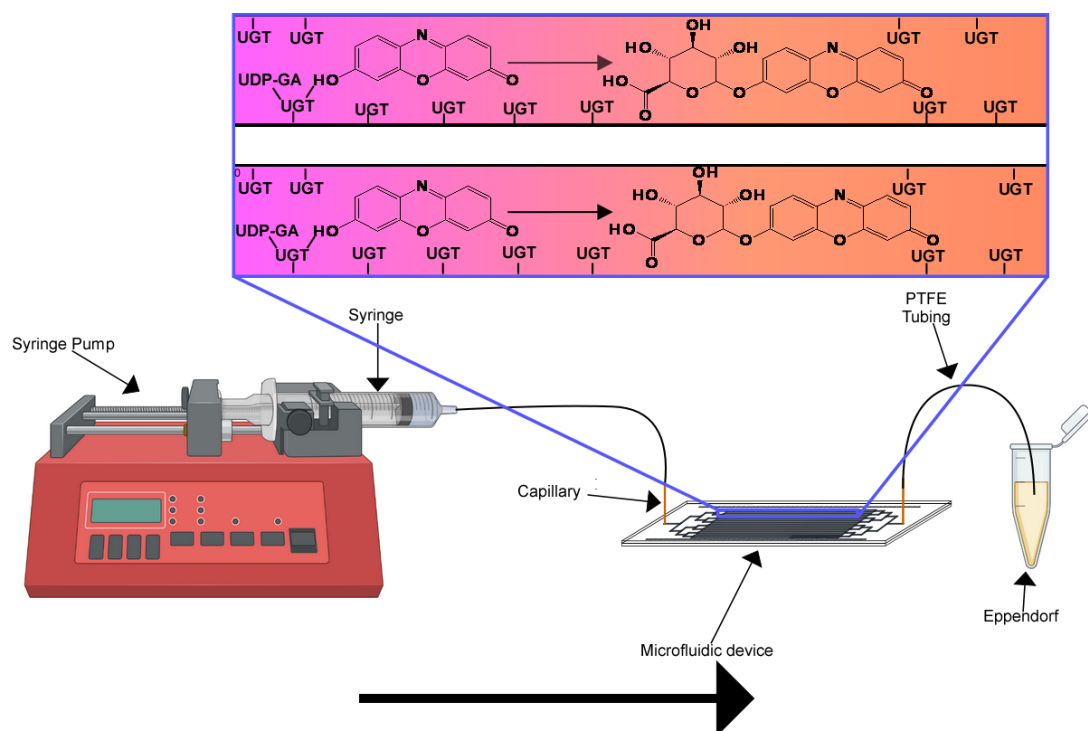


Figure 4.1: Schematic of the setup used for the metabolism of resorufin into resorufin glucuronide using UGT1a1.

This schematic shows the setup used for the metabolism of resorufin alongside the predicted metabolism of resorufin into resorufin  $\beta$ -D-glucuronide upon flow through of the device (Figure 4.1).

To allow comparison of the microfluidic approach to a typically used method the substrate ( $100 \mu\text{M}$  of resorufin) was directly incubated with  $1 \mu\text{L}$  of UGT supersomes ( $0.15 \text{ mg mL}^{-1}$ ) at  $37 \text{ }^\circ\text{C}$  for 2 h and measured using the plate reader method described above (section 2.5) to determine product formation.

## Mass spectrometry

Using the effluents from the reactor, in the presence and absence of appropriate cofactor, resorufin glucuronide was measured *via* LC-MS. Effluents were extracted from the matrix using  $10 \mu\text{L}$  C18 tips (Sigma Aldrich). The C18 tip was wetted using  $10 \mu\text{L}$  of 50% methanol in water twice, the tip was then equilibrated using  $10 \mu\text{L}$  0.1%

TFA in water twice. Next, the sample was aspirated for 10 cycles and left in the tip for 10 min. This was followed by 10  $\mu$ L rinsing with water twice and finally the sample was extracted from the tip using 10  $\mu$ L of methanol. Samples were analysed with a Shimadzu Nexera X2 series liquid chromatography system (Kyoto, Japan) connected to a Shimadzu Nexera X2 SIL-30AC coupled to a Shimadzu 7060 triple quadrupole mass spectrometer. Data acquisition and processing was performed by LabSolutions<sup>TM</sup> 5.93 software. The chromatographic separation was achieved on a Shim-pack GISS C18 column (50 mm x 2.1 mm, 1.9  $\mu$ m) (Shimadzu). The mobile phase consisted of water for phase A and methanol for phase B, both containing 0.1% formic acid. The separation was carried out using a gradient method with mobile phase A: B set to 95%:5% from 0 to 3 min, 25%:75% from 10 to 20 min and then back to 95%:5% from 22 to 25 min. The mass spectrometer was operated in the negative ion mode. The nebulizer gas, collision gas, ion spray voltage and source temperature were set at 3 L min<sup>-1</sup>, 17 kPa, 2.32 kV, and 250 °C, respectively. A product ion scan in negative mode was used for product confirmation of resorufin glucuronide with an m/z of 388, respectively. Alongside this, the multiple reaction mode (MRM) was used for further confirmation with selected transitions of 388 $\rightarrow$ 212 m/z.

### **Methanol crash**

In order to extract any enzyme that potentially leached from the surface of the device and causing an interfering matrix when injecting into the LC-TQ-MS methanol crashing of both a resorufin (100  $\mu$ M) and resorufin glucuronide standard (100  $\mu$ M). This was conducted by taking 10 $\mu$ L respective substrate and mixing 100  $\mu$ L of methanol. This mixture was then vortexed followed by centrifugation to settle any denatured proteins. The top layer of this mixture was then directly placed within the mass spectrometer following the method detailed above (2.6).

## **Liquid-liquid extraction (LLE)**

Liquid-liquid extraction was conducted by making a mixture of 4% ammonium hydroxide and 4% ethyl acetate in methanol. 10  $\mu$ L of sample was added 25 mL of the mixture. If extracted correctly, the sample should be found within the hydrophilic layer which in this case was the top layer. The sample was directly extracted and then analysed *via* the LC-TQ-MS method described in section 2.6.

## **C18 ZipTip extraction**

The final extraction method utilised was using C18 zip tips. Initially tips were wetted pipetting 10  $\mu$ L of MilliQ water. Then 10  $\mu$ L of 50% methanol in MilliQ water was then pipetted into the tip and then washed further with MilliQ water. At this point two different methods were tested. The first involved aspirating the sample within the device 10 times as per the instruction provided by the manufacturer. After this, the tip was rinsed with methanol and directly injected into the LC-TQ-MS. The other technique involved pipetting 10  $\mu$ L of sample and incubating it within the tip for 10 minutes. After this, the sample was removed, and 100% methanol was implemented within the pipette and injected into the LC-TQ-MS as per the method described in 2.6.

## 4.3. Results

### Plate reader analysis

#### *Absorbance scan*

To ascertain whether a plate reader method would be viable for determining resorufin concentration in the working range of the device (100  $\mu$ M) standards were initially assessed as described in the **Error! Reference source not found.** section. The development of a fluorometric method requires determining both resorufin and resorufin glucuronides  $\lambda_{\max}$  (Figure 4.2) and was determined using an absorbance scan as described in the Absorbance scan section.

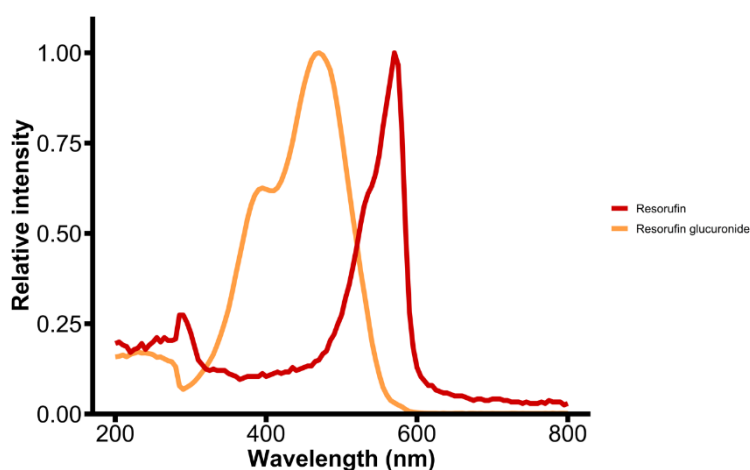


*Figure 4.2: Relative absorbance scan for both resorufin and resorufin glucuronide.*

As shown in the absorbance scans, a  $\lambda_{\max}$  of 570 nm and 470 nm were measured for resorufin and resorufin glucuronide, respectively. The next step was to determine the fluorescence emission value of resorufin using the excitation value determined from the scan in Figure 4.2.

### *Fluorescence scan*

**Due to resorufin's fluorescent properties, the plate reader method being optimised would provide a much larger increase in the gap between the upper and lower limits of product using fluorometric scans. Initially an absorbance scan was used to determine  $\lambda_{\text{ex}}$  which was subsequently applied to a fluorescence scan to determine  $\lambda_{\text{em}}$  using the method described in the Determination of resorufin concentration**

A calibration curve for resorufin was created by serial dilution of an initial concentration of 100  $\mu\text{M}$ . The dilution was carried out sixteen times by half in a V-shaped 96-well microplate (STARLAB). Fluorescence intensity was measured using a microplate reader set to 544 nm ( $\lambda_{\text{ex}}$ ) and 590 nm ( $\lambda_{\text{em}}$ ) as optimised in the UGT section, Plate reader analysis.

Determination of resorufins fluorometric properties section.

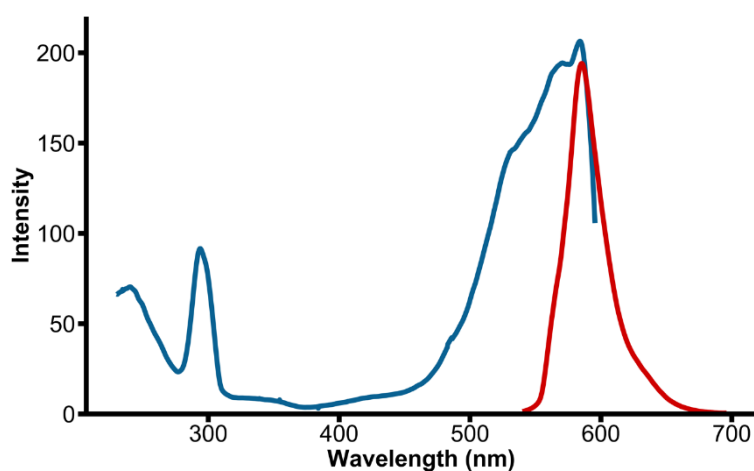


Figure 4.3: Fluorescence scan for resorufin (100  $\mu\text{M}$ ), with both (a) determination of  $\lambda_{\text{ex}}$  with  $\lambda_{\text{em}}$  set to 586 nm (blue line) and (b)  $\lambda_{\text{em}}$  with  $\lambda_{\text{ex}}$  set to 572 nm (red line).

Based on these data provided, the optimum  $\lambda_{\text{ex}}$  and  $\lambda_{\text{em}}$  were determined to be 572 and 573 nm respectively. The plate reader being used had select wavelength filter sets available, with the closest being 544 nm for excitation and 590 nm for emission. These wavelengths were then applied to the fluorescent plate reader for all future experiments.

#### *Calibration curve for resorufin*

Calibration curves were determined using the plate reader method shown in the **Error! Reference source not found.** section, with concentrations between both 10 and 100  $\mu\text{M}$  and 2 nm to 100  $\mu\text{M}$  measured for fluorescence (Figure 4.4).

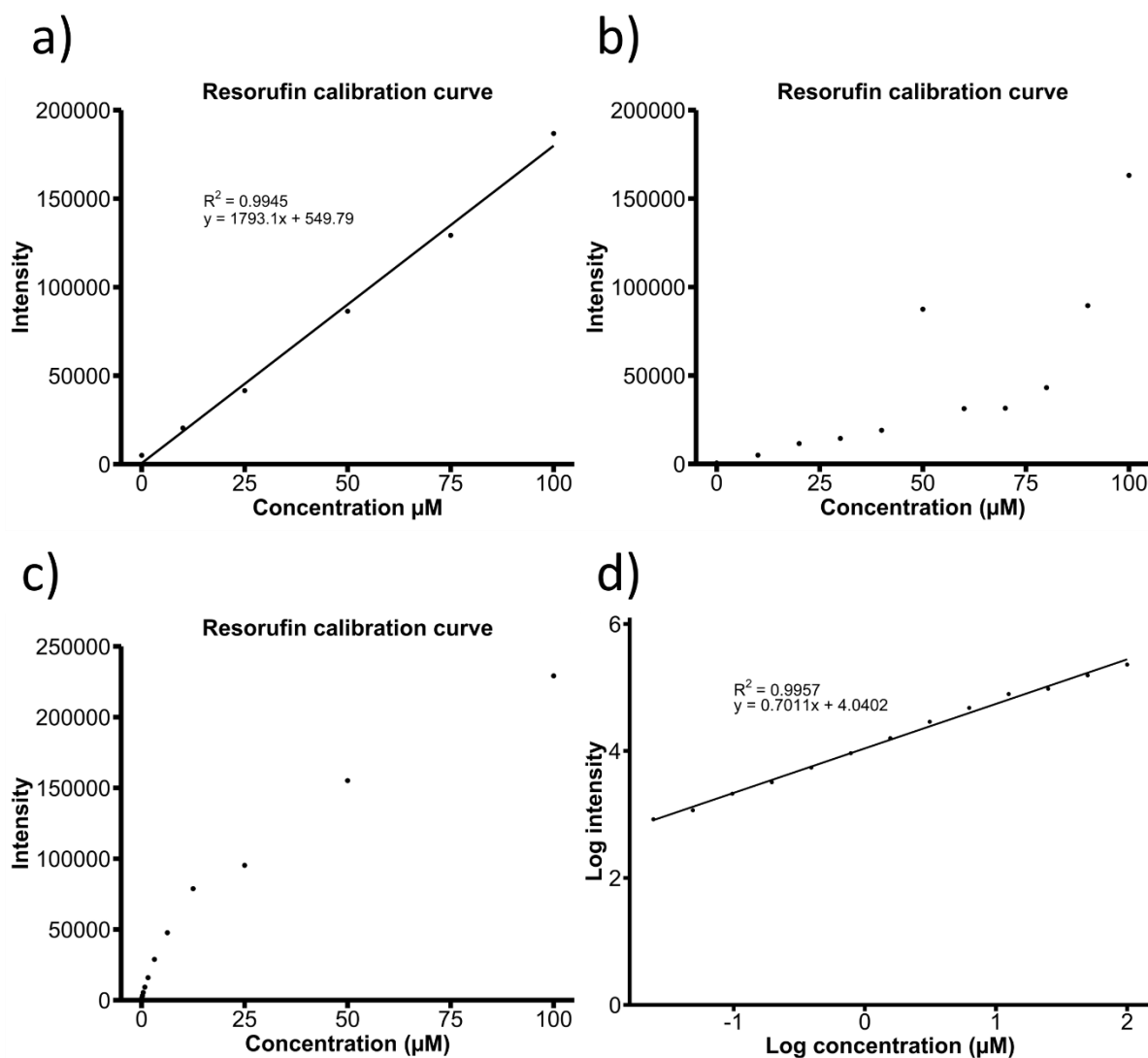


Figure 4.4: Two different calibration curves for resorufin varying concentration between 10 and 100  $\mu\text{M}$  on different days, yielding both (a) a linear calibration and (b) poorly correlating values both of which were under the same conditions and (c) an increased range of concentrations starting from 2 nM to 100  $\mu\text{M}$  and (d) its respective logarithmic transformation.

Due to the initial concentration of 100  $\mu\text{M}$  being utilised for metabolism studies, a calibration curve varying from 10 to 100  $\mu\text{M}$  was optimised. However very inconsistent results were found from day-to-day, illustrated in Figure 4.4 a and b. Due to these inconsistencies a higher range of concentrations were tested, starting at 100  $\mu\text{M}$  and sequentially diluting by half 13 times. Upon logarithmically transforming this data a linear correlation was found allowing for a much higher range of concentrations (49

nM to 100  $\mu$ M to be measured. Alongside this, a linear calibration for the logarithmic data was produced from day-to-day repeats. Due to the sensitive fluorescence nature of resorufin these measured intensities can fluctuate daily, so a calibration curve is necessary alongside the analysis of all samples and a representative reproducible calibration curve cannot be utilised. Despite this, throughout all repeats of this calibration a linear correlation was found, ensuring that it was viable for an accurate determination of resorufin concentration. This method was applied to all measurements of resorufin concentration throughout this chapter.

### **Proof of product formation for UGT1a1 reactor**

To determine if product could be formed within the microfluidic device the method shown in section 2.6 was used. Initially a flow rate of 0.1  $\mu$ L  $\text{min}^{-1}$  was tested, after immobilising UGT1a1 as described in the Immobilisation of UGT supersomes section. Additionally, three different blanks were conducted: enzyme immobilised with co-factor not included; no enzyme immobilised, but cofactor present; and an alternative enzyme (triosephosphate isomerase/ TPI) immobilised with co-factor present (Figure 4.5). The alternative enzyme (TPI) was chosen due to its similar size compared to UGT1a1 and lack of activity towards resorufin.

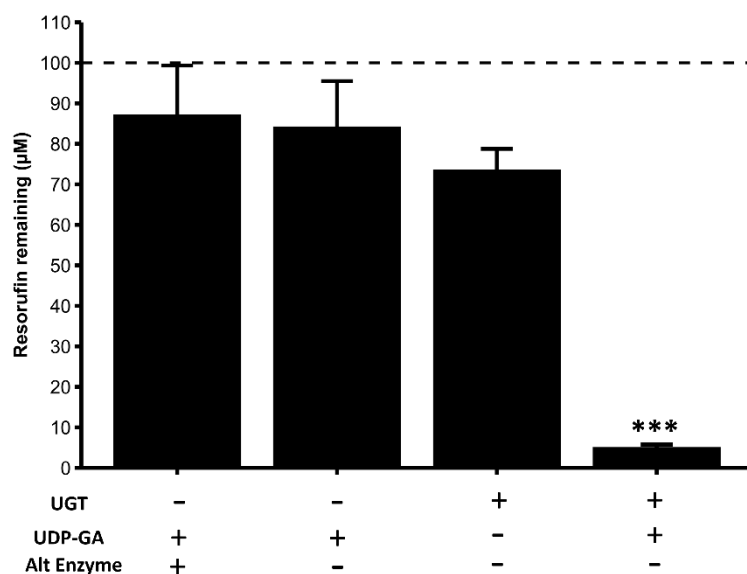


Figure 4.5: Comparison showing mean concentration  $\pm$  SD of resorufin remaining post flowing through the device between different blanks and a true enzymatic run. Dotted line represents concentration of resorufin added to the device ( $100 \mu\text{M}$ ). All bars have been conducted using an  $n=3$ . Statistics performed by ANOVA with Bonferroni corrections, comparing each blank to true run, \*\*\*  $p= >0.0001$ .

The data obtained showed that the true run yielded a fluorescence remaining of  $5.13 \pm 0.62 \mu\text{M}$ . Whereas the three blanks, no immobilised enzyme, no co-factor included within the system and the alternative enzyme (TPI) used demonstrated little to no measurable loss of fluorescence at  $84.28 \pm 11.20 \mu\text{M}$ ,  $73.66 \pm 5.11 \mu\text{M}$  and  $87.25 \pm 12.09 \mu\text{M}$  respectively. Unless otherwise stated all experiments were performed with  $n=3$  repeats.

The data shown in Figure 4.5 suggests that enzymatic activity is only observed when both the correct co-factor and correct enzyme are available within the microfluidic device simultaneously, highlighting that the observed decrease in resorufin concentration is a specific loss, and not due to non-specific binding of the substrate to the matrix of the microfluidic devices, or non-specific protein binding within the channels.

## Flow rate

Having demonstrated an enzyme and cofactor-dependent, specific loss of fluorescence when using the microfluidic devices, the next step was to optimise the parameters within the device. A comparison of reactor architecture (parallel channels vs serpentine channels) and the effect of different flow rates of substrate and cofactor through these devices was undertaken. (Figure 4.6).

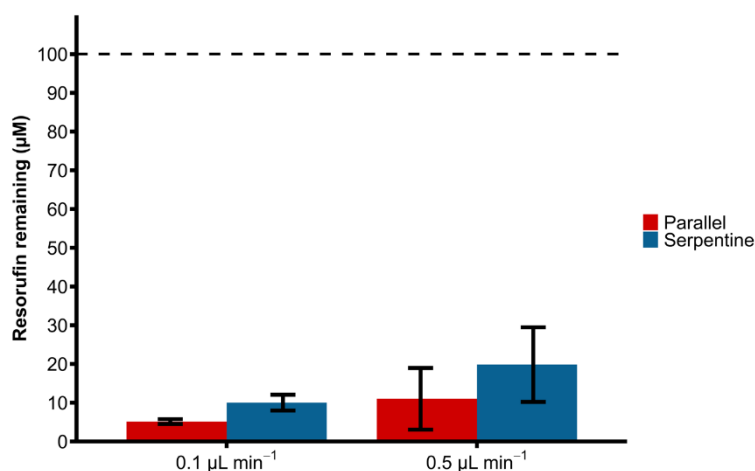


Figure 4.6: Comparison of mean concentration of resorufin remaining  $\pm$  SD comparing different flow rates and devices. Dotted line represents concentration of resorufin added to the device (100  $\mu$ M). An ANOVA with Bonferroni corrections was conducted; no significance difference was found between these parameters.

As this data obtained showed no significant difference was found when comparing parallel and serpentine devices, continuing to use the parallel device at 0.5  $\mu$ L min<sup>-1</sup> was decided. As upon collecting this data the use of the serpentine devices yielded multiple problems that hindered its general use. Most notable, this included blocking due to its much thinner channel width and bubbles causing pressure and preventing flow. This was due to the increased chances of blocking in the serpentine devices due to a single thinner channel which APTMS functionalisation further reduces. A flow rate of 1  $\mu$ L min<sup>-1</sup> was also tested, however in both serpentine and parallel devices, the PTFE tubing was detached from the capillary due to the increased backpressure.

Alongside this, the parallel device also yields a much higher surface area to volume ratio (section 2.2), allowing more potential immobilised enzyme per substrate within the device at any given time. Taken together flowing through the microfluidic device at  $1 \mu\text{L min}^{-1}$  at  $30 \text{ }^\circ\text{C}$  provides the optimum conditions to yield the highest conversion and overall product formation.

### Effect of temperature on resorufin metabolism

The previous experiments were undertaken at room temperature (controlled at approximately  $20 \pm 2 \text{ }^\circ\text{C}$  with an automated setting). As enzymatic reactions are well described to have a tightly controlled temperature dependency, the overall activity of the device may be further increased by increasing the reaction temperature towards physiological conditions ( $37 \text{ }^\circ\text{C}$ , Figure 4.7).

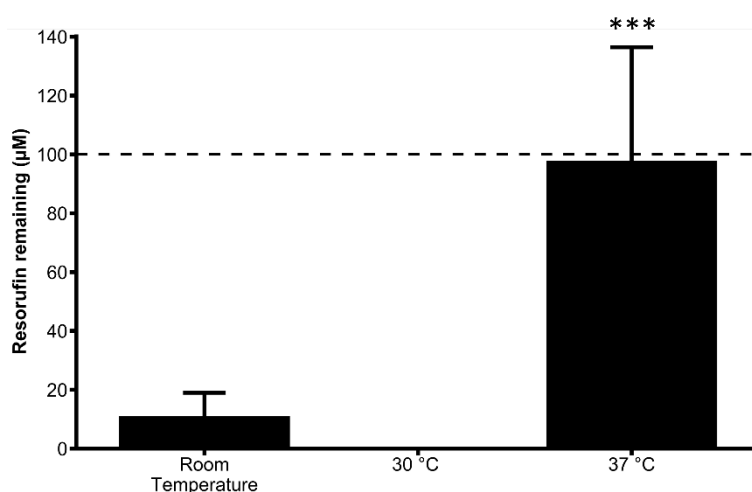


Figure 4.7: Comparison between mean concentration of resorufin remaining  $\pm$  SD between varying temperatures using the parallel device at  $0.5 \mu\text{L min}^{-1}$ . Dotted line represents concentration of resorufin added to the device ( $100 \mu\text{M}$ ). An ANOVA with Bonferroni corrections comparing the three different temperatures. \*\*\*,  $p = >0.0001$ ,  $n=3$ .

Due to the minimal amount of resorufin remaining the  $30 \text{ }^\circ\text{C}$  bar is not visible with only  $0.012 \pm 0.020 \mu\text{M}$  remaining. When compared to room temperature which was

monitored throughout the day using a thermometer ( $21 \pm 2$  °C) no significant difference was found between room temperature and 30 °C. However, 37 °C shows a significantly higher amount of resorufin remaining which equates to minimal formation of product. Due to the complicated setup of the device at 30 °C, room temperature was continued for subsequent experiments as there was no significant difference between the two temperatures. However, the optimal temperature would be 30 °C.

The next step was to compare the current microfluidic devices to one of the gold standard methods frequently used in literature, conducting the experiment without immobilising in static conditions.

### Static vs. Flow

A comparison between a static method, shown in 2.4 and the flow-through method optimised throughout this chapter was made to determine if the microfluidic flow-through method provided benefits over the static method in terms of product yielded (Figure 4.8).

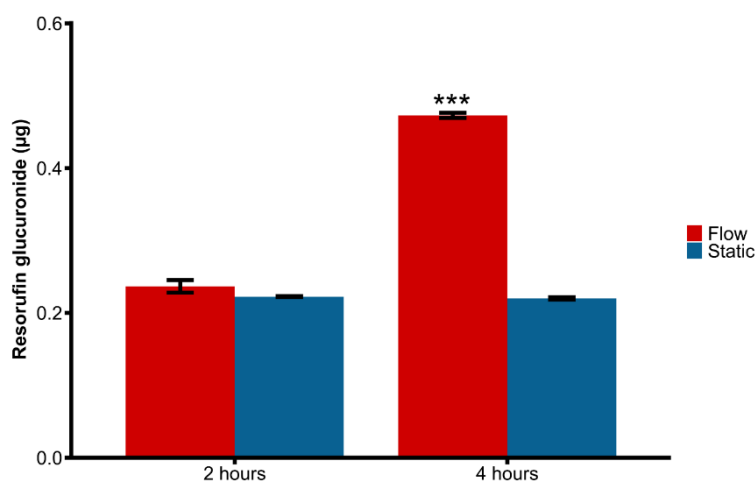


Figure 4.8: Potential resorufin glucuronide formed  $\pm$  SD based on fluorescence lost comparing batch vs. flow conditions. An ANOVA with Bonferroni corrections comparing the reaction time and devices. \*\*\*,  $p > 0.0001$ ,  $n = 3$ .

To allow for a comparison between the two methods converting the amount formed from concentration to mass (g) was necessary. This was calculated by utilising the yield measured from fluorimetry ( $\text{mol L}^{-1}$ ) and using the volume (L) collected and the molecular weight of resorufin glucuronide ( $\text{g mol}^{-1}$ ). Due to this it was necessary to assume a loss in fluorescence was directly related to conversion. So, if no resorufin was measured, 100% conversion was assumed.

Upon comparing both flow and static experiments, flow being the microfluidic device and static being an in-solution experiment; it was shown that the same overall amount of resorufin was converted over a 2-hour period. However, the reaction in batch conditions seemed to plateau after these two hours, leading to no additional product formation. Whereas the flow-through approach demonstrated continuous production of product across 4 hours yielding significantly more product than the static reactions.

## **Product confirmation**

After conducting the optimisation of the microfluidic parameters, it was important to prove that the loss of fluorescence that was being measured was in fact due to the formation of resorufin glucuronide and not any external factors or the production of alternative metabolites. It was decided that LC-TQ-MS would be the optimal method to prove product formation due to the sensitivity of the technique, and the low volume of sample formed from a single use of the microfluidic device.

Due to the large number of scans utilised, only the MRM scans for both resorufin and resorufin glucuronide are shown in Figure 4.9 for simplicity. Other HPLC chromatograms conducted and comparing resorufin standard (100  $\mu$ M) against DI water injections are shown within appendix Figure 0.1-Figure 0.11 for resorufin and their respective mass spectrum in appendix Figure 0.12-Figure 0.15. Additional resorufin glucuronide HPLC chromatograms shown in appendix Figure 0.16-Figure 0.21 and their respective mass spectrum in appendix Figure 0.22-Figure 0.25.

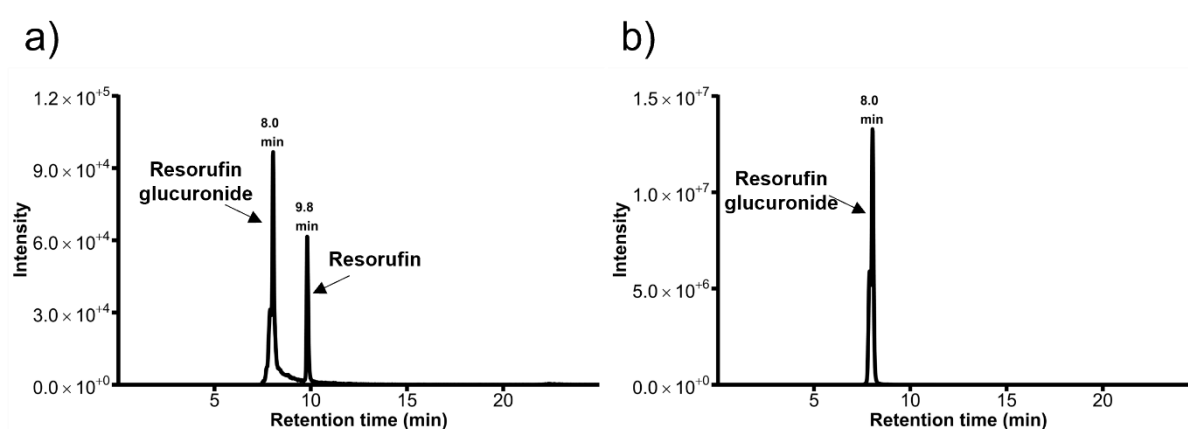


Figure 4.9: Representative MRM scans of resorufin glucuronide utilising the methods previously optimised in the section titled Gradient HPLC separation of resorufin and resorufin glucuronide. (a) MRM scan to measure resorufin (212>155 m/z) and (b) resorufin (388>212 m/z).

The MRM scan at 212>155 m/z (Figure 4.9a) optimised for the analysis of resorufin show that resorufin (9.8 min) and resorufin glucuronide (8.0 min) are both visible in the analysis of the resorufin glucuronide standard. This could be due to degradation of the resorufin glucuronide standard into resorufin prior to analysis. Whereas solely the resorufin glucuronide is seen at 388>212 m/z (Figure 4.9b). Due to the large difference in retention times and only the glucuronidic product being visible in one scan, a proof of metabolic product confirmation can be observed utilising this scan. Injecting the sample collected from the outlet of the device was the next step to confirm product formation within the device.

### Sample direct implementation

An effluent from the enzyme immobilised device was injected with no dilution to determine if any product had been formed/ could be measured (Figure 4.10).

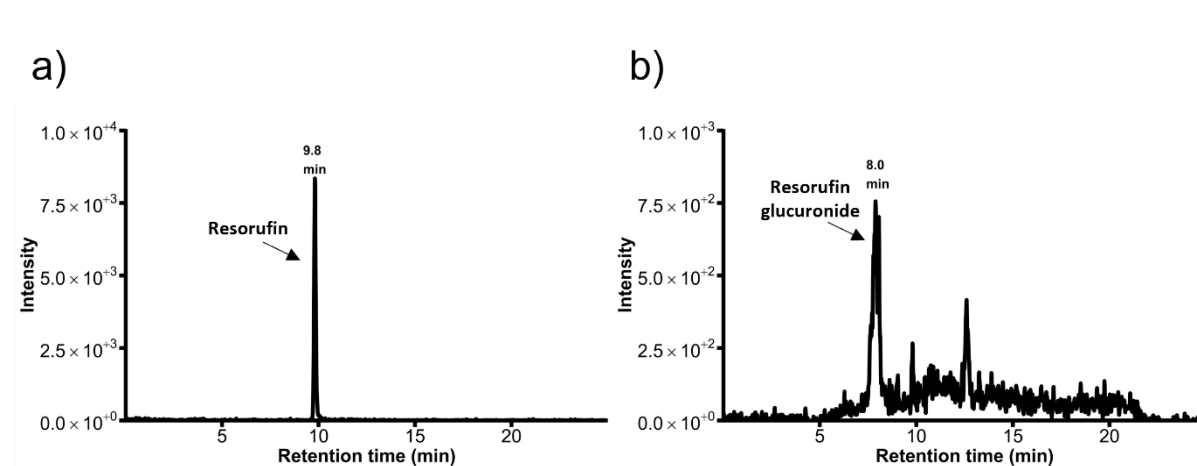


Figure 4.10: HPLC chromatograms of a collected effluent using MRM scan at (a)  $212 > 155$  m/z and at (b)  $388 > 212$  m/z.

The expected amount of product formed within the device was approximately 95% due to the loss of fluorescent measurements which should yield a peak comparable to Figure 4.9. However contrarily a very small peak for resorufin glucuronide at  $388 > 212$  m/z (Figure 4.10a) was observed which was almost at background level. A very small peak for resorufin at  $212 > 155$  m/z (Figure 4.10b). Due to both peaks being smaller in their respective scans it showed that either something completely unrelated was happening and not visible in the scans conducted or a matrix interference preventing the product/substrate from being measured by the detector. To determine if there was a matrix interference spiking a collected effluent with the equivalent concentration of the expected product formation ( $100 \mu\text{M}$ ).

## Sample spiking

Samples were spiked with the equivalent amount of resorufin glucuronide resulting in a final concentration of 100  $\mu\text{M}$  assuming no resorufin glucuronide was formed throughout the flow through (Figure 4.11).

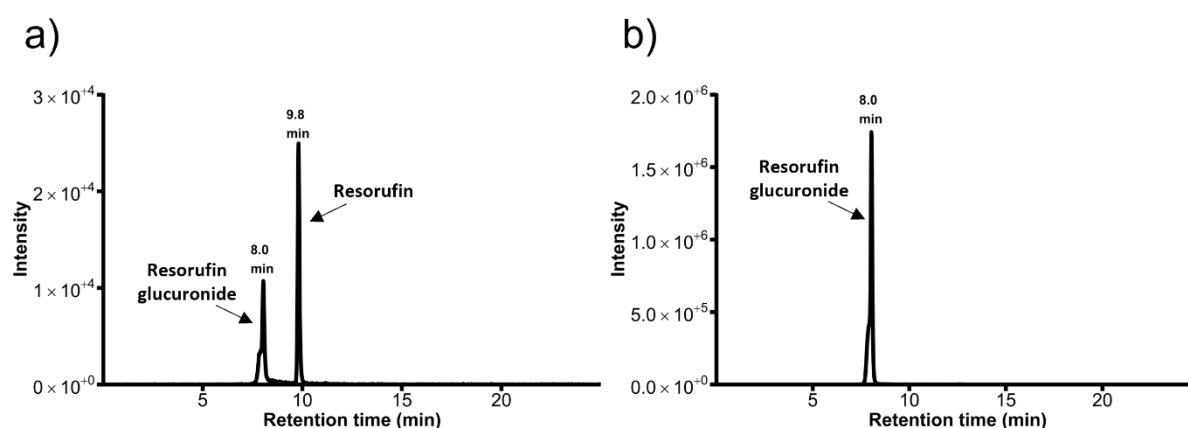


Figure 4.11: HPLC chromatograms of a sample spiked with resorufin glucuronide to the equivalent of 100  $\mu\text{M}$  resorufin glucuronide with (a) an MRM at 212>155 m/z and (b) at 388>212 m/z.

Upon spiking with the equivalent concentration of 100  $\mu\text{M}$  the samples were analysed *via* the same method as those previously. As theorised previously both spectrum at 212>155 m/z and 388>212 m/z (Figure 4.11a-b) for resorufin glucuronide (8.0 min) yielded approximately a 10-fold lower intensity than the standard prior to spiking (Figure 4.9). This showed that the matrix was having a significant effect on the measurement of any products formed within the device. Furthermore, as the peak intensity for resorufin is larger than the peak for resorufin glucuronide is shows that this interference is affecting its measurement more than that of resorufin (9.8 min), as

this is not comparable to what was observed in the standard measurements (Figure 4.9a).

Due to the standards being in MilliQ water and the samples containing both phosphate buffer and UDP-GA, the next step was the addition of these into the standard to determine if this was influencing the measured intensity.

### *Addition of matrix to standard*

The equivalent concentration of both phosphate buffer and UDP-GA were added to the resorufin glucuronide standards, resorufin glucuronide (100  $\mu$ M), UDP-GA (100  $\mu$ M) of phosphate buffer (0.1 M, pH 7.4) and was injected using the same method mentioned previously (Figure 4.12).

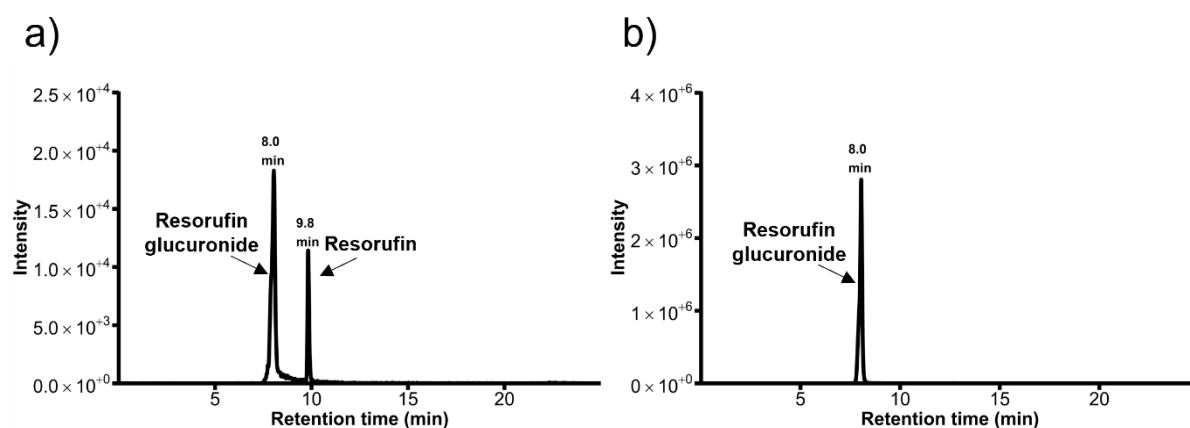


Figure 4.12: HPLC chromatograms of a standard and matrix with an MRM at (a) 212>155  $m/z$  and (b) at 388>212  $m/z$ .

The chromatograms obtained showed that the interfering matrix was created by either the buffer or the co-factor UDP-GA, as when compared to water only (Figure 4.9) as a large loss of intensity was observed. However, this was not comparable to that which

was observed in the effluent collected from the device meaning that there are multiple causes for the lack of measurable resorufin and resorufin glucuronide. The next step was to extract any potential protein from the sample as the enzyme covalent bond to the device may weaken throughout the reaction as it is liable to hydrolysis.

### *Methanol crash*

Methanol crash is a method utilised throughout literature for the extraction of protein from an aqueous based solution by denaturing its structure and causes the hydrophobic core to be exposed.<sup>285</sup> This causes the protein to become insoluble in the chosen solvent an aggregate of precipitated protein is subsequently formed. Then upon centrifugation proteins are settled allowing for the removal of the supernatant. It was determined that a methanol crash would be viable for the extraction of protein from the effluent if it had undergone hydrolysis and effectively removed from the device. This was conducted on a 100  $\mu\text{M}$  resorufin glucuronide standard (Figure 4.13) and a sample collected from the microfluidic device (Figure 4.14).

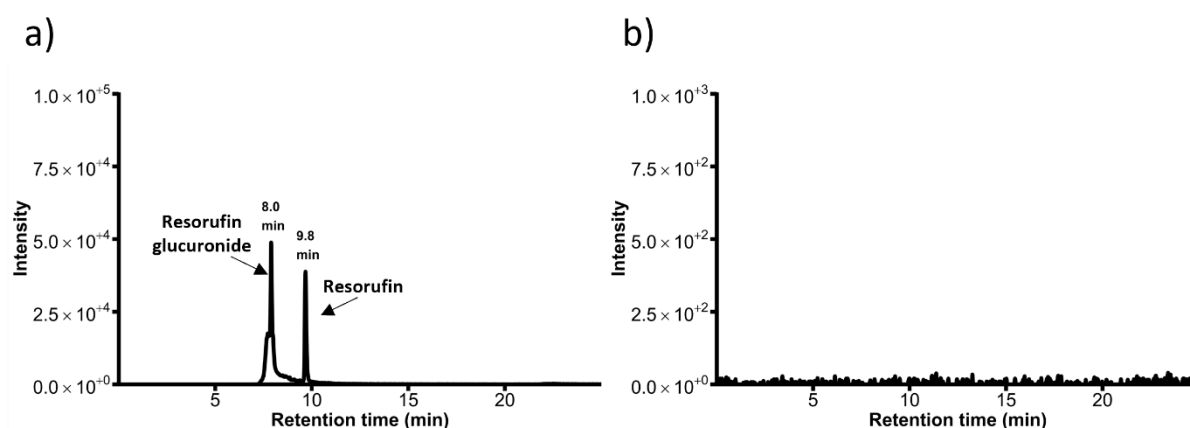


Figure 4.13: HPLC chromatograms of a resorufin glucuronide standard post methanol crash with an MRM scan at (a) 212 > 155 m/z and (b) 388 > 212 m/z.

The MRM scan of standard post methanol crash in Figure 4.13a set to 212>155 m/z yielded a peak for both resorufin (9.8 min) and resorufin glucuronide (8.0 min). Surprisingly no peak was found in the resorufin glucuronide optimised MRM fragmentation in Figure 4.13b (388>212 m/z). In order to prove that resorufin glucuronide was formed, ideally a peak would be found in both MRM spectrums to show that both resorufin and resorufin glucuronide were within the same device assuming less than 100% conversion. If the peak for resorufin glucuronide is not visible in the optimised scan at 388>212 m/z, then this could be due to another compound within the solution. However, regardless of this a test was conducted with the sample to determine if a large peak for the product could be found.

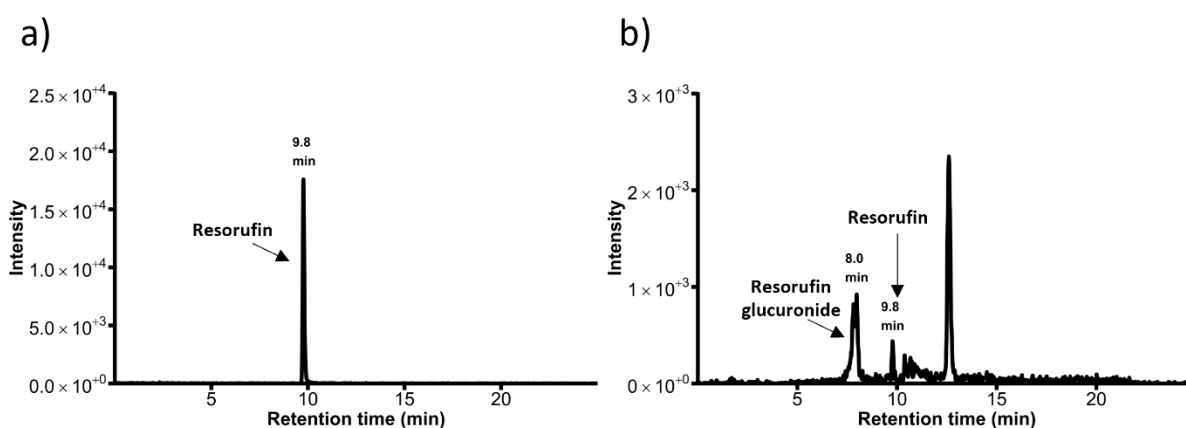


Figure 4.14: HPLC chromatograms of a sample extracted from device post methanol crash with an MRM at (a) 212>155 m/z and (b) at 388>212 m/z.

Comparably to the previous scan of a standard at 212>155 m/z (Figure 4.13a) a similar sized peak of resorufin was observed at 9.8 min however the peak for resorufin glucuronide at 8.0 min upon undergoing methanol crash on a sample (Figure 4.14a) it was not seen which is contrary to that of the standard. However in this case a very small peak for the resorufin glucuronide product (8.0 min) was seen in the MRM scan at 388>212 m/z (Figure 4.14b) which is also contrary to that which was observed in

this standard analysis in which a peak was not seen (Figure 4.13b). These observed peaks were smaller in size than those that were deemed too small for proof of product in the direct analysis, so it was decided to attempt alternative extraction methods.

### *Liquid-liquid extraction (LLE)*

One of the two different extraction techniques tested was LLE. The goal was to separate out the potential matrix causing the observed effect from the sample. The tested solvents were 4% ammonium hydroxide and ethyl acetate. These samples were then extracted into methanol and injected into the LC-TQ-MS using the optimised method (Figure 4.15).

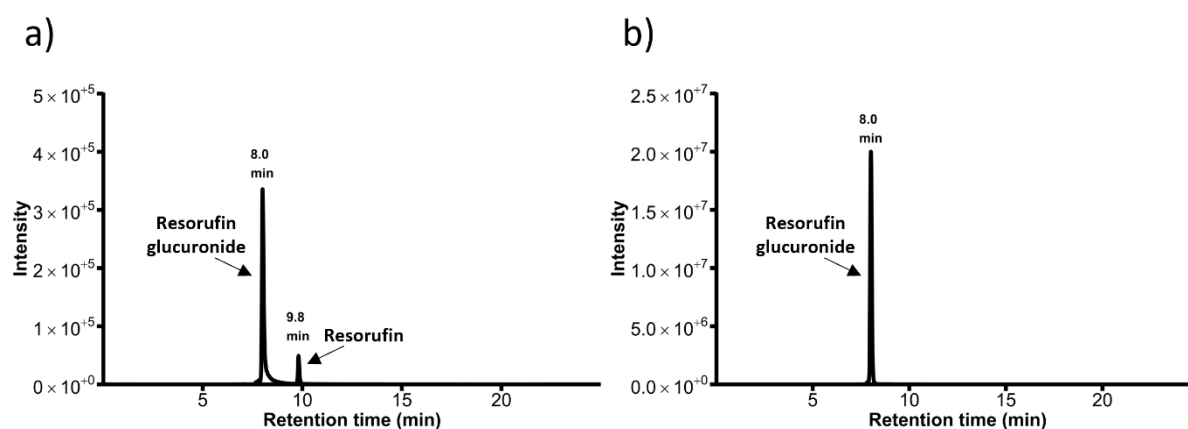


Figure 4.15: HPLC chromatograms of a resorufin glucuronide standard extracted via LLE with an MRM at (a) 212>155 m/z and at (b) 388>212 m/z.

Large and intense peaks were observed for both resorufin (9.8 min) and resorufin glucuronide (8.0 min) in the MRM scan at 212>155 m/z (Figure 4.15a). Alongside this resorufin glucuronide yielded a peak comparable to that of the standards that were implemented directly prior to any extractions or buffer additions (Figure 4.9b)

Due to the high intense peaks observed under this extraction, a sample was subjected to the same conditions. However, when implemented within the immiscible solution it

was noted that the pale orange colour of the sample was found throughout both layers showing that likely no separation was occurring, which was not comparable to the standard in which the collected layer was visibly orange due to the resorufin glucuronide. This was further shown by implementing the sample within the LC-TQ-MS and no peaks were found.

### *C18 zip tips*

The other extraction method tested was C18 zip tips. These were conducted by wetting the zip tip by pipetting 10  $\mu$ L of MilliQ water. The tip was then equilibrated using 50% methanol in MilliQ water and then washed further with MilliQ water. Then the resorufin glucuronide standard was aspirated within the tip 10 times and removed. MilliQ water was then pipetted and removed. Methanol was then pipetted and removed into a sample vial. This was then injected into the LC-TQ-MS (Figure 4.16)

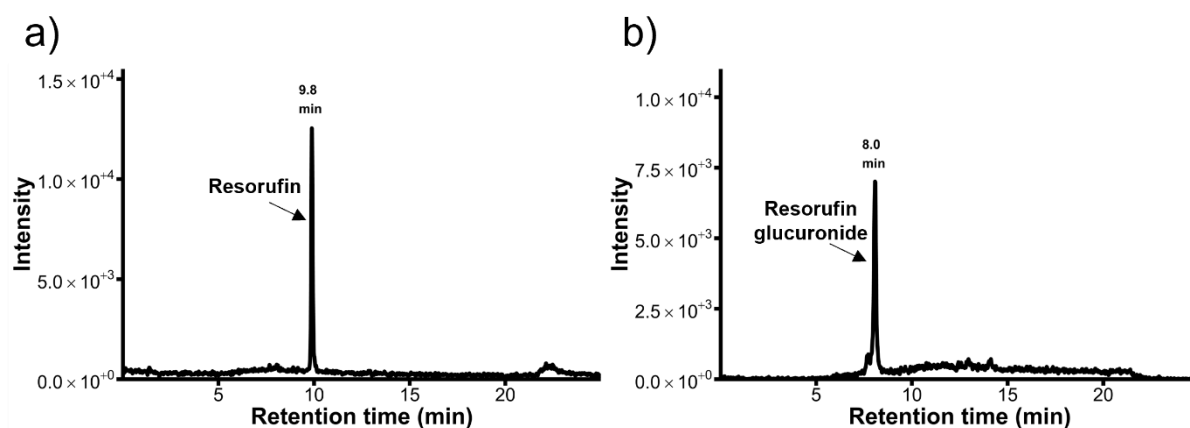


Figure 4.16: HPLC chromatograms of resorufin glucuronide incubated and extracted via C18 zip tips with an MRM scan at (a) 212>155  $m/z$  and at (b) 388>212  $m/z$ .

Upon analysing this sample *via* LC-TQ-MS a small peak comparable to the previous standards deemed too small were observed for both resorufin (212>155  $m/z$ , 9.8 min, Figure 4.16a) and resorufin glucuronide (388>212  $m/z$ , 8.0 min, Figure 4.16b). It was

noted that due to the also highly hydrophilic nature of resorufin glucuronide the standard was potentially not entering the pores of the C18 tip sufficiently and being flushed out when rinsed with water. Due to this it was theorised that after aspirating the sample within the tip it could be left incubating for an extended period (10 min).

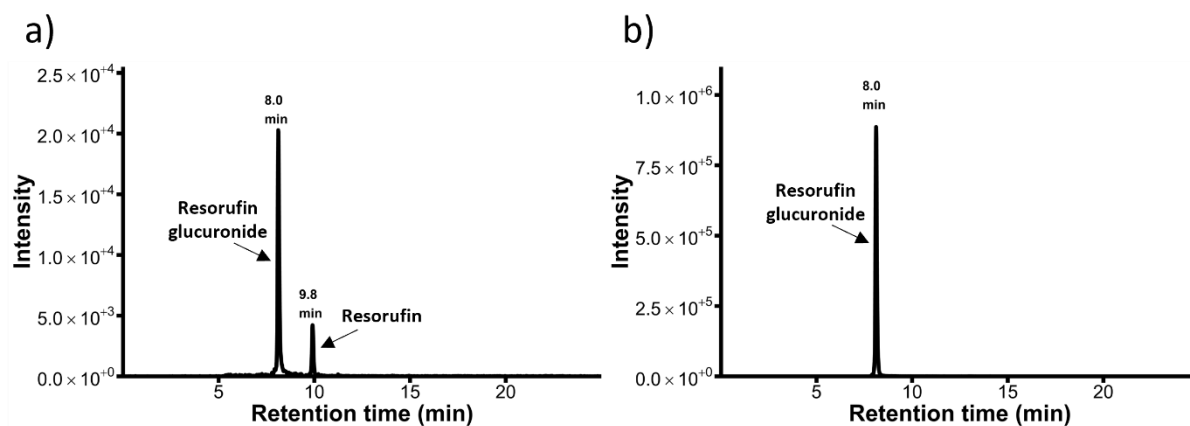


Figure 4.17: HPLC chromatogram of resorufin glucuronide standard after being incubated within a c18 ZipTip for 10 min and then extracted using an MRM scan set to (a) 212>155 m/z and (b) 388>212 m/z.

When comparing these standards to those of the initial direct injection of standard (Figure 4.9) at 100  $\mu$ M approximately 10% of the peak height was retained for both resorufin at 9.8 minutes (212>155 m/z, Figure 4.17a) and resorufin glucuronide and 8.0 minutes (388>212 m/z, Figure 4.17b). However, the peak for resorufin glucuronide was 100x higher than the low values measured previously. Due to this extracting the sample using the ZipTips was conducted to determine if product could be measured in the samples after potentially undergoing metabolism within the device (Figure 4.18).

Additional HPLC chromatograms shown in appendix

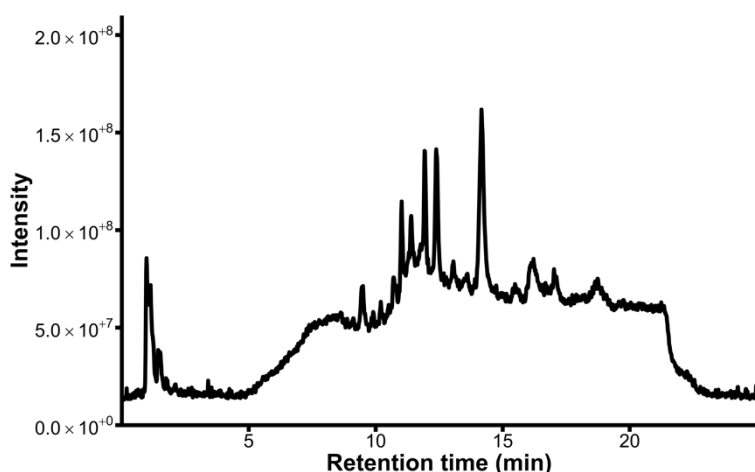


Figure 0.26 Figure 0.29 and their respective mass spectrum in appendix Figure 0.30- Figure 0.34.

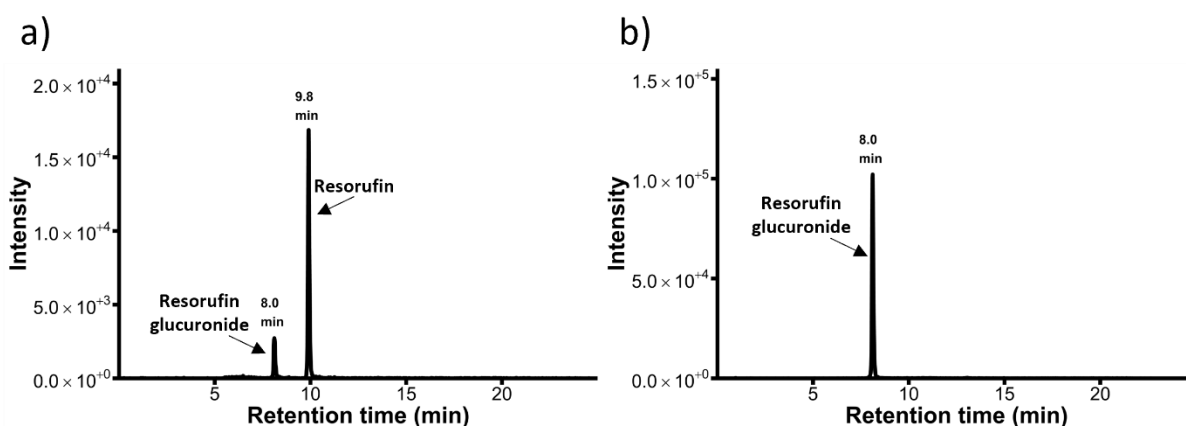


Figure 4.18: HPLC chromatogram of a sample after being incubated within a c18 ZipTip for 10 minutes and then extracted using an MRM scan set to (a) 212>155 m/z and (b) 388>212 m/z.

The retention times of both resorufin (212>155 m/z, 9.8 min, Figure 4.18a) and resorufin glucuronide (388>212 m/z, 8.0 min, Figure 4.18b) match those of the optimised standards (Figure 4.9). Although the peak heights of these compounds are not comparable to those of the pure standard, this could likely be due to the unoptimized extraction method utilised for their analysis. Despite this the motivation of this experiment was to allow for qualitative proof that the reactor could produce

metabolic products. Alongside this scan a product ion scan was conducted to further prove that the product formed was indeed resorufin glucuronide.

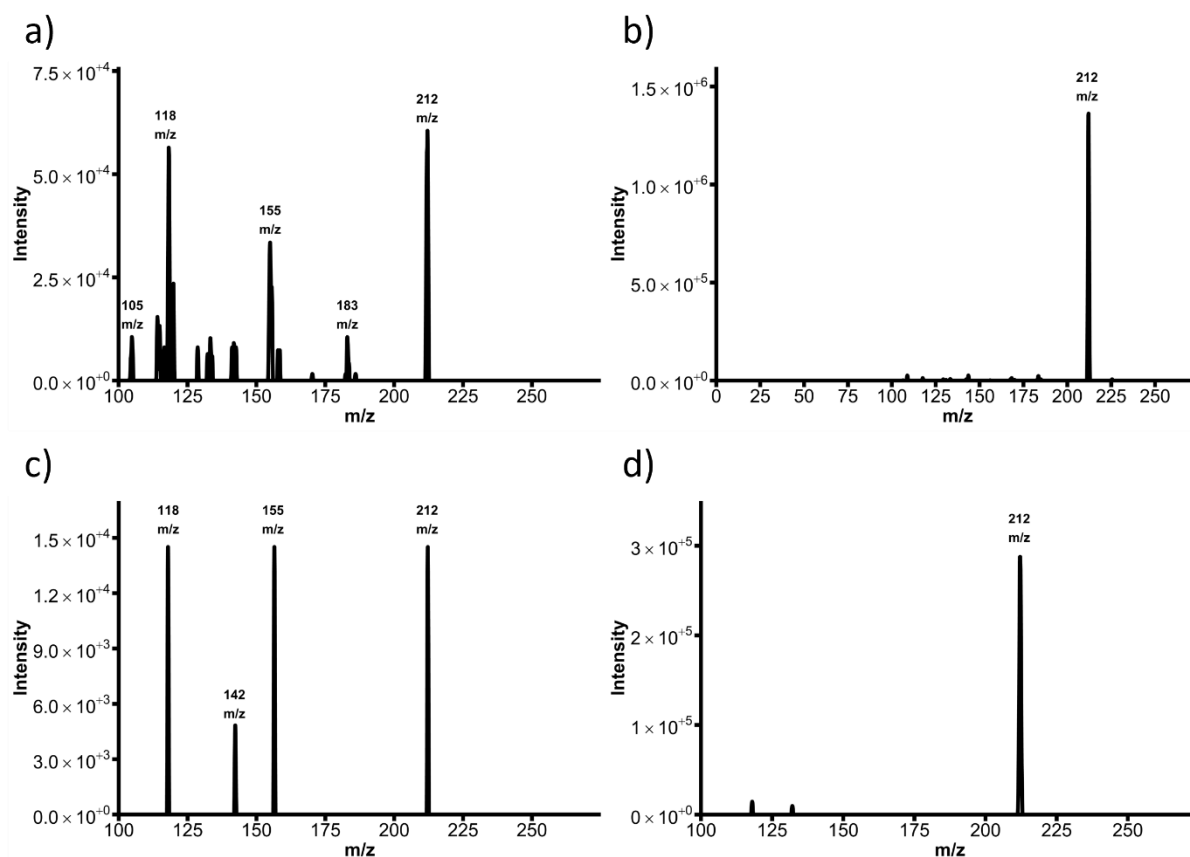


Figure 4.19 Mass spectrum of resorufin glucuronide standard for the area under the curve at 8.0 min utilising a product ion scan set at (a) 212 m/z and at (b) 388 m/z and (c) an effluent sample under the curve at 8.0 min utilising a product ion scan at 212 m/z and (d) 388 m/z.

When comparing the product ion scans at 212 m/z (a&c) and 388 m/z (b&d) for the area under the curve at 8.0 minutes the major peaks in both scans contain the exact same major peaks with 212, 155 and 118 m/z for the product ion scan set to 212 m/z and 212 m/z for the product ion scan set to 388.

The fragments observed in this sample were comparable to those for both resorufin (Figure 4.19a&c) and resorufin glucuronide standards (Figure 4.19b&d), showing the

same fragmentations and proving that the product is indeed formed within the device when both the correct co-factor and enzyme are contained within the microfluidic device simultaneously.

#### **4.4. Discussion**

The aim of this chapter was to optimise a method for the synthesis of naturally circulating metabolites using the enzyme UGT1a1. Specifically focusing on making a largely converted product bypassing the previous issues with current synthetic methods.

Two different microfluidic devices were optimised and tested, one device being the parallel device and the other being the serpentine device shown in 2.2a and 2.2b respectively. A variety of different parameters were tested in both devices. Including flow rate, temperature, and batch vs. flow.

#### **Optimisation of enzymatic reactor**

A variety of different blank devices were compared to the enzymatic run including incubating with UGT but not including UDP-GA within the device, incubating without UGT but including UDP-GA and finally incubating an alternative enzyme (TPI) and including UDP-GA. No loss of resorufin was measured when only the correct co-factor, enzyme or an alternative enzyme were found within the device. Which is comparable to previous studies have shown that when either the UGT enzyme or the co-factor (UDPGA) is not included within a system no conjugation will be measured (Kawase *et al.*, Ghosal *et al.*, Nardone-White *et al.*).<sup>286-288</sup> However,  $0.12 \mu\text{g h}^{-1}$  was found within

the device when both the correct cofactor and enzyme were available within the system at  $0.1 \mu\text{L min}^{-1}$ , the equivalent of ~95% conversion at the flow rate used.

The flow rate of substrate and co-factor combined was varied using the syringe pump, allowing for the variation in residence time (Figure 4.6). No significant difference was found between the flow rates compared. However, an increase in backpressure at the higher flow rate ( $1 \mu\text{L min}^{-1}$ ) was observed as it was noted that in some devices the tubing removed from the capillary it was attached to. This was likely due to the reduced volume available upon silanising the surface of the glass. Typically, the longer incubation times would allow for more product formation if a maxima of enzyme capacity was not reached. Due to the decrease in incubation times not having a significant difference on the yield on the three flow rates, it was likely that providing a way to bypass the backpressure issue an increase in flow rate would allow for more overall product to be formed and that the optimum flow rate was not fully discovered due to this drawback.

Alongside this comparison two different device structures were tested, a parallel device (shown in 2.2a) and a serpentine device (shown in 2.2b). It was also that there was no significant difference in resorufin glucuronide formation between the serpentine and parallel device. The serpentine device had a much lower surface area to volume ratio in comparison to the parallel device (detailed in section 2.2), which when typically increased would also yield an increase in overall product formed (Kim *et al.*).<sup>289</sup> The main problem with the serpentine was the device was much more prone to blockages upon silanising the device. This showed that even though the parallel device did not provide a significantly higher conversion, it was much more viable for the immobilism of the UGT1a1 microsomes. Although these two design types were tested there were multiple other designs that may have provided equivalent surface

area to volume ratio, alongside potentially bypassing the back pressure issue including packed bead beds (Choi *et al.*)<sup>281</sup> and porous polymer monoliths (Peterson *et al.*)<sup>202,</sup>

290

Due to the temperature sensitive nature enzymes typically providing increased activity upon heating until their denature point, at which it will rapidly decrease. The majority of human enzymes, UGT1a1 included, work optimally at physiological temperature (37 °C). Three different temperatures were measured room temperature (controlled at approximately  $20 \pm 2$  °C *via* an automated setting), 30 and 37 °C. Contrary to that which was expected 37 °C provided almost no loss of fluorescence at all. Whereas 30 °C provided almost 100% conversion. This may be due to the structural changes of the enzyme upon immobilising. It has previously been observed that immobilising an enzyme can alter its fundamental properties. For example, Mazlan *et al.* found that laccase's optimum temperature shifts from 40 °C to 50 °C.<sup>291</sup> Further studies have shown similar results that upon immobilising the enzyme can have an effect on its fundamental properties.<sup>292-296</sup> Although these typically show an increase, no studies to the Authors' knowledge have been conducted on immobilised conjugative enzymes which may provide a lower temperature stability allowing them to be used more effectively at room temperature.

A commonly used method throughout literature is incubating the microsomes directly with the substrate and co-factor within a solution; typically used for metabolite determination. Upon conducting both of these experiments, a 2-hour runtime showed no significant difference in amount of resorufin glucuronide formed was found between the batch and flow-through method. However, this precludes the need for separation

between the enzyme, co-factor, buffer and the product. Whilst bypassing the major drawback to incubation methods, where in some cases the products inhibit the enzyme preventing further metabolite formation (Fujiwara *et al.*, Nasrin *et al.*, Lv *et al.*).<sup>297-299</sup> To further show the improvement this setup provides, the experiments were conducted over a longer period of time. This showed that in the batch setup no significant difference was found upon collecting for 4 h compared to 2 h of the flow-through. The flow-through 4-hour collection combined with the 2-hour collection due to consistent running and effluent collection showed approximately double the product formed. This shows potential for use in a continuous system which may have commercial applications, such as allowing for the synthesis of a usable quantity of product for further pharmacological studies.

Analysis of samples post metabolism using the method optimised in sections 2.6 and 3.4 and identified resorufin (212>155 m/z, retention time 9.8 min) and resorufin glucuronide (388>212 m/z, retention time 8.0 min). This demonstrated the formation of resorufin glucuronide only when both the correct co-factor and substrate are available within the system.

In summary, all of the currently used methods are viable for the determination of metabolites formed *in vivo*. However, out of these mentioned none allow for the synthesis of a concentrated product without the need for a complex separation. The method developed throughout this chapter could potentially allow for the synthesis of metabolites as shown in the mass spectrometry section, without any significant matrix removal. Despite this there was an extraction of phosphate buffer that caused issues. However, this was simply extractable utilising C18 zip tips. These are readily extractable *via* variety of methods and would largely be applicable for a wide variety

of substrates without the need for much more optimisation. The next step would be to optimise a more effective extraction method as roughly 50% of the substrate and product were retained and then to quantify *via* mass spectrometry to develop a true measurement of product.

The limitation of this work is due to the drawbacks from increased flow rates causing large amounts of backpressure preventing a potentially much larger amount of metabolite formation. These could be overcome by either altering the design of the device which may also reduce the product formed due to the effect on the surface area to volume ratio, or by scaling up the number of devices and utilising the currently optimised device and flow rates. Ultimately the major limitation of this work is the assumption that a loss of fluorescence is roughly equal to the overall amount of product formed. Although product formation has been confirmed it is not currently known whether the 95% loss of fluorescence is due to complete metabolism of substrate. Another limitation of this work is due to the lack of knowledge on the actual immobilisation of the enzyme itself and catalytic activity has been used as a determination of device functionality.

#### **4.5. Conclusion**

The aim of this chapter was to develop and optimise a method allowing for the synthesis of naturally circulating metabolites. Two different device structures were tested with a variety of different parameters *i.e.*, flow rate and temperature whilst comparing to one of the currently used methods incubating enzyme co-factor and substrate under optimum conditions.

This chapter showed that when comparing this method to one of the gold standard methods for metabolite synthesis over a comparable amount of time (4-hours), more

product is formed alongside avoiding the need of a complex separation that needs the extraction of a variety of different products from a biological matrix.

In the following chapters, two other enzymes were optimised (SULT1a1 and CYP1a1) to utilise a similar method allowing for the synthesis of both oxidised and glucuronide conjugated metabolites that also naturally occur *in vivo*.

# 5. Optimisation of a method for the synthesis of naturally occurring metabolites using SULT1a1

## 5.1. Introduction

Sulfation is also one of the common elimination pathways for xenobiotics *via* the addition of a sulfate group onto small non-polar compounds utilising the co-factor PAPS, facilitating easier excretion *via* the kidneys in urine.<sup>300</sup> A sulfated compound may have significantly different therapeutic and toxicological effects from their respective precursors.<sup>301</sup> Xenobiotics that undergo sulfation are typically non-toxic, however this is not always the case. Paracetamol can undergo metabolism within the body *via* glucuronidation and sulfation. Upon being sulfated, paracetamol can deplete the body of available sulfates even at therapeutic levels potentially leading to an alternative more toxic metabolic pathway being followed.<sup>23</sup> Thus, understanding the effects xenobiotics can have prior to entering the body is necessary. Currently testing these pharmaceutically relevant xenobiotics is difficult due to a lack in availability of standards or synthetic methods.

The current methods for synthesising sulfated metabolites *in vitro* are the same as those mentioned in section 1.3; incubating s9 fractions, liver cell incubations, bacteria overexpressing the enzyme and computer simulations. These synthetic methods are usually optimised for the determination of products formed rather than a synthesis of

a singular bulk product. Currently there is no synthetic method available that will allow for the synthesis of xenobiotics that potentially yield pharmaceutical beneficially or toxicological effects in quantities that allows for further testing simply. For example, determination of a metabolites anti-tumour or antioxidative effects.

Microfluidic devices have already been applied for the immobilisation of enzymes and the synthesis of sulfate substituted metabolites. Baudoin *et al.* (2014)<sup>302</sup> conducted a study using a biochip platform, and primary hepatocytes that were incubated within the device. The device they have derived a utilised the parallelisation of 12 different microfluidic devices allowing for the variation and testing of multiple parameters simultaneously, Prior to incubating, seven different test compounds were flowed through the device individually one of which being the previously mentioned paracetamol. The formation of paracetamol sulfate was noted demonstrating merit in combining both microfluidics and enzymatic catalysis, allowing for the synthesis of sulfated metabolites as mentioned above.<sup>302</sup>

In this chapter the development and optimisation of a method for the synthesis of metabolites *via* sulfation reactions naturally occurring in the human body will be described. In which will include: optimisation of flow rate reaction temperature and then comparing against optimal batch conditions frequently utilised in the wider literature. Initial, biocatalysis was studied by fluorometric analysis in which the initial substrate was fluorescent and product confirmation was determined using LC-TQ-MS techniques.

## **5.2. Experimental procedure**

### **Microplate reader method**

A calibration curve for resorufin was created by serial dilution of an initial concentration of 100  $\mu\text{M}$ . The dilution was carried out sixteen times by half in a V-shaped 96-well microplate (STARLAB). Fluorescence intensity was measured using a microplate reader set to 544 nm ( $\lambda_{\text{ex}}$ ) and 590 nm ( $\lambda_{\text{em}}$ ) as optimised in the Calibration curve for resorufin section of chapter 4.3.

### **Fabrication of microfluidic devices**

Two different device structures were fabricated using The HF etching method described in section 2.2.

### **Immobilisation of SULT1a1 supersomes**

The immobilisation technique described in both section 2.3 was followed. However due to the concentration of enzyme available for purchase the initial concentration of enzyme was lowered to 10  $\text{ng mL}^{-1}$

### **Metabolism of test substrates**

Due to the cross reactivity with resorufin between both UGT and SULT enzymes the same method as described in section 2.3 was followed.

## Mass spectrometry

Using the effluents from reactor, in the presence and absence of appropriate cofactor, *p*-nitrophenyl sulfate was measured *via* LC-MS. Effluents were directly injected within the LC-TQ-MS as per the method described in section 2.6. A product ion scan in negative mode was used for product confirmation of *p*-nitrophenyl sulfate with an *m/z* of 218, respectively. Alongside this, the multiple reaction mode (MRM) was used for further confirmation with selected transitions of 218→138 *m/z*.

## 5.3. Results

### Comparison between controls and experimental enzymatic run

Prior to any optimisation steps the determination of device functionality was required. A true run was conducted consisting of immobilising SULT1a1 enzyme overnight and both resorufin and PAPS were flowed through the device. The three different controls consisted of not immobilising the enzyme (SULT1a1) but flowing co-factor and resorufin through the device, immobilising the enzyme and only flowing resorufin through and immobilising an alternative enzyme (TPI) and flowing both resorufin and co-factor through the device using the previously optimised method from section 2.3, the remaining concentration of resorufin was measured (Figure 5.1). Throughout this section unless stated otherwise concentration of resorufin was determined using a calibration curve utilising the fluorometric method described in section 2.5. A new calibration curve alongside each set of samples when analysed.

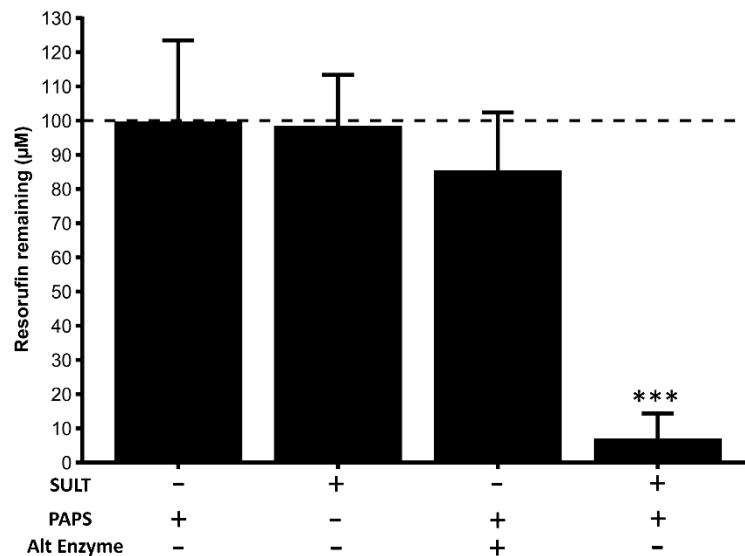


Figure 5.1: Comparison showing mean concentration of resorufin remaining  $\pm$  SD post flowing through the device between different blanks and a true enzymatic run. Dotted line represents concentration of resorufin flowed through the devices. All bars have been conducted using an  $n=3$ . Statistics performed by ANOVA with Bonferroni corrections, comparing each control to true run, \*\*\*  $p > 0.0001$ .

This data within Figure 5.1 shows that no fluorescence was lost when either the correct co-factor or enzyme were not available within the system. Showing that that enzymatic activity was only detected when both the correct co-factor and correct enzyme are available within the microfluidic device simultaneously resulting in a loss of fluorescence equating to  $92.9 \pm 7.2\%$  (error calculated using standard deviation). Whereas each of the controls equated to  $0.3 \pm 23.7\%$  without enzyme,  $1.6 \pm 14.9\%$  whilst excluding co-factor and  $14.6 \pm 16.9\%$  using an alternative enzyme (TPI) and in the presence of co-factor.

### Comparison between devices and flow rates

The next step was to optimise the device being used. To do this a variety of different flow rates were tested in two different device types: a parallel and a serpentine device (Figure 5.2).

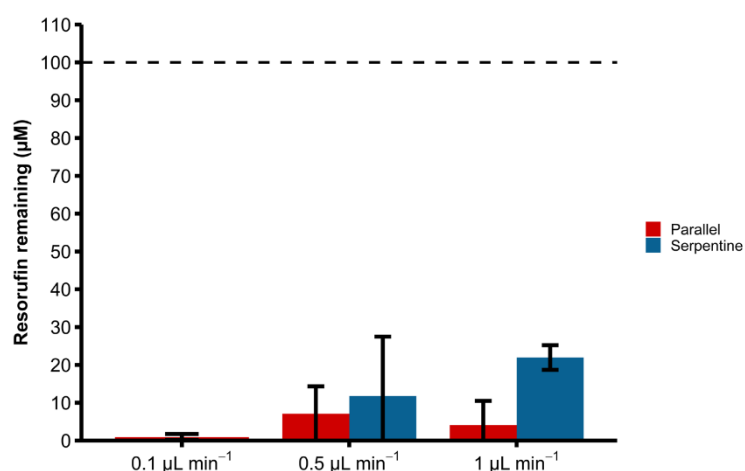


Figure 5.2: Comparison of mean resorufin remaining  $\pm$  SD comparing different flow rates and devices. Serpentine was not continued for  $1 \mu\text{L min}^{-1}$  due to consistent pressure and blocking issues. Dotted line represents concentration of resorufin flowed through the devices. An ANOVA with Bonferroni corrections was conducted,  $n=3$ ; no significance difference was found between these parameters.

Although no significant difference was found when comparing parallel and serpentine devices an average loss of  $88.2 \pm 15.7\%$  at  $0.5 \mu\text{L min}^{-1}$  and  $79.3 \pm 3.9\%$  at  $1 \mu\text{L min}^{-1}$  using the serpentine device but an average of  $95.9 \pm 6.4\%$  (Figure 5.2) was observed for the parallel device which is a further improvement than that which was measured in Figure 5.1 at  $0.5 \mu\text{L min}^{-1}$  of  $92.9 \pm 7.2\%$ . This data demonstrates that less overall resorufin is being lost within the serpentine device. Alongside this there was an increased chance of blocking in the serpentine devices at higher flow rates due to thinner channels. This was a limiting factor preventing more product formation over shorter periods of time at these faster flow rates. In rare cases the parallel devices also blocked upon silanisation for the development stage of this device to determine individual optimum parameters the flow rate of  $0.5 \mu\text{L min}^{-1}$  was continued. Alongside this due to the almost complete loss of fluorescence, any further optimisation would not be visible utilising this analysis technique due to its low amount of resorufin

remaining already. Upon optimising these devices, the flow rate of  $1 \mu\text{L min}^{-1}$  would be recommended due to the increase in potential product formation.

The next step was the comparison between different temperatures to determine if physiological relevant temperature ( $37^\circ\text{C}$ ) for the enzymes used provided an increase in activity.

### Comparison between temperatures

The previous experiments were conducted at room temperature. The overall activity may be further increased by changing the temperature to  $30^\circ\text{C}$  or physiological levels ( $37^\circ\text{C}$ ). These next steps were conducted at  $0.5 \mu\text{L min}^{-1}$  as it would allow for a determination of how much improvement in product formation the varying temperatures provided (Figure 5.3).

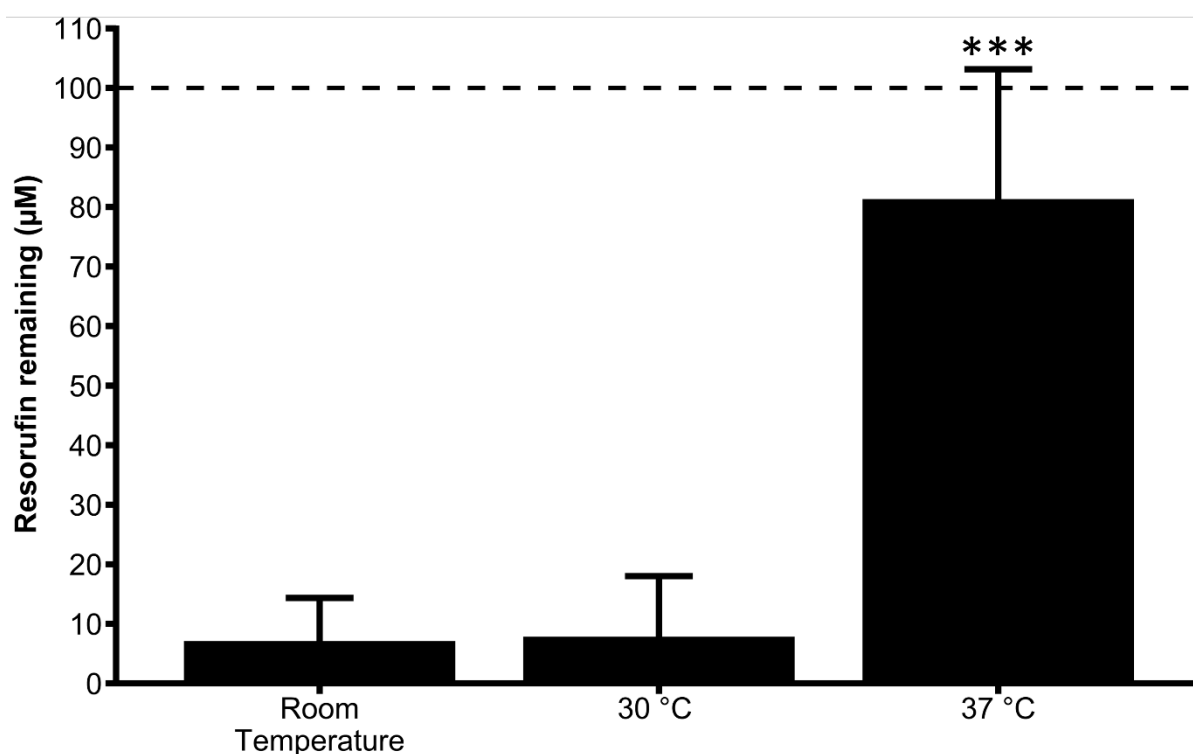


Figure 5.3: Comparison of mean resorufin remaining  $\pm$  SD between varying temperatures using the parallel device at  $0.5 \mu\text{L min}^{-1}$ . Dotted line represents concentration of resorufin flowed through the devices. An ANOVA with Bonferroni corrections comparing the three different temperatures. \*\*\*,  $p = >0.0001$ ,  $n=3$ .

This data in Figure 5.3 shows that there is no significant difference in loss of fluorescence between room temperature ( $92.9 \pm 7.2\%$ ) and  $30\text{ }^{\circ}\text{C}$  ( $92.2 \pm 10.2\%$ ) conditions. However, interestingly  $37\text{ }^{\circ}\text{C}$  shows significantly reduced conversion when compared ( $18.7 \pm 21.8\%$ ). This contradicts both the physiological optima of these enzymes which matches those described in the distributors details this is comparable to the data observed within the Effect of temperature on resorufin metabolism section within the UGT chapter.

The next step was to ensure that metabolites are being formed within the device and the loss of fluorescence is not due any fluorescence altering effects (*i.e.*, pH shifting) or the formation of alternative unexpected products.

## **Product confirmation**

Unfortunately, there is no commercially available standard for resorufin sulfate, the assumed metabolite formed throughout this chapter. In order to demonstrate that these devices are forming the expected metabolic products a substrate and metabolite that are commercially available was utilised instead. It was important to truly determine if a specific metabolite is formed within the device, as this will allow for a direct comparison yielding previously unobtainable information such as fragments beyond the expected loss of  $80\text{ }m/z$  being the sulfate group and retention time.

Nitrophenol and its sulfate conjugate, nitrophenyl sulfate which are both commercially available and have been frequently used in the literature for the study of sulfation *via* various SULT isoforms (as described in section 1.2). Due to its frequent use, the expected fragmentations are already readily available allowing for an improved direct

comparison further proving that it is definitely being formed within the device. Alongside this it also demonstrated that these devices are not solely viable for the formation of resorufin metabolites as this was previously the only tested substrate.

A variety of different HPLC chromatograms were ran within each injection but only the MRMs have been shown to allow this research to be easier to follow. Additional HPLC chromatogram for nitrophenol are shown in appendix Figure 0.35-Figure 0.36, nitrophenyl sulfate in appendix Figure 0.37-Figure 0.40.

As per the UGT chapter (4) a LC-TQ-MS was used to obtain HPLC chromatograms for nitrophenol (Figure 5.4a) and nitrophenyl standards (Figure 5.4b) at 100  $\mu\text{M}$  as described in section 2.6.

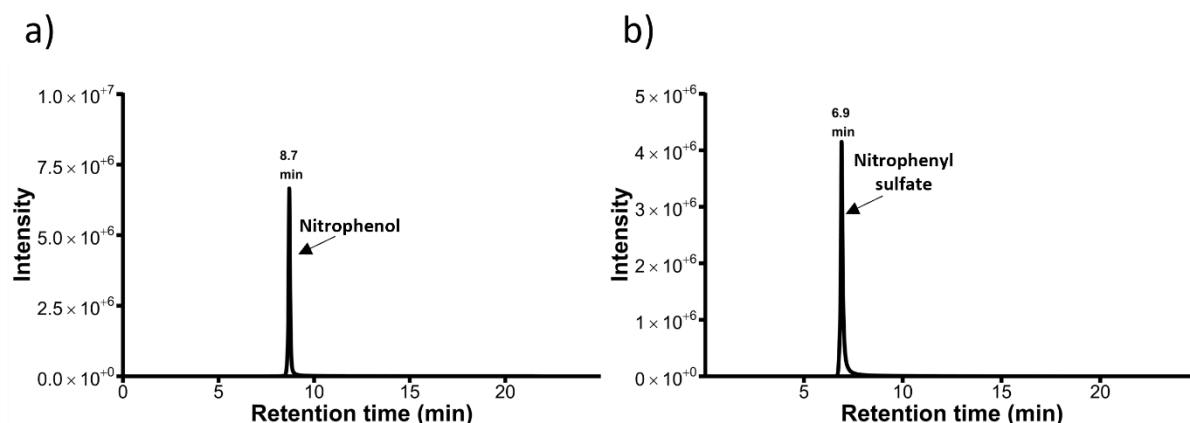


Figure 5.4: HPLC chromatograms of nitrophenol standard at 100  $\mu\text{M}$  using an MRM scan at (a) 138>108 m/z, and (b) 218>138 m/z.

The HPLC chromatogram obtained shows the retention times for both nitrophenol (8.7 minutes, 138>108 m/z, Figure 5.5a) and nitrophenyl sulfate (6.9 minutes, 218>138 m/z, Figure 5.5b) as previously determined in the optimisation sections within chapter 3 for Resorufin and Resorufin glucuronide. Due to the sharp, intense and clearly

separated peaks, implementing an effluent sample was the next step to determine if a sulphated metabolic product was formed within the device and if any nitrophenol remained. Additional HPLC chromatogram for a sample are shown in appendix Figure 0.41-Figure 0.43 with their respective mass spectrum shown in appendix Figure 0.53-Figure 0.56.

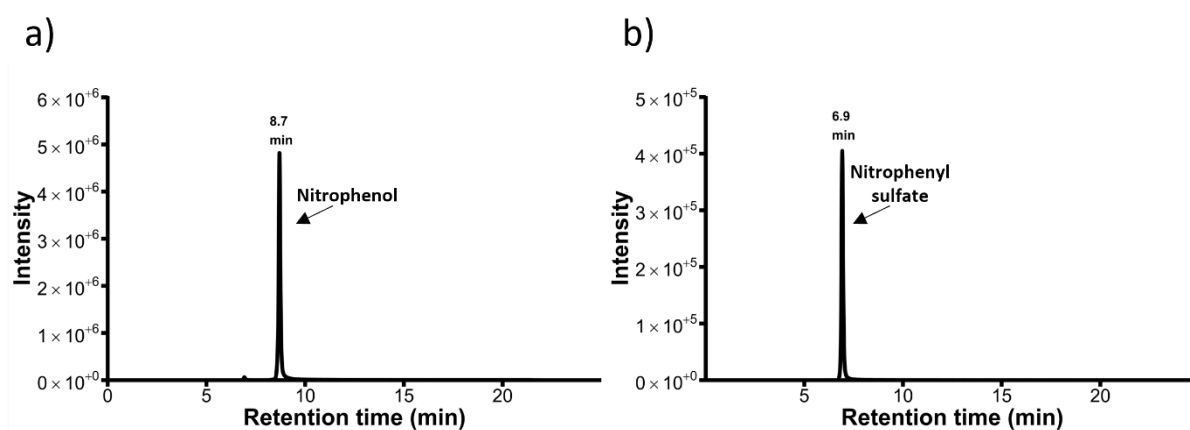
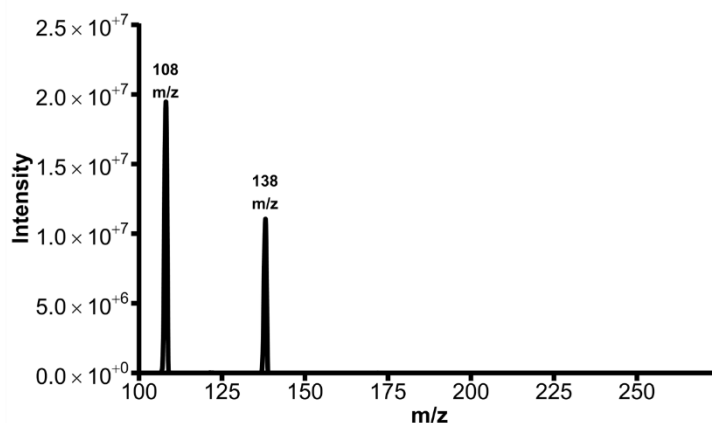


Figure 5.5: HPLC chromatograms of a sample using an MRM scan at (a)  $138 > 108$   $m/z$  and an MRM at (b)  $218 > 138$   $m/z$ .

Upon analysing both of these HPLC chromatograms it was noted that both the nitrophenol peak (8.7 minutes,  $138 > 108$   $m/z$ , Figure 5.6a) and the nitrophenyl sulfate peak (6.9 minutes,  $218 > 138$   $m/z$ , Figure 5.6b) were both visible at the same retention time as the previously analysed standards. To further determine that this was definitely these compounds A product ion scan analysing the area under the curves was conducted.

a)



b)

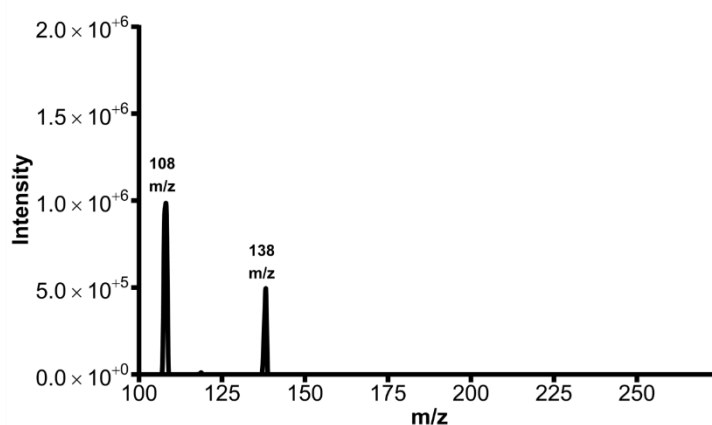


Figure 5.6: Mass spectrum for the area under the curve at 6.9 minutes using a product ion scan at 218 m/z for (a) a nitrophenyl sulfate standard and (b) a sample collected from the outlet of the microfluidic device.

When comparing the mass spectrum for the area under the curve at 6.9 minutes for a product ion scan at 218 m/z for both the nitrophenyl sulfate standard (Figure 5.7a) and a sample collected from the outlet of the microfluidic device (Figure 5.7b), it can be seen that both the fragmentations between the two are exactly the same m/z. This demonstrates that both the microfluidic device and the standard are the same compound and therefore the microfluidic device is producing the known metabolic product as previously theorised based on the fluorescence data throughout this chapter.

In order to demonstrate that the device only forms the metabolic product when the enzyme is present a device was run which did not include the enzyme, but the rest of the steps were followed and was simply left in phosphate buffer instead. Additional scans for the negative control are shown in appendix Figure 0.44-Figure 0.46 with their related mass spectrum in appendix Figure 0.47-Figure 0.49, appendix Figure 0.50-Figure 0.52.

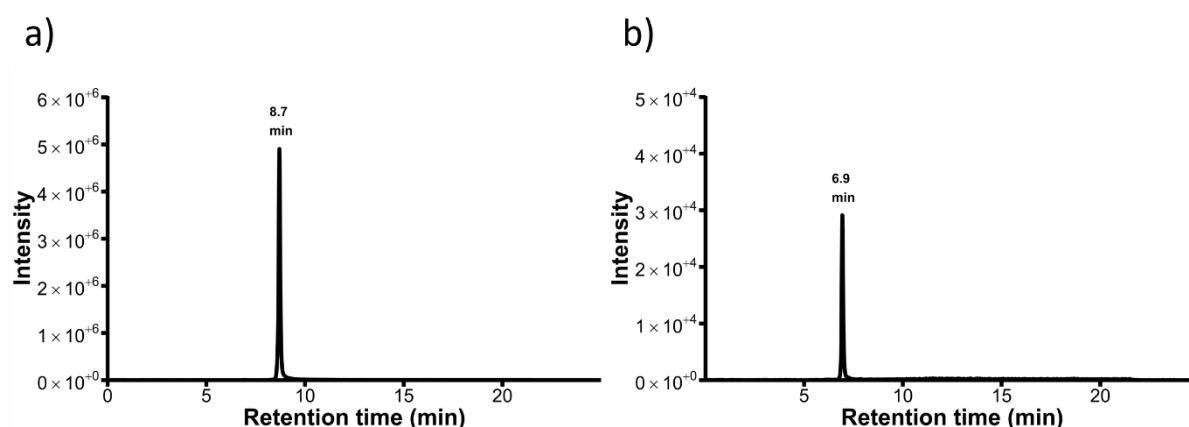


Figure 5.7: HPLC chromatograms of a blank sample where no cofactor was including using an MRM scan at  $138>108$  m/z (a) and an MRM at  $218>138$  m/z (b).

A HPLC chromatogram for both  $138>108$  m/z (nitrophenol) and  $218>138$  m/z (nitrophenyl sulfate) was conducted to determine if any of each was remaining/formed within the device. It was observed that a large peak was found for nitrophenol in all of the relevant scans. However, no peak was found for nitrophenyl sulfate in all scans except for in the MRM scan but only a very small peak (100x smaller than that of the standard) was found in comparison to the standards measured previously. This shows that some conjugation may have occurred without the use of an enzyme. However, this is not a sufficient amount to be viable for any further studies. As this peak was not seen in the product ion scan it was not possible to see the fragments of the area under the curve. This demonstrates that the enzyme is required to allow the formation of

sulfated metabolic products and is not a naturally forming compound when both PAPS (co-factor) and resorufin are both available within the same solution.

Finally, now that it has been demonstrated that metabolic products are formed within the device it was important to compare this method to a frequently used method for metabolic product synthesis being directly incubating the enzyme (SULT1a1) with the substrate (resorufin) and co-factor (PAPS).

### **Static vs. Flow**

The method for conducting static experiments is described in section 2.4 and the room temperature experiments optimised previously were conducted at the same time and are shown in Figure 5.8. In order to allow for a direct comparison between these two methods one assumption was required due to different effluent collections being compared and concentrations were not suitable. The assumption being that the loss of fluorescence was directly proportional to the production of metabolite, as this information is not available using this fluorescence analysis. These two methods were conducted simultaneously using the same PAPS and SULT solution, collections were made from both every hour for two hours.

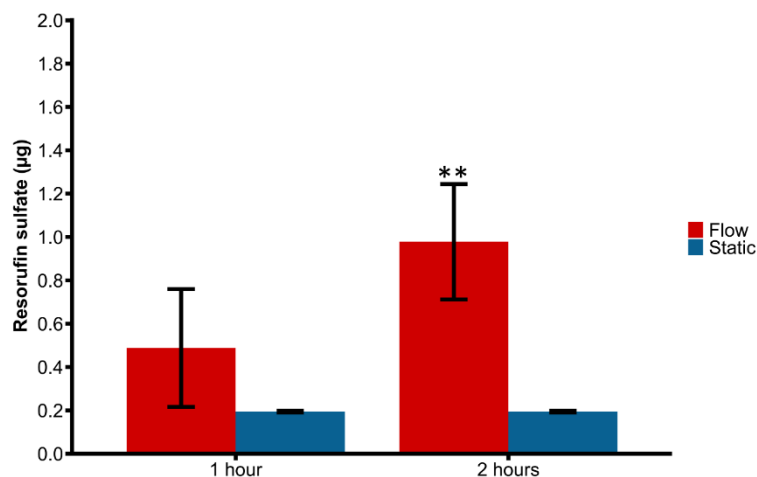


Figure 5.8: Potential mean resorufin sulfate formed  $\pm$  SD based on fluorescence lost comparing batch vs. flow conditions. An ANOVA with Bonferroni corrections comparing the reaction time and devices. \*\*,  $p = >0.001$ ,  $n=3$ .

Upon comparing both flow and static experiments, flow being the microfluidic device and static being an in-solution experiment, it was shown that there was no significant difference on the overall amount of potential resorufin that was converted over a 1-hour period (static = 0.19 ng, flow =  $0.48 \pm 0.27$  ng). However, upon allowing the reaction to continue for a further under both conditions a significant amount more of potential resorufin sulfate was formed over this time with the static reaction yielding no more overall potential product ( $0.19 \pm 0.00$  ng) over the extra hour period. In contrast the flow through yielded significantly more potential product at  $0.97 \pm 0.27$  ng).

## 5.4. Discussion

The aim of this chapter was to optimise and develop a method allowing for the synthesis of sulfated metabolites utilising the enzyme SULT1a1. Specifically focusing on high conversion to allow for the creation of standards for further studies.

Two different microfluidic device structures were tested, a parallel and a serpentine device shown in 2.2a and 2.2b, respectively. A variety of different parameters were also tested within the device to ensure optimum conversion, *i.e.*, temperature, flow rate and compared to a commonly used incubation method.

Upon conducting a true metabolism run by incubating both enzyme and co-factor alongside three different control conditions were also tested to allow for comparison for whether resorufin concentration is lost/converted under different conditions (Figure 5.1). These controls were, incubating without immobilising the enzyme, running the device but excluding the co-factor and immobilising an alternative enzyme. No significant loss of resorufin was observed (*via* fluorescence) throughout any of the blanks, in comparison to the true enzymatic run including both co-factor and the correct enzyme which was significantly higher conversion at  $0.48 \mu\text{g hr}^{-1}$  at a flow rate of  $0.5 \mu\text{L min}^{-1}$ . This is comparable to that which is found in literature in which all studies that use a control in which either no co-factor or enzyme are included within the system due to the limited product formation (Salman *et al.*, 2011, Kim *et al.*, 2004 and Stanley *et al.*, 2001<sup>303-305</sup>).

Alongside these experiments multiple flow rates ( $0.1$ ,  $0.5$  and  $1 \mu\text{L min}^{-1}$ ) were tested on both a parallel and a serpentine device (2.2a and 2.2b respectively). In which no significant difference was found between either the devices or the flow rates as detailed in Figure 5.2. Despite this, it was noted that there was a larger mean of resorufin lost within the parallel device ( $95.9 \pm 6.4\%$ ) than the serpentine device ( $88.2 \pm 15.7\%$ ). This demonstrates that whilst there was no significant difference the parallel device yields overall more product and in a more precise manor. The flow rate  $0.5 \mu\text{L}$

min<sup>-1</sup> was carried forward to avoid increasing back pressures from the high flow rates and low volume/product formation from the lower volumes. The serpentine device had much thinner channels (75 µm) and the parallel had thicker channels (300 µm) but more conjoined channels allowing for more interactions between the surface and the solution flowing through, both of which are described in section 2.2. Though the serpentine device provided statistically the same conversion, the device was much more prone to blocking due to the thinner channels and upon silanising the device even thinner and smaller moisture levels could have a much higher effect and lead to the formation of a thick amorphous layer due to polymerisation of the APTMS layer (Pasternack, 2008).<sup>306</sup> This backpressure led to the sole use of the parallel device throughout subsequent experiments.

The next set of experiments involved altering the temperature of the experiment. This was decided as a necessary optimisation due to the temperature sensitivity of enzymes. Typically, enzymes are optimal at ~37 °C however it has been noted that upon immobilising an enzyme these properties can be altered, as described in the discussion of chapter 4. Three different temperatures were tested: 20 ± 2 °C, 30 °C and 37 °C (Figure 5.3). The two lower temperatures at room temperature (20 ± 2 °C) and 30 °C showed no significant difference to each other (92.9 ± 7.2% and 92.2 ± 10.2% respectively) in terms of yield. Contrary to which was expected 37 °C provided little to no loss of resorufin (18.7 ± 21.8%). It was decided to continue using room temperature due to no significant difference between the two and an overall easier setup bypassing the requirement for an incubator.

A method currently used for the synthesis of naturally circulating metabolites is incubating the enzyme with the co-factor and substrate (Figure 5.8). Although, this method is generally good for the determination of metabolites that are naturally formed, it is generally less viable for the synthesis of a single product. This is due to a variety of reasons; including the enzyme being inhibited by the products formed, the product being formed within a complex matrix and extremely low yields in general. This method was conducted under optimum conditions as described by the manufacturers (37 °C, pH 7.4) and for the equivalent time of the microfluidic devices *i.e.*, two collections over 2 h. This data showed no significant difference between the initial timeframes. Which is still an overall improvement in comparison to the incubation method due to bypassing the need for a complicated separation. However, upon continuing the experiment for the extra hour a significantly higher product formation was found showing that over a longer period of time the device provides more product within a lower complexity environment (Figure 5.8). It is widely known in literature that upon incubating the substrate with a co-factor and enzyme environment weaves the resulting sample into a highly complex biological environment where only quantitative analysis is available and collecting a pure substrate is very difficult (Decsi *et al.*, 2019).<sup>307</sup>

Nitrophenol is another readily metabolised molecule. Upon conducting the same flowthrough protocol as for resorufin but with nitrophenol as a substrate these samples were then analysed *via* mass spectrometry as described in Chapter 3 section titled Mass spectrometry. Identifying nitrophenol (138>108 m/z, retention time 8.7 min, Figure 5.5a) and nitrophenyl sulfate (218>138 m/z, retention time 6.9 min, Figure 5.5 b) when compared to their respective spectrum and chromatograms (Figure 5.4a-b).

Demonstrating the formation of nitrophenyl sulfate when both the correct co-factor, PAPS and enzyme, SULT1a1 are available within the system. Comparatively a blank sample (no co-factor incubated with substrate, Figure 5.7) was also tested within the same method and only nitrophenol (138>108 m/z, retention time 8.7 min) was found. Demonstrating that as expected, when no co-factor was co-incubated within the device no product is formed.

The limitation of this work is comparable to that of the previous chapter in which currently an assumption is made on the overall amount of product formed as fluorescence is directly linked to metabolism. Due to the mass spectrometry data, it can be confirmed that a sulfated metabolite has been formed but this does not quantify the overall product (the quantification comparing static conditions and flow devices is based on potential formation assuming loss of fluorescence is directly proportional to allow a direct comparison between the two) and only partial metabolism may have occurred and a loss of fluorescence *via* an alternative reaction pathway or changes within the solution.

## **5.5. Conclusion**

The aim of this chapter was to optimise and develop a method allowing for the synthesis of naturally circulating sulfated metabolites. A variety of different parameters were tested namely, device structure, flow rate and temperature whilst also determining that both the correct co-factor and enzyme are required for metabolic activity. Providing both significant conversion and does not require any complex separations.

In the following chapter CYP1a1 will be optimised in a similar fashion which allowing for the potential of cascade reactions which commonly occur *in vivo*.

# 6. Optimisation of the synthesis of naturally occurring metabolites using CYP1a1

## 6.1. Introduction

The metabolites of cytochromes P450 enzymes are frequently observed as toxic on the human body, however they are usually conjugated quickly *via* conjugative enzymes preventing this toxicity from having a detrimental effect.<sup>308</sup> However, this is not always the case.<sup>309, 310</sup> Functionalisation of xenobiotics by oxidation/reduction reactions has been linked with promotion of carcinogenicity in some compounds, for example, CYP1A (a member of the P450 family) enzyme is associated with PCB and aryl hydrocarbon carcinogenicity. Due to this frequently observed toxicity and the fact they account for approximately 75% of all xenobiotic and clinical drugs metabolism.<sup>311, 312</sup> CYP facilitated metabolite formation has been much more extensively researched due to the frequency in which their metabolites are observed and due to their unique challenges when compared to conjugative enzymes.<sup>36, 313</sup> These are due to its complex catalytic cycle requiring substrate binding, two independent electron donating events oxygen binding and product release.<sup>314</sup> Due to these extra steps the orientation in which the enzyme is immobilised becomes much more important.

The current methods for synthesising these metabolic products, comparable to both the UGT and SULT section are include incubating s9 fractions, liver cell incubations,

bacteria overexpressing the enzyme and computer simulations (described in detail in section 1.3).

Cytochrome P450 immobilised microfluidic devices have previously been utilised for the synthesis of oxidised/reduced metabolites. For example, Sathyanarayanan, *et al.* immobilised CYP1a1 within a porous polymer IMER to allow the synthesis of resorufin from 7-ethoxyresorufin.<sup>315</sup>

Cypexpress enzymatic systems are advertised as having longer lifetimes, increased stability over a longer period of time and allow for more repeated uses in comparison to other enzyme systems. This would also demonstrate that this technique is applicable for a variety of different enzyme containing systems. Thus, contrarily to the previous chapters a Cypexpress enzyme was tested as well as coming supersomes.

In this chapter, the preliminary research for the development and optimisation of a method for the synthesis of metabolites *via* oxidation/reduction reactions naturally occurring in the human body will be described. In which will include:

Two different enzymatic systems with the first being CYP supersome optimisation were undertaken in which temperature, flow rate and alternative potential improvements were changed. This was compared to optimal batch conditions frequently utilised in the wider literature. Secondly Cypexpress systems in which optimisation of flow rate, immobilisation temperature and initial substrate concentration were tested. Initial, biocatalysis was studied by fluorometric analysis in which the product was fluorescent. Product confirmation was determined using LC-TQ-MS techniques and lastly semi quantification was then undertaken.

## **6.2. Experimental procedure**

### **Determination of resorufin concentration**

A calibration curve for resorufin was created by serial dilution of an initial concentration of 100  $\mu\text{M}$ . The dilution was carried out sixteen times by half in a V-shaped 96-well microplate (STARLAB). Fluorescence intensity was measured using a microplate reader set to 544 nm ( $\lambda_{\text{ex}}$ ) and 590 nm ( $\lambda_{\text{em}}$ ) as optimised in the Calibration curve for resorufin section in chapter 4.

### **Fabrication of microfluidic devices**

The devices used were fabricated using the HF etching technique as described in sections 2.2.

### **Immobilisation of CYP1a1 supersomes**

Both CYP supersomes and microsomes were immobilised comparatively immobilised as sections 2.3 and 0 at an initial enzyme concentration of 0.15 mg mL<sup>-1</sup> and 10 ng mL<sup>-1</sup> respectively. When immobilising supersomes the immobilisation temperature was altered to 20  $\pm$  2 °C, 4 °C and 37 °C as the Cypexpress supersomes were precipitating when cooled to 4 °C.

### **Metabolism of test substrates**

As a test substrate, the reverse of the two previous chapters was conducted in which the initial substrate (7-ethoxyresorufin) was metabolised into resorufin leading to a

formation of fluorescence when analysed *via* plate reader fluorimetry as described in sections 2.5.

## **Mass spectrometry**

The mass spectrometry method covered in detail in both sections 2.6 and 0 was followed. The difference being the scans where a product ion scan was used for product confirmation of both 7-ethoxyresorufin in positive mode and resorufin in negative mode with  $m/z$  of 242 and 212, respectively. Alongside this, the multiple reaction mode (MRM) was used for further confirmation with selected transitions of  $242 \rightarrow 214$  and  $212 \rightarrow 155$   $m/z$ , respectively.

## **6.3. Results**

### **CYP supersomes**

The immobilisation of cytochrome P450 was conducted as previously mentioned in both the UGT and SULT chapter and is described in 2.3.

#### *Comparison of a true run vs a variety of controls*

A comparison between a true run (a run containing both the CYP1a1 and NADPH) and the three different controls, as described in chapters 4 and 5 (co-factor no enzyme, enzyme no cofactor and using an alternative non-reactive enzyme) was conducted at a substrate (7-ethoxyresorufin, 100  $\mu\text{M}$ ) flow rate of 0.5  $\mu\text{L min}^{-1}$  and at room temperature, the optimal parameters from the previous chapters in order to determine if resorufin was only formed when both the correct co-factor and enzyme were available within the system. Effluent was collected after 24 minutes and analysed

utilising the fluorescence plate reader analytical technique described in section 2.5 (Figure 6.1).

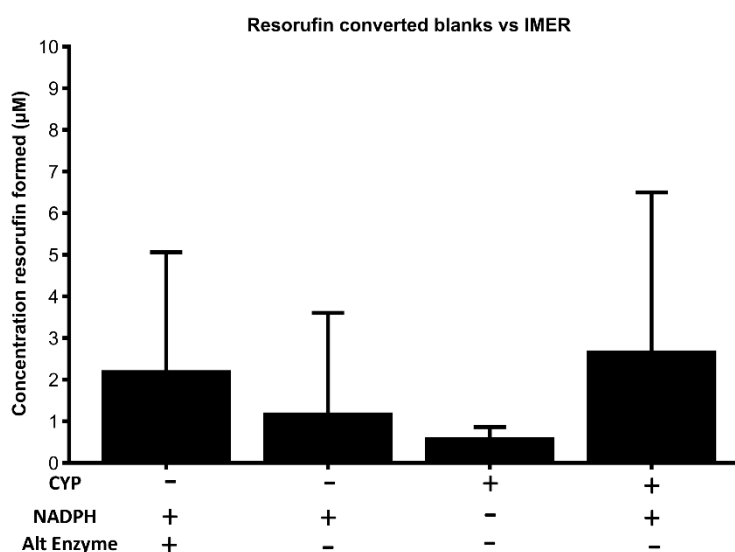


Figure 6.1: Comparison of mean resorufin formed  $\pm$  SD between a true run and three blanks with an initial substrate concentration of 100  $\mu$ M. No significant difference found between all tests using a one-way ANOVA with Bonferroni corrections,  $p > .05$ ,  $n=3$ )

The data in this figure shows that when both the correct co-factor and enzyme are available in the system  $2.70 \pm 3.79 \mu$ M is found. Due to the high degree of irreproducibility in this data there is no significant difference between this and any of the conducted blanks. However, a trend comparable to the previous chapters was found in which the true run containing both enzyme and co-factor yielded the highest result, the with the rest being smaller due to the lack of available necessary co-factor/enzyme. This conversion equated to approximately  $2.7 \pm 3.8\%$  (Figure 6.1) utilising the supersomes. All reactions up until this point have been conducted at room temperature ( $20 \pm 2 \text{ }^\circ\text{C}$ ) and typically human enzymes have an optimum of  $37 \text{ }^\circ\text{C}$ . Both the UGT and SULT chapter demonstrated that this optimum was altered upon immobilising the enzyme *via* covalent bonding. However due to the low overall

conversion there was a chance that increasing the temperature would increase this overall conversion.

### Temperature

Also, as previously for UGT and SULT three different temperatures were tested simultaneously at the previous optimum flow rate for chapter 4 and 5 of  $0.5 \mu\text{L min}^{-1}$  ( $20 \pm 2 \text{ }^\circ\text{C}$ ,  $30 \text{ }^\circ\text{C}$  and  $37 \text{ }^\circ\text{C}$ ), shown in Figure 6.2.

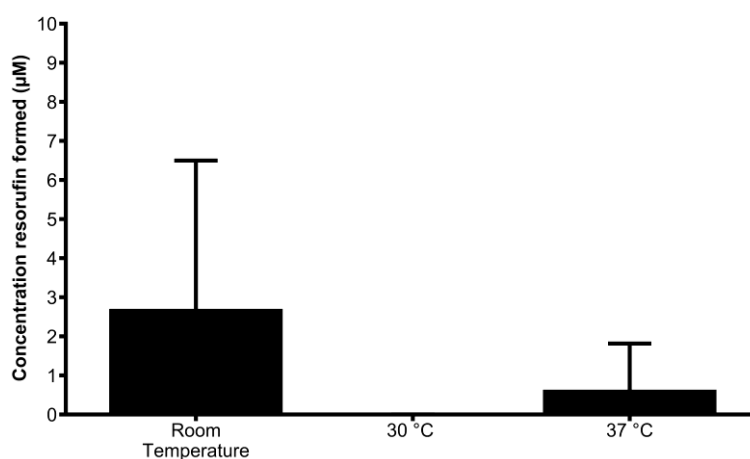


Figure 6.2: Comparison of mean resorufin formed  $\pm$  SD under different incubation temperatures. No significant difference found between all tests using a one-way ANOVA with Bonferroni corrections,  $p > .05$ ,  $n=3$ ).

Conversely to the previous chapters  $30 \text{ }^\circ\text{C}$  provided very little conversion and both room temperature and  $37 \text{ }^\circ\text{C}$  provided some conversion ( $2.70 \pm 3.79 \mu\text{M}$  and  $0.63 \pm 1.18 \mu\text{M}$ , respectively (Figure 6.2). However, due to the inconsistencies between comparable conditions alongside the relatively low yield it was deemed unsuitable for the bulk synthesis of metabolic products. It was determined that potentially increasing the amount of time the substrate was within the device (slowing the flow rate) would increase the overall conversion provided due to increased chances of collisions with the enzymes active site.

## Flow rate

As previously reported for SULT and UGT, different flow rates (0.1, 0.5 and 1  $\mu\text{L min}^{-1}$ ) were tested *via* the addition of the correct co-factor and immobilised enzyme utilising the fluorescence plate reader analysis described in section 2.5 to assess the relationship between flow rate and the devices output and yield (Figure 6.3).

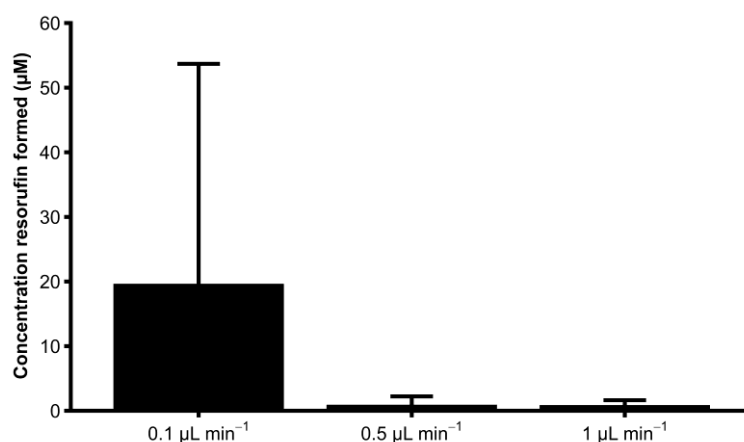


Figure 6.3: Comparison of mean resorufin formed  $\pm$  SD under different flow rates using CYP1a1 supersomes. No significant difference found between all tests using a one-way ANOVA with Bonferroni corrections,  $p > .05$ ,  $n=3$ ).

This fluorescence data obtained from demonstrates that a much larger amount of product ( $19.65 \pm 34.03 \mu\text{M}$ ) was formed at the lower flow rate of  $0.1 \mu\text{L min}^{-1}$  compared to both  $0.5$  and  $1 \mu\text{L min}^{-1}$  ( $0.94 \pm 1.28 \mu\text{M}$  and  $0.88 \pm 0.75 \mu\text{M}$ , but this was not consistent, and a large error/inter-device variability is obtained.

To attempt to increase overall substrate conversion, two different tests were viable options. One of which includes cooling the syringe to prevent potential NADPH degradation, the other being incubating NADPH within the device for an hour allowing for the initial step in the reaction to occur prior to flowing substrate.

### *Alternative potential improvements*

Upon conducting a wide variety of optimisation steps comparable to both the UGT and the SULT immobilised devices a maximum of  $19.65 \pm 34.03 \mu\text{M}$  has been formed comparable to a yield of  $20 \pm 34\%$  which whilst this is not inconsequential a large variation is observed between each device even in comparable conditions, demonstrating a lack of reproducibility and reliability with the devices as they are currently.

Two different tests were conducted to determine if this could be improved; incubating the NADPH co-factor ( $100 \mu\text{M}$ ) within the microfluidic devices for an hour to allow the initial step in the reaction to occur prior to flowing substrate through the device at the previously optimised  $0.1 \mu\text{L min}^{-1}$ ; and cooling the syringe whilst flowing through the device to prevent the NADPH from degrading prior to any reaction occurring due to its relatively short half-life (Figure 6.4).

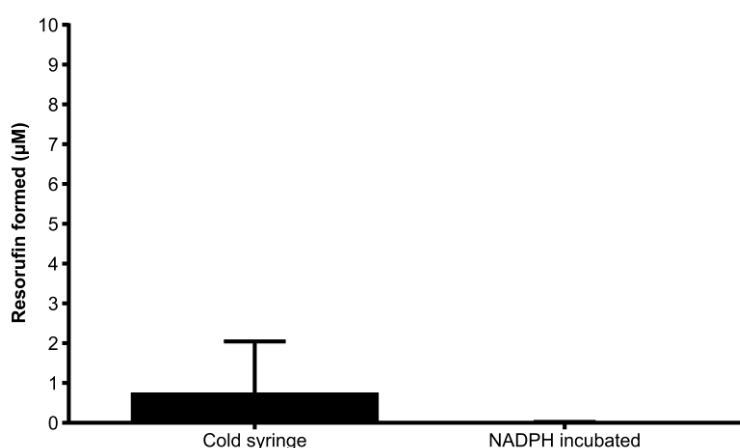


*Figure 6.4: Comparison of mean resorufin formed  $\pm$  SD between two different tests, cooling the syringe and incubating the NADPH for an hour prior to flowing substrate. Scaled to  $10 \mu\text{M}$  to allow visualisation of data typical  $100 \mu\text{M}$  used in this chapter would not allow visible bars. No significant difference found between both tests using a one-way ANOVA with Bonferroni corrections,  $p > .05$ ,  $n=3$ ).*

The data described in Figure 6.4 shows the observations made when conducting two potential improvements which also appeared to have negative effect on the amount of product formed. Cooling the NADPH was a potentially desirable parameter due to its low stability and readily undergoing spontaneous degradation at room temperature. This yielded only  $0.76 \pm 1.28 \mu\text{M}$  representing lower product formation than the method utilising a syringe at room temperature.<sup>316</sup>

Alternatively, incubating the NADPH with the immobilised CYP enzyme was decided, as throughout literature it is common for the enzyme and the NADPH co-factor to be within one solution prior to being incubated within the sample. For example, Kosaka *et al.* observed a 50-fold increase in enzyme activity upon pre-incubating CYP enzyme with NADPH compared to no pre-incubation.<sup>317</sup> This yielded no measurable product formation demonstrating that neither of these steps were beneficial on product formation in flowthrough conditions, thus were not carried forward due to even less product formed than the initial method at  $0.1 \mu\text{L min}^{-1}$ .

As all of the optimisation options have been exhausted and some measurable product was observed, the next step was to use the optimised steps available to determine if the frequently used methods provide any product formation. This will determine whether the method optimised in this section is comparable or better than the literature derived method of directly incubating CYP enzyme, substrate and co-factor. These two methods will be compared allowing the devices to undergo metabolism over a longer period of time similar to the UGT and SULT chapter, all of the experiments conducted in this chapter up until now were conducted over a maximum of a 2 hour period and for the comparison to incubation allowing the devices to continue running

over 6 hours was studied to determine if the devices yield more product if allowed to run over a longer period of time.

### *Static vs. Flow*

A comparison to the commonly used method of incubating substrate, co-factor and enzyme as described in section 2.3 and was compared to the optimised parameters throughout this chapter (temperature  $20 \pm 2$  °C and flow rate at  $0.1 \mu\text{L min}^{-1}$ ,

Figure 6.5.

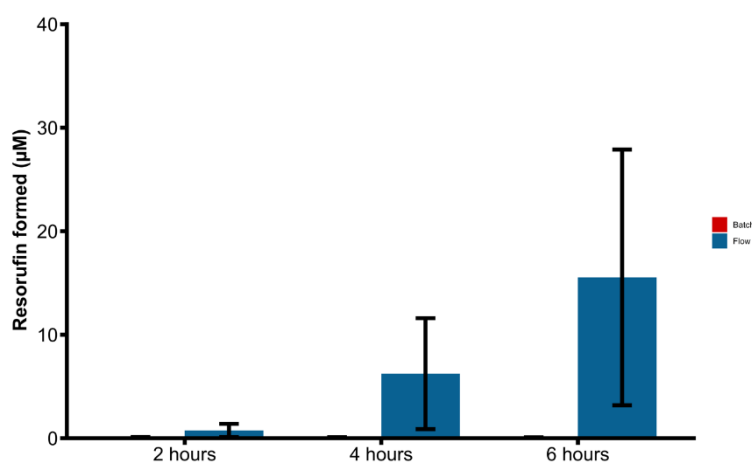


Figure 6.5: Comparison of mean resorufin formed  $\pm$  SD within both an incubation and a flowthrough method over time. No significant difference found between all tests using a one-way ANOVA with Bonferroni corrections,  $p > .05$ ,  $n=3$ ).

Figure 6.5 demonstrates a comparison between the frequently used method directly incubating co-factor enzyme and substrate (batch) with the optimised immobilised CYP reactor (flow). A concentration of  $0.76 \pm 0.64 \mu\text{M}$  was obtained over a 2-hour period,  $6.24 \pm 5.36 \mu\text{M}$  over 4 hours and  $15.54 \pm 12.36 \mu\text{M}$  over 6 hours. For batch conditions for the first 2 hours  $0.10 \pm 0.02 \mu\text{M}$  was measured and no further product was measured upon any extended times. Despite these large differences in mean due to the lack of reproducibility between the data no significant difference is found between any of these values. It was theorised that, due to the difference between

supersomes and the previously used microsomes, that this may have had a large effect on the enzymes overall metabolic activity upon undergoing covalent immobilisation or that the enzyme was not being immobilised as effectively due to structural differences in supersomes to microsomes.

It was noted that this was the first time the device yielded measurable quantities of product in which the error bar does not include no product formation at all. Although a large variation is observed within this data set at 6 hours, it demonstrates that measurable quantities of product can be formed and that running this device for more than 6 hours may have yielded further conversion. Alongside this it is demonstrated that the direct incubation method yielded no measurable product formed over any period of time and that throughout these experiments the flowthrough devices at  $0.1 \mu\text{L min}^{-1}$  are vastly improving on the previous method of directly incubating the enzyme co-factor and substrate.

## **Cypexpress**

### *Flow rate*

Due to the property differences between the Cypexpress and the supersomes enzymes, it was noted that there was a significant loss of solubility for Cypexpress enzyme *i.e.*, the equivalent concentration used in chapter 4 ( $0.15 \text{ mg mL}^{-1}$ ) was not soluble in phosphate buffer. Due to this the first step was to determine solubility of the Cypexpress enzyme across a variety of different solvents. The previously used phosphate buffer was used and little to no enzyme appeared to dissolve, then chloroform, methanol and DMF were tested with significant solubility found with DMF

at least in high concentration (between 50-100% in water). These high concentrations however in literature a significant impact on the activity of the enzyme thus reducing/halting catalytic activity concentrations of only 2.5% have previously been tested on Cypexpress systems by the commercial provider (Oxford Biomedical Research, Inc.).<sup>318</sup> The decision was made to lower the DMF concentration to 2%, which appeared to be the minimum needed to dissolve the previously tested concentration of enzyme in chapter 4 ( $0.15 \text{ mg mL}^{-1}$ ). This was tested by sequentially lowering the concentration of DMF and observing the amount of precipitate. After determining this, the enzyme was immobilised using the technique described in 2.3 at  $4 \text{ }^{\circ}\text{C}$ . Upon doing this, a determination of optimum flow rate was the next logical step.

In the previous chapters typically, a higher conversion was found utilising slower flow rates. It was determined that lowering the flow rate and allowing the substrate to reside within the device for 5 times longer may significantly affect the overall conversion. Two different substrate flow rates were tested on the same day  $0.1 \text{ }\mu\text{L}$  and  $0.5 \text{ }\mu\text{L min}^{-1}$  at the equivalent concentration of 7-ethoxyresorufin to the previous two chapters (4 and 5), to allow further understanding if cascading these two devices together utilising the method described in 2.2 and 2.3 would demonstrate if these faster flow rates yield the equivalent amount of product over shorter periods of time. Effluent was collected at respective times ensuring that the same volume was collected for each sample. The flow rate  $1 \text{ }\mu\text{L min}^{-1}$  was not tested due to typically the faster flow rates yield lower overall conversion and very little conversion was observed for both of the tested flow rates as shown in Figure 6.6.

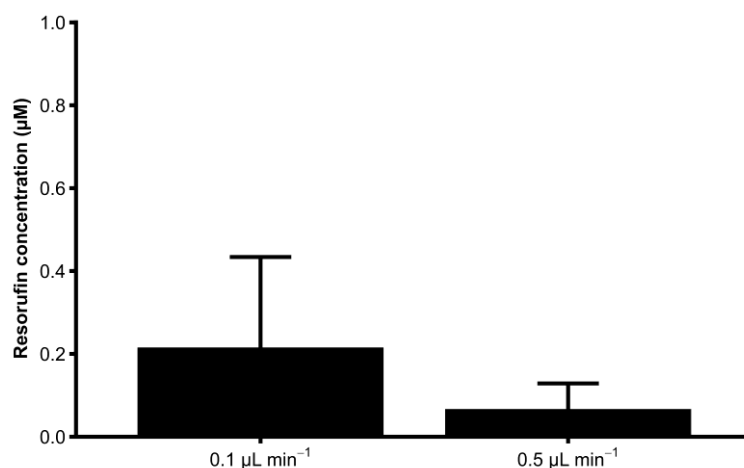


Figure 6.6: Mean concentration of resorufin formed  $\pm$  SD upon flowthrough at different flow rates with an initial concentration of 100  $\mu\text{M}$ . No significant difference found between all tests using a one-way ANOVA with Bonferroni corrections,  $p > .05$ ,  $n=3$ ).

Previous experience with conjugative enzymes suggested that altering flow rate can yield an increase in metabolite production but this was not observed with the Cypexpress enzyme. Concentration of resorufin was measured at these two flow rates at which neither yielded a significant or measurable amount of resorufin (Figure 6.6). Due to the initial concentration of 7-ethoxyresorufin being 100  $\mu\text{M}$ , an overall yield of  $\sim 0.2\%$  was observed showing that this method was not currently viable for the formation of standard quantities that can be utilised for further research. It was noted that when flushing the device of the leftover Cypexpress solution that some of the powder had dropped out of solution. This demonstrated that at the typical immobilisation strategy utilised throughout this thesis for supersomes was not applicable for Cypexpress systems. The next step was to optimise the solubility of the Cypexpress enzymes without significantly affecting catalytic activity. Alongside this as no conversion was measurable at this substrate concentration this was lowered to ensure that the enzyme was not saturated preventing product formation.

### *Substrate concentration and immobilisation temperature variation*

Once this was determined immobilising the enzyme was then tested as discussed in previous chapters and in section 2.3. It was noted that although at room temperature the enzyme stayed in solution at 4 °C overnight, very little remained and a precipitate visually comparable to the neat Cypexpress powder. This caused minor, fixable blockages with flowthrough of the DMF solution. However, there is an increased chance of enzyme degradation at higher temperatures, especially as the immobilisation required an incubation overnight. Due to this in contrast to chapter 4 and 5, immobilising the enzyme at 3 different temperatures was tested (4 °C, room temperature, and 37 °C) due to the observed precipitation of the Cypexpress based enzymes. For both 4 °C and 37 °C the enzyme was no longer dissolved for different reasons. At 4 °C the temperature cooling lowered the solvation limit causing the enzyme to precipitate out of solution causing device blockages. Upon attempting to immobilise the enzyme at 37 °C the solution within the device evaporated leaving only the enzyme residue. This did cause some blocking issues however devices were still able to flow in some cases.

Alongside, these temperature variations, lower substrate concentrations were also varied to ensure device was not reaching catalytic limits, demonstrating that with further optimisation there is potential for more overall product formation (Figure 6.7). Upon immobilising the enzyme at each of the three temperatures, determining whether these devices yielded any metabolic activity was conducted using the method described in 2.3 and 2.5. Three different initial substrate concentrations were tested (5, 10 and 50 µM) and for 50 µM three different enzyme immobilisation incubation temperatures (4, 20 ± 2 and 37 °C) were tested within the enzyme immobilised microfluidic devices at 0.5 µL min<sup>-1</sup> utilising the method detailed in 2.3 to determine if

there is a way to bypass the enzyme dropping out of solution without causing enzyme degradation at the increased temperatures.

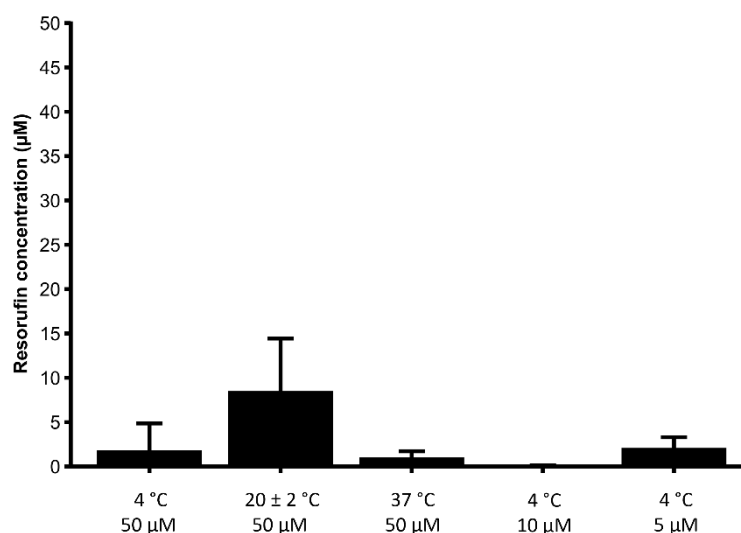


Figure 6.7: Mean concentration of resorufin formed  $\pm$  SD upon flowthrough after immobilising the enzyme within the device at different temperatures under varying initial substrate concentrations (between 5 and 50  $\mu\text{M}$ ) at  $0.5 \mu\text{L min}^{-1}$ . No significant difference found between all tests using a one-way ANOVA with Bonferroni corrections,  $p > .05$ ,  $n=3$ )

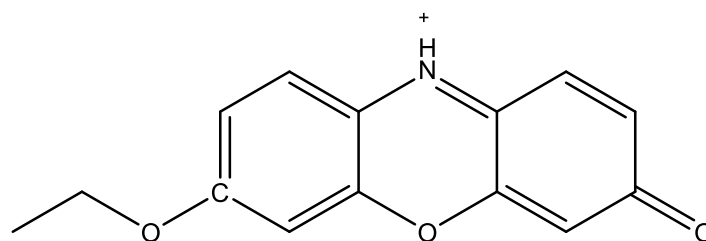
Initially the substrate concentration was varied utilising the immobilisation temperature ( $4 \text{ }^\circ\text{C}$ ) used in both chapter 4 and 5 and no significant effect was observed, with both 5 and 50  $\mu\text{M}$  initial concentration yielding comparable results with  $2.08 \pm 1.21 \mu\text{M}$  and  $1.82 \pm 3.04 \mu\text{M}$  respectively and no fluorescence was observed at 10  $\mu\text{M}$ . This demonstrated that the enzyme was not saturated but independent of concentration inconsistent results were obtained (Figure 6.7). Due to the precipitate forming within the device altering the temperature utilised when incubating the enzyme in the immobilisation process. Previously in chapters 4 and 5, a temperature of  $4 \text{ }^\circ\text{C}$  was utilised when immobilising due to an enzymes increased degradation occurring at higher temperatures. However, these Cypexpress enzymes boast higher thermal stability and longevity which may allow a bypass of the enzyme precipitating within the device which is unique to the Cypexpress enzymes and was not observed with supersomes. It was noted that at both room temperature ( $20 \pm 2 \text{ }^\circ\text{C}$ ) and  $37 \text{ }^\circ\text{C}$  the

precipitate was not formed. The fluorescence data showed that both 4 °C and 37 °C yielded minimal product formation at  $1.82 \pm 3.04 \mu\text{M}$  and  $1.02 \pm 0.70 \mu\text{M}$  respectively. Whereas  $20 \pm 2 \text{ }^\circ\text{C}$  showed much higher product formation ( $8.50 \pm 5.93 \mu\text{M}$ ). However, a large amount of variability was still observed demonstrating that this method was not viable for the synthesis of bulk quantities of metabolic products.

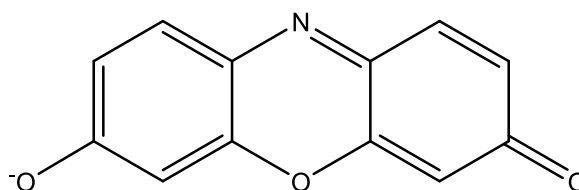
With all data obtained utilising the Cypexpress enzymes a much higher variability and lower comparable yield to the previous two chapters. This may be due to the increased complexity of CYP based reactions over conjugative reactions or could be due to the use of Cypexpress enzymes alternatively to supersomes. In order to determine if product was being formed within the devices but was not being measured due to an unexpected effect analysing the samples and blanks from Figure 6.1 *via* the LC-TQ-MS method optimised in chapter 2.6.

## **Product confirmation**

To this point, all assessment of CYP1A conversion from 7-ethoxyresorufin to resorufin has been conducted using a fluorescence assay. In order to determine if resorufin was formed within these devices an LC-MS approach was used and compared to the standards optimised in chapter 0 and 0. Figure 6.8 shows the likely parent ions observed for both 7-ethoxyresorufin and resorufin.



7-ethoxyresorufin  
Molecular Weight: 242.25



resorufin  
Molecular Weight: 212.18

*Figure 6.8: Structure of both 7-ethoxyresorufin and resorufin ions with their respective  $m/z$  utilised for the product ion scan and MRM fragmentation.*

7-Ethoxyresorufin and resorufin standards for the determination of their respective retention time and maximal intensity at the utilised concentration were analysed with spray voltage 2.32 kV, capillary temperature 300 °C, oven temperature at 40 °C using a C18 column optimised as discussed in 2.6, with representative traces shown in Figure 6.9. Additional HPLC chromatogram for resorufin standard is shown in appendix Figure 0.57 and 7-ethoxyresorufin is shown in appendix Figure 0.58-Figure 0.61.

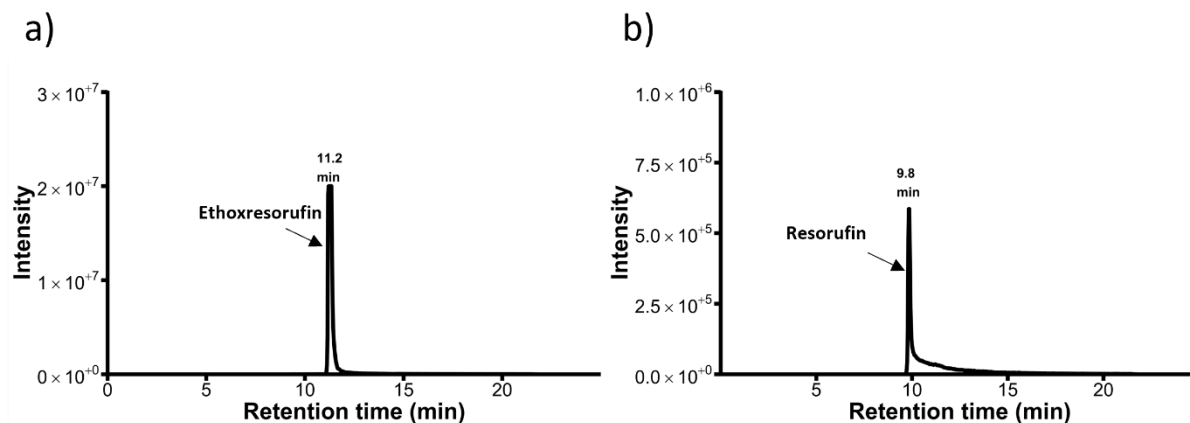


Figure 6.9: HPLC chromatogram for using the previously optimised MRM scan, for both 7-ethoxyresorufin (a)  $242 > 214$  m/z and resorufin, (b)  $212 > 155$  m/z at the concentration flowed through the devices using standards ( $100 \mu\text{M}$ ).

This MRM scan shows that the retention time of both 7-ethoxyresorufin (11.2 minutes,  $242 > 214$  m/z) and resorufin (9.8 minutes,  $212 > 155$  m/z) both peaks' maxima would not overlap, allowing them to be independently measured alongside them not appearing in the scans optimised for the other respective analyte. It was worth noting that 7-ethoxyresorufin saturated the detector, so an accurate peak area was not calculatable, although an accurate retention time was determined using the product ion scan instead of MRM. This was not comparable to the respective metabolites for the other chapters (resorufin glucuronide and nitrophenyl sulfate) which may have been due to positive mode being used rather than negative in which typically there is a 10-fold increase in intensity. Due to these sizable peaks the next step was to determine if any resorufin could be measured upon undergoing metabolism within the microfluidic device.

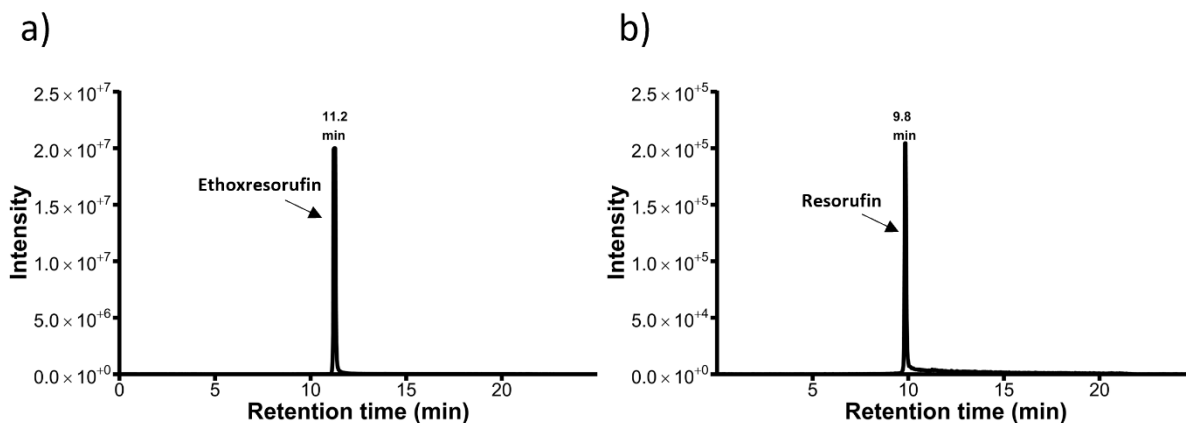


Figure 6.10: HPLC chromatogram for effluent collected post flowthrough of 7-ethoxyresorufin ( $100 \mu\text{M}$ ) through the device at room temperature utilising an MRM set to (a)  $242>214 \text{ m/z}$  and (b)  $212>155 \text{ m/z}$ .

Upon analysing the sample chromatograms, a sizeable peak for 7-ethoxyresorufin (11.2 minutes, Figure 6.10a) was observed as expected, although the peak is no longer saturating the detector and could be measured as an accurate peak area. Although unexpectedly for resorufin a much larger peak than was expected based on the previous fluorescence data throughout this chapter (9.8 minutes, Figure 6.10b), which was approximately 30% of the peak area of resorufin standard at  $100 \mu\text{M}$  (comparing Figure 6.9b and Figure 6.10b). This demonstrates that although the fluorescence data showed little to no product formation, resorufin was indeed being formed within the device, and suggests that there was some unidentified issue with the fluorescence-based plate reader assay for quantifying resorufin production.

The mass spectrum for both 7-ethoxyresorufin and resorufin are shown below (Figure 6.11), confirming the correct identification of both substrate and product in the reactor effluent. Additional sample HPLC chromatograms are shown in appendix Figure 0.62- Figure 0.64 with their respective mass spectrum are shown in appendix Figure 0.65- Figure 0.67.

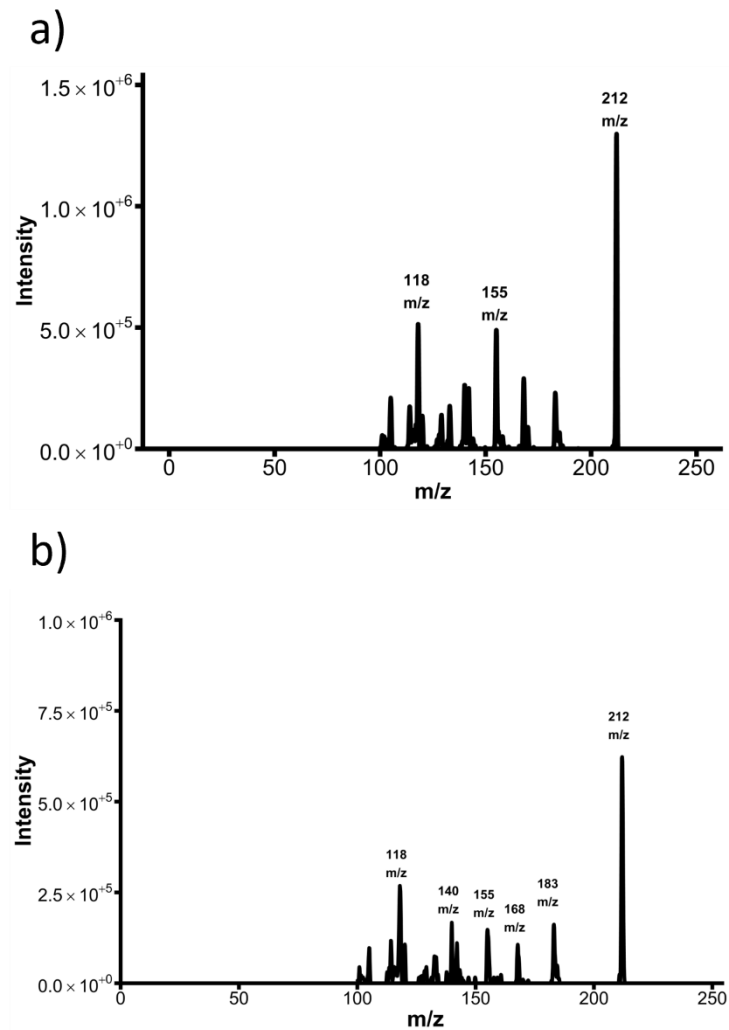


Figure 6.11: Mass spectrum of a product ion scan (212 m/z) for the area under the curve at 9.8 minutes for both (a) resorufin standard and (b) effluent from enzyme immobilised microfluidic device.

Upon comparing both product ion scans at 212 m/z for both a 7-ethoxyresorufin standard (100  $\mu$ M) and a sample collected from the outlet of the device. Both yielded exactly the same major fragments, demonstrating that resorufin was indeed formed within this metabolic device and that the results from the fluorescence data was largely unreliable in the amount of product formed. This is contradictory to that which was observed in the previous chapters where resorufin and its metabolic products were readily observed, and the overall trends observed were further proven *via* LC-TQ-MS analysis. Whereas, what would have been an immeasurable amount of product based on the concentration measured in fluorescence was a very clear and visible peak in

LC-TQ-MS. This is potentially due to the difference in matrix between the CYP and UGT/SULT enzymes and something within the co-factor or enzyme solution was quenching the natural fluorescence of the product resorufin.

A blank sample was then injected to determine if similar peaks were found and that there was a resorufin like substrate forming naturally within the device or whether resorufin was actually forming within the device. Additional HPLC chromatograms for a negative control are shown in appendix Figure 0.68-Figure 0.70 with their respective mass spectrum in appendix Figure 0.71-Figure 0.74.

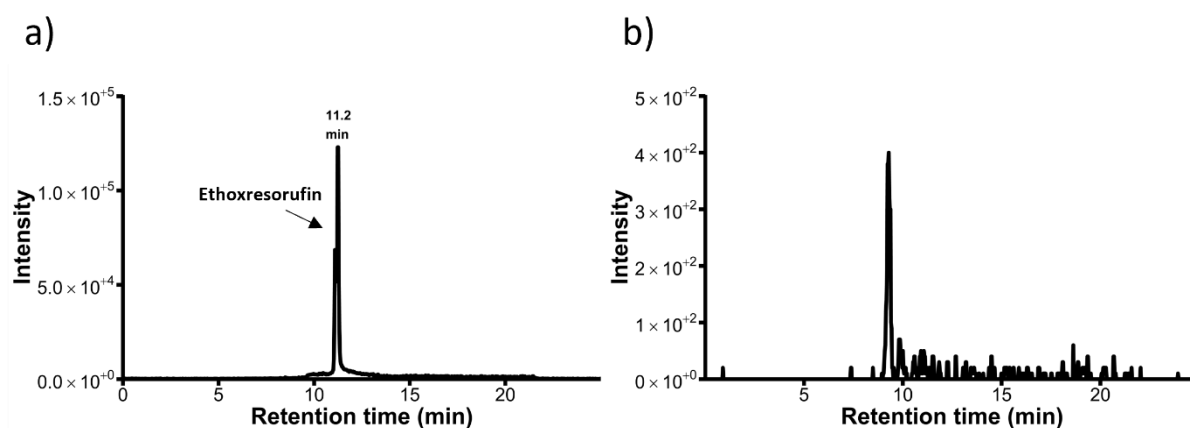


Figure 6.12: HPLC chromatogram for a blank sample on a LC-TQ-MS using an MRM scan at (a) 242>214 m/z and (b) 212>155 m/z.

The chromatogram of a blank sample where the cofactor was not implemented within the flow-through device showed a small peak for 7-ethoxyresorufin (242>214 m/z) much lower than the comparable standard. However no visible peak for resorufin was found above the levels of the background. This demonstrates that, while the device did show a loss of 7-ethoxyresorufin, it did not metabolise into resorufin showing that metabolic products are only formed when the co-factor is included in the flow-through.

All of these HPLC and MS experiments show that the fluorescence data is largely unreliable in determining the amount of product formed. However an approximation can be gathered by using a ratio between the equivalent of 100% conversion (100  $\mu$ M resorufin) and any measured sample. Due to this LC-TQ-MS analysis was conducted on the three different flow rates measured previously alongside the three different blanks.

### **Mass spectra semi-quantification**

Due to the contradictory information measured in the fluorescence plate reader method, it was decided to repeat some key experiments using LC-TQ-MS detection of resorufin as an endpoint. Initially the true run against different controls (no cofactor, no enzyme, different enzyme controls) which demonstrated, contrary to the fluorescence assay data, that the CYP1A reactors reproducibly produce resorufin from 7-ethoxyresorufin only when both NADPH and CYP1A enzyme is present in the reactors (Figure 6.13).

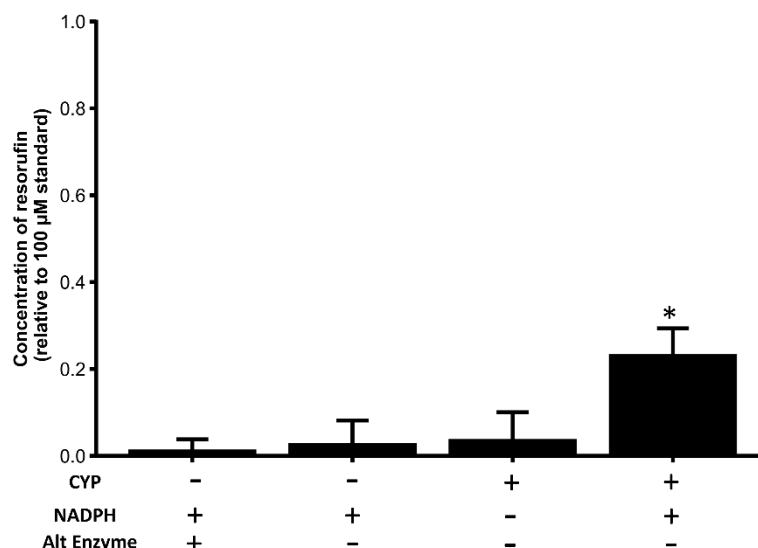


Figure 6.13: Comparison between mean resorufin formed  $\pm$  SD in a true run against a variety of different blanks using the exact same samples as Figure 6.1 which were frozen immediately after analysed. An ANOVA with Bonferroni corrections comparing the blanks and true run. \*,  $p < 0.05$ .

Contradictory to the fluorescence analysis method this shows that there is a significant difference between the blanks and the true run. This shows that upon metabolising using the CYP1a1 enzyme, an interferent is formed prior to or during the reaction causing a lack of fluorescence. The peak area was approximately 25% that of a 100  $\mu$ M standard in which assuming linearity up to this level, would have been visible in the working range of the plate reader fluorometric method but was not seen in the comparable experiments. It was noted that the trend in which the solution containing both the correct enzyme and co-factor yielded the highest overall product formed and the others showed almost no resorufin formation.

The determination of relative 7-ethoxyresorufin concentration was not viable for this analysis due to the concentration implemented within the device saturating the detector so an accurate peak area was not determined, but it is worth noting that the detector was no longer saturated upon flowing through the enzyme immobilised

device. Finally representative samples obtained using the previous flow rate experiments were analysed on the same method. Unfortunately, due to the amount of time remaining within the research phase of this study, very few repeats or samples were measured on the LC-MS to repeat the previous experiments to determine a true optimisation.

A small  $n=1$  study was undertaken on the 3 different flow rates (0.1, 0.5 and 1  $\mu\text{L min}^{-1}$ ) tested previously on this chapter by implementing them into the LC-TQ-MS. A small increase in relative peak area was visible at 0.1  $\mu\text{L min}^{-1}$ . No difference was visible between 0.5 and 1  $\mu\text{L min}^{-1}$ . Alongside this another  $n=1$  was analysed halving the initial substrate concentration for the 0.5  $\mu\text{L min}^{-1}$  flow rate from 100 to 50  $\mu\text{M}$ , this lowered the overall relative peak area by half demonstrating that the enzyme within the device was not saturated/limiting the product formation.

Future work would focus on the analysis of each of the parameters measured throughout this chapter *via* the use of LC-MS to determine more accurate concentration values.

#### **6.4. Discussion**

Throughout this chapter a wide variety of optimisation techniques have been tested including flow rate, temperature, incubating co-factor and syringe cooling and compared to three different blanks. The commonly used method of fluorescence analysis was used throughout this chapter for the determination of resorufin concentration. However, towards the end of this study it was determined that this was not accurate for this particular enzyme system as the highly fluorescent product was formed as shown by the mass spectrometry data in Figure 6.9-Figure 6.11 Due to time

constraints only, a select few samples were measured and compared to that of a standard equivalent to 100% conversion (100  $\mu\text{M}$ ). Due to this the data demonstrated in Figure 6.1-Figure 6.7 are not representative of the amount of product formed within the device. However, similar trends within this data are found comparable to the previous chapters such as blanks yielding lower results and lower flow rates typically providing a higher yield.

The first set of samples analysed *via* the mass spectrometry method described and optimised in section 2.6 were a comparison of a true enzymatic run to the three different blanks (Figure 6.13). This data showed a relative peak area of  $\sim 0.25$  equating to a 25% conversion assuming that there is a linear correlation between peak area and resorufin concentration; leading to a potential overall conversion of 25  $\mu\text{M}$ . Whereas very little 7-ethoxyresorufin was measured for any of the blanks showing that conversion is occurring only when both the correct co-factor and enzyme are available within the system. This is comparable to both of the previous chapters for UGT and SULT alongside that which has been described in the literature (Stiborová *et al.*<sup>319</sup> and Yu *et al.*<sup>320</sup>).

The other samples analysed were the 3 different flow rates and altering their initial concentration (data not shown). However, no repeats were conducted throughout these experiments. From the data obtained very little difference was found in conversion upon the three different flow rates and by lowering the initial substrate concentration by half, half of the product appeared to be formed. This shows that at the current conditions the enzyme is not saturated with substrate and that there is potential for product formation with further optimisation. Upon reaching the end of these experiments a repeat of the optimisation is required to determine whether the

parameters tested throughout this chapter were indeed the optimum. Although these problems have been identified, proof of conversion *via* this method has been shown. This demonstrates with further optimisation it will potentially be viable for the synthesis of naturally circulating metabolites. The next step of this research would be to recomplete the previous optimisation steps and quantify *via* mass spectrometry to allow a true measurement of product formed and bypass the fluorescence issues previously experienced.

The limitations of this work include the fluorescence data not correlating with that which was observed *via* mass spectrometry when comparing the different blanks vs. the true runs, in which a much larger resorufin peak was observed and was significantly different to the blanks.

The success of the previous chapters fluorescence analysis which was overarchingly proven *via* the use of LC-TQ-MS. The overarching trends in the previous two chapters were largely followed upon comparing the two different analytical techniques. Despite this, an interfering effect appears to have occurred within the matrix of the effluent of this immobilised enzyme device. Either *via* another reaction pathway which inhibits the resorufin fluorescence or the unreacted co-factor or degradation product (due to its relatively short half-life) also having an inhibitory effect.

Due to this, only limited results have been gained determining the optimum parameters in which only a comparison between blanks and true runs was obtained and a lack of repeats at different flow rates. Alongside this, due to a lack of fluorescence the use of Cypexpress enzymes were disregarded. However, after discovering a lack of fluorescence although a formation of resorufin was found these may also have yielded positive metabolism results.

## 6.5. Conclusion

This chapter aimed to optimise and develop a method allowing for the synthesis of oxidative metabolites utilising the enzyme CYP1a1. This method shows merit for the synthesis for these metabolites with mass spectrometry results showing fairly large peaks of resorufin. However, a quantitative analysis of product formed have unfortunately not been determined due to fluorometric issues within this biological matrix. Despite this, due to the mass spectrometry data it has been demonstrated that this device is functional in the formation of a CYP catalysed metabolite. However, further research and optimisation is necessary for the synthesis of necessary quantities allowing for further studies on a metabolite's effects on the human body.

## 7. General discussion

Within the human body, the beneficial or toxicological effects of compounds can be significantly changed by undergoing the metabolism of xenobiotics. In some cases, a previously beneficial compound can be metabolised into something that causes toxic effects on the body. For example, paracetamol if an alternative pathway is undertaken leading to the formation of NADPQI. This has led to the USFDA to altering their rules on the development of drugs when continuing to animal and later human testing; in which an understanding of metabolites formed is now required and the rules will become even more strict in the future.<sup>29</sup> Due to this, a method that allows for the synthesis of metabolic products for use as standards or test compounds for bioactivity/toxicity assessment is becoming increasingly necessary. In 2018 there was a recommendation highlighting that the use of metabolites will largely increase the pharmacological worth of a given study, but very little progress has been made due to the lack of availability of the pharmacologically relevant metabolites.<sup>30</sup> For example for propranolol which is a widely used beta blocker which is readily metabolised by CYP enzymes but their synthesis has been largely halted due to low yields, unwanted side products and the necessity for harsh reaction conditions.<sup>321</sup>

The current methods that focus on metabolite synthesis typically focus on the determination of which metabolites are formed *in vivo* and do not allow for the collection of sufficient quantities of product for the determination of a metabolite's pharmacological effects *via in vitro* analysis. The most common metabolites are typically formed *via* Cytochrome P450 (CYP) and UDP-glucuronosyl transferase (UGT) equating to over 90% of the observed metabolic products; with the third most

common being sulfotransferase (SULT).<sup>49, 322, 323</sup> Based on this, CYP1A, UGT1A and SULT1A were the chosen enzyme systems for that the development of enzyme-immobilised flow-through reactors that could bypass the frequently observed issues with currently used methods.

The use of immobilised enzymes has typically focussed solely on metabolite determination and rate measurements and very little focus has been made on the formation of these products in sufficient quantities. For example, immobilised laccase onto nano-porous silica was utilised by Dehghanifard *et al.*<sup>312</sup> to determine the biodegradation rate of 2,4- DNP and Gahlout *et al.*<sup>324, 325</sup> identified reactive violet 1 dye degradation metabolites *via* immobilised laccase on nano-porous silica beads using a silanization-glutaraldehyde linkage, comparable to that which was utilised throughout this thesis. Demonstrating that whilst the overarching methods utilised throughout this thesis have been thoroughly researched and utilised the large novelty of this research is the focus on synthesis bulk amounts of metabolic products which addresses an important limitation in pharmacology and drug discovery.

This thesis has demonstrated that this research shows advantages over many of the limitations (as discussed in 1.3) with the currently used methods for synthesising xenobiotic and drug metabolites. Key things which allow the reactors to do this are: (1) the flow-through nature of the devices means that there is constant removal of reaction products, preventing inhibition of the reaction by the products of the reaction; (2) The effects mentioned in point (1) and the microscale nature drive the reaction in the device (the effects of changes in temperature and flow rate suggest that the enzyme in the reactors do not behave the same as in free solution); (3) the immobilisation of

individual enzymes ensures that the complexity of reaction products is simplified as much as practical (such as extracting the products from a biologically complex matrix including enzyme/ enzyme system, substrate and co-factor).

Another limitation of previous methods is due to the particularly low yield that is frequently observed. It has been noted that throughout this thesis that in both the UGT and SULT optimised devices almost all of the available co-factor and substrate were utilised in the formation of their respective metabolic products, leading to  $\mu\text{g}$  quantities of metabolites within 2 hours as demonstrated in Figures Figure 4.8 and Figure 5.8. This thesis has focused on showing the reactors produce – *i.e.*, showing the production of expected reaction products, and thus has not explored the scalability of the reactors. Throughout all experiments in this thesis only a singular reactor has been assessed at a time, running multiple devices at a time would increase the obtained yield significantly and could lead to the formation of usable quantities (typically mg to allow sufficient repeats) of metabolic products. There have been multiple examples of scaling up and scaling out such as Chemtrix's Plantrix® MR555 device and IMT's glass moulding system.

Despite this there are still a variety of different optimisation steps that can be utilised to further drive the formation of metabolic products. For example, the use of alamethicin which has demonstrated the ability to enhance enzymatic activity for UGT microsomes and albumin has been demonstrated to increase some isoforms of both CYP and UGT microsomes.<sup>213</sup> Due to this research focussing on optimising a method for the synthesis of metabolic product and resorufin, the optimum parameters in conjunction were not tested as an already almost 100% conversion was found at 0.5

$\mu\text{L min}^{-1}$  so no measurable increase was observable altering other potential improvements such as temperature. The best alternative would be to increase the initial concentration of resorufin going into the inlet, but this is not available for the analysis of resorufin as it is not soluble at a much larger concentration. Dependant on the initial substrate flowing through the device a higher concentration would be available allowing for potentially more product formation, leading to less scaling up being necessary to provide sufficient mg amounts.

### **7.1. Limitations of this work**

There are five major limitations to this work: (1) a non-specific immobilization technique was used for throughout this thesis, and how enzymes were immobilized was not investigated; (2) The use of a fluorescence assay for substrate and product quantification during the optimisation steps for each reactor; (3) Use of very simple classical substrates for these reactions; (4) Only undertaking limited assessment of microfluidic reactor designs; (5) Not undertaking quantitative measurements of immobilised enzyme.

Initially, due to its ease of use, a general non-specific immobilisation protocol was used. This allowed for a higher applicability for more enzyme families

Any metabolite just by varying the co-factor and enzyme entering the system and due to the almost 100% yields that were observed for UGT, this method was continued for the use of SULT in which the overall conversion was comparable. In literature it has been demonstrated that there is significantly more variability in the orientation in which an enzyme is immobilised using an APTMS-glutaraldehyde linkage and that other

alternative methods yield more control and reproducibility.<sup>289, 326</sup> For example, affinity binding can be utilised to gain complete control on enzyme orientation upon immobilising, whilst this may be beneficial for a variety of different applications, based on the data observed in this thesis the consistent results in the amount of product formed in both the UGT and SULT devices demonstrates that there is high reproducibility using this immobilisation technique. This bypasses the need for altering the enzyme in any further modification such as biotinylation which has the potential to alter the active site and allows for a much more general assay method for a variety of different enzymes.

The second major limitation is due to the method of quantification. The method used for quantification was the fluorescence of resorufin, which as a substrate is highly fluorescent and when metabolised loses this fluorescence. This allows for a distinct measurement for the loss of resorufin. However, this is potentially not directly linked to the formation of metabolic products. A loss of fluorescence could be due to a shift in pH or the formation of an interfering compound. Despite this a proof of product formation was undertaken to demonstrate that, whilst direct quantification was not taken, product formation was measurable in a comparable size to that of a standard of the equivalent concentration. The conversion of 7-ethoxyresorufin into resorufin *via* CYP activity is frequently documented and used as a go to method for the determination of a CYP metabolic activity.<sup>327-329</sup> Concentrations ranges as low as 0.5 to 90 nM have been seen to yield linear calibrations.<sup>60</sup> Interestingly, this study demonstrated that in some cases the formation of resorufin is not visible *via* fluorometric analysis as contradictory results were found when the exact same sample was analysed *via* mass spectrometry. Initially it was theorised that very little metabolism was occurring within the device under the parameters tested as the

fluorescence analysis demonstrated very little product formation over two-hour periods. Whereas the LCMS analysis showed a yield of approximately 30% of initial substrate assuming peak area is directly proportional to concentration. This is comparable to the work presented here where approximately 30% of the substrate is observed in its respective metabolic form. With regards to UGT this may be due to the extraction method used and the ZipTips not being fully optimised. In order to determine if this method is viable for the synthesis of drug metabolites it is necessary to determine whether comparable formation is found for a variety of different substrates. To determine if a sulfate conjugated metabolite was formed an alternative substrate was required as resorufin sulfate is not commercially available, leading to the use of nitrophenol and its widely available metabolite nitrophenyl sulfate. Upon doing this it was observed that whilst the devices could metabolise resorufin, they could also metabolise nitrophenol demonstrating confidence in their ability to yield metabolic products rather than a device which can only facilitate reactions for a singular substrate.

Another limitation was due to the initial time-restricting issues that occurred throughout the CYP1a1 immobilised device, in which little quantification was observed due to the fluorescence of the product not being observed when peaks were measured under LC-TQ-MS analysis. For other fluorescence assays this may not be the most accurate method of quantification due to the issues noted with the CYP based device. Future experiments should include quantification using mass spectrometry or other alternative techniques.

A further limitation being a lack of device designs tested. There are a wide variety of devices designs that have yielded vastly superior surface area to volume ratio such as those with increased amounts of channels packed channels and micropillars within the channels. This increase in surface area to volume ratio may allow for considerably more interactions between the co-factor, enzyme and substrate allowing for more potential conversion. However, these devices structures may also yield excess backpressure comparable to those which were observed in the serpentine device. The final noteworthy limitation was the lack of immobilised enzyme quantification, this would allow for an accurate representation of rate of product formation and would allow further optimisation of enzyme concentration needed to be flowed through the device potentially saving costs on enzyme usage.

## **7.2. Future Work**

The work presented in this thesis has demonstrated the viability of the microfluidic approach for metabolite synthesis. The next steps to advance this work are as follows:

- Assessment of potential reactors to specifically metabolise more complex substrates (e.g., dietary polyphenols)
- Quantification of enzyme immobilisation which can be conducted by undergoing UV absorbance analysis at 280 nm prior to analysis and the value compared to a standard curve of known protein concentration<sup>330</sup>
- Scaling reactors to demonstrate synthesis of usable quantities of a specific metabolite
- Combining reactors to produce more complex metabolites

Other experiments which could be done, and may advance the work are:

- Look at different reactor designs
- Metabolism enhancers (alamethicin)
- Different immobilisation strategies

Initially observing the enzymes immobilised structure on the surface of the glass utilising a technique such as Fourier transform infrared (FT-IR) or scanning electron microscopy (SEM). This would demonstrate how the enzyme appears on the surface of the device. Undergoing this after the device has been used can demonstrate if the device can be repeatedly used and determine if or how much of the enzyme has been lost through a typical use. The next major test would be to optimise the extraction method using the C18 ZipTips further for the UGT1a1 metabolised substrates to allow for a true measurement of the product obtained and to determine the recoverability for this method. Undergoing this quantification would be undertaken utilising a method that is truly representative on the formation of product and not due to a loss of fluorescence as was undertaken in this study. For example, if the LC-TQ-MS method was optimised further and a calibration curve was utilised alongside the potentially optimised extraction method will allow for an accurate representative quantification of product.

Further optimisation steps of the device are available such as the addition of alamethicin which is known to increase enzymatic activity and has been used in cascade reactions to sequentially oxidise and conjugate glucuronic acid to 7-ethoxycoumarin by Fisher *et al.* This could potentially allow for an increase in product formation leading to a further improvement over alternative comparable methods.<sup>331</sup> However, as previously mentioned it has also some studies have shown that within flowthrough conditions this activity increase is not observed.<sup>213, 214</sup>

Upon fully optimising and developing truly representative quantitative analyses of these devices and products formed combining two of these devices together would be the next step of these devices. This would allow for the metabolism of more complex naturally forming products that require the use of multiple different enzymes. This prevents the need to add multiple enzymes to the same device, further complicating the immobilisation process and potentially significantly reduced catalytic activity. This could allow for the formation of multiply conjugated substrates that have been observed in some cases. This could apply to any of the previously optimised devices allowing for an almost endless variation of formation of metabolic products which will allow for their testing to determine their beneficial and toxicological effects on the human body.

The final step would be to apply this device to both drugs and nutraceuticals to allow the determination of their pharmacological effects *via* other *in vitro* studies to prevent the need for animal testing. This could be achieved by connecting the reactor outlet to for example, immobilised human cells, cell spheroids or tissue sections. This will also allow for the studies of compounds that have had contradictory information observed. This is frequently noticed when researching polyphenolic compounds where a single compound has been revealed to have no effect on the human body and both negative and beneficial effects. This is likely due to the variety of metabolites that can be formed within the human body in which can have significantly different pharmacological effects. As mentioned previously there is currently no method that allows for the formation of these metabolic products in quantities that allow for these studies. However, when fully optimised and scaled up, this method will allow for these studies

and in turn allow for the determination of a metabolic products beneficial and toxicological effects, preventing this contradictory information from arising.

## 8. Conclusion

The determination of a metabolic product's beneficial and toxicological effects is becoming increasingly important for the effective development of drugs, and in order to facilitate this testing a method that allows for their synthesis is necessary.

The current methods that focus on metabolite formation typically focus on measuring their formation *in vivo* and not on synthesising usable quantities. Testing potential drug candidates involved determining which metabolites are formed and whether they are likely to be toxic or beneficial in the concentration they are found. However, in some cases this can lead to contradictory information. Polyphenols are an example of this in which contradictory information is found showing that these compounds possess both beneficial and toxicological of the same effect such as anti-oxidative/oxidative effects.

In this study a method has been developed that can potentially allow for the formation of conjugative metabolic products simply, without the need for a complex extraction from a biological matrix. Using this method, a much simpler c18 extraction was effective in extracting the sample from the phosphate buffer and allowing for product measurement. Due to the concentration being determined *via* loss of fluorescence an assumption was made in which the loss of fluorescence was directly linked to the amount of product formed. However, if this assumption was correct for both UGT and SULT devices the synthesis of  $\mu\text{g}$  quantities which is less than the needed amount for further studies. However, testing higher concentrations was not available due to the solubility limit of resorufin (the test substrate used). With further optimisations, scaling

up or running the device for a longer period of time (if the device is stable over this longer period) sufficient product could potentially be formed using this method.

The CYP based device requires much more optimisation and further understanding prior to and significant synthetic use due to issues with fluorescence analysis. Analysing these oxidative metabolites using quantitative mass spectrometry would allow a more accurately determined amount of product formed and with further optimisations if necessary to be used for the synthesis of sufficient quantities for further studies that can be used as an analytical standard.

Overall, these devices provide promise for the production of these metabolic products in high quantity when compared to other methods with a similar focus, but further quantitative measurements are required to ensure that the fluorescence-based measurements demonstrate an accurate representation of product formed is needed. If these are determined to be comparable, this demonstrates that with scaling up this method can allow for the synthesis of metabolic products and the next step would be to test a known drug/nutraceutical to determine if a single isomeric product is formed or if a mixture of potential metabolites is obtained. If a single isomer of a product is formed within the device, this will allow for simpler testing of these compounds and would not require and complex extraction. However, if multiple metabolites are formed, whilst an extraction would be required between similar metabolites this could potentially allow for the testing of multiple metabolites singularly from one device.

# References

1. H. Gao, A. Jacobs, R. E. White, B. P. Booth and R. S. Obach, *AAPS J*, 2013, **15**, 970-973.
2. N. Koppel, V. Maini Rekdal and E. P. Balskus, *Science*, 2017, **356**, eaag2770.
3. S. Phang-Lyn and V. A. Llerena, in *StatPearls*, Treasure Island (FL), 2022.
4. R. Yang, T. Wei, H. Goldberg, W. Wang, K. Cullion and D. S. Kohane, *Adv Mater*, 2017, **29**, 1606596.
5. C. J. Omiecinski, J. P. Vanden Heuvel, G. H. Perdew and J. M. Peters, *Toxicol Sci*, 2011, **120 Suppl 1**, S49-75.
6. A. Z. Garza, S. B. Park and R. Kocz, in *StatPearls*, Treasure Island (FL), 2022.
7. M. S. Alavijeh, M. Chishty, M. Z. Qaiser and A. M. Palmer, *NeuroRx*, 2005, **2**, 554-571.
8. P. K. Robinson, *Essays Biochem*, 2015, **59**, 1-41.
9. P. David Josephy, F. Peter Guengerich and J. O. Miners, *Drug Metab Rev*, 2005, **37**, 575-580.
10. M. Evans, E. Paterson and D. M. Barnes, *BMC Complement Altern Med*, 2014, **14**, 475.
11. P. Jancova, P. Anzenbacher and E. Anzenbacherova, *Biomed Pap Med Fac Univ Palacky Olomouc Czech Repub*, 2010, **154**, 103-116.
12. S. Ge, Y. Tu and M. Hu, *Curr Pharmacol Rep*, 2016, **2**, 326-338.
13. H. Raunio, M. Kuusisto, R. O. Juvonen and O. T. Pentikainen, *Front Pharmacol*, 2015, **6**, 123.
14. V. Mordvinov and M. Pakharukova, *Biomedicines*, 2022, **10**, 12: 3039.
15. E. E. J. Kasteel, K. Darney, N. I. Kramer, J. Dorne and L. S. Lautz, *Arch Toxicol*, 2020, **94**, 2637-2661.
16. Q. Zhou, Z. Zheng, B. Xia, L. Tang, C. Lv, W. Liu, Z. Liu and M. Hu, *Pharm Res*, 2010, **27**, 1568-1583.
17. R. de la Torre, M. Farre, A. Verdejo-Garcia, E. Cuyas and R. Pardo, *Biological Research on Addiction: Comprehensive Addictive Behaviors and Disorders, Volume 2*, 2013, **2**, 441.
18. M. Kumondai, E. M. Gutierrez Rico, E. Hishinuma, A. Ueda, S. Saito, D. Saigusa, S. Tadaka, K. Kinoshita, T. Nakayoshi, A. Oda, A. Abe, M. Maekawa, N. Mano, N. Hirasawa and M. Hiratsuka, *Drug Metab Dispos*, 2021, **49**, 212-220.
19. S. J. Richardson, A. Bai, A. A. Kulkarni and M. F. Moghaddam, *Drug Metab Lett*, 2016, **10**, 83-90.
20. K. A. Norris, M. Dobrota, F. S. Issa, R. H. Hinton and E. Reid, *Biochem J*, 1974, **142**, 667-671.
21. Z. Bibi, *Nutr Metab (Lond)*, 2014, **11**, 11.
22. Y. Liu, J. Ramirez and M. J. Ratain, *Br J Clin Pharmacol*, 2011, **71**, 917-920.
23. L. L. Mazaleuskaya, K. Sangkuhl, C. F. Thorn, G. A. FitzGerald, R. B. Altman and T. E. Klein, *Pharmacogenet Genomics*, 2015, **25**, 416-426.
24. M. R. McGill and H. Jaeschke, *Pharm Res*, 2013, **30**, 2174-2187.
25. M. Sciskalska, M. Sliwinska-Mosson, M. Podawacz, W. Sajewicz and H. Milnerowicz, *Drug Chem Toxicol*, 2015, **38**, 121-125.
26. S. S. Kalsi, P. I. Dargan, W. S. Waring and D. M. Wood, *Open Access Emerg Med*, 2011, **3**, 87-96.
27. Y. L. Teo, H. K. Ho and A. Chan, *Br J Clin Pharmacol*, 2015, **79**, 241-253.
28. P. R. Ortiz de Montellano, *Future Med Chem*, 2013, **5**, 213-228.
29. S. Schadt, B. Bister, S. K. Chowdhury, C. Funk, C. Hop, W. G. Humphreys, F. Igarashi, A. D. James, M. Kagan, S. C. Khojasteh, A. N. R. Nedderman, C. Prakash, F. Runge, H. Scheible, D. K. Spracklin, P. Swart, S. Tse, J. Yuan and R. S. Obach, *Drug Metab Dispos*, 2018, **46**, 865-878.
30. M. A. Avila-Galvez, A. Gonzalez-Sarrias and J. C. Espin, *J Agric Food Chem*, 2018, **66**, 7857-7858.
31. P. Mena and D. Del Rio, *J Agric Food Chem*, 2018, **66**, 8221-8223.
32. B. Wu, K. Kulkarni, S. Basu, S. Zhang and M. Hu, *J Pharm Sci*, 2011, **100**, 3655-3681.
33. S. Basiliere and S. Kerrigan, *J Anal Toxicol*, 2020, **44**, 301-313.

34. C. C. J. Fitzgerald, R. Hedman, D. R. Uduwela, B. Paszerbovics, A. J. Carroll, T. Neeman, A. Cawley, L. Brooker and M. D. McLeod, *Front Mol Biosci*, 2022, **9**, 829511.
35. M. Srejber, V. Navratilova, M. Paloncycova, V. Bazgier, K. Berka, P. Anzenbacher and M. Otyepka, *J Inorg Biochem*, 2018, **183**, 117-136.
36. M. Zhao, J. Ma, M. Li, Y. Zhang, B. Jiang, X. Zhao, C. Huai, L. Shen, N. Zhang, L. He and S. Qin, *Int J Mol Sci*, 2021, **22**, (23):12808.
37. K. Monostory and Z. Dvorak, *Current Drug Metabolism*, 2011, **12**, 154-172.
38. B. Zhao, F. P. Guengerich, M. Voehler and M. R. Waterman, *J Biol Chem*, 2005, **280**, 42188-42197.
39. T. Laursen, K. Jensen and B. L. Moller, *Biochim Biophys Acta*, 2011, **1814**, 132-138.
40. T. Ge, J. Yang, S. Zhou, Y. Wang, Y. Li and X. Tong, *Front Endocrinol (Lausanne)*, 2020, **11**, 365.
41. P. R. Bradshaw, T. J. Athersuch, A. V. Stachulski and I. D. Wilson, *Drug Discov Today*, 2020, **25**, 1639-1650.
42. R. Klimas and G. Mikus, *Br J Anaesth*, 2014, **113**, 935-944.
43. S. S. Lewis, M. R. Hutchinson, N. Rezvani, L. C. Loram, Y. Zhang, S. F. Maier, K. C. Rice and L. R. Watkins, *Neuroscience*, 2010, **165**, 569-583.
44. B. Dudas, D. Toth, D. Perahia, A. B. Nicot, E. Balog and M. A. Miteva, *Sci Rep*, 2021, **11**, 13129.
45. J. van den Boom, D. Heider, S. R. Martin, A. Pastore and J. W. Mueller, *J Biol Chem*, 2012, **287**, 17645-17655.
46. K. V. Venkatachalam, *IUBMB Life*, 2003, **55**, 1-11.
47. L. Barre, S. Fournel-Gigleux, M. Finel, P. Netter, J. Magdalou and M. Ouzzine, *FEBS J*, 2007, **274**, 1256-1264.
48. N. L. Dang, T. B. Hughes, V. Krishnamurthy and S. J. Swamidass, *Bioinformatics*, 2016, **32**, 3183-3189.
49. R. Fujiwara, E. Yoda and R. H. Tukey, *Drug Metab Pharmacokinet*, 2018, **33**, 9-16.
50. L. A. Reinke and M. J. Moyer, *Drug Metab Dispos*, 1985, **13**, 548-552.
51. A. Mahli, W. Erwin Thasler and C. Hellerbrand, *Toxicol Mech Methods*, 2019, **29**, 219-223.
52. S. X. Hu, *J Vet Pharmacol Ther*, 2017, **40**, 270-278.
53. U. D. Kuhn, M. Rost and D. Muller, *Exp Toxicol Pathol*, 2001, **53**, 81-87.
54. G. A. Gowda and D. Djukovic, *Methods Mol Biol*, 2014, **1198**, 3-12.
55. A. Kanakubo and M. Isobe, *J Mass Spectrom*, 2004, **39**, 1260-1267.
56. R. Csepregi, B. Lemli, S. Kunsagi-Mate, L. Szenté, T. Koszegi, B. Nemeti and M. Poor, *Molecules*, 2018, **23**, (2), 382.
57. D. Slowinski, M. Swierczynska, J. Romanski and R. Podsiadly, *Molecules*, 2022, **27**, (23) 8305.
58. A. A. Bunaciu, E. G. Udristioiu and H. Y. Aboul-Enein, *Crit Rev Anal Chem*, 2015, **45**, 289-299.
59. M. P. M. Letertre, P. Giraudeau and P. de Tullio, *Front Mol Biosci*, 2021, **8**, 698337.
60. G. Zamaratskaia and V. Zlabek, *Sensors (Basel)*, 2009, **9**, 2134-2147.
61. P. Heinrich, U. Diehl, F. Forster and T. Braunbeck, *Comp Biochem Physiol C Toxicol Pharmacol*, 2014, **164**, 27-34.
62. L. Tian, H. Feng, Z. Dai and R. Zhang, *J Mater Chem B*, 2021, **9**, 53-79.
63. D. Havrylyuk, A. C. Hachey, A. Fenton, D. K. Heidary and E. C. Glazer, *Nat Commun*, 2022, **13**, 3636.
64. Y. Djoumbou-Feunang, J. Fiamoncini, A. Gil-de-la-Fuente, R. Greiner, C. Manach and D. S. Wishart, *J Cheminform*, 2019, **11**, 2.
65. Z. Gagic, D. Ruzic, N. Djokovic, T. Djikic and K. Nikolic, *Front Chem*, 2019, **7**, 873.
66. M. Huang, C. Lou, Z. Wu, W. Li, P. W. Lee, Y. Tang and G. Liu, *J Cheminform*, 2022, **14**, 46.
67. J. da Veiga Moreira, M. Hamraz, M. Abolhassani, L. Schwartz, M. Jolicoeur and S. Peres, *Sci Rep*, 2019, **9**, 3153.
68. J. Weber, M. Vaclavikova, G. Wiesenberger, M. Haider, C. Hametner, J. Frohlich, F. Berthiller, G. Adam, H. Mikula and P. Fruhmam, *Org Biomol Chem*, 2018, **16**, 2043-2048.

69. D. C. Blakemore, L. Castro, I. Churcher, D. C. Rees, A. W. Thomas, D. M. Wilson and A. Wood, *Nat Chem*, 2018, **10**, 383-394.
70. K. A. Fay, P. N. Fitzsimmons, A. D. Hoffman and J. W. Nichols, *Environ Toxicol Chem*, 2017, **36**, 463-471.
71. P. Jithavech, P. Ratnatilaka Na Bhuket, W. Supasena, G. Qiu, S. Ye, J. Wu, T. W. Wong and P. Rojsitthisak, *Front Pharmacol*, 2020, **11**, 577998.
72. R. de Cassia Ribeiro Goncalves, R. Rezende Kitagawa, E. Aparecida Varanda, M. Stella Goncalves Raddi, C. Andrea Leite and S. Regina Pombeiro Sponchiado, *Pharm Biol*, 2016, **54**, 1014-1021.
73. A. Hakura, S. Suzuki, S. Sawada, T. Sugihara, Y. Hori, K. Uchida, W. D. Kerns, F. Sagami, S. Motooka and T. Satoh, *Regul Toxicol Pharmacol*, 2003, **37**, 20-27.
74. S. A. Nowell, J. E. Leakey, J. F. Warren, N. P. Lang and L. T. Frame, *J Biol Chem*, 1998, **273**, 33342-33346.
75. L. Jia and X. Liu, *Curr Drug Metab*, 2007, **8**, 822-829.
76. Y. Iwasaki, T. Sawada, K. Hatayama, A. Ohyagi, Y. Tsukuda, K. Namekawa, R. Ito, K. Saito and H. Nakazawa, *Metabolites*, 2012, **2**, 496-515.
77. S. Chen, L. Liu, Y. Yang, Z. Dai and F. Zeng, *J Tongji Med Univ*, 2000, **20**, 253-256.
78. V. Palchevskiy and S. E. Finkel, *J Bacteriol*, 2006, **188**, 3902-3910.
79. C. T. Chung and R. H. Miller, *Methods Enzymol*, 1993, **218**, 621-627.
80. Q. Tu, J. Yin, J. Fu, J. Herrmann, Y. Li, Y. Yin, A. F. Stewart, R. Muller and Y. Zhang, *Sci Rep*, 2016, **6**, 24648.
81. A. Froger and J. E. Hall, *J Vis Exp*, 2007, DOI: 10.3791/253, 253.
82. H. Potter, *Curr Protoc Mol Biol*, 2003, **Chapter 9**, Unit 9 3.
83. E. T. Jordan, M. Collins, J. Terefe, L. Ugozzoli and T. Rubio, *Journal of biomolecular techniques: JBT*, 2008, **19**, 328.
84. G. L. Rosano and E. A. Ceccarelli, *Front Microbiol*, 2014, **5**, 172.
85. B. Jia and C. O. Jeon, *Open Biol*, 2016, **6**, (8) 160196.
86. D. M. Francis and R. Page, *Curr Protoc Protein Sci*, 2010, **Chapter 5**, 5 24 21-25 24 29.
87. C. Langlais, B. Guilleaume, N. Wermke, T. Scheuermann, L. Ebert, J. LaBaer and B. Korn, *BMC Biotechnol*, 2007, **7**, 64.
88. Y. C. Wang, S. E. Peterson and J. F. Loring, *Cell Res*, 2014, **24**, 143-160.
89. P. Goettig, *Int J Mol Sci*, 2016, **17**, 12.
90. S. Nanjappan, D. Paul and L. Bolla, *Studies in natural products chemistry*, 2018, **59**, 283-322.
91. K. Zeilinger, N. Freyer, G. Damm, D. Seehofer and F. Knospel, *Exp Biol Med (Maywood)*, 2016, **241**, 1684-1698.
92. P. J. Walsh, T. W. Moon and T. P. Mommsen, *Physiological zoology*, 1985, **58**, 727-735.
93. L. Docci, N. Milani, T. Ramp, A. A. Romeo, P. Godoy, D. O. Franyuti, S. Krahenbuhl, M. Gertz, A. Galetin, N. Parrott and S. Fowler, *Lab Chip*, 2022, **22**, 1187-1205.
94. M. J. Gomez-Lechon, J. V. Castell and M. T. Donato, *Expert Opin Drug Metab Toxicol*, 2008, **4**, 837-854.
95. M. J. Bailey and R. G. Dickinson, *J Pharmacol Toxicol Methods*, 1999, **41**, 27-32.
96. M. Sudo, M. Nishihara, J. Takahashi and S. Asahi, *Drug Metab Dispos*, 2017, **45**, 734-736.
97. J. G. Hengstler, D. Utesch, P. Steinberg, K. L. Platt, B. Diener, M. Ringel, N. Swales, T. Fischer, K. Biefang, M. Gerl, T. Bottger and F. Oesch, *Drug Metab Rev*, 2000, **32**, 81-118.
98. M. Saliem, F. Holm, R. B. Tengzelius, C. Jorns, L. M. Nilsson, B. G. Ericzon, E. Ellis and O. Hovatta, *World J Hepatol*, 2012, **4**, 176-183.
99. C. Terry, A. Dhawan, R. R. Mitry, S. C. Lehec and R. D. Hughes, *Liver Transpl*, 2010, **16**, 229-237.
100. S. Jitraruch, A. Dhawan, R. D. Hughes, C. Filippi, S. C. Lehec, L. Glover and R. R. Mitry, *Cell Transplant*, 2017, **26**, 1341-1354.

101. M. J. Gomez-Lechon, A. Lahoz, N. Jimenez, J. Vicente Castell and M. T. Donato, *Xenobiotica*, 2006, **36**, 457-472.
102. X. Liu, K. Lam, H. Zhao, S. Sakane, H. Y. Kim, A. Eguileor, K. Diggle, S. Wu, R. C. Gontijo Weber, P. Soroosh, M. Hosseini, K. Mekeel, D. A. Brenner and T. Kisseleva, *STAR Protoc*, 2023, **4**, 102391.
103. Z. C. Nwosu, N. Battello, M. Rothley, W. Pioronska, B. Sitek, M. P. Ebert, U. Hofmann, J. Sleeman, S. Wolfl, C. Meyer, D. A. Megger and S. Dooley, *J Exp Clin Cancer Res*, 2018, **37**, 211.
104. S. R. Nagarajan, M. Paul-Heng, J. R. Krycer, D. J. Fazakerley, A. F. Sharland and A. J. Hoy, *Am J Physiol Endocrinol Metab*, 2019, **316**, E578-E589.
105. J. Shi, X. Wang, L. Lyu, H. Jiang and H. J. Zhu, *Drug Metab Pharmacokinet*, 2018, **33**, 133-140.
106. K. Matsuyama, T. Tanaka, A. Noda, S. Goto and S. Iguchi, *J Pharmacobiodyn*, 1985, **8**, 193-198.
107. M. Ooka, C. Lynch and M. Xia, *Int J Mol Sci*, 2020, **21**, (21) 8182.
108. F. Li, J. Lu and X. Ma, *Chem Res Toxicol*, 2011, **24**, 744-751.
109. L. Zhang, X. Qu, Y. Teng, J. Shi, P. Yu, T. Sun, J. Wang, Z. Zhu, X. Zhang, M. Zhao, J. Liu, B. Jin, Y. Luo, Z. Teng, Y. Dong, F. Wen, Y. An, C. Yuan, T. Chen, L. Zhou, Y. Chen, J. Zhang, Z. Wang, J. Qu, F. Jin, J. Zhang, X. Jin, X. Xie, J. Wang, L. Man, L. Fu and Y. Liu, *J Clin Oncol*, 2017, **35**, 3558-3565.
110. E. R. Lepper, N. F. Smith, M. C. Cox, C. D. Scripture and W. D. Figg, *Curr Drug Metab*, 2006, **7**, 677-685.
111. R. Fujiwara, T. Yokoi and M. Nakajima, *Front Pharmacol*, 2016, **7**, 388.
112. J. Swann, J. Murry and J. A. Young, *Virology*, 2016, **13**, 30.
113. N. Tsamandouras, T. Kostrzewski, C. L. Stokes, L. G. Griffith, D. J. Hughes and M. Cirit, *J Pharmacol Exp Ther*, 2017, **360**, 95-105.
114. R. E. Pearce, C. J. McIntyre, A. Madan, U. Sanzgiri, A. J. Draper, P. L. Bullock, D. C. Cook, L. A. Burton, J. Latham, C. Nevins and A. Parkinson, *Arch Biochem Biophys*, 1996, **331**, 145-169.
115. M. V. Krishna, K. Padmalatha and G. Madhavi, *Drug Metabolism*, 2021, **77**.
116. C. Wegler, P. Matsson, V. Krogstad, J. Urdzik, H. Christensen, T. B. Andersson and P. Artursson, *Mol Pharm*, 2021, **18**, 1792-1805.
117. L. Di, C. Keefer, D. O. Scott, T. J. Strelevitz, G. Chang, Y. A. Bi, Y. Lai, J. Duckworth, K. Fenner, M. D. Troutman and R. S. Obach, *Eur J Med Chem*, 2012, **57**, 441-448.
118. J. Kiebitz, K.-U. Schmidtke, M. Schramm, R. König, S. Quint, J. Kohlmann, R. Zuhse, R. Ullrich, M. Hofrichter and K. Scheibner, *Journal of Fungi*, 2021, **7**, 752.
119. G. Tuffal, S. Roy, M. Lavisse, D. Bresseur, J. Schofield, N. D. Touchard, P. Savi, N. Bremond, M.-C. Rouchon and F. Hurbin, *Thrombosis and haemostasis*, 2011, **105**, 696-705.
120. A. A. Homaei, R. Sariri, F. Vianello and R. Stevanato, *J Chem Biol*, 2013, **6**, 185-205.
121. Y. Zhu, Q. Chen, L. Shao, Y. Jia and X. Zhang, *Reaction Chemistry & Engineering*, 2020, **5**, 9-32.
122. M. J. Uddin, N. H. Bhuiyan and J. S. Shim, *Sci Rep*, 2021, **11**, 1986.
123. M. Thiele, A. Knauer, D. Malsch, A. Csaki, T. Henkel, J. M. Kohler and W. Fritzsche, *Lab Chip*, 2017, **17**, 1487-1495.
124. S. Sharma, M. Srisa-Art, S. Scott, A. Asthana and A. Cass, *Methods Mol Biol*, 2013, **949**, 207-230.
125. P. Dimitriou, J. Li, G. Tornillo, T. McCloy and D. Barrow, *Glob Chall*, 2021, **5**, 2000123.
126. S. Damiani, U. B. Kompella, S. A. Damiani and R. Kodzius, *Genes (Basel)*, 2018, **9**.
127. O. Sartipzadeh, S. M. Naghib, F. Haghirsadat, F. Shokati and M. Rahmadian, *Sci Rep*, 2022, **12**, 8382.
128. W. M. Zhou, Y. Y. Yan, Q. R. Guo, H. Ji, H. Wang, T. T. Xu, B. Makabel, C. Pilarsky, G. He, X. Y. Yu and J. Y. Zhang, *J Nanobiotechnology*, 2021, **19**, 312.
129. C. W. Fung, S. N. Chan and A. R. Wu, *Biomicrofluidics*, 2020, **14**, 021502.

130. X. Luo, J. Y. Chen, M. Ataei and A. Lee, *Biosensors (Basel)*, 2022, **12**, (2) 58.
131. G. Vladislavljević, R. Al Nuumani and S. Nabavi, *Journal*, 2017, **8**, (3) 75.
132. W. Wang, B.-Y. Li, M.-J. Zhang, Y.-Y. Su, D.-W. Pan, Z. Liu, X.-J. Ju, R. Xie, Y. Faraj and L.-Y. Chu, *Chemical Engineering Journal*, 2023, **452**, 139277.
133. M. J. Männel, E. Baysak and J. Thiele, *Molecules*, 2021, **26**, 2817.
134. Y. Sun, in *Multidisciplinary Microfluidic and Nanofluidic Lab-on-a-chip*, Elsevier, 2022, pp. 99-142.
135. S.-u. Hassan, *Encyclopedia*, 2020, **1**, 30-41.
136. A. Mashhadian and A. Shamloo, *Anal Chim Acta*, 2019, **1083**, 137-149.
137. K. B. Lynch, A. Chen and S. Liu, *Talanta*, 2018, **177**, 94-103.
138. C. Heuer, J. A. Preuß, T. Habib, A. Enders and J. Bahnemann, *Engineering in life sciences*, 2022, **22**, 744-759.
139. G.-Y. Kim, J.-I. Han and J.-K. Park, *BioChip Journal*, 2018, **12**, 257-267.
140. X. Xue, H. Ye and Z. Hu, *J. Phys.: Conf. Ser.* 2021, **2012**, 012129.
141. D. Jiang, C. Ni, W. Tang, D. Huang and N. Xiang, *Biomicrofluidics*, 2021, **15**, 041501.
142. K. Choi, H. Ryu, K. J. Siddle, A. Piantadosi, L. Freimark, D. J. Park, P. Sabeti and J. Han, *Analytical chemistry*, 2018, **90**, 4657-4662.
143. J. Lim, B. Kang, H. Y. Son, B. Mun, Y.-M. Huh, H. W. Rho, T. Kang, J. Moon, J.-J. Lee and S. B. Seo, *Biosensors and Bioelectronics*, 2022, **197**, 113753.
144. N. Bargahi, S. Ghasemali, S. Jahandar-Lashaki and A. Nazari, *Biological Procedures Online*, 2022, **24**, 1-20.
145. C. Li, W. He, N. Wang, Z. Xi, R. Deng, X. Liu, R. Kang, L. Xie and X. Liu, *Frontiers in Bioengineering and Biotechnology*, 2022, **10**, 907232.
146. E. Noviana, T. Ozer, C. S. Carrell, J. S. Link, C. McMahon, I. Jang and C. S. Henry, *Chem Rev*, 2021, **121**, 11835-11885.
147. H. Heidari-Bafroui, A. Kumar, C. Hahn, N. Scholz, A. Charbaji, N. Rahmani, C. Anagnostopoulos and M. Faghri, *Biosensors*, 2023, **13**, 310.
148. M. S. Verma, M.-N. Tsaloglou, T. Sisley, D. Christodouleas, A. Chen, J. Milette and G. M. Whitesides, *Biosensors and Bioelectronics*, 2018, **99**, 77-84.
149. D. Lin, B. Li, L. Fu, J. Qi, C. Xia, Y. Zhang, J. Chen, J. Choo and L. Chen, *Microsystems & Nanoengineering*, 2022, **8**, 53.
150. X. Wang, X.-Z. Hong, Y.-W. Li, Y. Li, J. Wang, P. Chen and B.-F. Liu, *Military Medical Research*, 2022, **9**, 1-27.
151. T. Bhardwaj, L. N. Ramana and T. K. Sharma, *Biosensors*, 2022, **12**, 357.
152. K. Jiang, D. S. Jokhun and C. T. Lim, *Journal of Biomechanics*, 2021, **117**, 110235.
153. T. Pinheiro, A. R. Cardoso, C. E. Sousa, A. C. Marques, A. P. Tavares, A. M. Matos, M. T. Cruz, F. T. Moreira, R. Martins and E. Fortunato, *ACS omega*, 2021, **6**, 29268-29290.
154. J. Wang, J. L. Davidson, S. Kaur, A. A. Dextre, M. Ranjbaran, M. S. Kamel, S. M. Athalye and M. S. Verma, *Biosensors*, 2022, **12**, 1094.
155. S. Kim and J.-H. Lee, *Biochip journal*, 2022, 1-21.
156. S. Sarkar, A. F. Nieuwenhuis and S. G. Lemay, *Anal Chem*, 2023, **95**, 4266-4270.
157. J. Aleman, T. Kilic, L. S. Mille, S. R. Shin and Y. S. Zhang, *Nature Protocols*, 2021, **16**, 2564-2593.
158. M. B. Kulkarni, N. H. Ayachit and T. M. Aminabhavi, *Biosensors*, 2022, **12**, 543.
159. Y.-S. Chen, C.-H. Huang, P.-C. Pai, J. Seo and K. F. Lei, *Biosensors*, 2023, **13**, 83.
160. R. Vasiliadou, M. M. Nasr Esfahani, N. J. Brown and K. J. Welham, *Sensors*, 2016, **16**, 1418.
161. E. Nouri-Nigjeh, R. Bischoff, A. P Bruins and H. P Permentier, *Current drug metabolism*, 2011, **12**, 359-371.
162. M. Odijk, A. Baumann, W. Lohmann, F. T. G. van den Brink, W. Olthuis, U. Karst and A. van den Berg, *Lab on a Chip*, 2009, **9**, 1687-1693.

163. D. Huh, D. C. Leslie, B. D. Matthews, J. P. Fraser, S. Jurek, G. A. Hamilton, K. S. Thorneloe, M. A. McAlexander and D. E. Ingber, *Sci Transl Med*, 2012, **4**, 159ra147.
164. F. Shahabipour, S. Satta, M. Mahmoodi, A. Sun, N. R. de Barros, S. Li, T. K. Hsiai and N. Ashammakhi, *Biofabrication*, 2022, **15**, (2) .
165. K. T. Lawlor, J. M. Vanslambrouck, J. W. Higgins, A. Chambon, K. Bishard, D. Arndt, P. X. Er, S. B. Wilson, S. E. Howden and K. S. Tan, *Nature Materials*, 2021, **20**, 260-271.
166. M. A. Polidoro, E. Ferrari, S. Marzorati, A. Lleo and M. Rasponi, *Liver international*, 2021, **41**, 1744-1761.
167. P. Yu, Z. Duan, S. Liu, I. Pachon, J. Ma, G. P. Hemstreet and Y. Zhang, *Micromachines*, 2022, **13**, 3.
168. P. Zoio and A. Oliva, *Pharmaceutics*, 2022, **14**, 682.
169. X. Dong, L. Liu, Y. Tu, J. Zhang, G. Miao, L. Zhang, S. Ge, N. Xia, D. Yu and X. Qiu, *TrAC Trends in Analytical Chemistry*, 2021, **143**, 116377.
170. M. B. Kulkarni and S. Goel, *Engineering Research Express*, 2020, **2**, 042001.
171. K. Wu, X. He, J. Wang, T. Pan, R. He, F. Kong, Z. Cao, F. Ju, Z. Huang and L. Nie, *Frontiers in Bioengineering and Biotechnology*, 2022, **10**, 2373.
172. Y. Shi, P. Ye, K. Yang, J. Meng, J. Guo, Z. Pan, Q. Bayin and W. Zhao, *Journal of Healthcare Engineering*, 2021, **2021**, 1-24.
173. Q. Lin, D. Wen, J. Wu, L. Liu, W. Wu, X. Fang and J. Kong, *Analytical chemistry*, 2020, **92**, 9454-9458.
174. K. S. Elvira, X. C. i Solvas, R. C. Wootton and A. J. Demello, *Nature chemistry*, 2013, **5**, 905-915.
175. Y. Liu and X. Jiang, *Lab on a Chip*, 2017, **17**, 3960-3978.
176. W. D. Ristenpart, J. Wan and H. A. Stone, *Analytical chemistry*, 2008, **80**, 3270-3276.
177. F. W. Ling, H. A. Abdulbari and S. Y. Chin, *ChemBioEng Reviews*, 2022, **9**, 265-285.
178. R. Rosenthal, X. Zhang, K. Ilic Durdic, J. J. Collins and D. A. Weitz, *Angewandte Chemie*, 2023, e202303112.
179. E. Roy, A. Pallandre, B. Zribi, M. C. Horny, F. D. Delapierre, A. Cattoni, J. Gamby and A. M. Haghiri-Gosnet, *Advances in Microfluidics-New Applications in Biology, Energy, and Materials Sciences*, 2016.
180. S. M. Scott and Z. Ali, *Micromachines (Basel)*, 2021, **12**, 319.
181. S. I. Funano, N. Ota and Y. Tanaka, *Lab Chip*, 2021, **21**, 2244-2254.
182. H. E. Skallevoid, D. Rokaya, Z. Khurshid and M. S. Zafar, *Int J Mol Sci*, 2019, **20**, (23) 5960.
183. T. Nakao, K. Mawatari, Y. Kazoe, E. Mori, H. Shimizu and T. Kitamori, *Analyst*, 2019, **144**, 6625-6634.
184. C. Mazio, L. S. Scognamiglio, R. Passariello, V. Panzetta, C. Casale, F. Urciuolo, L. J. V. Galietta, G. Imperato and P. A. Netti, *ACS Biomater Sci Eng*, 2023, **9**, 2780-2792.
185. W. Wu, P. Rezai, H. Hsu and P. Selvaganapathy, in *Microfluidic devices for biomedical applications*, Elsevier, 2013, pp. 3-62.
186. A. Bahadorimehr and B. Y. Majlis, *Elektronika ir Elektrotechnika*, 2011, **116**, 45-48.
187. S. Johari, N. Tamilchelvan, M. N. M. Nor, M. M. Ramli, B. N. Taib, M. Mazalan and Y. Wahab, 2014.
188. A. O. AlSuhaimi and T. McCreedy, *Arabian Journal of Chemistry*, 2011, **4**, 195-203.
189. C. Iliescu, H. Taylor, M. Avram, J. Miao and S. Franssila, *Biomicrofluidics*, 2012, **6**, 16505-1650516.
190. J. Lee and M. Kim, *Biosensors (Basel)*, 2022, **12**, 1162.
191. C. W. Tsao and W. C. Syu, *RSC Adv*, 2020, **10**, 30289-30296.
192. T. Ito, K. Sobue and S. Ohya, *Sensors and Actuators B: Chemical*, 2002, **81**, 187-195.
193. M. Castaño-Álvarez, D. F. P. Ayuso, M. G. Granda, M. T. Fernández-Abedul, J. R. García and A. Costa-García, *Sensors and Actuators B: Chemical*, 2008, **130**, 436-448.
194. A. G. Niculescu, C. Chircov, A. C. Birca and A. M. Grumezescu, *Int J Mol Sci*, 2021, **22**, 2011.

195. K. L. Włodarczyk, D. P. Hand and M. M. Maroto-Valer, *Sci Rep*, 2019, **9**, 20215.
196. A. M. Clark, K. M. Sousa, C. Jennings, O. A. MacDougald and R. T. Kennedy, *Anal Chem*, 2009, **81**, 2350-2356.
197. X. Xie, Y. Wang, S. Y. Siu, C. W. Chan, Y. Zhu, X. Zhang, J. Ge and K. Ren, *Biomicrofluidics*, 2022, **16**, 041301.
198. X. Li, X. Fan, Z. Li, L. Shi, J. Liu, H. Luo, L. Wang, X. Du, W. Chen, J. Guo, C. Li and S. Liu, *Biosensors (Basel)*, 2022, **12**.
199. Z. Zhang and W. Tang, *Acta Pharm Sin B*, 2018, **8**, 721-732.
200. W. Buchegger, A. Haller, S. van den Driesche, M. Kraft, B. Lendl and M. Vellekoop, *Biomicrofluidics*, 2012, **6**, 12803-128039.
201. A. Enders, A. Grunberger and J. Bahnemann, *Mol Biotechnol*, 2022, DOI: 10.1007/s12033-022-00626-6.
202. D. S. Peterson, T. Rohr, F. Svec and J. M. Frechet, *Anal Chem*, 2002, **74**, 4081-4088.
203. S. Amalia, S. C. Angga, E. D. Iftitah, D. Septiana, B. O. D. Anggraeny, Warsito, A. N. Hasanah and A. Sabarudin, *Heliyon*, 2021, **7**, e07707.
204. J. Groenesteijn, M. J. de Boer, J. C. Lötters and R. J. Wiegerink, *Microfluidics and nanofluidics*, 2017, **21**, 1-12.
205. K. Szymańska, M. Pietrowska, J. Kocurek, K. Maresz, A. Koreniuk, J. Mrowiec-Białoń, P. Widłak, E. Magner and A. Jarzębski, *Chemical Engineering Journal*, 2016, **287**, 148-154.
206. P.-C. Chen, W.-Z. Zhang, W.-R. Chen, Y.-C. Jia, Y.-H. Wu, Y.-H. Liu, P.-Z. Chen, L.-Y. Chen and P.-S. Chen, *Sensors and Actuators B: Chemical*, 2022, **350**, 130888.
207. S. Sodergren, K. Svensson and K. Hjort, *Sci Rep*, 2021, **11**, 22504.
208. M. Utz, B. Patra, M. Sharma and W. Hale, *Sci Rep*, 2020, **11**, 53.
209. P. M. van Midwoud, M. T. Merema, E. Verpoorte and G. M. Groothuis, *J Lab Autom*, 2011, **16**, 468-476.
210. R. Edmondson, J. J. Broglie, A. F. Adcock and L. Yang, *Assay Drug Dev Technol*, 2014, **12**, 207-218.
211. Z. S. Marinkovic, C. Vulin, M. Acman, X. Song, J. M. Di Meglio, A. B. Lindner and P. Hersen, *Elife*, 2019, **8**, e47951.
212. T. Frisk, S. Rydholm, T. Liebmann, H. A. Svahn, G. Stemme and H. Brismar, *Electrophoresis*, 2007, **28**, 4705-4712.
213. I. Kiiski, E. Ollikainen, S. Artes, P. Jarvinen, V. Jokinen and T. Sikanen, *Eur J Pharm Sci*, 2021, **158**, 105677.
214. I. M. A. Kiiski, T. Pihlaja, L. Urvas, J. Witos, S. K. Wiedmer, V. P. Jokinen and T. M. Sikanen, *Adv Biosyst*, 2019, **3**, e1800245.
215. D. G. Filho, A. G. Silva and C. Z. Guidini, *Appl Microbiol Biotechnol*, 2019, **103**, 7399-7423.
216. K. Scott, E. H. Yu, M. M. Ghangrekar, B. Erable and N. M. Duțeanu, *Comprehensive Renewable Energy*, 2012, 277-230.
217. M. D. Trevan, *Methods Mol Biol*, 1988, **3**, 495-510.
218. P. Zucca and E. Sanjust, *Molecules*, 2014, **19**, 14139-14194.
219. M. P. Nicholas, L. Rao and A. Gennerich, *Methods Mol Biol*, 2014, **1136**, 137-169.
220. S. Smith, K. Goodge, M. Delaney, A. Struzyk, N. Tansey and M. Frey, *Nanomaterials (Basel)*, 2020, **10**, 2142.
221. P. Singh, H. Morris, A. V. Tivanski and A. Kohen, *Anal Biochem*, 2015, **484**, 169-172.
222. M. T. Kinirons and M. S. O'Mahony, *Br J Clin Pharmacol*, 2004, **57**, 540-544.
223. S. Crettol, N. Petrovic and M. Murray, *Curr Pharm Des*, 2010, **16**, 204-219.
224. S. Tanvir, S. Morandat, N. Frederic, H. Adenier and S. Pulvin, *N Biotechnol*, 2009, **26**, 222-228.
225. M. Taylor, D. C. Lamb, R. J. Cannell, M. J. Dawson and S. L. Kelly, *Biochem Biophys Res Commun*, 2000, **279**, 708-711.
226. C. Parsajoo, J.-M. Kauffmann and M. Elkaoutit, in *Biosensors for Medical Applications*, Elsevier, 2012, pp. 233-262.

227. V. V. Shumyantseva, T. V. Bulko and A. I. Archakov, *J Inorg Biochem*, 2005, **99**, 1051-1063.
228. Y. Mie, M. Suzuki and Y. Komatsu, *J Am Chem Soc*, 2009, **131**, 6646-6647.
229. V. Shumyantseva, A. Makhova, T. Bulko, A. Kuzikov, E. Shich, V. Kukes and A. Archakov, *RSC advances*, 2015, **5**, 71306-71313.
230. J. Zhou, J. Chen, N. Zhuang, A. Zhang, K. Chen, N. Xu, F. Xin, W. Zhang, W. Dong and M. Jiang, *Front Bioeng Biotechnol*, 2020, **8**, 579.
231. M. E. Hassan, Q. Yang and Z. Xiao, *Bulletin of the National Research Centre*, 2019, **43**, 1-11.
232. M. Sharma, V. Sharma and D. K. Majumdar, *Int Sch Res Notices*, 2014, **2014**, 936129.
233. Y. Zhu, Z. Jiang, L. Zhang, J. Shi and D. Yang, *Industrial & engineering chemistry research*, 2012, **51**, 255-261.
234. Q. Ai, D. Yang, Y. Zhu and Z. Jiang, *Industrial & Engineering Chemistry Research*, 2013, **52**, 14898-14905.
235. H. T. Imam, P. C. Marr and A. C. Marr, *Green Chemistry*, 2021, **23**, 4980-5005.
236. L. Cao, F. van Rantwijk and R. A. Sheldon, *Org Lett*, 2000, **2**, 1361-1364.
237. M. Jannat and K. L. Yang, *Langmuir*, 2018, **34**, 14226-14233.
238. G. Sathyanarayanan, M. Haapala and T. Sikanen, *Analytical Chemistry*, 2020, **92**, 14693-14701.
239. P. M. van Midwoud, M. T. Merema, E. Verpoorte and G. M. Groothuis, *JALA: Journal of the Association for Laboratory Automation*, 2011, **16**, 468-476.
240. E. Jutila, R. Koivunen, I. Kiiski, R. Bollström, T. Sikanen and P. Gane, *Advanced Functional Materials*, 2018, **28**, 1802793.
241. D. P. Wasalathanthri, R. C. Faria, S. Malla, A. A. Joshi, J. B. Schenkman and J. F. Rusling, *Analyst*, 2013, **138**, 171-178.
242. Z. Li, J. Li, M. Sun, L. Men, E. Wang, Y. Zhao, K. Li and X. Gong, *Frontiers in Pharmacology*, 2023, **14**, 1046722.
243. Y. Liu, K. Hu and Y. Wang, *Polymers*, 2017, **9**, 215.
244. S. Mao, D. Gao, W. Liu, H. Wei and J.-M. Lin, *Lab on a chip*, 2012, **12**, 219-226.
245. C. Ma, L. Zhao, E.-M. Zhou, J. Xu, S. Shen and J. Wang, *Analytical chemistry*, 2016, **88**, 1719-1727.
246. E. Novik, T. J. Maguire, P. Chao, K. Cheng and M. L. Yarmush, *Biochemical pharmacology*, 2010, **79**, 1036-1044.
247. G. Sathyanarayanan, M. Haapala and T. Sikanen, *Micromachines*, 2018, **9**, 649.
248. I. Kiiski, E. Ollikainen, S. Artes, P. Järvinen, V. Jokinen and T. Sikanen, *European Journal of Pharmaceutical Sciences*, 2021, **158**, 105677.
249. S. Han, P. Zhang, H. Lin, H. Li, Y. Guo, N. Xu and J.-M. Lin, *Talanta*, 2022, **243**, 123331.
250. T. Alebić-Kolbah and I. Wainer, *Chromatographia*, 1993, **37**, 608-612.
251. H. S. Kim and I. W. Wainer, *Journal of Chromatography B*, 2005, **823**, 158-166.
252. K. Sakai-Kato, M. Kato and T. Toyō'oka, *Journal of Chromatography A*, 2004, **1051**, 261-266.
253. T. Kampe, A. König, H. Schroeder, J. G. Hengstler and C. M. Niemeyer, *Analytical chemistry*, 2014, **86**, 3068-3074.
254. M. D'Archivio, C. Filesi, R. Vari, B. Scazzocchio and R. Masella, *Int J Mol Sci*, 2010, **11**, 1321-1342.
255. A. Bertelli, M. Biagi, M. Corsini, G. Bainsi, G. Cappellucci and E. Miraldi, *Foods*, 2021, **10**, (11) 2595.
256. U. Lewandowska, K. Szewczyk, E. Hrabec, A. Janecka and S. Gorlach, *J Agric Food Chem*, 2013, **61**, 12183-12199.
257. E. K. Lumley, C. E. Dyer, N. Pamme and R. W. Boyle, *Org Lett*, 2012, **14**, 5724-5727.
258. A. G. Ryder, S. Power and T. J. Glynn, *Sage journals*, 2003, **1**, 73-79.
259. J. Liu and Z. Yin, *Analyst*, 2019, **144**, 3221-3225.
260. M. S. Thakare, D. B. Patil, S. V. Kokate and N. S. Pawar, *Chemistry Proceedings*, 2021, **8**, 50.

261. J. Reinen, S. Ferman, E. Vottero, N. P. Vermeulen and J. N. Commandeur, *J Biomol Screen*, 2011, **16**, 239-250.
262. B. C. Covington, J. A. McLean and B. O. Bachmann, *Nat Prod Rep*, 2017, **34**, 6-24.
263. I. Aretz and D. Meierhofer, *Int J Mol Sci*, 2016, **17** (5) 632.
264. X. Shi, Y. Huang, Y. Mao, H. Naimy and J. Zaia, *J Am Soc Mass Spectrom*, 2012, **23**, 1498-1511.
265. M. Johansson, J. Tomankova, S. Li and G. Zamaratskaia, *Interdiscip Toxicol*, 2012, **5**, 150-154.
266. F. Wang, J. Liigand, S. Tian, D. Arndt, R. Greiner and D. S. Wishart, *Analytical chemistry*, 2021, **93**, 11692-11700.
267. Y. Djoumbou-Feunang, A. Pon, N. Karu, J. Zheng, C. Li, D. Arndt, M. Gautam, F. Allen and D. S. Wishart, *Metabolites*, 2019, **9**, 72.
268. F. Allen, A. Pon, R. Greiner and D. Wishart, *Analytical chemistry*, 2016, **88**, 7689-7697.
269. F. Allen, R. Greiner and D. Wishart, *Metabolomics*, 2015, **11**, 98-110.
270. F. Allen, A. Pon, M. Wilson, R. Greiner and D. Wishart, *Nucleic acids research*, 2014, **42**, W94-W99.
271. D.-H. Han, D.-G. Jung and H.-S. Shin, *Bulletin of the Korean Chemical Society*, 2008, **29**, 985-987.
272. W. M. Draper, F. R. Brown, R. Bethem and M. J. Miille, *Biomedical & environmental mass spectrometry*, 1989, **18**, 767-774.
273. C. Yu, Y. G. Shin, J. W. Kosmeder, J. M. Pezzuto and R. B. van Breemen, *Rapid communications in mass spectrometry*, 2003, **17**, 307-313.
274. W. Xinxin, L. Xia, G. Guangbo, F. Lei, X. Hong, L. Yaoguang, C. Yunfeng, H. Guanying and G. Bin, *CHEMICAL JOURNAL OF CHINESE UNIVERSITIES-CHINESE*, 2015, **36**, 1321-1327.
275. P. Xu, C. Xu, X. Li, D. Li, Y. Li, J. Jiang, P. Yang and G. Duan, *Molecules*, 2019, **24**, 1994.
276. S. Oda, T. Fukami, T. Yokoi and M. Nakajima, *Drug Metab Pharmacokinet*, 2015, **30**, 30-51.
277. R. Dupuis, A. Yuen and F. Innocenti, *Clin Chim Acta*, 2012, **413**, 1318-1325.
278. P. J. Bosma, J. Seppen, B. Goldhoorn, C. Bakker, R. O. Elferink, J. R. Chowdhury, N. R. Chowdhury and P. Jansen, *Journal of Biological Chemistry*, 1994, **269**, 17960-17964.
279. X. Liu, H. Wang, X. Liang and M. Roberts, in *Liver Pathophysiology*, Elsevier, 2017, pp. 391-400.
280. G. Yang, S. Ge, R. Singh, S. Basu, K. Shatzer, M. Zen, J. Liu, Y. Tu, C. Zhang, J. Wei, J. Shi, L. Zhu, Z. Liu, Y. Wang, S. Gao and M. Hu, *Drug Metab Rev*, 2017, **49**, 105-138.
281. R. C. Mohs and N. H. Greig, *Alzheimers Dement (N Y)*, 2017, **3**, 651-657.
282. D. Sun, W. Gao, H. Hu and S. Zhou, *Acta Pharm Sin B*, 2022, **12**, 3049-3062.
283. L. De Bartolo, S. Salerno, S. Morelli, L. Giorno, M. Rende, B. Memoli, A. Procino, V. E. Andreucci, A. Bader and E. Drioli, *Biomaterials*, 2006, **27**, 4794-4803.
284. A. M. I, D. E. Sastre, C. M. F and C. G. C. Marques Netto, *Molecules*, 2018, **23**.
285. T. von der Haar, *PLoS one*, 2007, **2**, e1078.
286. A. Kawase, R. Yamashita, T. Yoshizato, M. Yoshikawa, H. Shimada and M. Iwaki, *Int J Mol Sci*, 2022, **23**, 4724.
287. A. Ghosal, N. Hapangama, Y. Yuan, J. Achanfuo-Yeboah, R. Iannucci, S. Chowdhury, K. Alton, J. E. Patrick and S. Zbaida, *Drug Metabolism and Disposition*, 2004, **32**, 314-320.
288. D. T. Nardone-White, J. E. Bissada, A. A. Abouda and K. D. Jackson, *Drug Metab Dispos*, 2021, **49**, 233-244.
289. D. Kim and A. E. Herr, *Biomicrofluidics*, 2013, **7**, 41501.
290. J. W. Choi, K. W. Oh, J. H. Thomas, W. R. Heineman, H. B. Halsall, J. H. Nevin, A. J. Helmicki, H. T. Henderson and C. H. Ahn, *Lab Chip*, 2002, **2**, 27-30.
291. S. Z. Mazlan and S. A. Hanifah, *International Journal of Polymer Science*, 2017, **2017**.
292. R. Bussamara, L. Dall'agnol, A. Schrank, K. F. Fernandes and M. H. Vainstein, *Enzyme Res*, 2012, **2012**, 329178.
293. Z. Gan, T. Zhang, Y. Liu and D. Wu, *PLoS One*, 2012, **7**, e47154.

294. L.-E. Shi, Z.-X. Tang, Y. Yi, J.-S. Chen, H. Wang, W.-Y. Xiong and G.-Q. Ying, *Biotechnology & Biotechnological Equipment*, 2010, **24**, 1997-2003.
295. F. Risso, M. Mazutti, F. Costa, H. Treichel, F. Maugeri and M. Rodrigues, *Brazilian Journal of Chemical Engineering*, 2010, **27**, 507-516.
296. C. H. Lee, E. S. Jin, J. H. Lee and E. T. Hwang, *Front Bioeng Biotechnol*, 2020, **8**, 553591.
297. R. Fujiwara, M. Nakajima, H. Yamanaka, M. Katoh and T. Yokoi, *Drug Metab Dispos*, 2008, **36**, 361-367.
298. S. Nasrin, C. J. W. Watson, K. Bardhi, G. Fort, G. Chen and P. Lazarus, *Drug Metab Dispos*, 2021, **49**, 1081-1089.
299. X. Lv, Y. Xia, M. Finel, J. Wu, G. Ge and L. Yang, *Acta Pharm Sin B*, 2019, **9**, 258-278.
300. L. L. Pan, Y. Yang, M. Hui, S. Wang, C. Y. Li, H. Zhang, Y. H. Ding, L. Fu, X. X. Diao and D. F. Zhong, *Acta Pharmacol Sin*, 2021, **42**, 311-322.
301. B. H. Chen, C. C. Wang, Y. H. Hou, Y. C. Mao and Y. S. Yang, *Expert Opin Drug Metab Toxicol*, 2015, **11**, 1053-1071.
302. R. Baudoin, A. Legendre, S. Jacques, J. Cotton, F. Bois and E. Leclerc, *J Pharm Sci*, 2014, **103**, 706-718.
303. E. D. Salman, D. He, M. Runge-Morris, T. A. Kocarek and C. N. Falany, *J Steroid Biochem Mol Biol*, 2011, **127**, 315-323.
304. M. S. Kim, J. Shigenaga, A. Moser, C. Grunfeld and K. R. Feingold, *Am J Physiol Endocrinol Metab*, 2004, **287**, E731-738.
305. E. L. Stanley, R. Hume, T. J. Visser and M. W. Coughtrie, *J Clin Endocrinol Metab*, 2001, **86**, 5944-5955.
306. R. M. Pasternack, S. Rivillon Amy and Y. J. Chabal, *Langmuir*, 2008, **24**, 12963-12971.
307. B. Decsi, R. Krammer, K. Hegedus, F. Ender, B. Gyarmati, A. Szilagyi, R. Totos, G. Katona, C. Paizs, G. T. Balogh, L. Poppe and D. Balogh-Weiser, *Micromachines (Basel)*, 2019, **10**, 668.
308. F. P. Guengerich, *Toxicol Res*, 2021, **37**, 1-23.
309. R. E. Hodges and D. M. Minich, *J Nutr Metab*, 2015, **2015**, 760689.
310. S. Zienolddiny, D. Campa, H. Lind, D. Ryberg, V. Skaug, L. B. Stangeland, F. Canzian and A. Haugen, *Carcinogenesis*, 2008, **29**, 1164-1169.
311. O. Kweon, S. J. Kim, J. H. Kim, S. W. Nho, D. Bae, J. Chon, M. Hart, D. H. Baek, Y. C. Kim, W. Wang, S. K. Kim, J. B. Sutherland and C. E. Cerniglia, *BMC Bioinformatics*, 2020, **21**, 160.
312. F. Guengerich, E. Gillam, M. Martin, T. Baba, B.-R. Kim, T. Shimada, K. Raney and C.-H. Yun, *Bio phys*, 1994 **104**, 557-562.
313. A. M. McDonnell and C. H. Dang, *Journal of the advanced practitioner in oncology*, 2013, **4**, 263.
314. D. Valikhani, J. M. Bolivar and J. N. Pelletier, *ACS Catalysis*, 2021, **11**, 9418-9434.
315. G. Sathyanarayanan, M. Haapala, I. Kiiski and T. Sikanen, *Anal Bioanal Chem*, 2018, **410**, 6677-6687.
316. J. Jung, J. Braun, T. Czabany and B. Nidetzky, *Chembiochem*, 2020, **21**, 1534-1543.
317. M. Kosaka, D. Zhang, S. Wong and Z. Yan, *Drug Metab Dispos*, 2020, **48**, 655-661.
318. M. Z. Kamal, P. Yedavalli, M. V. Deshmukh and N. M. Rao, *Protein Sci*, 2013, **22**, 904-915.
319. M. Stiborova, R. Indra, M. Moserova, M. Sulc, P. Hodek, E. Frei, H. H. Schmeiser and V. M. Arlt, *Monatsh Chem*, 2016, **147**, 847-855.
320. K. N. Yu, S. Y. Kang, S. Hong and M. Y. Lee, *Arch Toxicol*, 2018, **92**, 2501-2516.
321. P. Gomez de Santos, M. Cañellas, F. Tieves, S. H. Younes, P. Molina-Espeja, M. Hofrichter, F. Hollmann, V. Guallar and M. Alcalde, *ACS Catalysis*, 2018, **8**, 4789-4799.
322. F. Esteves, J. Rueff and M. Kranendonk, *J Xenobiot*, 2021, **11**, 94-114.
323. N. Gamage, A. Barnett, N. Hempel, R. G. Duggleby, K. F. Windmill, J. L. Martin and M. E. McManus, *Toxicol Sci*, 2006, **90**, 5-22.
324. E. Dehghanifard, A. Jonidi Jafari, R. Rezaei Kalantary, A. H. Mahvi, M. A. Faramarzi and A. Esrafil, *Iranian J Environ Health Sci Eng*, 2013, **10**, 25.

325. M. Gahlout, D. M. Rudakiya, S. Gupte and A. Gupte, *International Nano Letters*, 2017, **7**, 195-208.
326. P. E. Erden and E. Kilic, *Talanta*, 2013, **107**, 312-323.
327. J. R. Petrulis, G. Chen, S. Benn, J. LaMarre and N. J. Bunce, *Environ Toxicol*, 2001, **16**, 177-184.
328. B. L. Montgomery, *Frontiers in bioengineering and biotechnology*, 2014, **2**, 22.
329. A. Schiwy, M. Brinkmann, I. Thiem, G. Guder, K. Winkens, K. Eichbaum, L. Nusser, B. Thalmann, S. Buchinger, G. Reifferscheid, T. B. Seiler, B. Thoms and H. Hollert, *Nat Protoc*, 2015, **10**, 1728-1741.
330. N. J. Anthis and G. M. Clore, *Protein Sci*, 2013, **22**, 851-858.
331. M. B. Fisher, K. Campanale, B. L. Ackermann, M. VandenBranden and S. A. Wrighton, *Drug metabolism and disposition*, 2000, **28**, 560-566.

# Appendix

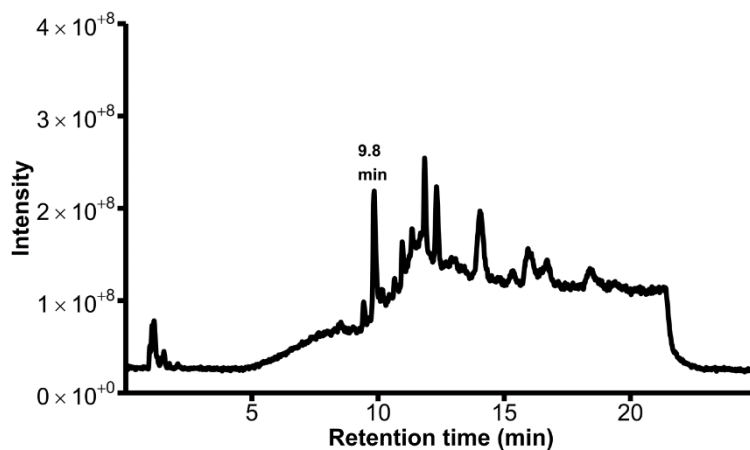


Figure 0.1: Signal traces from injection of resorufin standard into the LC-TQ-MS in negative mode obtained in a Q1 scan.

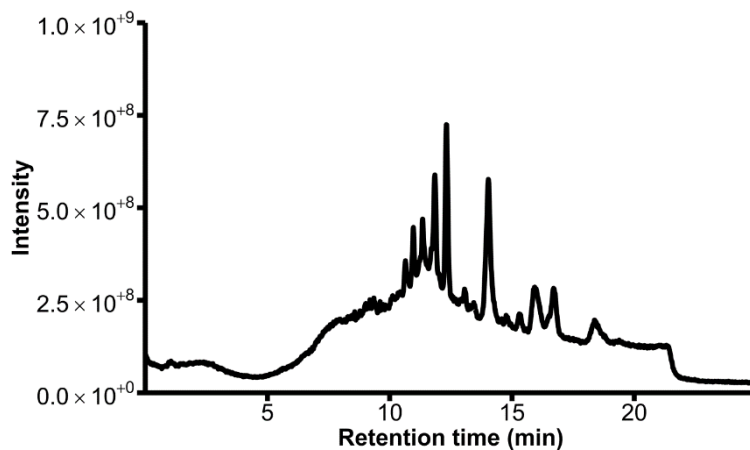


Figure 0.2: Signal traces from injection of DI water into the LC-TQ-MS in negative mode obtained in a Q1 scan.

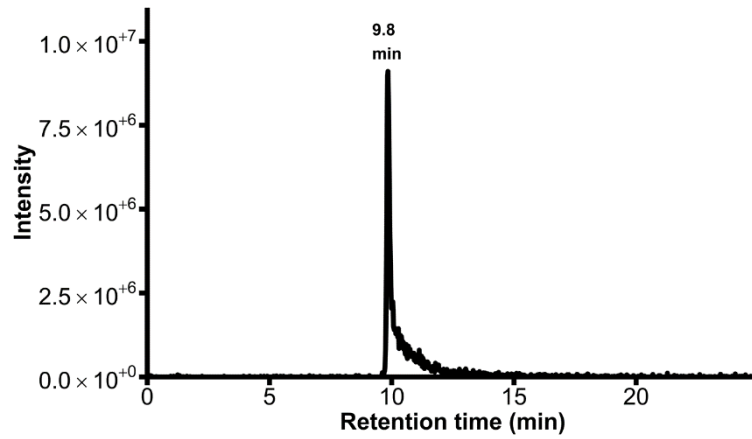


Figure 0.3: Signal traces from injection of resorufin standard into the LC-TQ-MS in negative mode obtained in product ion scan set to 212 m/z.

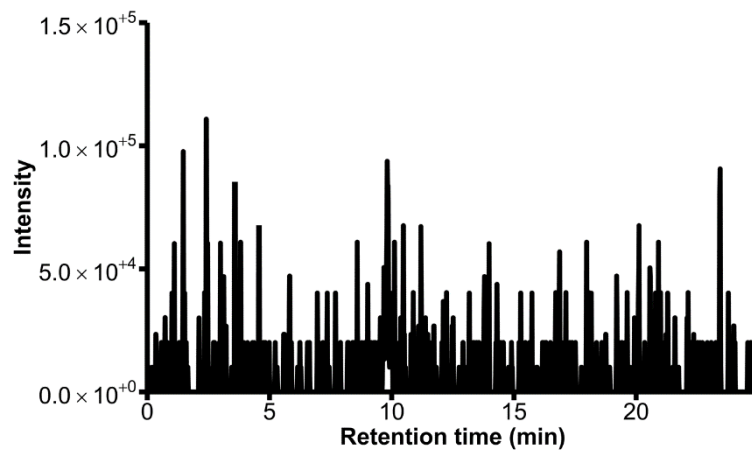


Figure 0.4: Signal traces from injection of DI water standard into the LC-TQ-MS in negative mode obtained in product ion scan set to 212 m/z.

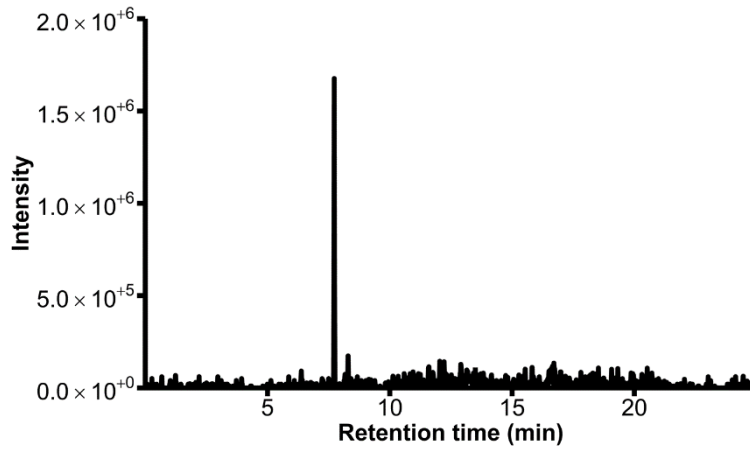


Figure 0.5: Signal traces from injection of resorufin standard into the LC-TQ-MS in negative mode obtained in a product ion scan set to 388 m/z.

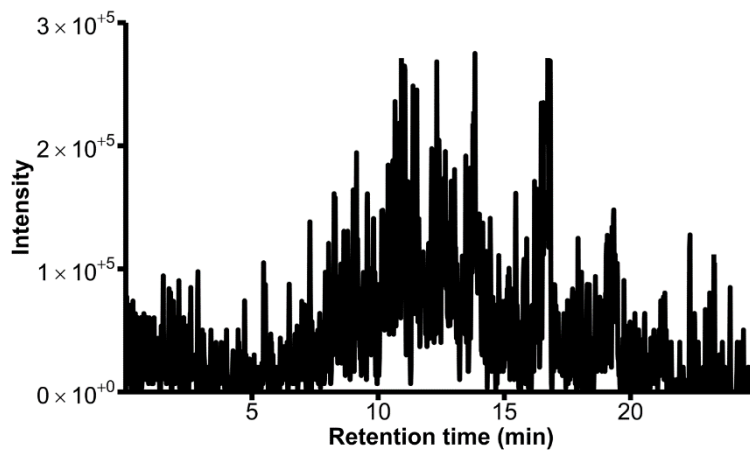


Figure 0.6: Signal traces from injection of DI water into the LC-TQ-MS in negative mode obtained in a product ion scan set to 388 m/z.

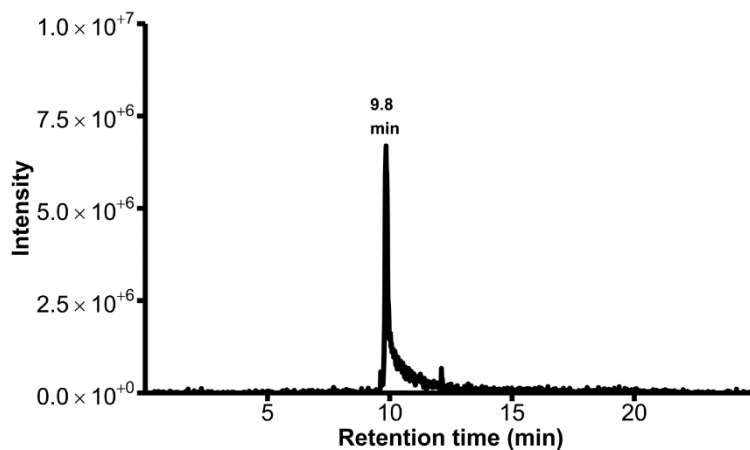


Figure 0.7: Signal traces from injection of resorufin standard into the LC-TQ-MS in negative mode obtained in precursor ion scan set to 212 m/z.

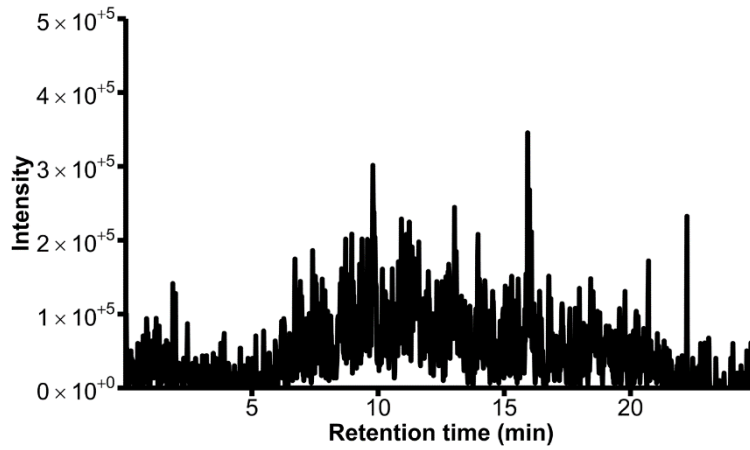


Figure 0.8: Signal traces from injection of DI water into the LC-TQ-MS in negative mode obtained in precursor ion scan set to 212 m/z.

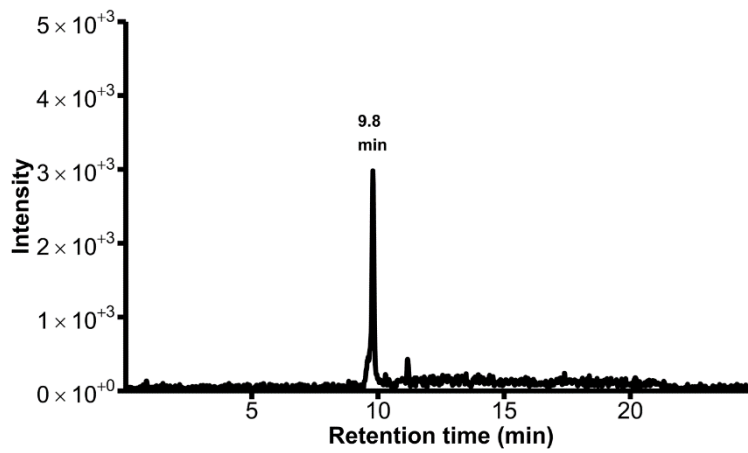


Figure 0.9: Signal traces from injection of resorufin standard into the LC-TQ-MS in negative mode obtained in MRM scan set to 212>155 m/z.

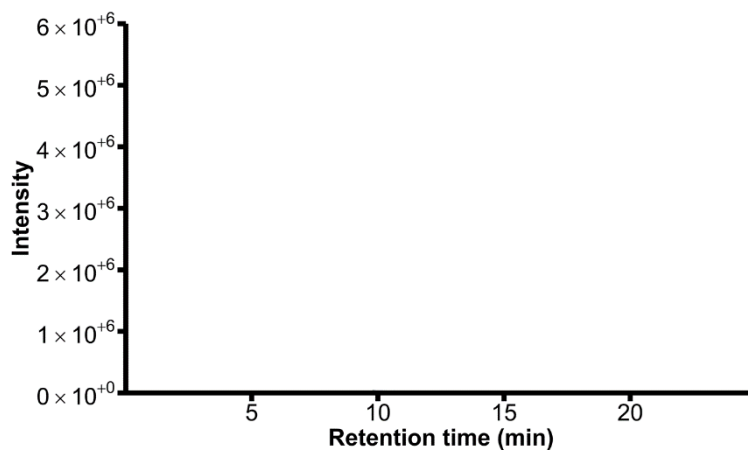


Figure 0.10: Signal traces from injection of resorufin standard into the LC-TQ-MS in negative mode obtained in MRM scan set to 388>212 m/z.

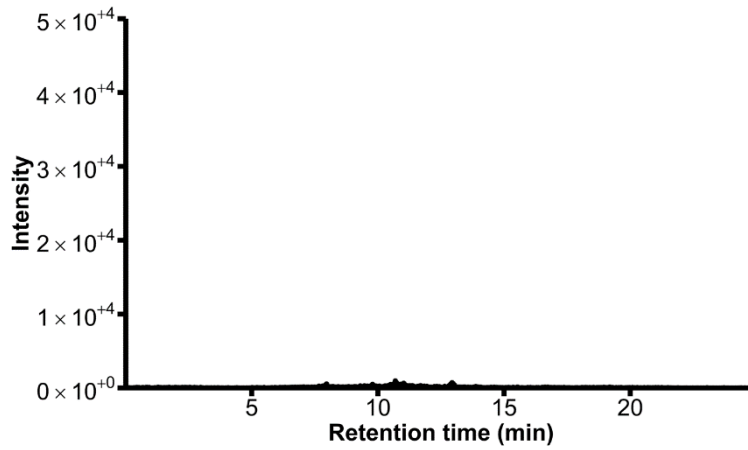


Figure 0.11: Signal traces from injection of DI water into the LC-TQ-MS in negative mode obtained in MRM scan set to 388>212 m/z.

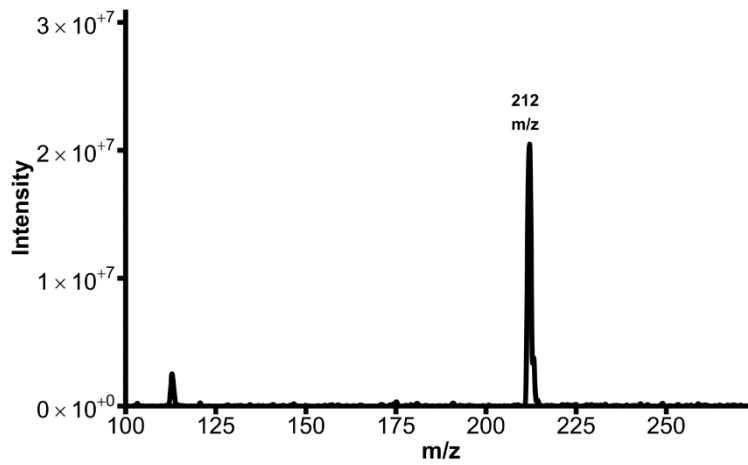


Figure 0.12: Mass spectrum for the area under the curve at 9.8 minutes using a Q1 scan for Figure 0.1.

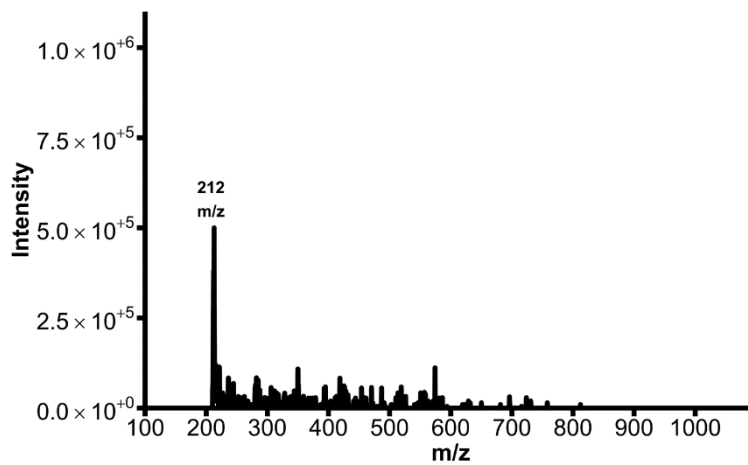


Figure 0.13: Mass spectrum for the area under the curve at 9.8 minutes using a product ion scan set to 388 m/z for Figure 0.5.

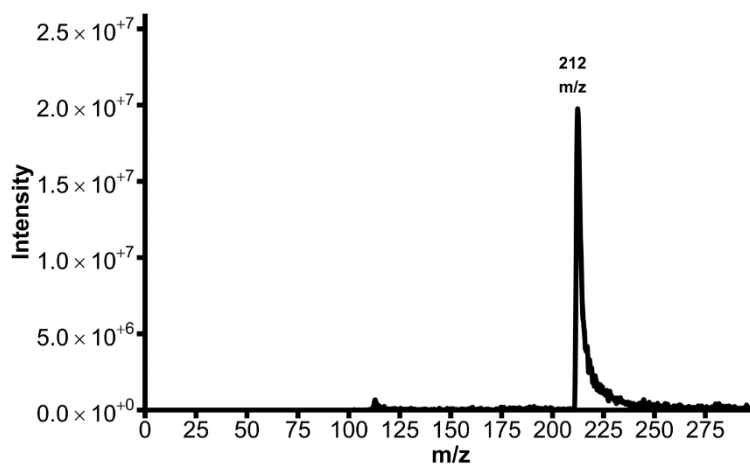


Figure 0.14: Mass spectrum for the area under the curve at 9.8 minutes using a precursor ion scan set to 212 m/z for Figure 0.7.

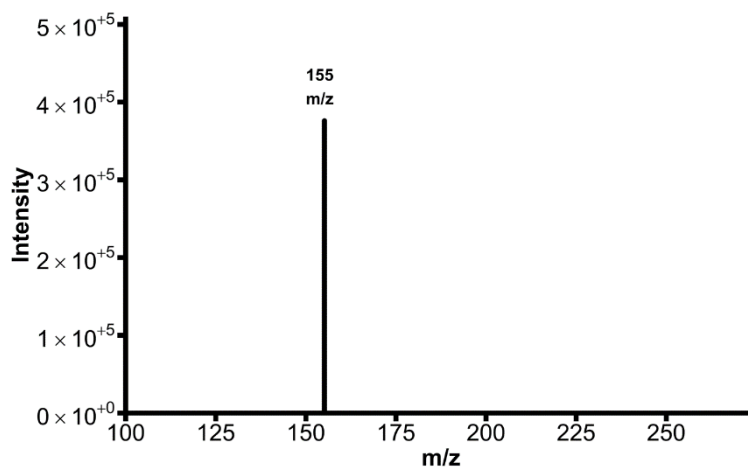


Figure 0.15: Mass spectrum for the area under the curve at 9.8 minutes using an MRM scan set to 212>155 m/z for Figure 0.9.

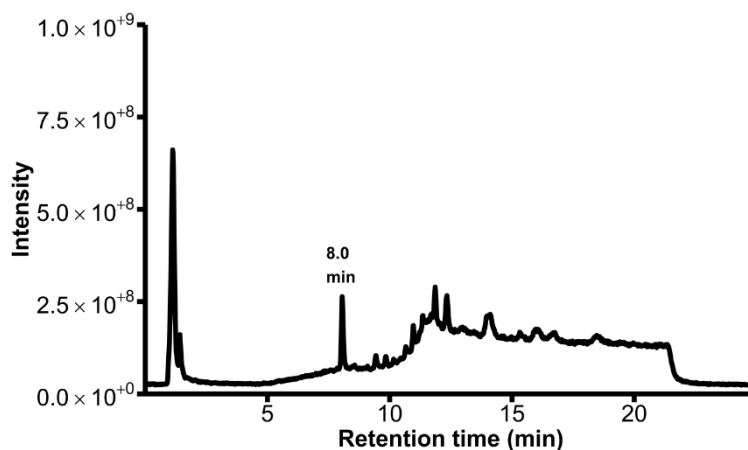


Figure 0.16: Signal traces from injection of resorufin glucuronide standard into the LC-TQ-MS in negative mode obtained in Q1 scan.

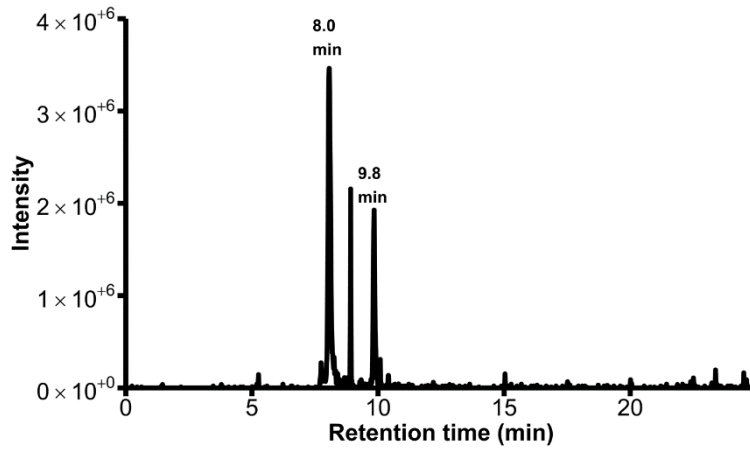


Figure 0.17: Signal traces from injection of resorufin glucuronide standard into the LC-TQ-MS in negative mode obtained in product ion scan set to 212 m/z.

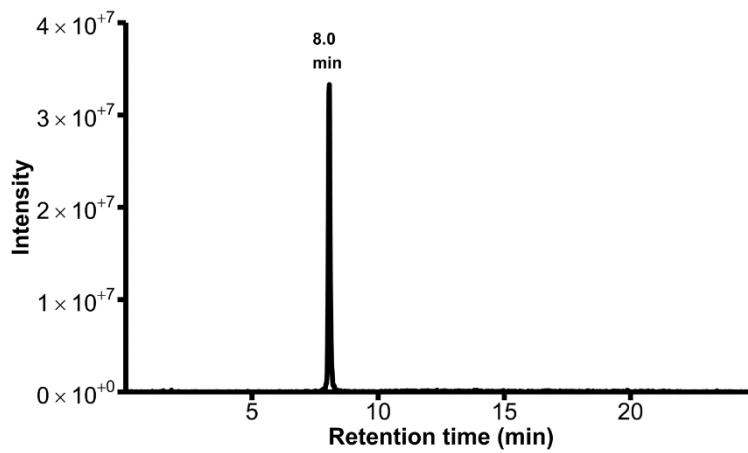


Figure 0.18: Signal traces from injection of resorufin glucuronide standard into the LC-TQ-MS in negative mode obtained in product ion scan set to 388 m/z.

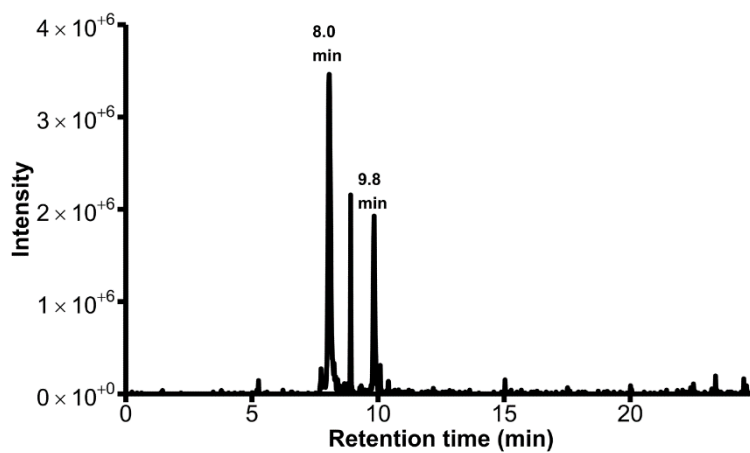


Figure 0.19: Signal traces from injection of resorufin glucuronide standard into the LC-TQ-MS in negative mode obtained in precursor ion scan set to 212 m/z.

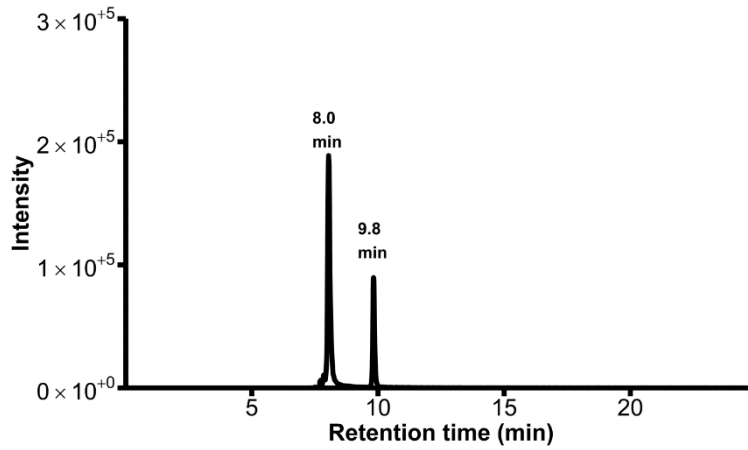


Figure 0.20: Signal traces from injection of resorufin glucuronide standard into the LC-TQ-MS in negative mode obtained in MRM scan set to 212>155 m/z.

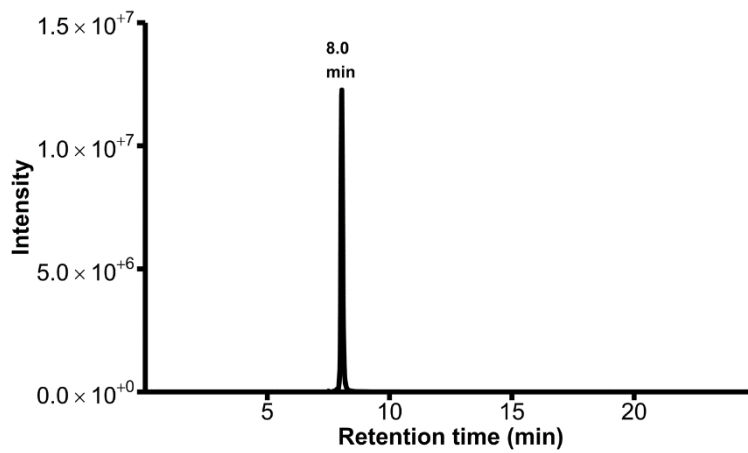


Figure 0.21: Signal traces from injection of resorufin glucuronide standard into the LC-TQ-MS in negative mode obtained in MRM scan set to 388>212 m/z.

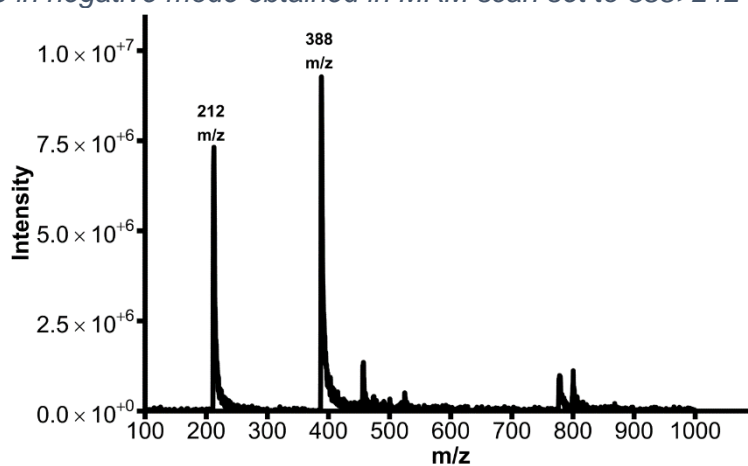


Figure 0.22: Mass spectrum for the area under the curve at 8.0 minutes using a product ion scan set to 388 m/z for Figure 0.16.

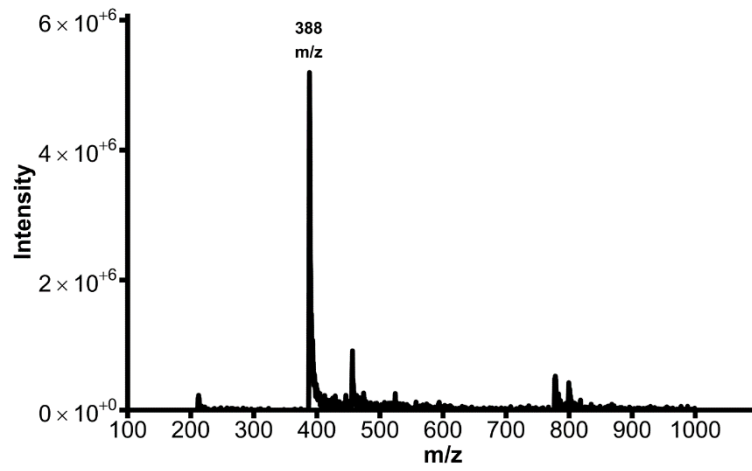


Figure 0.23: Mass spectrum for the area under the curve at 8.0 minutes using a precursor ion scan set to 212 m/z for Figure 0.19.

Figure 0.19.

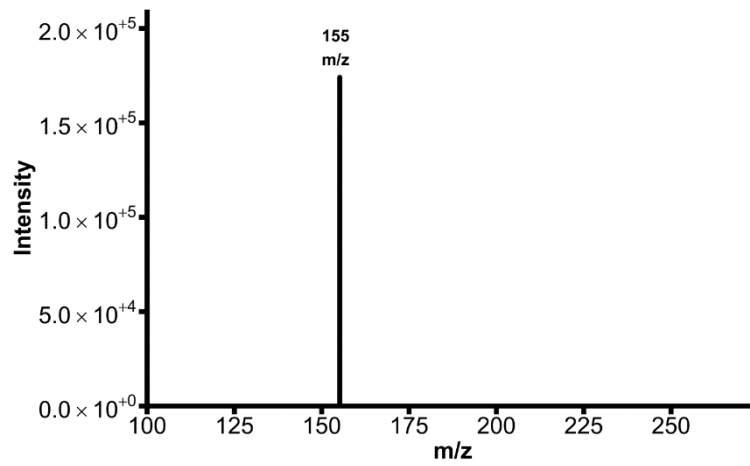


Figure 0.24: Mass spectrum for the area under the curve at 8.0 minutes using an MRM scan set to 212>155 m/z for Figure 0.20.

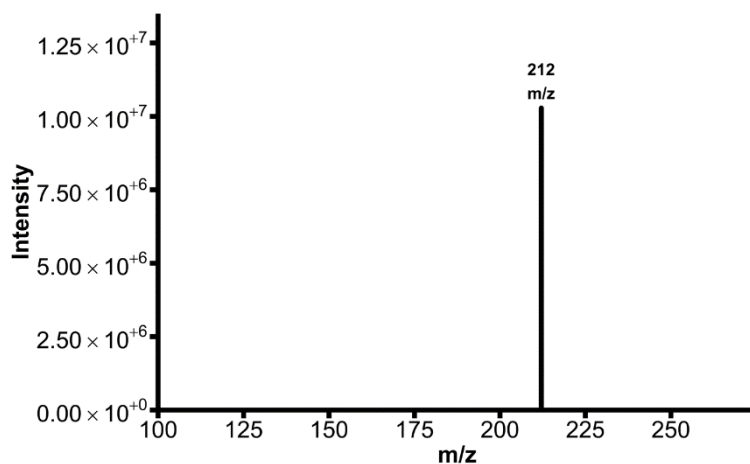


Figure 0.25: Mass spectrum for the area under the curve at 8.0 minutes using an MRM scan set to 388>212 m/z for Figure 0.21.

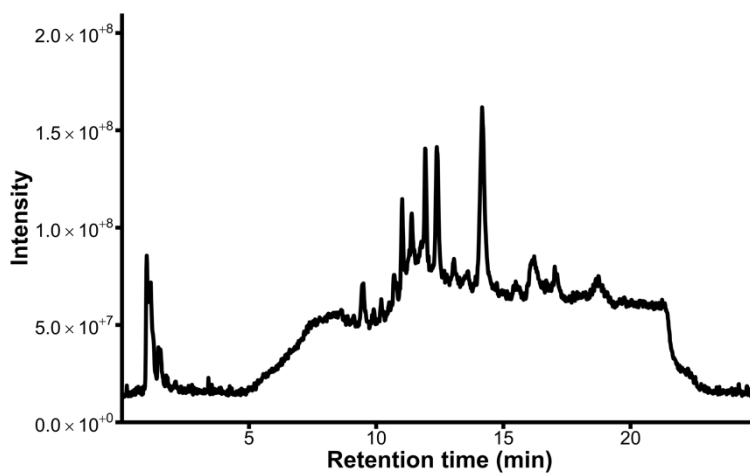


Figure 0.26: Signal traces from injection of a sample into the LC-TQ-MS in negative mode obtained in a Q1 scan.

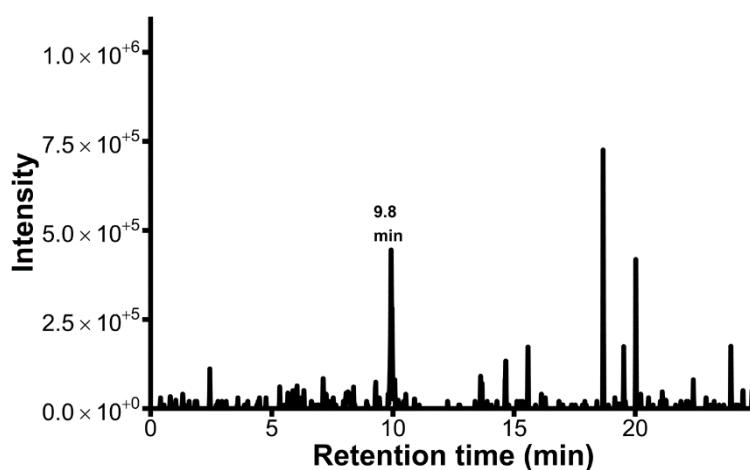


Figure 0.27: Signal traces from injection of a sample into the LC-TQ-MS in negative mode obtained in a product ion scan set to 212 m/z.

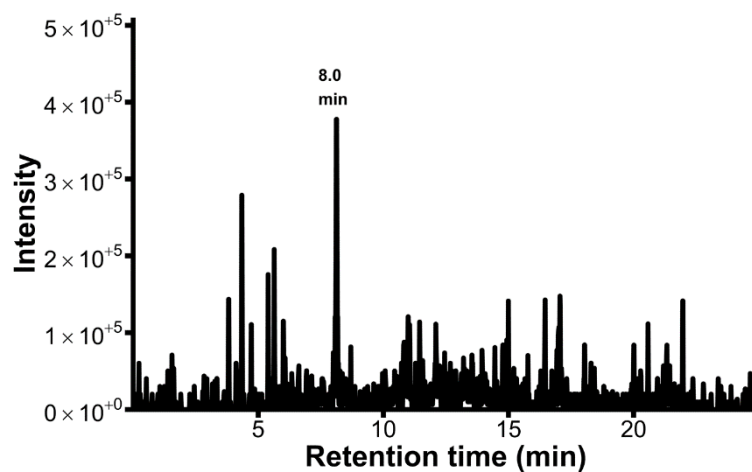


Figure 0.28: Signal traces from injection of a sample into the LC-TQ-MS in negative mode obtained in a product ion scan set to 388  $m/z$ .

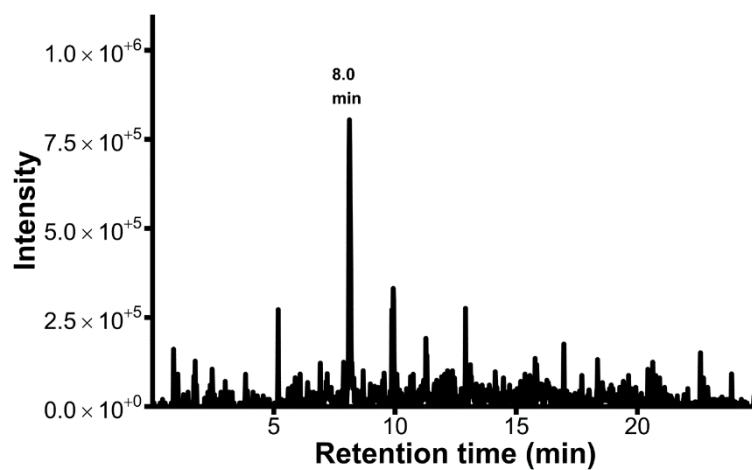


Figure 0.29: Signal traces from injection of a sample into the LC-TQ-MS in negative mode obtained in a precursor ion scan set to 212  $m/z$ .

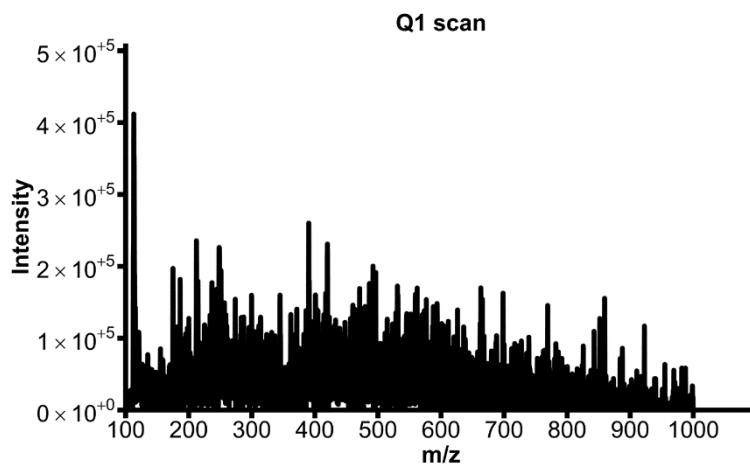


Figure 0.30: Mass spectrum for the area under the curve at 8.0 minutes using a Q1 scan of

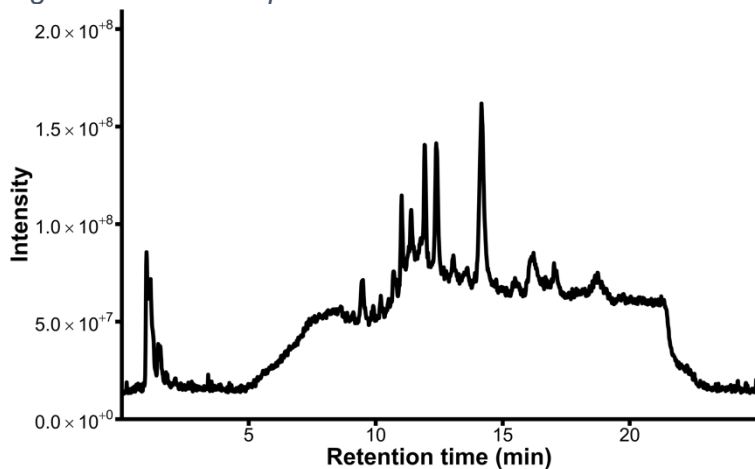


Figure 0.26.

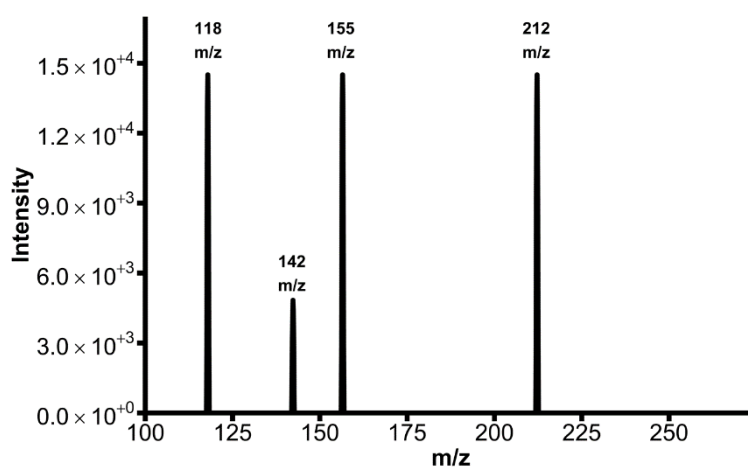


Figure 0.31: Mass spectrum for the area under the curve at 9.8 minutes using an product ion scan set to 212m/z of Figure 0.27.

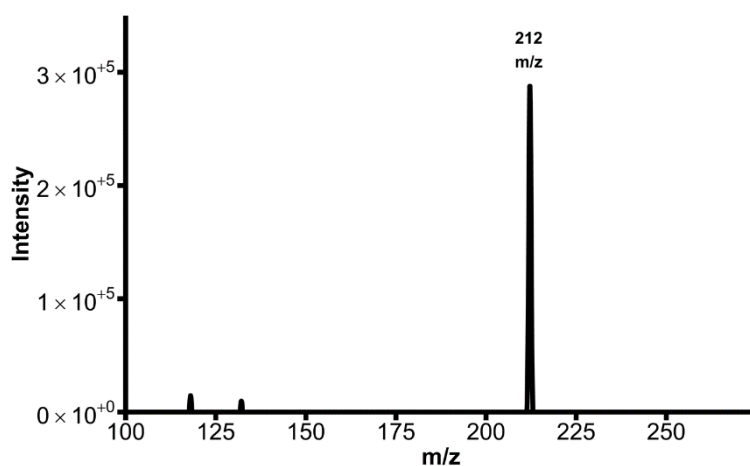


Figure 0.32: Mass spectrum for the area under the curve at 8.0 minutes using a product ion scan set to 388 m/z of Figure 0.28.

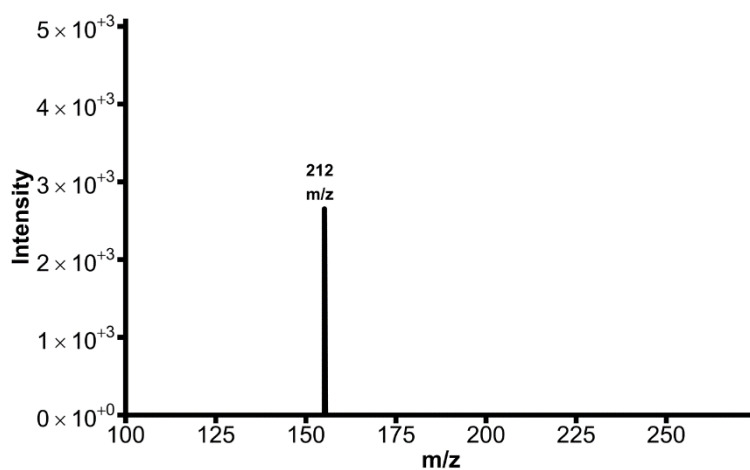


Figure 0.33: Mass spectrum for the area under the curve at 9.8 minutes using an MRM scan set to 212 > 155 m/z of.

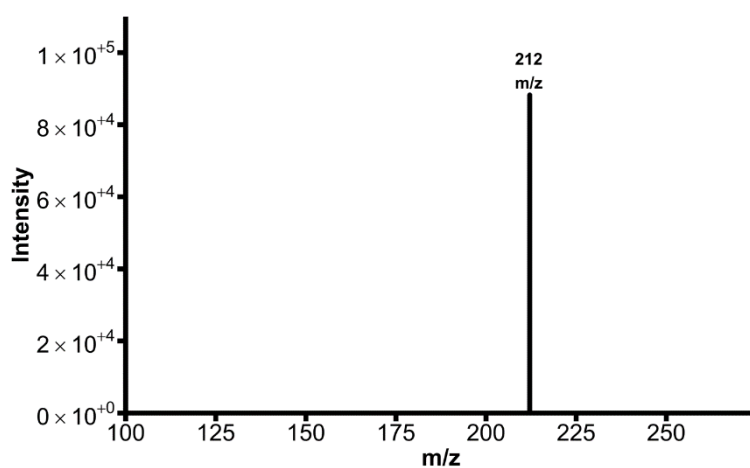


Figure 0.34: Mass spectrum for the area under the curve at 8.0 minutes using an MRM scan set to 388 > 212 m/z for Figure 4.18b.

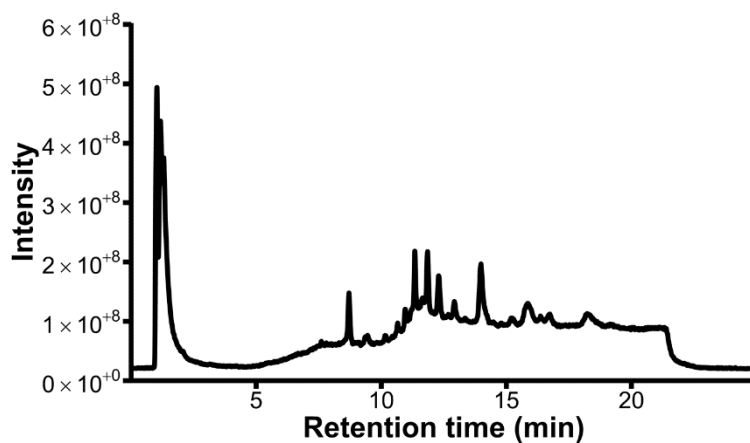


Figure 0.35: Signal traces from injection of a nitrophenol standard into the LC-TQ-MS in negative mode obtained in a Q1 scan.

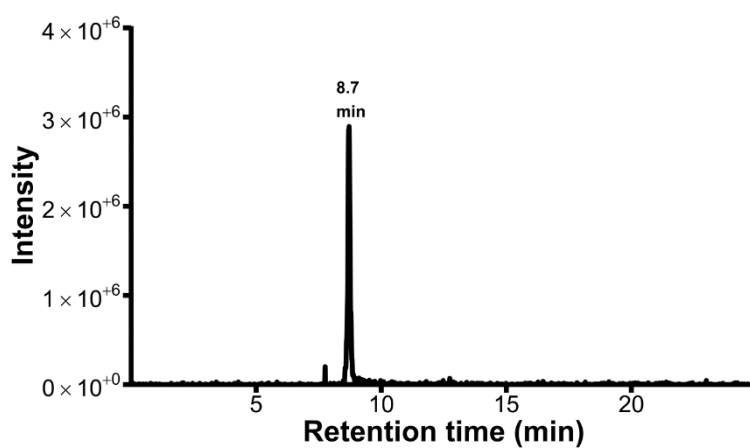


Figure 0.36: Signal traces from injection of a nitrophenol standard into the LC-TQ-MS in negative mode obtained in a product ion scan set to 138  $m/z$ .

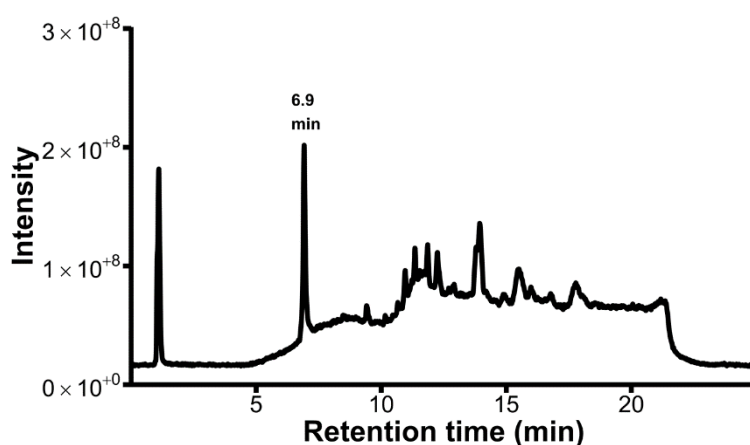


Figure 0.37: Signal traces from injection of a nitrophenyl sulfate standard into the LC-TQ-MS in negative mode obtained in a Q1 scan.

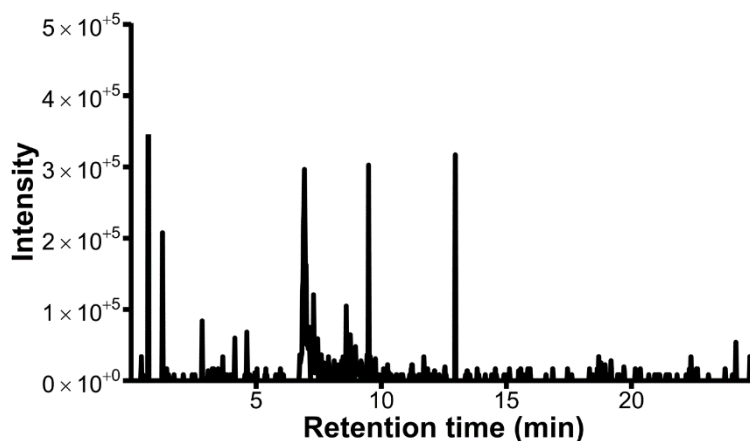


Figure 0.38: Signal traces from injection of a nitrophenyl sulfate standard into the LC-TQ-MS in negative mode obtained in a product ion scan set to 138 m/z.

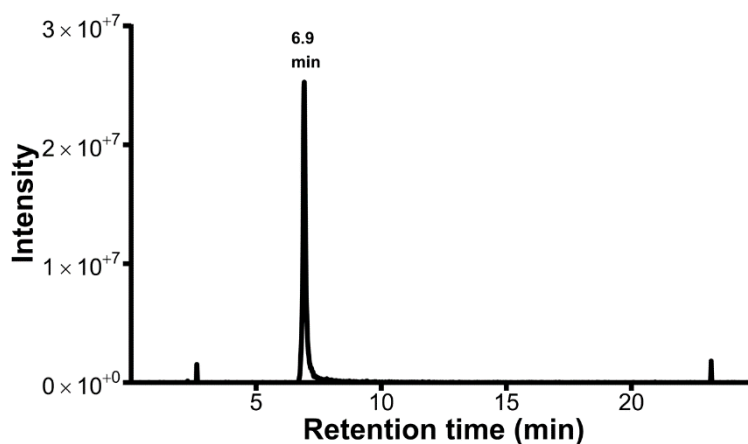


Figure 0.39: Signal traces from injection of a nitrophenyl sulfate standard into the LC-TQ-MS in negative mode obtained in a product ion scan set to 218 m/z.

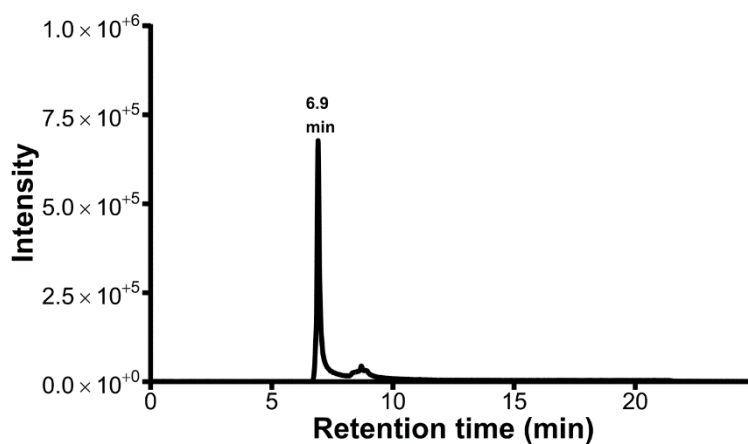


Figure 0.40: Signal traces from injection of a nitrophenyl sulfate standard into the LC-TQ-MS in negative mode obtained in an MRM scan set to 138>108 m/z.

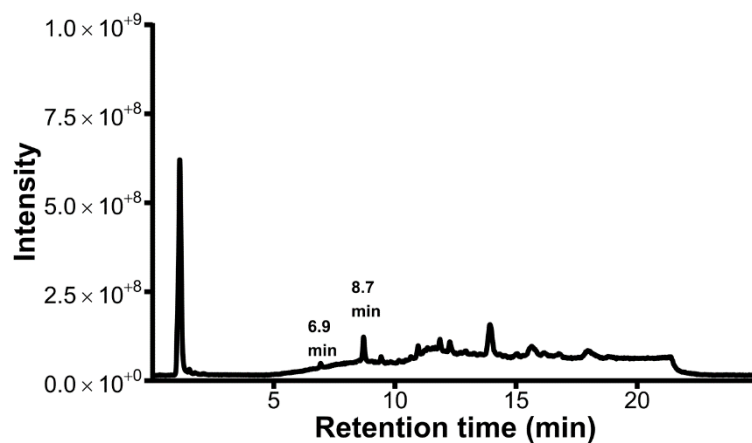


Figure 0.41: Signal traces from injection of a sample into the LC-TQ-MS in negative mode obtained in a Q1 scan.

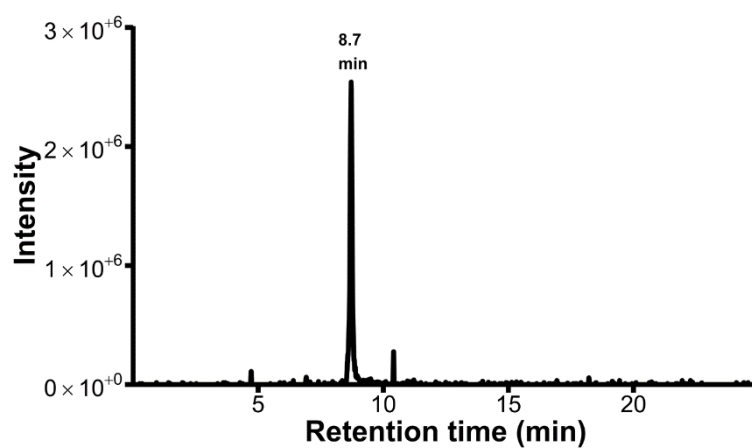


Figure 0.42: Signal traces from injection of a sample into the LC-TQ-MS in negative mode obtained in a product ion scan set to 138 m/z.

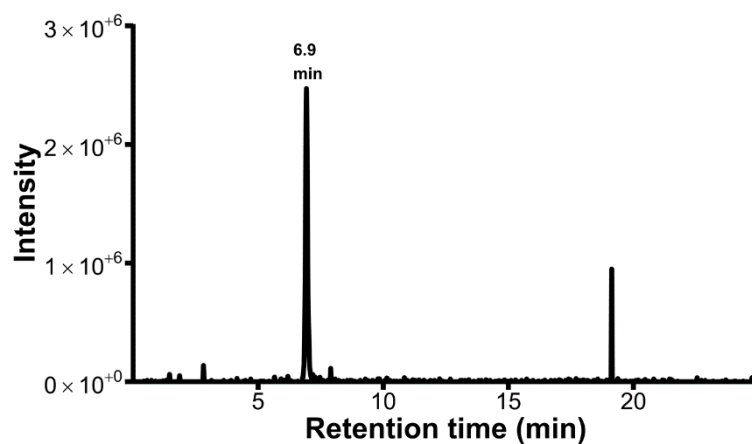


Figure 0.43: Signal traces from injection of a sample into the LC-TQ-MS in negative mode obtained in a product ion scan set to 218 m/z.

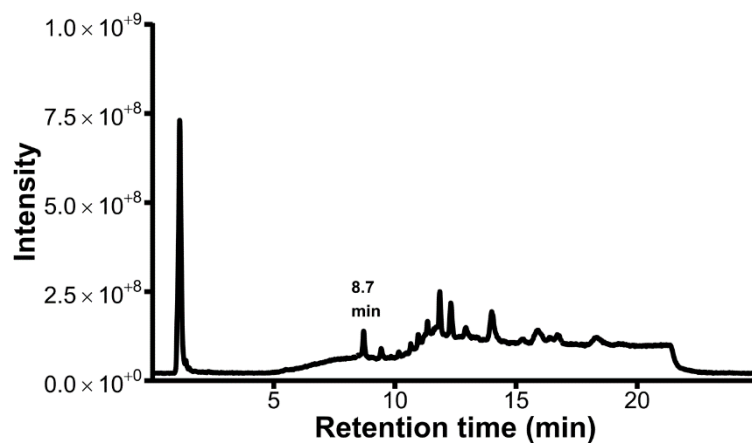


Figure 0.44: Signal traces from injection of a negative control sample into the LC-TQ-MS in negative mode obtained in a Q1 scan.

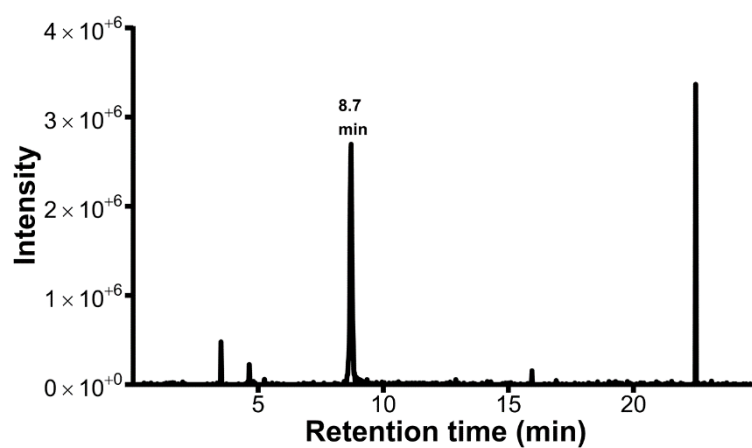


Figure 0.45: Signal traces from injection of a negative control sample into the LC-TQ-MS in negative mode obtained in a product ion scan set to 138 m/z.

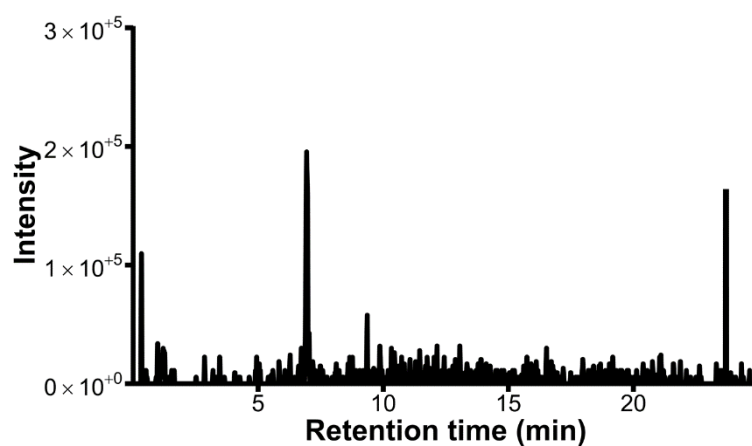


Figure 0.46: Signal traces from injection of a negative control sample into the LC-TQ-MS in negative mode obtained in a product ion scan set to 218 m/z.

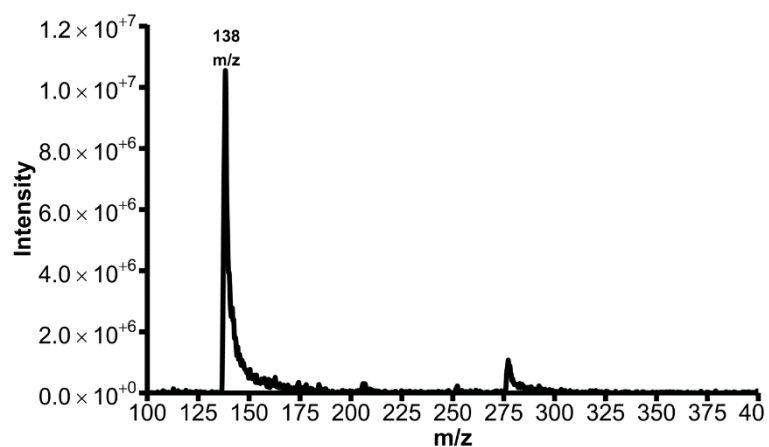


Figure 0.47: Mass spectrum for the area under the curve at 8.7 minutes using a Q1 scan for Figure 0.35.

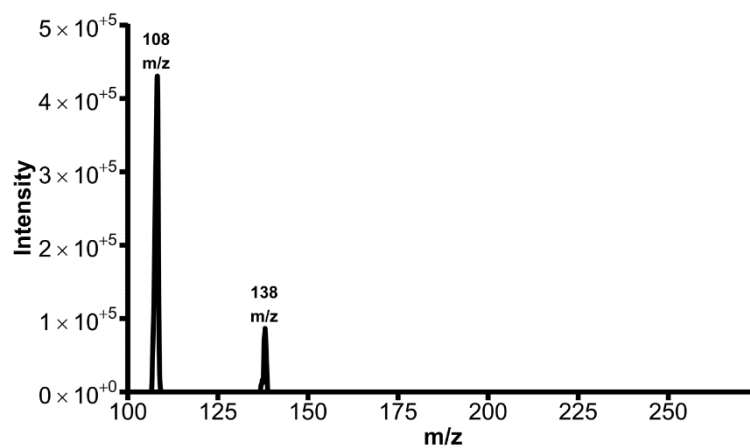


Figure 0.48: Mass spectrum for the area under the curve at 8.7 minutes using a product ion scan set to 138 m/z for Figure 0.36.

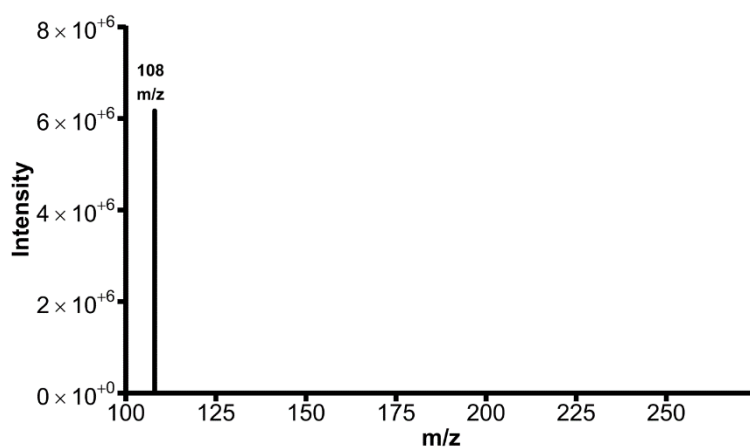


Figure 0.49: Mass spectrum for the area under the curve at 8.7 minutes using an MRM scan set to  $138 > 108$   $m/z$  for Figure 5.4aF.

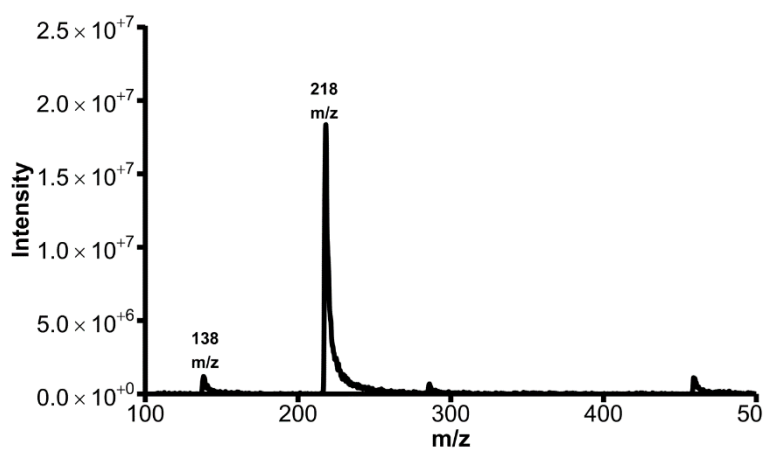


Figure 0.50: Mass spectrum for the area under the curve at 6.9 minutes using a Q1 scan for Figure 0.37.

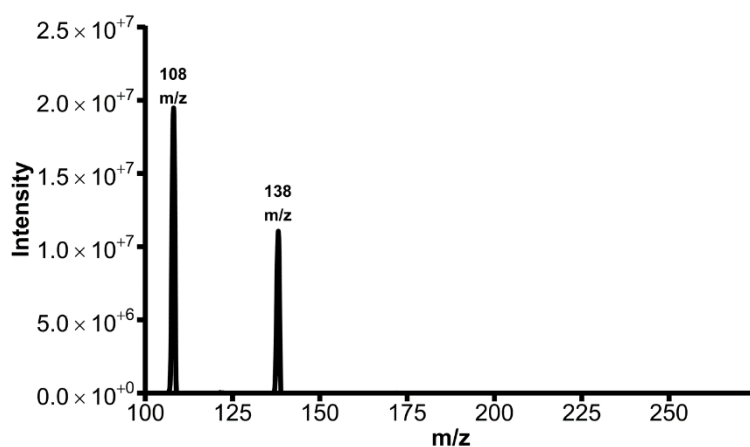


Figure 0.51: Mass spectrum for the area under the curve at 6.9 minutes using a product ion scan set to 218  $m/z$  for Figure 0.39.

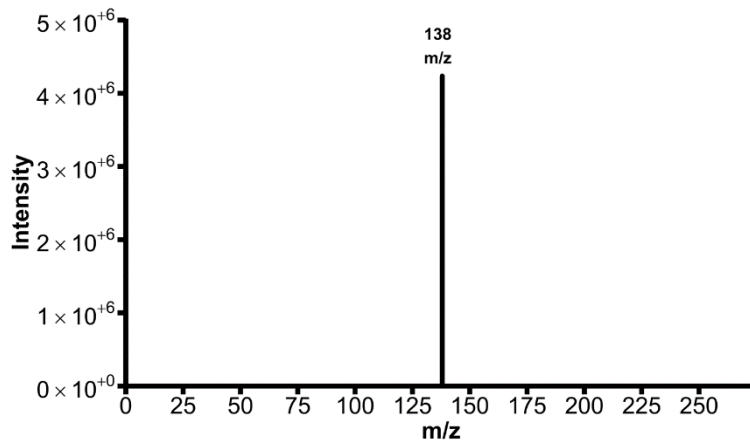


Figure 0.52: Mass spectrum for the area under the curve at 6.9 minutes using an MRM scan set to 218>138 m/z.

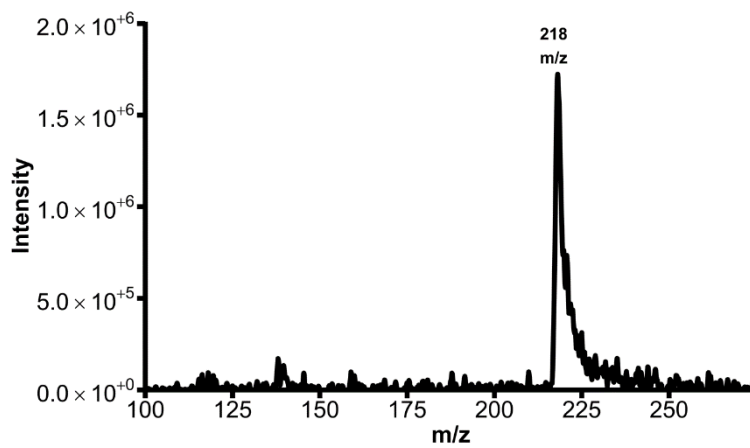


Figure 0.53: Mass spectrum for the area under the curve at 6.9 minutes using a Q1 scan for Figure 0.41.

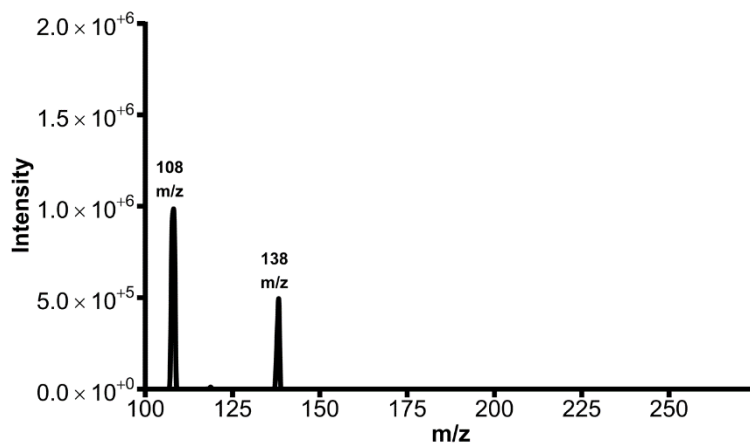


Figure 0.54: Mass spectrum for the area under the curve at 6.9 minutes using a product ion scan set to 218 m/z for Figure 0.43.

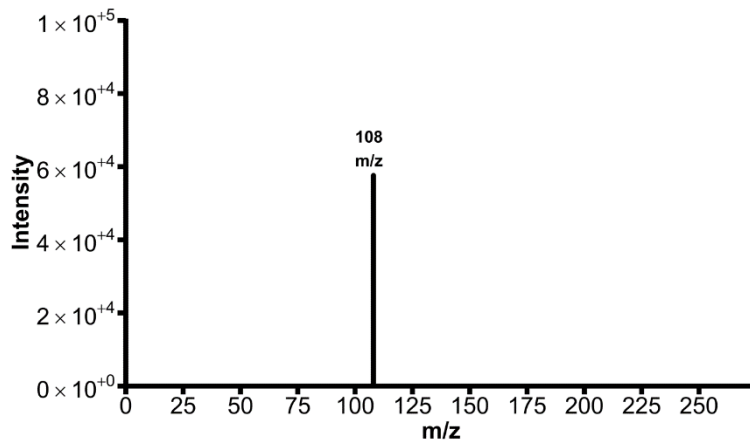


Figure 0.55: Mass spectrum for the area under the curve at 6.9 minutes using an MRM scan set to 138>108 m/z for Figure 5.5a.

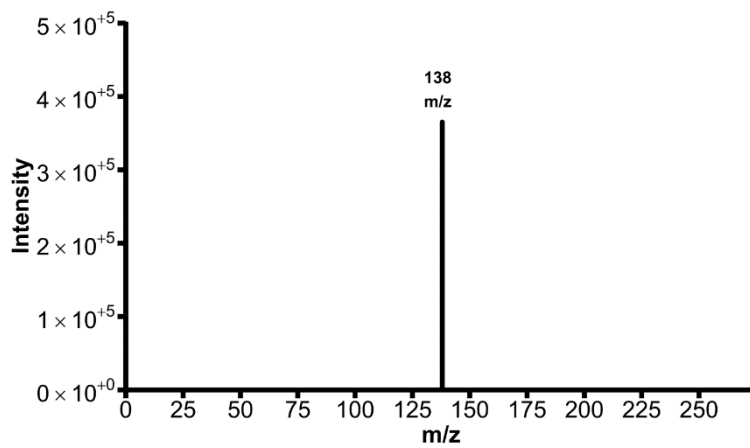


Figure 0.56: Mass spectrum for the area under the curve at 6.9 minutes using an MRM scan set to 218>138 m/z for Figure 5.5b.

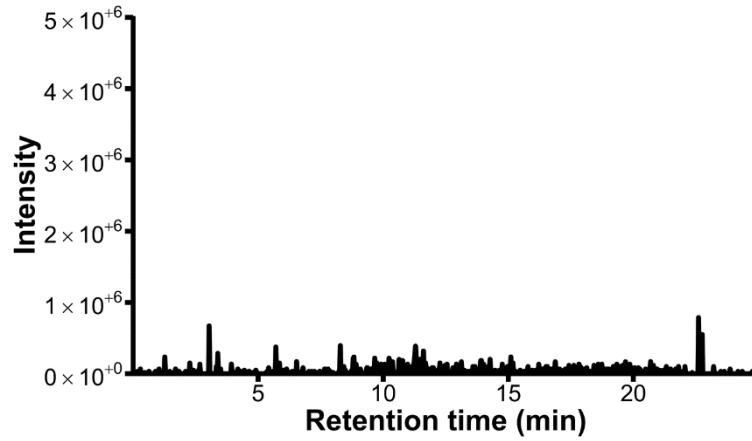


Figure 0.57: Signal traces from injection of a resorufin standard into the LC-TQ-MS in positive mode obtained in a product ion scan set to 242 m/z.

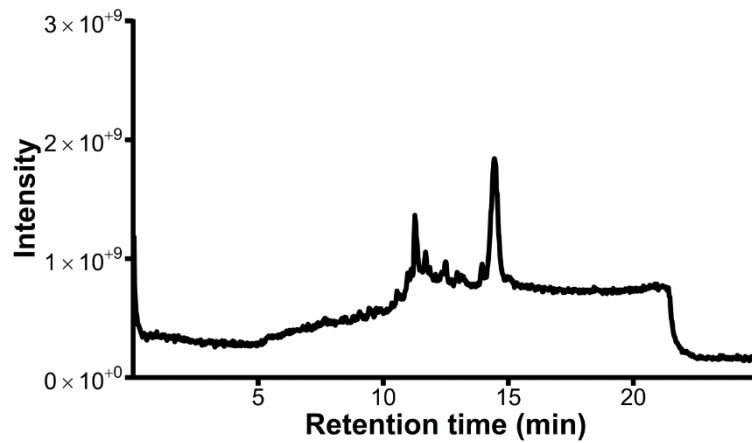


Figure 0.58: Signal traces from injection of a 7-ethoxyresorufin standard into the LC-TQ-MS in positive mode obtained in a Q1 scan.

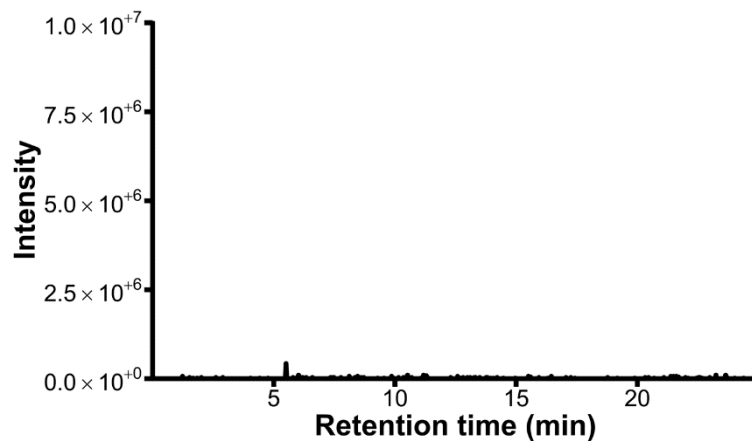


Figure 0.59: Signal traces from injection of a 7-ethoxyresorufin standard into the LC-TQ-MS in positive mode obtained in a Q1 product ion scan set to 212 m/z.

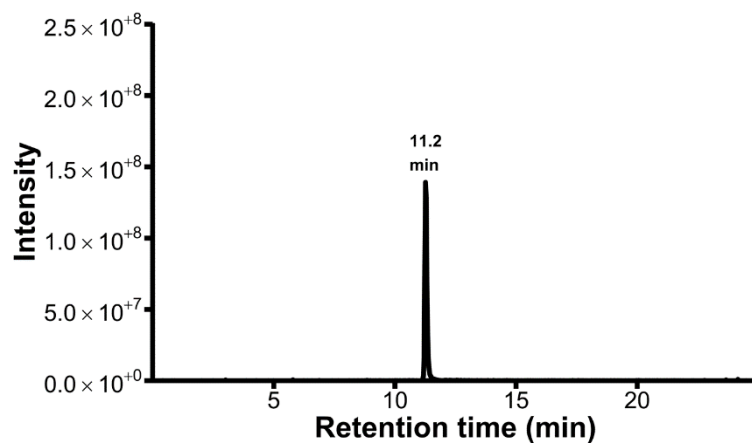


Figure 0.60: Signal traces from injection of a 7-ethoxyresorufin standard into the LC-TQ-MS in positive mode obtained in product ion scan set to 242 m/z.

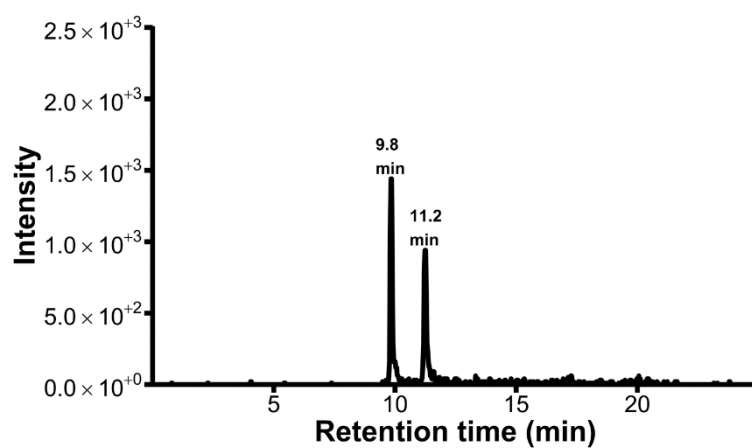


Figure 0.61: Signal traces from injection of a 7-ethoxyresorufin standard into the LC-TQ-MS in positive mode obtained in an MRM scan set to 212>155 m/z.

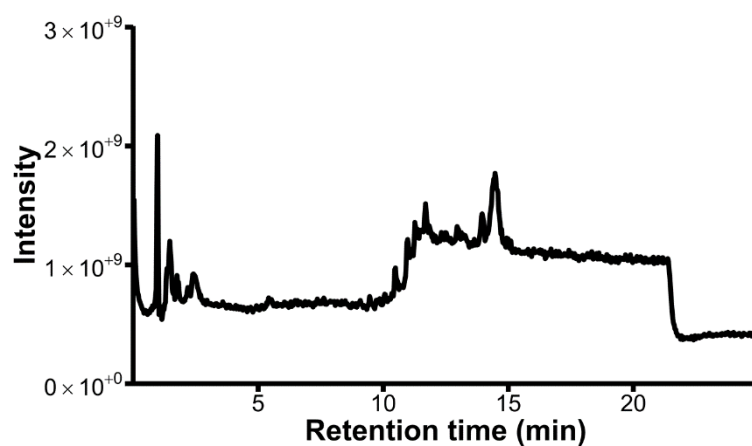


Figure 0.62: Signal traces from injection of a sample into the LC-TQ-MS in positive mode obtained in a Q1 scan.

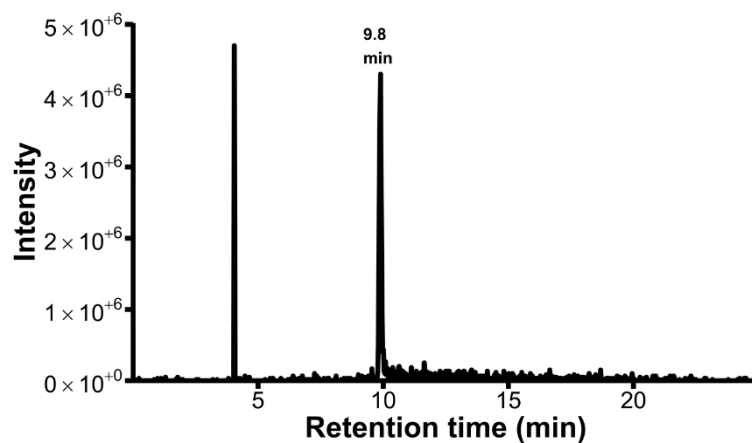


Figure 0.63: Signal traces from injection of a sample into the LC-TQ-MS in positive mode obtained in a product ion scan set to 212 m/z.

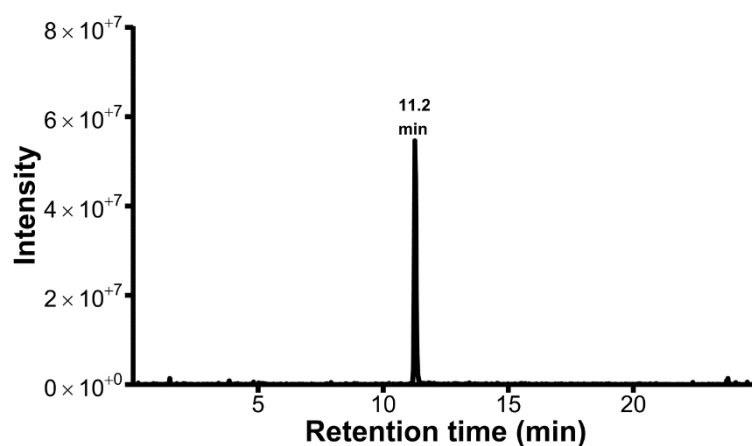


Figure 0.64: Signal traces from injection of a sample into the LC-TQ-MS in positive mode obtained in a product ion scan set to 242 m/z.

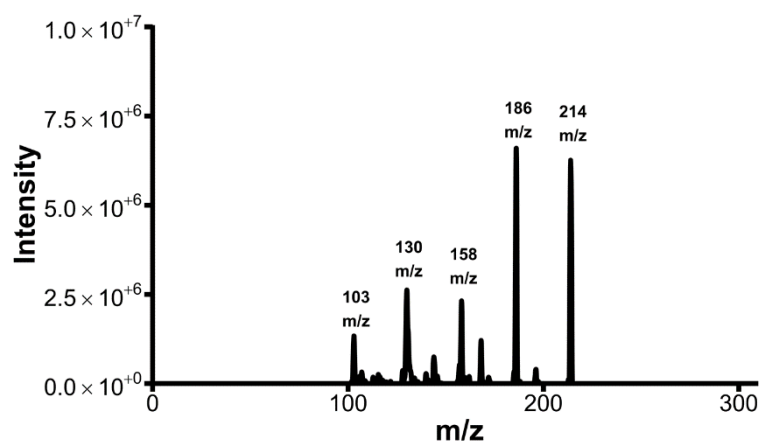


Figure 0.65: Mass spectrum for the area under the curve at 11.2 minutes using a product ion scan set to 242 m/z of Figure 0.64.

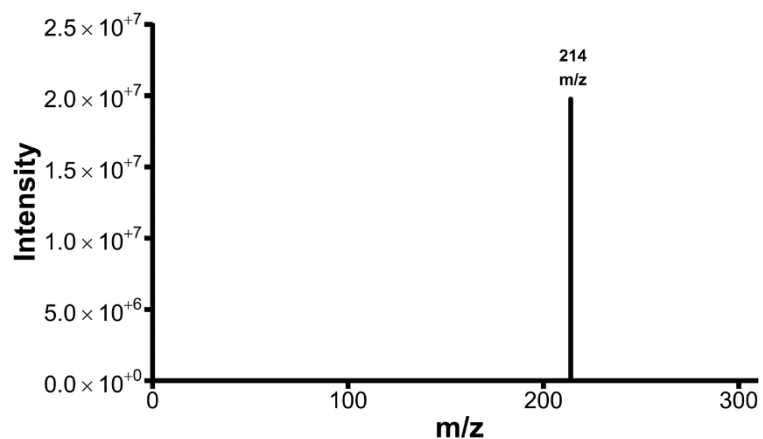


Figure 0.66: Mass spectrum for the area under the curve at 11.2 minutes using an MRM scan set to  $242 > 214$  m/z of Figure 6.12a.

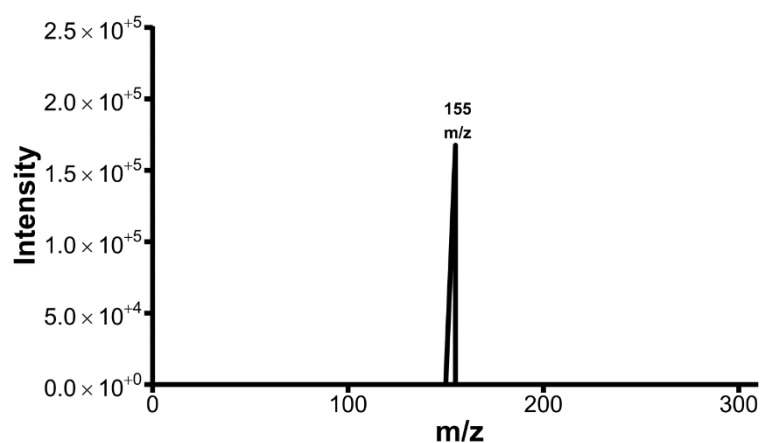


Figure 0.67: Mass spectrum for the area under the curve at 11.2 minutes using an MRM scan set to  $212 > 155$  m/z of Figure 6.12b.

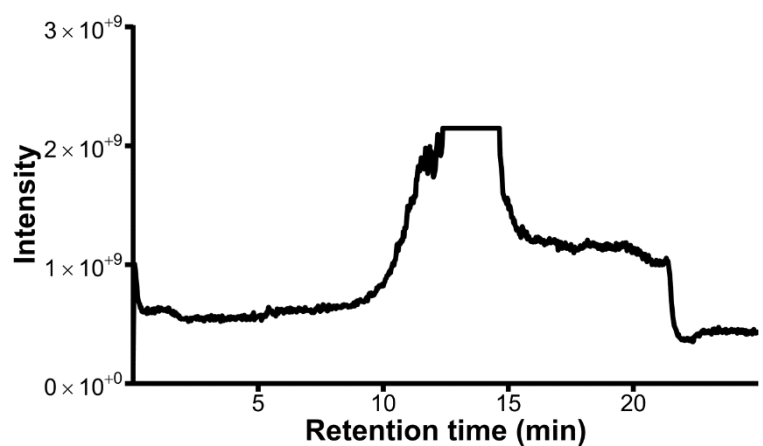


Figure 0.68: Signal traces from injection of a negative control sample into the LC-TQ-MS in positive mode obtained in a Q1 scan.

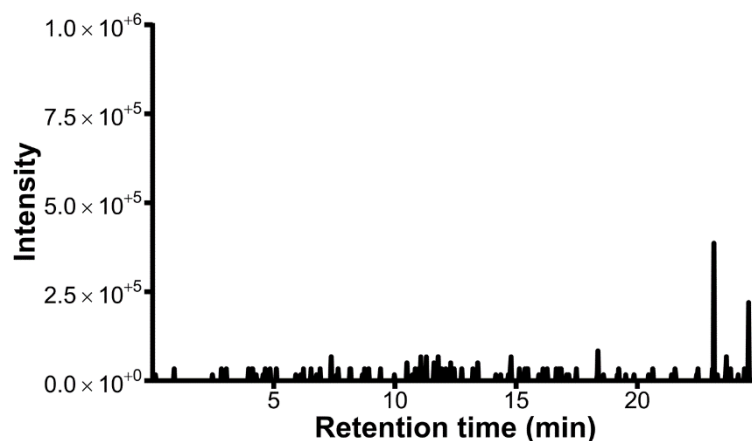


Figure 0.69: Signal traces from injection of a negative control sample into the LC-TQ-MS in positive mode obtained in a product ion scan set to 212 m/z.

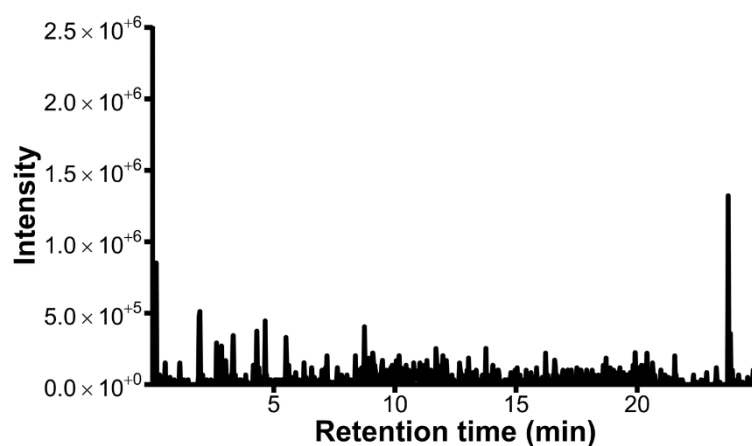


Figure 0.70: Signal traces from injection of a negative control sample into the LC-TQ-MS in positive mode obtained in a product ion scan set to 242 m/z.

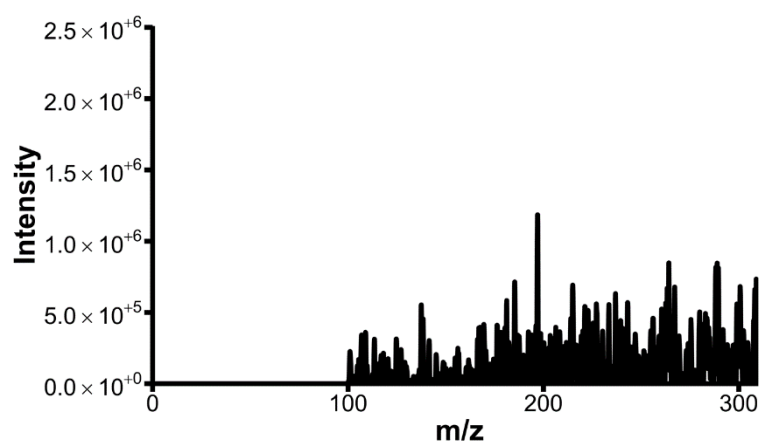


Figure 0.71: Mass spectrum for the area under the curve at 9.8 minutes using a product ion scan set 212 m/z of Figure 0.69.

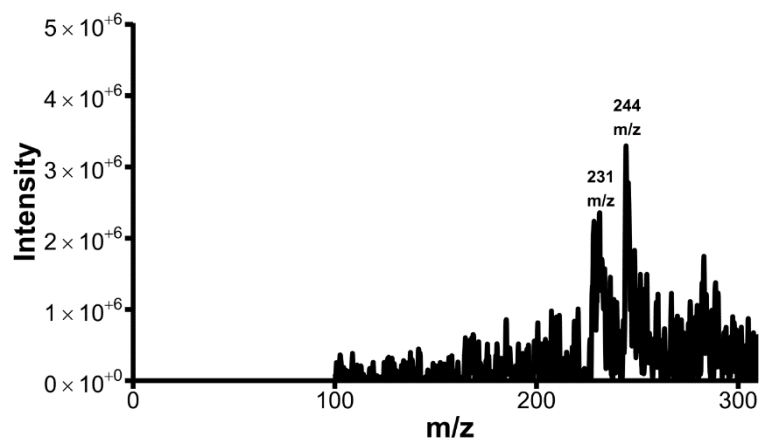


Figure 0.72: Mass spectrum for the area under the curve at 11.2 minutes using a product ion scan set to 242 m/z of Figure 0.70.

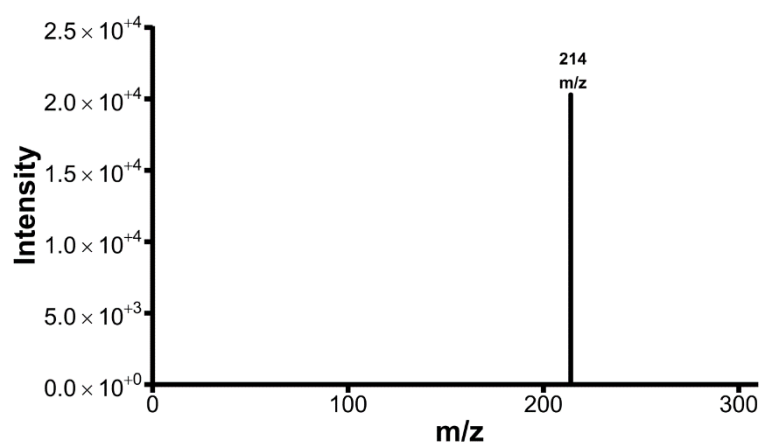


Figure 0.73: Mass spectrum for the area under the curve at 11.2 minutes using an MRM scan set to 242 > 214 m/z of Figure 6.12a.

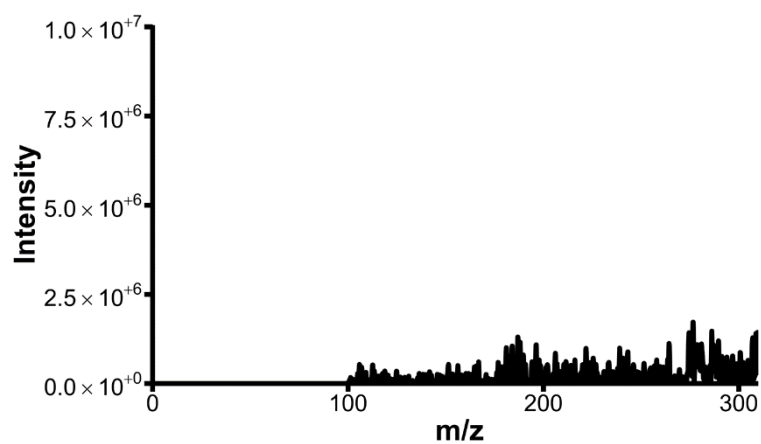


Figure 0.74: Mass spectrum for the area under the curve at 9.8 minutes using an MRM scan set to 212 > 155 m/z of Figure 6.12b.